

Title	高耐久性リチウムイオン二次電池用高分子化イオン液体バインダー
Author(s)	PINDI JAYAKUMAR, TEJKIRAN
Citation	
Issue Date	2020-09
Type	Thesis or Dissertation
Text version	ETD
URL	http://hdl.handle.net/10119/17011
Rights	
Description	Supervisor:松見 紀佳

Poly(ionic liquid) Based Binders for Highly
Durable Li-ion Secondary Batteries

TEJKIRAN PINDI JAYAKUMAR

Japan Advanced Institute of Science and Technology

Doctoral Dissertation

Poly(ionic liquid) Based Binders for Highly
Durable Li-ion Secondary Batteries

TEJKIRAN PINDI JAYAKUMAR

Supervisor: Professor Noriyoshi Matsumi

Graduate School of Advanced Science and Technology

Japan Advanced Institute of Science and Technology

Materials Science

September 2020

Poly(ionic liquid) Based Binders for Highly Durable Li-ion Secondary Batteries.

Chapter 1: Background

The current thesis is based on the design and development of poly(ionic liquid) (PIL) based materials for Li-ion secondary battery (LiB) applications. Most of the commercial LiBs have graphite-based anodes. The performance and safety of these LiBs depend predominantly on the electrode-electrolyte interface, generally referred to as the solid electrolyte interface (SEI). Hence, it is very crucial to tune the SEI both compositionally and morphologically to enhance the performance of LiBs. PILs is a class of innovative polymers which combines the properties of ionic liquids such as ionic conductivity, electrochemical and chemical stability and non-flammability with the mechanical toughness and processability of polymers. Ohno et al. have explored the use of PILs as in the energy application as electrolytes and have derived very promising results. Yuan et al. have reported the ability of the PIL to enhance the charge carrier ability at the electrode-electrolyte interface by creating a PIL/electrolyte heterojunction. This ability of PILs can be exploited to enhance the interfacial properties of the electrodes. The availability of a plethora of structurally diverse PILs allows for interfacial tuning to obtain the desired properties. This thesis explores the interfacial tuning using PIL based binders and surface modification of the active material by PILs as shown in Figure 1. The relation of PIL structure vis-à-vis its performance has been investigated to understand the role of the substituent and the counter-ion.

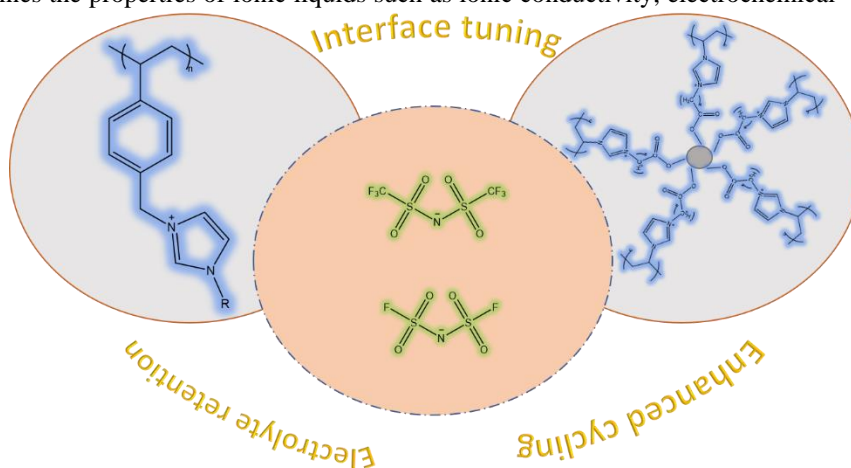


Figure 1. Graphical abstract of the current research

Chapter 2: Allylimidazolium Based Poly(ionic liquid) Anodic Binder for Lithium-ion Batteries with Enhanced Cyclability.

In this chapter, the design and synthesis of an allylimidazolium based PIL as a binder for graphite anode were carried out. Engineering the structure and HOMO-LUMO levels of the binder is very crucial in tuning its properties. Though the binder constitutes a very small fraction of the gravimetric weight of the electrode, it can have a great effect on the performance of the LiB. Poly(vinylbenzylallylimidazolium bis(trifluoromethane)sulfonylimide) (PVBCAImTFSI) comprising an imidazole heterocycle and allyl substituent (Figure 2) was used as a binder for graphite anodes in lithium-ion batteries. DFT based theoretical studies also speculated the suppression in the electrolyte degradation in the case of PVBCAImTFSI binder due to the positioning of its HOMO-LUMO levels as compared to the electrolyte. As predicted, anodes with the PVBCAImTFSI binder exhibited lesser electrolyte degradation, decrease in intercalation-deintercalation overpotential and higher lithium-ion diffusion. Electrochemical Impedance Spectroscopy (EIS) results showed decreased interfacial and diffusion resistance for PVBCAImTFSI based electrodes after cycling. Dynamic Electrochemical Impedance Spectroscopy (DEIS) results indicated that the SEI resistance for the PVBCAImTFSI based anodes to be three times lesser than the PVDF based anodes. A reversible discharge capacity of 210 mAh/g was obtained for PVBCAImTFSI based half-cells at 1C rate as compared to the 140 mAh/g obtained for PVDF based anodic half-cells. After 500 cycles, 95% retention in the discharge capacity was

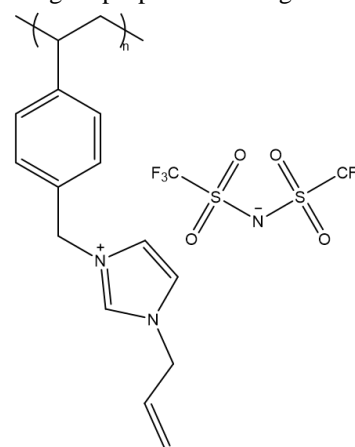


Figure 2. Structure of PVBCAImTFSI

observed. Also, PVBCAImTFSI based anodes exhibited better charge-discharge stability than the PVDF based anodes. Suppression of electrolyte degradation, reduction in the interfacial resistance, enhanced wettability and optimal SEI layer formed in the case of PVBCAImTFSI based anodes cumulatively led to enhanced stability and cyclability during the charge-discharge studies as compared to the commercially employed PVDF based anodes. Thus, the tuning of the interfacial properties leads to the improvement in the performance of the lithium-ion batteries with PVBCAImTFSI as a binder. A graphical representation of functioning of the binder is shown in the Figure 3. However, it is crucial to understand the effect of the substituent and the counter-ion on the PIL vis-à-vis its performance as a binder. This is investigated in the next chapter by evaluating the performance of the PILs with different substituent and counter-ion.

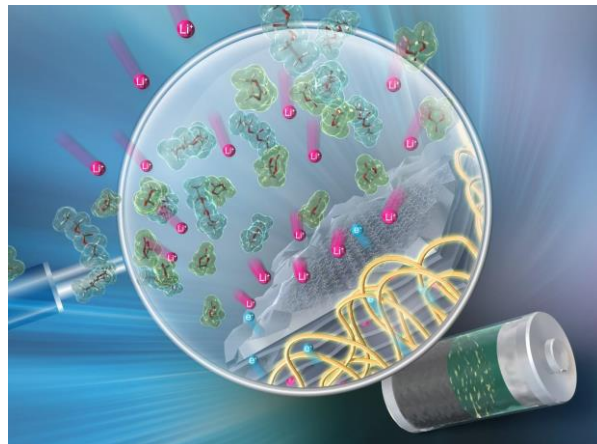


Figure 3. Graphical abstract of the functioning of PVBCAImTFSI binder

Chapter 3: Effect of the PIL Binder Structure on the Performance of the Lithium-ion Batteries.

Two structurally varying poly(ionic liquids) were synthesized to understand the effect of the PIL structure on its performance as a binder in LiBs. This will help in the tuning of the polymer structure to optimize its performance in LiBs. The properties of ionic liquids such as ion conductivity, glass transition temperature, viscosity etc. can be tuned by a simple modification of the side-chain or changing the counter-ion. Side-chains such as allyl group increases the ionic conductivity and decreases the viscosity of the ionic liquids. Counter-ions especially FSI assists in the formation of a better electrode-electrolyte interface. Therefore, in this study, the design of PILs was carried such that one of the PILs PVBCAImFSI contain both the allyl side-chain and FSI anion. The other PIL PVBCBImTFSI has an alkyl chain and TFSI anion. Cyclic voltammetry studies indicated a suppressed electrolyte degradation for PVBCAImFSI based anodes leading to the formation of a better interface. This was supported by the DEIS measurements whose results indicated lesser R_{SEI} values for the PVBCAImFSI based anodes. Also, the lithium-ion diffusion kinetics was found to be better in these electrodes. The charge-discharge measurements were carried out to evaluate the durability and stability of the electrodes. Half-cells with PVBCAImFSI based graphite anodes showed enhanced durability up to 1500 cycles with a 60% capacity retention. By changing the TFSI anion to FSI in PVBCAImTFSI, a 400% increase in capacity retention was observed after 1500 cycles. Whereas PVBCBImTFSI based LiBs showed lower capacities with lesser durability. The current study highlights the importance of the side-chain and the counter-ion present on the PIL vis-à-vis its performance as a binder in LiBs as shown in Figure 4.

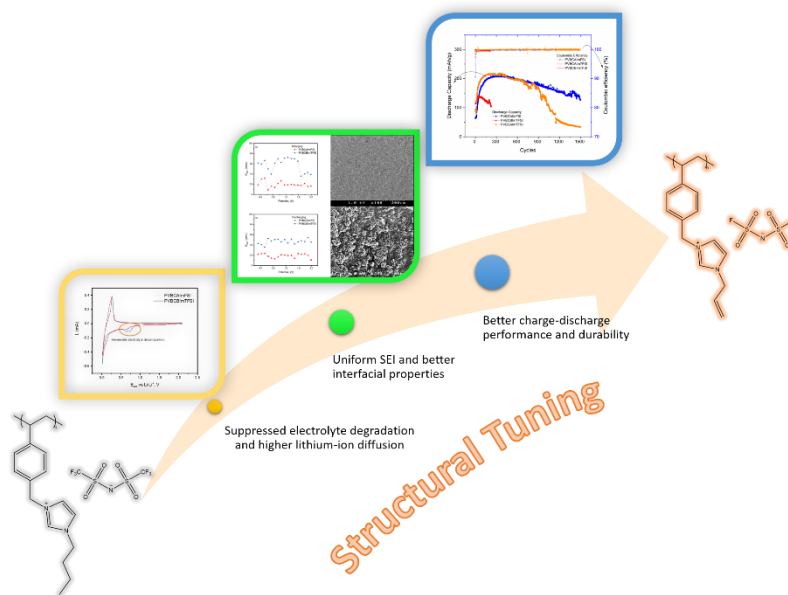


Figure 4. Graphical abstract showing the effect of tuning of PIL structure on its performance

Half-cells with PVBCAImFSI based graphite anodes showed enhanced durability up to 1500 cycles with a 60% capacity retention. By changing the TFSI anion to FSI in PVBCAImTFSI, a 400% increase in capacity retention was observed after 1500 cycles. Whereas PVBCBImTFSI based LiBs showed lower capacities with lesser durability. The current study highlights the importance of the side-chain and the counter-ion present on the PIL vis-à-vis its performance as a binder in LiBs as shown in Figure 4.

Chapter 4: Surface Tethered Poly(ionic liquid) for Silicon Nanoparticles in Li-ion Battery Composite Anodes.

The above results show the ability of the PILs to tune the electrode-electrolyte interfacial properties. This led us further to design surface-modified silicon nanoparticles for composite anodes to obtain higher capacities than the conventional graphite anodes. In this chapter, poly(ionic liquid) (PIL) tethered silicon nanoparticles were investigated (Figure 5) as active material in combination with graphite for lithium-ion battery composite anodes. The results obtained are encouraging and calls for more optimization of functionalization and PIL structure. Silicon falls into the category of high energy density materials with a gravimetric energy density of over 4000 mAh/g, has immense potential to plug the current energy demand. However, due to the inherent volumetric changes researchers have failed in many attempts to commercialize silicon anode based lithium-ion batteries. Formation of a passivation layer (SEI) at the electrode-electrolyte interface is very crucial in preventing the damage to the electrode in the harsh cycling conditions. An ideal SEI layer must be ionically conductive and electronically non-conducting. The PILs are known to possess good ionic conductivity and can act as interface enhancing agents to design a better interface. In this work, PIL functionalized silicon nanoparticles were prepared by esterification of poly[1-(5-carboxypentyl)-3-vinyl-1H-imidazol-3-ium bromide] with hydroxyl functionalized silicon nanoparticles. Cyclic voltammetry studies of PIL functionalized silicon nanoparticles based composite anodes indicated an increase in the lithiation-delithiation currents with the cycling. They also exhibited a very high lithium-ion diffusion coefficient of about 1.01×10^{-8} cm/s which indicated a robust and conductive SEI formation. These electrodes exhibited about 735 mAh/g of reversible discharge capacity after 34 cycles. This chapter presents preliminary results and performance of the anodes can be improved by more fine-tuning of the PIL structure and functionalization.

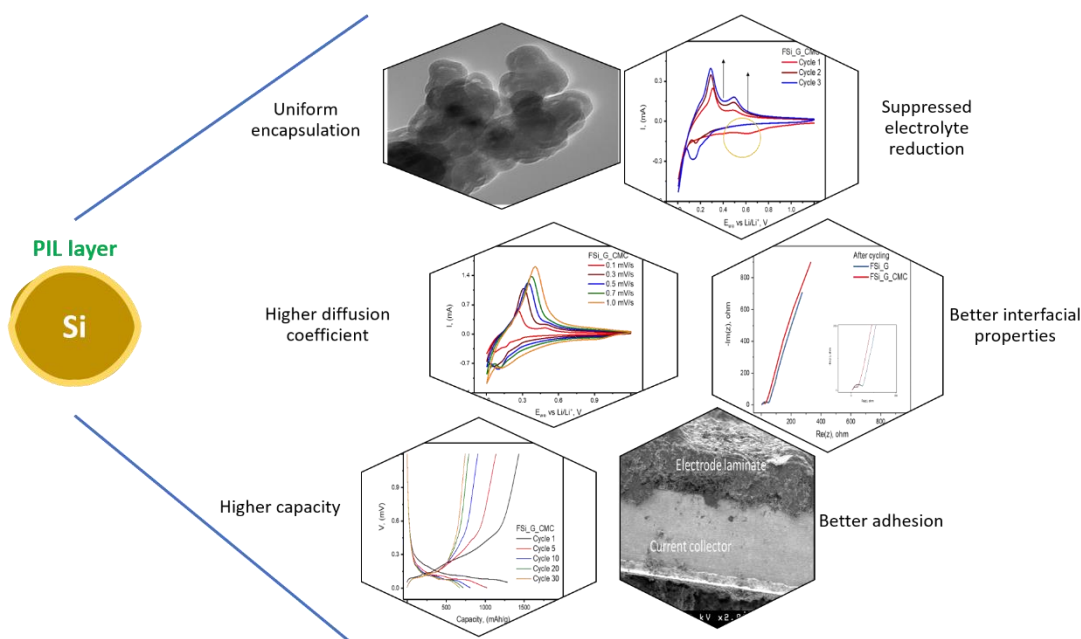


Figure 5. Summary of Surface Tethered Poly(ionic liquid) for Silicon Nanoparticles for LiB anodes

Keywords: Poly(ionic liquids), lithium-ion batteries, graphite anodes, binders, interfacial tuning, surface-functionalized silicon nanoparticles, structure-activity relationship.

Dedicated in gratitude to my family...

Preface

This thesis is the consolidation of the results of my doctoral research work titled “Poly(ionic liquid) Based Binders for Highly Durable Li-ion Secondary Batteries.” This work was carried out under the supervision of *Prof. Noriyoshi Matsumi* at the Graduate School of Advanced Science and Technology, Japan Advanced Institute of Science and Technology during the period 2017-2020.

Society today is plagued serious issues such as global warming, pollution and depletion of natural resources. In this context, the research and development of electrochemical energy sources like batteries, fuel cells etc. are picking up to be an alternative for the traditional fossil fuel-based technologies. Lithium-ion batteries (LiBs) is one of these technologies that has been widely commercialized for a variety of applications. One of the key components that determine the performance of the LiB is the passivation layer referred to as the solid electrolyte interface. The composition and the morphology of this layer are very crucial to achieve optimal performance. Many approaches have been explored to tune this layer to achieve the desired results. Some of the popular approaches include the use of functional polymeric binders, electrolyte additives, surface modification of electrode material etc. Poly(ionic liquid)s (PILs) is an innovative class of polymers which is gaining wide popularity due to chemical and electrochemical stability, non-flammability, electrolyte uptake etc. This thesis explores the applicability of the PILs as polymeric binders and surface modification to tune the interfacial properties in the LiBs. The effect of the PIL structure on its performance as a binder was investigated. Also, the PIL functionalization of silicon nanoparticles was carried out and its electrochemical performance was evaluated. The final chapter concludes all the studies carried out in the thesis.

Tejkiran Pindi Jayakumar

Graduate School of Advanced Science and Technology

Japan Advanced Institute of Science and Technology

September 2020.

Acknowledgements

This work has been carried out under the supervision of *Prof. Noriyoshi Matsumi* at Graduate School of Advanced Science and Technology, Japan Advanced Institute of Science and Technology in the period 2017-2020. The author expresses his deepest gratitude to his supervisor *Prof. Noriyoshi Matsumi* for his constant guidance, support, motivation and encouragement throughout this work.

The author also takes this opportunity to thank the members of the review committee, *Assoc. Prof. Hajime Matsumoto*, *Assoc. Prof. Yuki Nagao*, *Prof. Yoshifumi Oshima* and *Assoc. Prof. Shun Nishimura* for their valuable time to evaluate my thesis and comments that improved the overall quality of the thesis.

The author is also grateful to *Assoc. Prof. Arun Venkatnathan* for allowing carrying out the minor research in his laboratory at the Department of Chemistry, IISER Pune, India. The author also expresses his gratitude to *Assoc. Prof. Toshiaki Taniike* for his valuable guidance for the minor project.

In the course of work at JAIST, the author is thankful to *Asst. Prof. Rajashekar Badam* for his constant motivation, all the useful discussions, suggestions and contributions made to this thesis. The author is grateful to all the past and present members for all their cooperation, support and stimulating discussions during this work. The author would also like to thank Dr Takahiro Kitano from TEC ONE Co. Ltd for his timely support, technical help during the battery fabrication. The author is grateful to Dr. G Krishna Prasad for his characterization support for Chapter 4 and to Dr. Maninder Singh for TGA measurements.

The author is eternally grateful to his parents, family and close friends for providing constant support, love and standing by the author in difficult times and providing all the emotional and mental strength to keep the work going.

Finally, the author expresses his deep reverence and gratitude to the almighty for everything bestowed upon him.

Tejkiran Pindi Jayakumar

Graduate School of Advanced Science and Technology

Japan Advanced Institute of Science and Technology

September 2020.

Table of Contents

Preface

Acknowledgement

Chapter 1. Introduction

1.1. Abstract	1
1.2. Energy	2
1.3. Batteries and its evolution	5
1.4. Overview of Anode Materials in LiBs	17
1.5 Solid Electrolyte Interface and its Importance	24
1.6. Polymeric Binders in LiBs	29
1.7. Poly(ionic liquid)s in Energy Application.....	31
1.8. Objective and Scope of the Thesis	36
References	38

Chapter 2. Allylimidazolium Based Poly(ionic liquid) Anodic Binder for Lithium-ion Batteries with Enhanced Cyclability

2.1. Abstract	48
2.2. Introduction	49
2.3. Materials and Methods.....	51
2.3.1. Materials	51
2.3.2. Instrumentation	51
2.3.3. Synthesis	52
2.3.4. Characterization.....	54
2.3.5. Electrode and Cell Fabrication	57
2.3.6. Electrochemical Instrumentation	57
2.4. Results and Discussions	58
2.4.1. Theoretical Simulations	58

2.4.2. Electrochemical Characterization	60
2.4.3. Morphology and Composition Analysis	75
2.4.4. Adhesion and Electrolyte Interaction	79
2.5. Conclusions	82
References.....	5284

Chapter 3. Effect of the PIL Binder Structure on the Performance of the Lithium-ion Batteries

3.1. Abstract.....	89
3.2. Introduction	90
3.3. Materials and Methods.....	93
3.3.1. Materials	93
3.3.2. Instrumentation	93
3.3.3. Synthesis	93
3.3.4. Characterization.....	96
3.3.5. Electrode and Cell Fabrication	96
3.3.6. Electrochemical Instrumentation	97
3.4. Results and Discussions	98
3.4.1. Electrochemical Characterization	98
3.4.2. Morphology and Composition Analysis	112
3.5. Conclusions	116
References	117

Chapter 4. Surface Tethered Poly(ionic liquid) Silicon Nanoparticles for Li-ion Battery Composite Anodes

4.1. Abstract.....	121
4.2. Introduction	122
4.3. Materials and Methods.....	124
4.3.1. Materials	124
4.3.2. Instrumentation	124
4.3.3. Synthesis	125

4.3.4. Characterization.....	127
4.3.5. Electrode and Cell Fabrication	131
4.3.6. Electrochemical Instrumentation	131
4.4. Results and Discussions	132
4.4.1. Electrochemical Characterization	132
4.5. Composition Analysis	140
4.6. Conclusions	140
Chapter 5. Summary and Outlook	144
List of Publications and Conferences	149

Chapter 1

Introduction

1.1 Abstract

Energy drives every aspect of human life today. Since the industrial revolution, a variety of sources has been explored to derive energy. In this chapter, a brief account of primary sources of energy is given highlighting difficulties in their harvesting and impact on the environment. The evolution of the batteries with Li-ion batteries (LiBs) as game-changer has been detailed. A comprehensive account of various components in LiBs like electrodes, electrolytes etc., has been presented with few important examples. The significance of solid electrolyte interface (SEI) and its composition in the performance of LiBs is also highlighted. This chapter also further introduces poly(ionic liquids) underlining their attractive properties which can revolutionize the functioning of the LiBs.

1.2 Energy

Energy is simply defined as the ability to do work and is a cause for any change in the state of an entity. Energy can be classified based on its source or form into various forms. The conservation law of energy rules governs that energy can neither be created nor destroyed but converted from one form to another. An energy source is defined as an entity capable of producing energy. For instance, Sun is the primary source of energy for our planet. In general, the sources of energy can be classified as primary or secondary based on the state in which they are available. Primary energy sources consist of sources in original or unconverted form like coal, crude oil etc., and have to be mined, harvested or extracted. The secondary sources of energy are readily available for consumption and are obtained from a primary source of energy. For example, petroleum is not available directly in nature but has to be obtained from crude oil. Also, based on their availability, primary energy sources can be classified as renewable and non-renewable. Non-renewable sources of energy are those which are available in limited quantities and take a long time to be replenished. This category includes fossil fuels like coal and crude oil and natural gas.

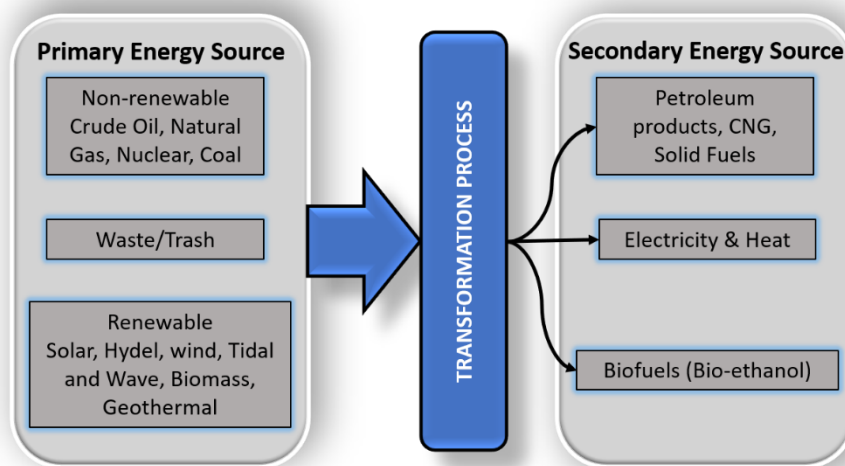


Figure 1.1 Classification of common sources of energy.

Whereas, renewable energy is obtained from sources that are naturally replenished in over short periods. This class predominantly includes solar, wind, hydel, biomass and geothermal energies. Figure 1.1 shows the classification of the common energy sources based on their state. The industrial revolution of the 19th century made way for many inventions which were driven by steam obtained by converting the fossil fuel-based non-renewable sources of energy. These

inventions led to the growth of the trade, economy and wide-scale development of mankind. The fossil fuel-based energy sources mainly constitute coal, crude oil and natural gas. These are formed under the crust of the earth by subjecting organic flora and fauna to high pressure and temperature over a long period. Fossil fuels especially coal were the easily available source of energy during the industrial revolution. The steam engines used in industries, as well as transportation, were powered by the coal. One of the advantages of using coal as a source of energy is its availability just a few feet below the ground. This is the reason why even most of the current day electricity-generating power plants are thermal power plants powered by coal. With the gradual development of the technology, extraction of the other fossil fuels such as crude oil and natural gas has become possible and their wide-scale application. Crude oil products such as petroleum and diesel power most of today's automobiles, whereas kerosene-based fuels are used in space applications. In addition to this, other petroleum products are used as fuel oils for electricity and heat generation, as asphalt and road oil. Many other petroleum-based products are used as chemical feedstocks in the manufacture of plastics and other kinds of chemicals. Liquefied petroleum gas commonly known as LPG is the most commonly used as cooking gas all across the world in addition to its automobile applications. As the fossil fuel-based energy sources are non-renewable, they are available in limited quantity and non-uniformly distributed. More importantly, their adverse effect on the environment was understood only in the last few decades. Use of these fuels is known to generate greenhouse gases such as carbon monoxide, carbon dioxide, SO_x and NO_x gases which cause global warming. The effect of global warming on the melting of polar ice caps, increasing seawater levels, disturbed climatic patterns etc., has caught global attention in the last few decades. The current situation demands more sustainable and environmentally friendly technologies to achieve a sustainable society. To achieve a perfect balance between the availability of natural resources and societal demands, the current energy policies need to be completely reformed. Hence, many countries are heavily investing in developing and adopting renewable energy sources for the generation of electricity and other applications. The Global Status Report (GSR) released by the thinktank Renewable Energy Policy Network for the 21st Century (Ren21) released in the year 2019 puts the share of the renewables at 26.2% in the production of the electricity. Hydel power contributes as much as a whopping 15.8% followed by wind power at 5.5%. Countries such as China, the USA, Germany, India and Japan are heavily investing in the renewable sources of energy especially in the solar photovoltaics for power generation in the last few years. These

countries produced almost 75% of the global solar photovoltaic based electricity. India has commissioned the world's largest solar power plant in the year 2019 with a capacity of 2 GW. However, these technologies involve the use of bulky equipment and are mostly stationary. Hence, it is very crucial to explore alternative sources of renewable energies which can be mobile, more safe, efficient, cost-effective, highly durable, better shelf life and easier to scale up with wide-scale applicability.

Energy production based on the principles of electrochemistry has been one of the most promising technologies developed in the 21st century. It is very important to explore electrochemical energy production as an alternative source of energy production to achieve sustainability and scalability. In this regard, various technologies have been developed and many of them have been commercialized. Batteries, supercapacitors and fuel cells are some of the technologies that have found great commercial success in the last few decades. These technologies involve the conversion of chemical energy into electrical energy and vice versa. These energy sources can be the best substitute available if they meet the current requirements for the sustainability and environmentally friendly approach. With most of these devices being smaller and mobile, they are in high demand in transportation, communications, defence and many other areas of society. Therefore, immense efforts have been directed towards improving these technologies as well as explore newer ones. Many automobile manufacturers have already commercialized vehicles based on batteries and fuel cells generally referred to as Electric Vehicles (EVs) with an attractive drive range as shown in Figure 1.2. For instance, Leaf from Nissan and Model 3 from Tesla are some of the very popular battery-based EVs currently available. These vehicles may cost between 30000 to 100000 USD and have a driving range of 200 – 400 miles on a single charge. Luxury car makers such as Porsche, Audi, BMW and Mercedes Benz have also introduced some of their EVs already and are also planning to reveal more models soon. There are



Figure 1.2 From left to right, Nissan Leaf (battery based), Mitsubishi Fuso eCanter, Tata motors Starbus (fuel cell based). (Pictures taken from internet)

EVs that are fuel cell-based such as Mirai from Toyota, Tuscan from Hyundai and Clarity from Honda. However, these are mostly on a leasing agreement from the company in many cases. There also been an attempt to develop heavy vehicles such as buses and trucks based on batteries and fuel cells by Daimler AG, Mitsubishi Fuso and Tata motors. Batteries among the other electrochemical technologies have found greater interest and success leading to its commercialization in many fields. A variety of batteries were developed with unique features based on the device or technology it is integrated with it. They have been custom made to the needs of the consumers with keeping the performance, production feasibility, environmental impact etc., in mind. We come across many types of batteries ranging from lead-acid batteries used for uninterrupted power supplies (UPS) to lithium-ion batteries (LiBs) which powers most of our portable electronics. The gravimetric energy density of the lithium-ion battery is about 200 kWh/kg as compared to 12000 kWh/kg of gasoline. But the effective energy delivery of LiB compared to any thermal engine has lead LiBs to gain immense popularity. It can be seen used in mobile phones, laptops and also in electric vehicles. With the current progress in batteries, we can foresee a very promising future in many of the crucial sectors. However, there is a lot more to be done to improve its performance, safety, longevity etc. This calls for much more fundamental research to understand the working of components and improvising them systematically, which is the underlying current for this thesis.

1.3 Batteries and its Evolution

A battery can be simply defined as a power source that can generate a definite amount of electrical energy driven by a chemical reaction. Energy storage and energy discharge over some time are the two basic qualifications for any battery. The root of the word battery is from old French word *batterie*, meaning to strike relating to the use of cannons in the battle. The first instance of using the term battery relating to electricity was done by the U.S. scientist Benjamin Franklin in 1749 to describe the arrangement of capacitors used in experiments with electricity. The discovery of the Baghdad battery in 1983 in Baghdad dates the use of this technology back to 2000 years. The typical structure of a battery is made up of a negative electrode referred to as anode and a positive electrode referred to as cathode along with ion-conducting electrolyte as shown in Figure 1.3. The electrical energy is generated by the conversion of the chemical energy produced due to the redox reactions at the respective electrodes. The electrolyte functions as a medium for ion

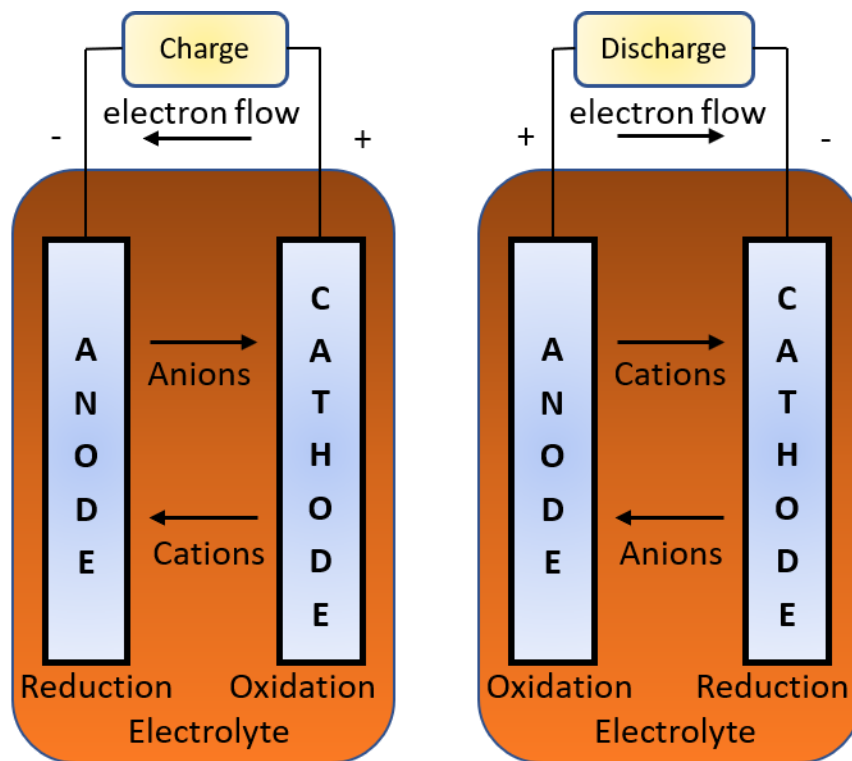


Figure 1.3 Schematic representation of a battery explaining the ionic as well as electronic flow during the charging and discharging of a battery.

transport as well as a separator between the electrodes. An external assembly connecting both the electrodes completes the circuit by providing a pathway for the electron flow. Based on this concept, batteries can be made using different sorts of electrodes and electrolytes. However, it is not as simple as mentioned and the evolution of the batteries has been slower than other areas of electronics. The chronological milestones in the development of the batteries have been tabulated in Table 1.1.^{1,2} We can understand that the battery technology has made advancements in leaps and bounds in the last few decades. With the most commonly used lead-acid batteries and nickel or zinc hydride batteries reaching their performance and output thresholds, more efficient and newer LiBs have made their mark replacing them. Especially, the progress made with LiB technology in the last two decades had a huge impact on the development of society. In recognizing this, the Nobel prize for the year 2019 in chemistry was awarded to Akira Yoshino, John Goodenough and M. Stanley Whittingham for their contributions in the development of the LiBs. The award declaration states, “Through their work, they have created the right conditions for a wireless and fossil-fuel-free society, and so brought the greatest benefit to the humankind”. This statement summarizes the impact that LiBs on today’s society.

Table 1.1 Major breakthroughs in the development of batteries highlighting their evolution.

Year	Contribution	Event
250 B.C.	Archaeologists (1983)	Baghdad battery – porcelain jars with rolled copper sheets around an iron rod filled with an acidic liquid.
1748	Benjamin Franklin	Coins the word battery
1800	Alessandro Volta	Devised the first battery – voltaic pile (silver or brass or copper and zinc or tin discs separated by cloth wet with brine).
1836	John Fredric Daniell	Developed Daniell cell – a constant source of electricity.
1859	Glaston Plante	Developed first rechargeable battery – lead-acid battery with 2.0V voltage output.
1866	George Lionel Lechlanche	Developed the prototype of the modern dry cell – zinc rod(anode) and carbon rod (cathode) in ammonium chloride with 1.5V voltage output.
1878	Maiche	Developed first air cell – gelled zinc powder anodes and carbon cathodes. Air is passed into the cathode where it gets reduced on the carbon surface.
1899	Waldmar Jungner	Invented Ni/Cd batteries with Ni(OH) ₂ as anodes and cadmium-iron powder cathodes in KOH with an output voltage of 1.2V. One of the most successfully commercialized batteries.
1901	Thomas Edison	Developed Ni/Fe batteries with all iron cathodes similar to Ni/Cd batteries with an output voltage of 1.2V. This also has gained commercial interest.
1945	Samuel Ruben	Designed Zn-HgO battery with Zn amalgam as anode and HgO-Carbon composite as a cathode in conc.KOH solution as the electrolyte.

1951	Union Carbide	Developed first button cell for use in batteries with Zn leads and HgO which was later changed to Ag ₂ O with a voltage output of 1.55V.
1959	Lew Urry/Eveready	Commercialization of the first alkaline battery with Zn anode and MgO ₂ cathode and strong KOH electrolyte. Could be operated at lower temperatures.
1970	Oxford researchers	Established the intercalation of Li ions intercalation in spinel materials to form LiA _z B _y which can be used as the active material.
1970	Stanley Wittingham	Developed Li-TiS ₂ battery with good potential and voltage output of 2V. However, was commercially not viable due to the presence of metallic lithium.
1973	SAFT Batteries	Developed first commercial Li-ion primary batteries for military applications.
1978	Rachid Yazami	Demonstrated successful reversible Li-ion intercalation in graphite which is anodic active material in most of the LiBs.
1980	John Goodenough	Demonstrated that the Li-ion intercalation into cobalt oxide can produce about 4V paving way for more powerful batteries.
1985	Akira Yoshino	Developed the first commercially viable secondary LiB with LiCoO ₂ cathode and petroleum coke as the anode.
1991	Sony Corporation	Commercialized the first secondary Li-ion battery which revolutionized the concept of portable devices.
1994	Bellcore	The invention of Li-ion polymer battery (one of the most successful commercial variant of LiB).
1996	University of Texas	Identification LiFePO ₄ as a potential cathode material for LiBs. Many commercially available LiBs are made up of this cathode.

2019	Stanley Wittingham / John Goodenough / Akira Yoshino	Nobel prize was awarded to three scientists for their contribution to the development of LiBs. The award read, “Lithium-ion batteries have revolutionized our lives since they first entered in 1991. They have laid the foundation of a wireless, fossil-fuel-free society, and are of the greatest benefit to humankind.”
------	--	---

The most basic classification of the batteries can be made based on their ability to be recharged as primary and secondary batteries. Few examples of each kind have been mentioned in Table 1.2. Primary batteries are designed for single-use purposes and cannot be recharged. The chemistry of the primary batteries does not allow for recharge and reuse. The chemical reactions that happen in the battery are not reversible. Hence they are limited to few applications. There are multiple reasons as to why primary batteries cannot be recharged.

1. **Formation of gases:** Most of these batteries employ aqueous electrolytes which electrolyze at higher potentials. Upon the reversal of potential, they release gases which might lead to cell rupture and loss of contact. These lead to the complete collapse of the battery.
2. **Electrode structural changes:** Some of these primary batteries contain electrodes which undergo dissolution on discharging via redox reactions. On the subsequent reversal of the potential to recharge the battery may lead to the formation of the electrode not similar in its initial structure. This makes its recharging difficult and hazardous.
3. **Shorting:** Shorting of a cell occurs when the two opposite electrodes come in contact with each other leading to permanent damage of the battery. This happens when the separator separating the electrodes is damaged. Many times recharging a primary battery leads to the extensive formation of dendrites which pierces through the separator leading to the shorting of the battery.

Table 1.2 . Few examples of primary and secondary batteries. (Wikipedia)

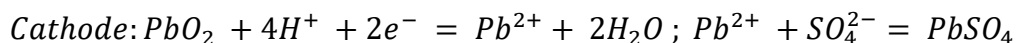
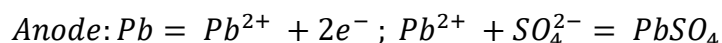
Primary Batteries	Secondary Batteries
<ul style="list-style-type: none"> • Alkaline battery • Aluminium-air • Chromic acid cell • Clark cell (Zn/Hg) • Dry cell • Daniell cell (Zn/Cu) • Galvanic cell • Leclanché cell • Magnesium battery • Mercury battery • Organic radical battery • Silver – oxide battery • Voltaic pile • Weston cell • Zinc-air battery • Zinc chloride battery 	<ul style="list-style-type: none"> • Aluminium – ion battery • Carbon battery • Glass battery • Lead-acid battery • Lithium-air battery • Lithium-ion battery • Lithium-ion polymer battery • Lithium iron phosphate battery • Lithium cobalt oxide battery • Lithium titanate battery • Lithium-sulfur battery • Lithium ceramic battery • Magnesium ion battery • Nickel-cadmium battery • Nickel iron battery • Potassium ion battery • Silver zinc battery • Sodium-ion battery • Zinc ion battery

On the other hand, secondary batteries, storage battery or charge accumulator can be reused multiple times by recharging. This is possible due to the reversibility of the chemical reactions and the battery can be recharged just by changing the direction of the chemical reaction. This implies that the original state can be restored by passing electricity through the battery (charging) from an external source. This ability is bestowed by the presence of redox couples present in the batteries. The cathode undergoes oxidation releasing electrons into the external circuit during the charging cycle and anodes get reduced by taking the electrons. During the discharging, the reverse of the

above process takes place. The flow of electrons in the external circuit constitutes for the electricity generated. The ion transfer occurs through the electrolyte which is stable in the battery operational potential window. This process can be repeated many times, usually in terms of a few hundred cycles and a few thousand cycles for certain types. It is still considered a renewable source of energy due to its rechargeability, recyclability and environmentally friendliness. The lead-acid battery was the first secondary battery designed and developed by Glaston Plante in 1859 and is one of the most popular secondary battery used today. Other popular secondary batteries include nickel-cadmium battery, Li-ion based batteries and silver-zinc battery. The ideal criterion for a storage battery is low resistance, design flexibility, stability, durability and low cost. The chemistry, advantages and disadvantages of a few secondary battery systems and the need to develop more efficient and safer batteries are discussed below

Lead-acid battery:

The lead-acid battery has a history of about 160 years and no other battery has replaced its applications in certain sectors. These batteries are utilized in lighting, UPS, as emergency power for pumps, as traction batteries in vehicles and other current demanding applications. The battery is generally represented electrochemically as $\text{Pb}/\text{H}_2\text{SO}_4/\text{PbO}_2$, Pb^+ or Pb/PbSO_4 , $\text{H}_2\text{SO}_4/\text{PbSO}_4/\text{PbO}_2/\text{Pb}^+$. Lead-acid batteries comprise of a sponge metallic lead anode, lead dioxide cathode and dilute aqueous sulphuric acid as an electrolyte as shown in Figure 1.4. During discharge of the battery lead in both the electrodes react with the sulphuric acid leading to the formation of lead sulphate and water as represented by the below reaction.



The overall reaction is: $\text{Pb} + \text{PbO}_2 + 2\text{H}_2\text{SO}_4 \rightleftharpoons 2\text{PbSO}_4 + 2\text{H}_2\text{O}$

During the charging of the battery, the lead sulphate breaks down and combines with the oxygen from the water regenerating the electrodes. Though the stepwise mechanism is not completely understood, the overall reaction is confirmed. A maximum of 2.2V is achieved on

proper charging of this battery. 80% efficiency can be obtained and sometimes this can be as high as 95%. The prime advantages of this battery are its low cost, higher shelf life and toughness.

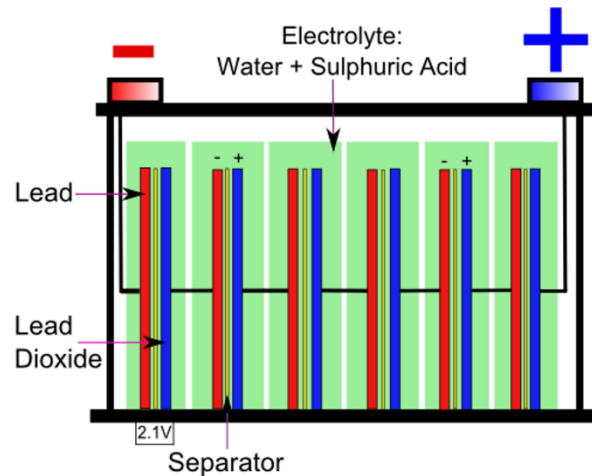


Figure 1.4 Schematic representation of a Lead-acid battery with its components.

Nickel-cadmium battery:

Nickel-cadmium batteries are known for their performance in high-discharge and ability to operate at lower temperatures. These batteries contain a cadmium-based anode and nickel-based cathode with aqueous KOH as the electrolyte as shown in Figure 1.5. In the charging cycle, nickel hydroxide in the cathode gets converted to nickel oxide hydroxide whereas cadmium hydroxide in the anode releases cadmium ions. During the discharge cycle, the reverse of the process occurs regenerating back the active material. The applications of these batteries include portable power tools, flashlights, emergency lighting etc. These batteries also have a long shelf and use life similar to lead-acid batteries. However, an extreme drawback these batteries suffer is memory effect. This refers to the loss of capacity when a cell is charged without completely discharging.

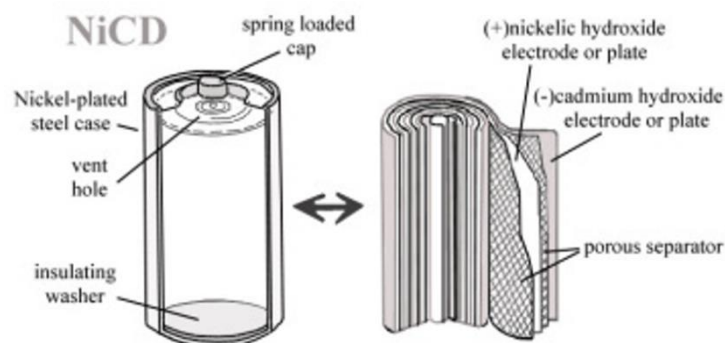


Figure 1.5 Schematic representation of a nickel-cadmium battery with its components.

Lithium-ion battery

Lithium-ion batteries (LiBs) have gained significance and attention in the last few decades due to their attractive features over other conventional secondary batteries. A typical lithium-ion battery contains graphite anode and lithium cobalt oxide cathode separated by a separator as shown in Figure 1.6. LiBs due to the higher gravimetric energy density was a ray of hope to replace the heavier batteries such as lead-acid or nickel-cadmium batteries for the more ubiquitous portable electronic devices being developed. Once commercialized in 1991, LiBs became the battery of choice due to its high energy density, lightweight, design flexibility, and longer life span as compared to the existing battery technologies.^{3,4} Though its impressive advancement compared to other battery technologies, the advancement of the science behind the battery chemistry has often under criticism due to slower progress. The increase in the energy storage capacity of a battery

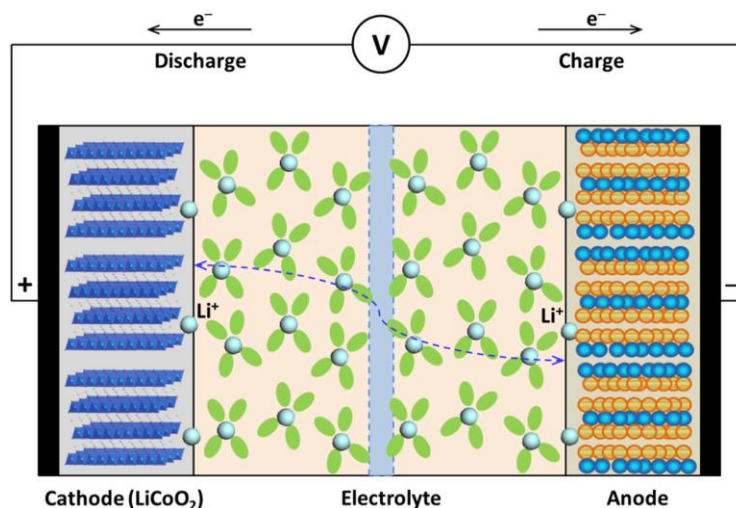


Figure 1.6 Schematic representation of LiB with graphite anode, lithium cobalt oxide cathode separated by separator and electrolyte.

could never keep up with the progress in other electronic components such as processors, hard drives etc. In most of these cases, as shown in Figure 1.7, their capacity doubled once in two years as predicted by Moore's law. Nevertheless, the technological advancements in LiBs and Ni-metal hydride batteries supplementing and replacing the older technologies have been spectacular and encouraging. Table 1.3 gives various features of the rechargeable batteries such as specific energy, cell voltage, cutoff limits etc. Specific energy of a battery is defined as the amount of electrical energy that can be obtained from a battery expressed in terms of Wh/kg or Wh/l as a function of

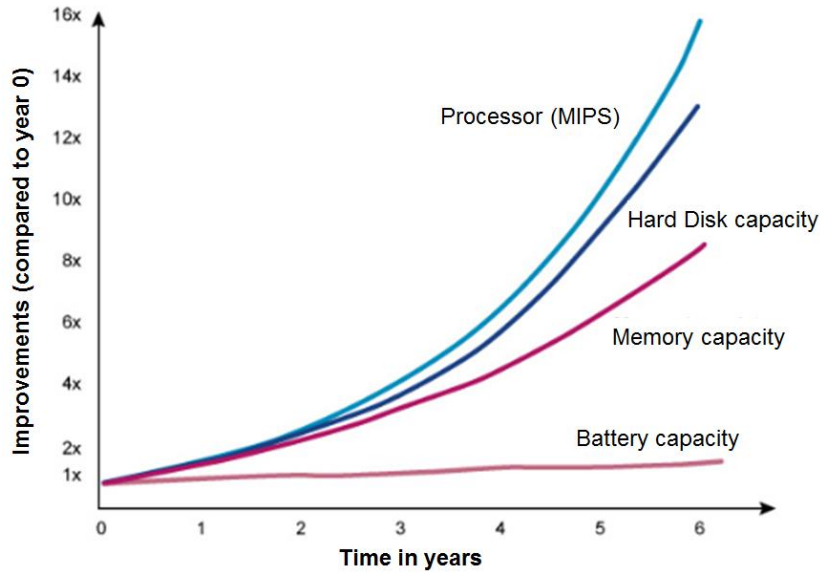


Figure 1.7 Evolution of battery and computing technologies.

the cell potential (V) and capacity Ah/g. These factors are directly linked to the inherent chemistry of the batteries. Lithium being most electropositive (-3.04 V vs SHE) as well as lightest (equivalent weight = 6.94 g/mol and specific gravity $\rho = 0.53 \text{ g/cm}^3$) was considered initially an attractive choice as an anode. This facilitated energy storage systems with high energy density. Lithium

Table 1.3 Comparison of features of popular secondary batteries.

Specifications	Lead-Acid	NiCd	NiMH	Li-Ion		
				Cobalt	Manganese	Phosphate
Specific energy density (Wh/kg)	30 – 50	45 – 80	60 – 120	150 – 190	100 – 135	90 – 120
Internal resistance (mΩ/V)	<8.3	17 – 33	33 – 50	21 – 42	6.6 – 20	7.6 – 15.0
Cycle life (80% discharge)	200 – 300	1,000	300 – 500	500 – 1,000	500 – 1,000	1,000 – 2,000
Fast-charge time (hrs.)	8 – 16	1 typical	2 – 4	2 – 4	1 or less	1 or less
Overcharge tolerance	High	Moderate	Low	Low	Low	Low
Self-discharge/month (room temp.)	5 – 15%	20%	30%	<5%	<5%	<5%
Cell voltage	2.0	1.2	1.2	3.6	3.8	3.3
Charge cutoff voltage (V/cell)	2.40 (2.25 float)	Full charge indicated by voltage signature	Full charge indicated by voltage signature	4.2	4.2	3.6
Discharge cutoff volts (V/cell, 1C*)	1.75	1	1	2.5 – 3.0	2.5 – 3.0	2.8
Peak load current**	5C	20C	5C	> 3C	> 30C	> 30C
Peak load current* (best result)	0.2C	1C	0.5C	<1C	< 10C	< 10C
Charge temperature	-20 – 50°C	0 – 45°C	0 – 45°C	0 – 45°C	0 – 45°C	0 – 45°C
Discharge temperature	-20 – 50°C	-20 – 65°C	-20 – 65°C	-20 – 60°C	-20 – 60°C	-20 – 60°C
Maintenance requirement	3 – 6 months (equalization)	30 – 60 days (discharge)	60 – 90 days (discharge)	None	None	None
Safety requirements	Thermally stable	Thermally stable, fuses common		Protection circuit mandatory		
Time durability				>10 years	>10 years	>10 years
In use since	1881	1950	1990	1991	1996	1999
Toxicity	High	High	Low	Low	Low	Low

metal was initially used in the primary batteries during the 1970s which provided high capacity, and variable discharge rate. During the same period, many inorganic materials were designed which can reversibly intercalate lithium ions which led to the development of reversible high-density energy batteries. First such system technology was developed by Exxon in 1972 which employed Li metal anode, TiS_2 cathode and lithium perchlorate in dioxolane as the electrolyte.^{5,6} Though TiS_2 cathode was displaying impeccable performance, this battery was not commercialized due to the uneven lithium dendrite formation resulting due to the lithium metal-liquid electrolyte combination. The uneven growth of the dendrites resulted in the puncture of the separator leading to short of the battery and explosion. Meanwhile, many metal oxide-based cathode material was discovered at Bell Labs which exhibited higher voltage and capacities. The discovery of Li_xMO_2 class of material by Goodenough revolutionized the cathode materials and are in use in most of the current day LiBs.^{7,8} To overcome the dendrite formation, metallic lithium was replaced with a second insertion material as shown in Figure 1.8. This class of battery referred to as lithium-ion battery or rocking battery contained lithium in ionic form, eliminated the dendrite problem and improved the safety of the battery. Then it took almost a decade to optimize the right

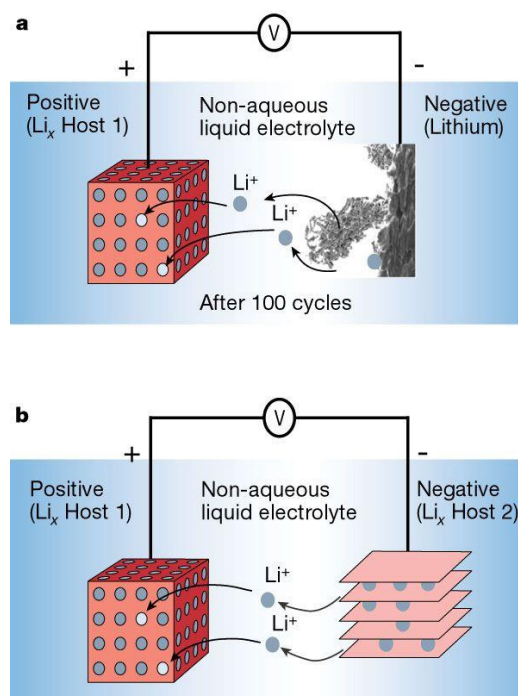
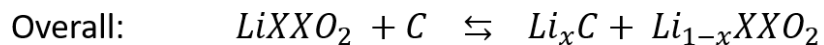
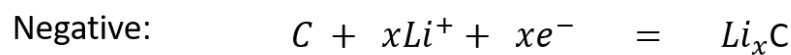
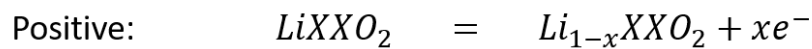


Figure 1.8 Schematic representation of rechargeable lithium batteries
a) Rechargeable Li-metal battery with dendrite formation b) Li-ion battery (LiB).
 (adopted from 3)

anode material and electrolyte combination. Finally taking advantage of the previous finding of reversible and low potential lithium-ion intercalation-deintercalation by Rachid Yazami and other researchers,^{9,10} and the LiCoO₂ by Goodenough, C/LiCoO₂ battery rocking chair battery was commercialized by Sony Corporation in 1991. This battery containing carbonaceous coke based anode and LiCoO₂ cathode exhibited a voltage of about 3.6 V and specific energy of about 120-150 Wh/kg. The general chemical reactions that take place in the cell is represented in Figure 1.9.



XX = Various combining elements including cobalt and manganese

Figure 1.9 Chemical reaction taking place at each electrode and overall reaction in a LiB.

Another approach adopted was to completely replace the liquid electrolyte by an alternative polymer-based electrolyte giving rise to lithium solid polymer battery (Li-SPE). However, it was restricted to use in traction and backup power systems and were not portable. Also, it required an operational temperature of about 80 °C. These drawbacks led to the development of lithium hybrid polymer electrolyte (Li-HPE) battery wherein, the electrolyte comprised of three components: polymer matrix, liquid solvent and a salt. This design allowed for exploiting the advantages of the polymer electrolyte and also decreasing the hazards arising from the electrolytes. One of the most successful Li-HPE batteries was developed by Bellcore referred to as plastic lithium-ion batteries (PLiON)¹¹. These batteries offered shape versatility, flexibility and were thin and light. In recent years, to improve the safety and performance, researchers are working on developing all-solid-state batteries (ASSBs) containing solid electrolytes (metal oxides, sulphides or phosphates). Researchers at Samsung have successfully developed ASSB with the specific capacity of about 210 mAh/g corresponding to an energy density of about 900 Wh/l.¹² This is being considered as a breakthrough and is being hoped to be commercialized soon. This chapter further discusses the

various electrode and electrolyte materials currently being used in LiBs to understand how the need for higher specific energies is driving the research in developing new materials.

1.4 Overview of Anode Materials in LiBs

Since the successful commercialization of the LiBs by Sony Corporation, there has been an active drive for designing newer materials with higher specific energy to meet the ever-expanding need for energy. Improving the specific energy is very crucial for meeting the demands for developing EVs, which is greatly dependant on the materials breakthroughs. Anodes play a very crucial role in the performance of LiB as the features of anodic material will have a direct implication on the electrochemical performance of the battery. Hence, both the physical as well as chemical properties of the anode material must be carefully considered and controlled. The expected properties of an ideal anode include high specific energy, high reversible volumetric and gravimetric energy densities, lower potential vs Li/Li^+ , good mechanical strength, long durability and rate capability, and environmental compatibility. Pure lithium metal is an attractive choice due to its high gravimetric energy density as well as low potential. However, lithium electroplating and dendrite formation during the battery operation have been a grave safety concern for its use as an anode. Figure 1.10 illustrates the gravimetric capacity and voltage characteristics of a variety of anode active materials. Therefore a variety of carbon and non-carbon based materials have been investigated to evaluate their application as an anode. Broadly, most of the anode active materials

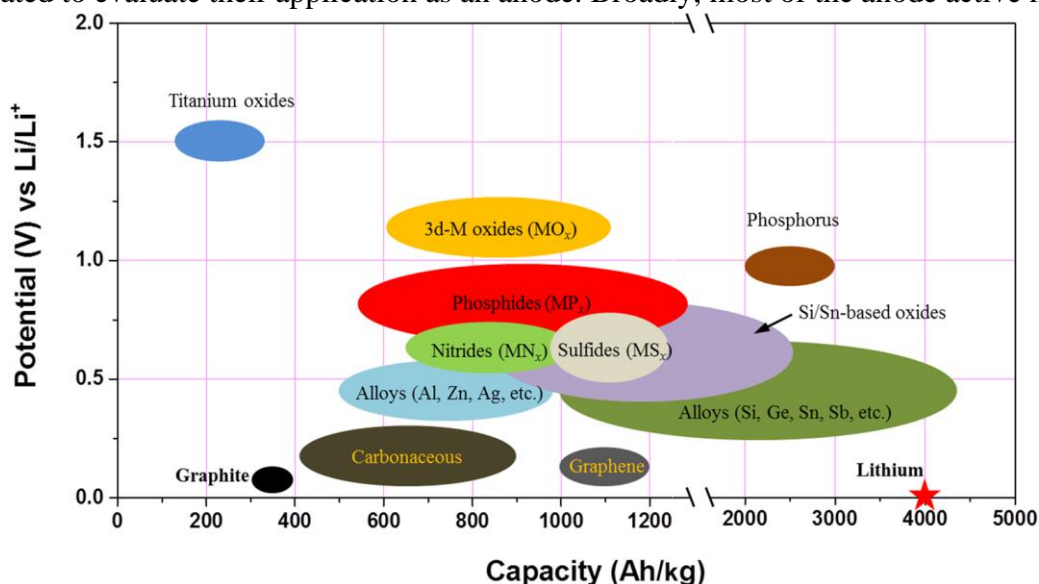


Figure 1.10 Schematic illustrating the gravimetric capacities vs voltage characteristics of anode active materials for LiBs. (adopted from 3)

can be classified as intercalation, alloy, metal oxide and other carbonaceous based materials.^{13,14} However, so far carbonaceous materials have gained great interest after the successful commercialization of carbon-based LiB by Sony Corporation.

Intercalation based material:

Carbon-based intercalation material especially graphite is the most commonly used anode materials in the commercial LiBs. Unlike other soft and hard carbons, graphite exhibit a flat potential profile while intercalation and deintercalation of lithium ions below 0.5 V vs Li/Li⁺. Graphite offers a gravimetric energy density of 372 mAh/g corresponding to one lithium per six carbon atoms (LiC₆) with limited irreversible capacity.¹⁵⁻¹⁷ Graphene layers in graphite are stacked as AB or ABC sequence, held by van der Waals forces.¹⁸ Lithiation and de-lithiation occur by

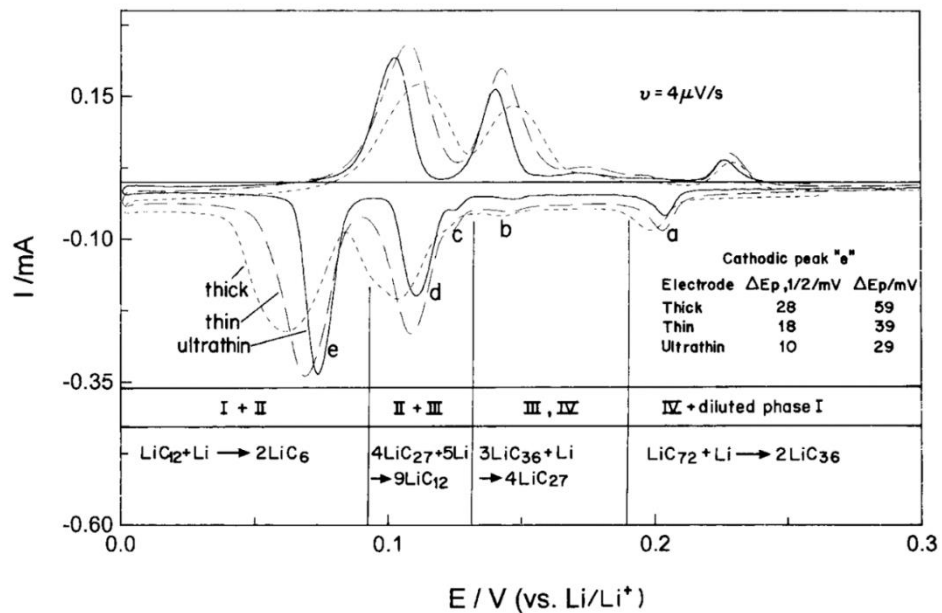
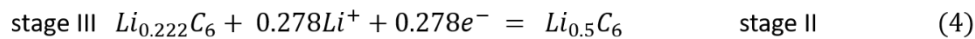
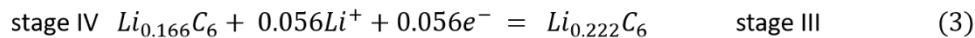
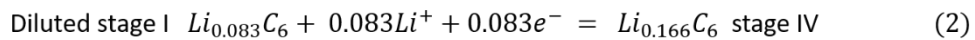


Figure 1.11 Voltammetric behaviour of graphite anodes of different thickness at slower scan rate in EC-DMC 1:3/LiAsF₆ solution. (adopted from 19)

staging mechanism and leads to AA stacking configuration. Another great advantage of graphite is its electronic conductivity arising due to the sp^2 -hybridization of the carbon atoms present on the planar, hexagonal structures in the graphene sheets. Aurbach et al¹⁹ have studied the voltammetric behaviour of graphite anodes with different thickness of coatings at very slow scan rate to understand the intercalation mechanisms involved. The reactions (1-5) were established corresponding to each stage shown in the voltammogram in Figure 1.11. One of the drawbacks observed with the graphite anodes was the co-intercalation of propylene carbonate electrolyte resulting in 150% volume expansion and subsequent exfoliation of the graphene layers.¹⁷ In addition to this, the working potentials of the electrodes were outside the potential stability window of the electrolytes leading to the continuous degradation of the electrolyte over the electrode resulting in the capacity fade, drying up of the cell and battery failure. However, the problem of the co-intercalation was overcome by replacing the propylene carbonate electrolytes with short-chain linear alkyl carbonates like diethyl carbonate, dimethyl carbonate etc. Although these solvents not being stable at the lower potentials, their initial decomposition leads to the formation of a passivating layer referred to as the solid electrolyte interface (SEI). This layer being electronically insulating will prevent further electrolyte degradation and also the co-intercalation of the solvent molecules into graphite. The formation mechanisms and theories proposed for the formation of SEI are discussed in the latter part of this chapter. Though the use of graphite anodes in the commercial LiBs was a great success, there are some drawbacks such as lithium plating, limited rate capability and high reactivity of the lithiated graphite towards solvents. These pose safety hazards due to thermal runaways and even causing fires sometimes.^{20,21} Hence, more research has to be carried out to overcome these drawbacks. Other carbon-based materials such as hard carbon²², graphene,²³ carbon nanotubes,²⁴ fullerenes etc. were also explored as anodic materials. Yoo et al demonstrated that by controllably adjusting the d-spacing between the graphene sheets, the reversible capacity can be increased. For instance, by increasing the d-spacing from 0.34 nm to 0.4 nm, the reversible capacity derived can be increased to as much as 784 mAh/g. Another approach to improve the electrochemical performance was to incorporate heteroatoms like nitrogen in the graphene sheets. Presence of these heteroatoms will increase the lithium coverage by strengthening the lithium graphene binding energies.^{25,26} However, graphene-based materials often suffer from lower specific capacity due to the restacking of the graphene layers. Also, due to their high surface area, the irreversible capacity observed is very high due to high

consumption of lithium ions resulting in lower coulombic efficiencies. This remains an open question to be solved and at present limited research has been focused.

Among the non-carbon based anodes, lithium titanate (LTO) with a spinel structure is very promising. Lithium titanate ($\text{Li}_4\text{Ti}_5\text{O}_{12}$) was initially reported in the year 1994.²⁷ On lithiation

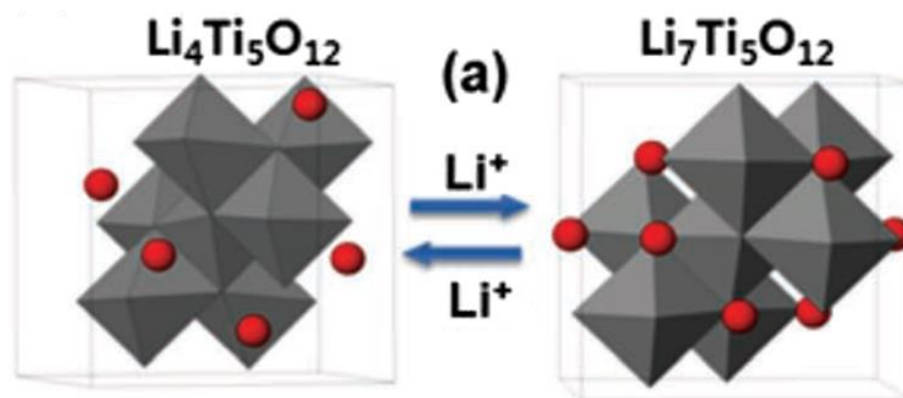


Figure 1.12 Structures of $\text{Li}_4\text{Ti}_5\text{O}_{12}$ and $\text{Li}_7\text{Ti}_5\text{O}_{12}$ showing no volume change during charge-discharge cycling. (adapted from 27)

lithium titanate converts to $\text{Li}_7\text{Ti}_5\text{O}_{12}$ which is separated by an almost ideal heterointerface. LTO offers a theoretical capacity of about 175 mAh/g with very less irreversible capacity. LTO is well known as zero-strain material for LiBs due to a negligible volume expansion of about 0.2% during the phase transition. This allows for cycling stability of a few tens of thousand fast charge-discharge cycles. Also, due to higher working potential around 1.5 V vs Li/Li^+ , there is no rigorous electrolyte degradation occurs. Also, due to its operating potential being far away from the potential where lithium plating takes place, the dendrite formation is avoided making them safer.¹³ However, LTO suffers from poor electronic conductivity ($\sim 10^{-13}$ S/cm) leading fast lithiation and de-lithiation processes. Many approaches such as surface treatment,²⁸ size reduction,²⁹ increasing porosity³⁰ etc were carried out to overcome the above drawback. Other titanium-based material like TiO_2 has been investigated as anode material and was established that the performance is highly dependent on the crystal structure. TiO_2 (B) (monoclinic) was found to be an ideal host for lithium insertion and extraction. However, experimentally it was found to be very challenging to achieve its theoretical capacity of 330 mAh/g.³¹ To obtain high capacity, very careful control of the size, morphology and crystal structure is necessary.³² Armstrong et al established that TiO_2 -B nanotubes or nanowires with a diameter of about 40-60 nm and length of few microns exhibited enhanced rate capability and high capacity of 305 mAh/g.³³

Alloy based material:

Many elements such as silicon, tin, germanium, phosphorus etc. are capable of forming reversible alloys with lithium at lower potentials. The capacity of these alloy-based anodes is 2-11 times higher than the graphite anodes. Unlike intercalation anodes, alloy-based anodes have a different lithiation mechanism and this gives rise to multiple new issues. But their higher theoretical specific capacities and energy densities are driving for intense research. One of the major problem associated with alloy-based anodes is volume changes occurring due to the lithiation and de-lithiation. The volume expansion during lithiation is about 4 times in silicon, 2.6 times in tin, 3.7 times in germanium and 3 times in phosphorus. Due to this expansion and contractions, they undergo pulverization leading to loss of electronic contact and capacity fade. Also, due to the volume expansion and contraction, the electrode-electrolyte interface is unstable and dynamic. This movement of the interface poses a challenge in developing a stable SEI. Finally, at the electrode level, expansion of individual particles cumulatively results in the swelling of the electrode which leads to difficulty in the battery design.

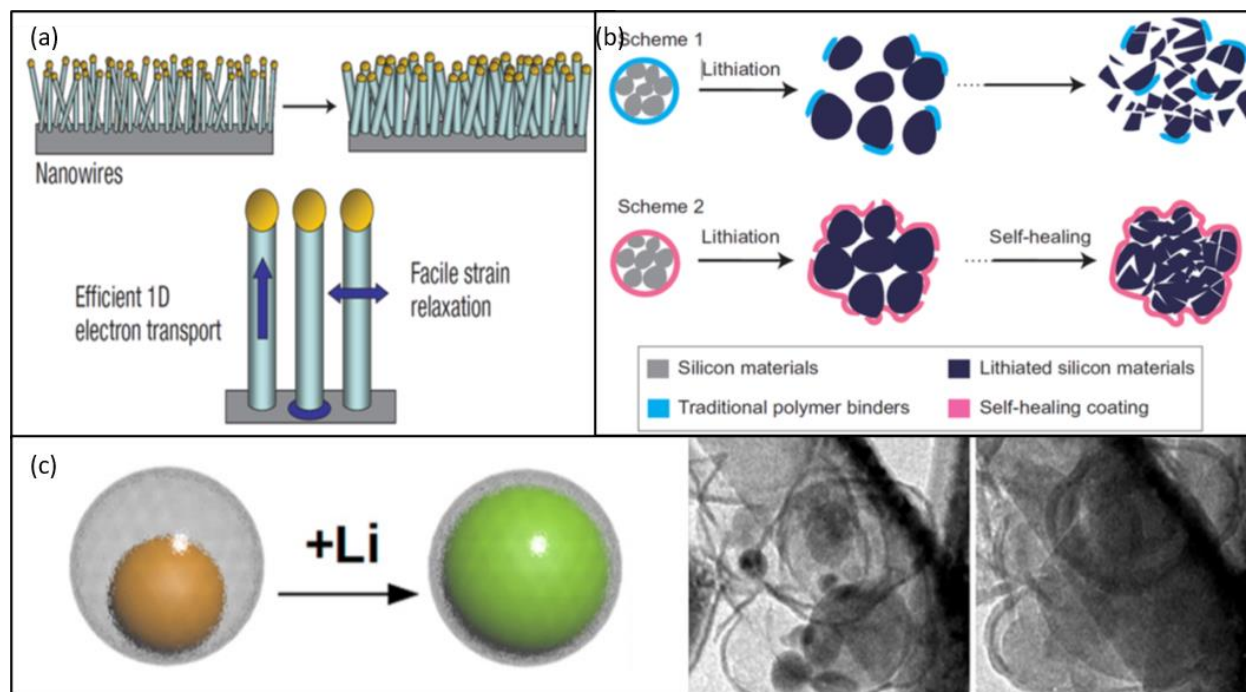


Figure 1.13 (a) Si nanowires grown directly on steel current collector allowing for efficient 1D electron transport, (b) Use of self-healing polymer to limit the pulverization of Si, (c) Si-C yolk-shell particle design which allows for the expansion of Si particle without breaking carbon coating or disrupting the SEI layer.

In the last decade, immense research has been focused on developing technologies to accommodate silicon as the active material for LiBs. Silicon with a gravimetric energy density of over 3300 mAh/g is almost 10 times higher than graphite. A variety of approaches such as material design, use of matrix, use of functional binders etc. has been investigated. Silicon nanowires due to their small diameter do not fracture and can maintain good electronic contact as shown in Figure 1.13a.³⁴ Silicon nanowires were grown over steel current collector directly and were subjected to charge-discharge cycling. A capacity of >2100 mAh/g was observed at 1C rate. Another approach is using a self-healing binder which can self-heal by the virtue of its dynamic hydrogen bonding and limit the pulverization of silicon as shown in Figure 1.13b.³⁵ Figure 1.13c shows silicon-carbon yolk-shell particle which contains a silicon nanoparticle encased in a carbon sphere with a buffer space to accommodate for the volume changes during lithiation and de-lithiation. However, more optimization and fine-tuning of the technology has to be done before we can see Si-based commercial LiBs. This might be possible soon with companies like Enevate. They have already demonstrated the high energy density Si-based LiBs and are in the process of scale-up and commercialization.

Metal oxide-based material:

The first report of using metal oxide anodes was by Poizot et al³⁶ in which metal oxides of cobalt, nickel, copper and iron were investigated. These electrodes offered specific capacities of about 700-1200 mAh/g. Since then the interest in these class of electrodes has been growing.³⁷ Figure 1.14 shows lithiation in spinel cobalt oxide. On lithiation, lithium comprising compound Li_zA_y (Where A represents O, N, F and others) forms reversibly by the displacement reaction. During the discharge, the electrode reverts to its original state by releasing lithium ion into the electrolyte. Similar to alloy-based anodes, metal oxide-based anodes also suffer from volume expansion, pulverization, unstable SEI and volume changes at the electrode level. They also suffer

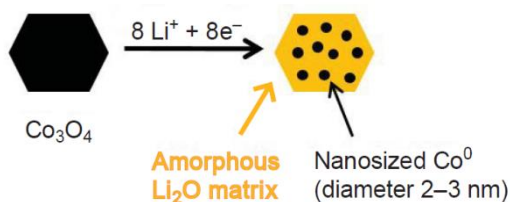


Figure 1.14 Schematic representation of the lithiation in spinel cobalt oxide based conversion anode. (adapted from 37)

from large voltage hysteresis of almost 1V due to sluggish pathways during charge-discharge cycling. This might be due to the interconversion of multiple solid phases with different structures involving the breaking of strong chemical bonds. The de-lithiation potential is also spread over 1 to 2 V which reduces the overall cell potential.

Figure 1.15 gives an overview of the different classes of anodic materials with their advantages and disadvantages. The above brief overview of the most popular anode materials for LiBs reflects only partially the intensive and continuous research efforts being carried out since the last few decades. Many more interesting materials designs have been proposed and are still in the nascent stage of optimization. One of the most crucial factors affecting the performance most of the anodes for LiBs is the nature of the electrode-electrolyte interface (SEI). Hence it is very crucial to understand the basis of SEI and how its growth can be controlled.

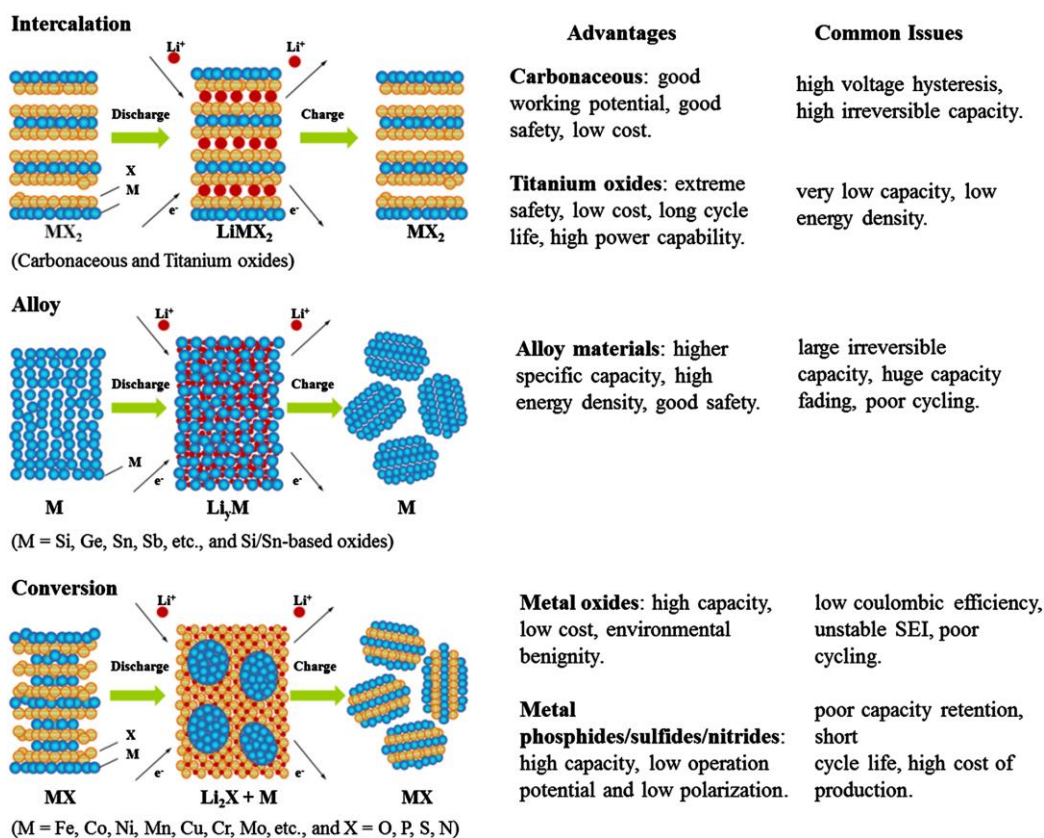


Figure 1.15 Schematic representation different types anodes along with their advantages and disadvantages. (adapted from 37)

1.5 Solid Electrolyte Interface and its Importance

Understanding the electrode-electrolyte interface is the key to enhance the electrochemical performance of a battery, as it is where the ions meet electrons and get stored in the electrode via intercalation, alloying or on lithium metal.^{19,38,39} In 1979, Peled introduced the concept of a passivation layer. This was found to be formed on the surface of graphite which was acting as a solid electrolyte and hence referred it as solid electrolyte interface (SEI).³⁸ This was supplemented with the compositional information by the research carried out in the next couple of decades by Peled et al⁴⁰ and Aurbach et al⁴¹. It was understood with more understanding that SEI to be a complex layer formed due to the decomposition of the electrolyte over the surface of the active material. Schematic representation of the SEI formation on the graphite surface at the electrode-

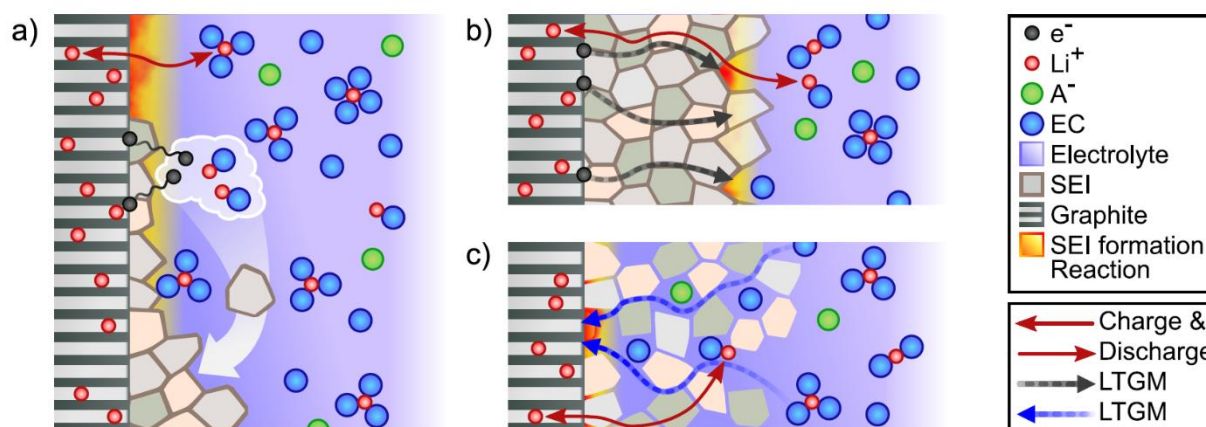


Figure 1.16 (a) Cross-sectional view through the anode and electrolyte showing the initial SEI formation (b) Long-term SEI growth via a mechanism that transport negative charge to the interface (c) Long term SEI growth via electrolyte diffusion to the interface. (adapted from 43)

electrolyte interface is given in Figure 1.16. This layer consists of insoluble and partially soluble products of the electrolyte components. The thickness of this layer is determined by the tunnelling range of the electrons and can vary between few Å to a few hundreds of Å. On one hand, a thick and dense SEI can limit the electron tunnelling preventing the further degradation of the electrolyte. On the other, SEI formation and further growth lead to irreversible electrolyte and lithium consumption leading to high irreversible capacity, capacity fade, increased cell resistance and lower power densities. An ideal SEI layer must have high electrical resistance, high cation selectivity and permeability, high strength, tolerant to expansion/contraction during cycling, insoluble in electrolyte and stability over a wide range of operational temperatures and potentials.

However, in reality, the SEI does not have all the above properties. For instance, the continuous growth of SEI is observed over repeated charge-discharge cycling. SEI is the most important and crucial component for the performance of the LiBs but least understood. The formation of SEI occurs due to the thermodynamic instability of the electrolyte components in the operational

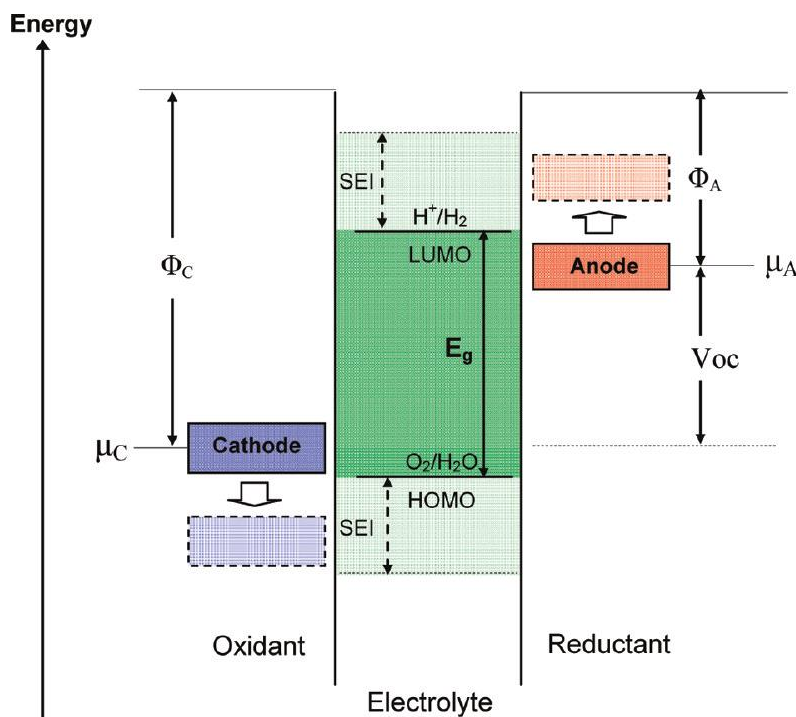


Figure 1.17 Open circuit diagram of an electrolyte illustrating the electrolyte's electrochemical stability window (E_g), anode and cathode work functions (Φ_A & Φ_C) and electrode redox potentials (μ_A & μ_C). (adapted from 42)

potential window of the electrodes as shown by Goodenough et al⁴². The anode is reductant and cathode is the oxidant. Understanding of HOMO-LUMO levels of the electrolyte gives an insight into their thermodynamic stability. When the anode electrochemical potential is above the LUMO of the electrolyte component, reduces the electrolyte unless a passivation layer is created as shown in Figure 1.17. Many models have been proposed ranging from electronic to atomic scales and theoretical evaluations of SEI were also carried out.^{43,44} One of the most popular models is a dual-structure model which describes SEI to contain two layers, an inner compact layer rich in inorganic species closer to the electrode (Li_2CO_3 , LiF, LiO_2) and an outer organic layer closer to the electrolyte (ROLi, Li_2EDC). The outer layer is porous, heterogeneous in nature and permeable to lithium ions as well as the electrolyte solvent molecules.^{40,41,45,46} One other theory based on continuum model was put forth by Broussely et al⁴⁷ based on a continuous capacity fade due to

the SEI growth. They derive an equation for the evolution of the SEI thickness. This model demonstrates the sluggish electron transport through the SEI explains the square root of time-dependence of capacity fade. Further developments to this model and long-term growth mechanisms (LGTM) allows for better modelling of the SEI.⁴⁸ Long term growth of the SEI can be perceived in two equivalent ways. As described by Figure 1.16b, the diffusion of the electrons from the graphite/SEI interface to the graphite/electrolyte interface predicts the SEI growth and on the other hand, the diffusion of the electrolyte components towards the graphite/SEI interface from the electrolyte/SEI interface as shown in Figure 1.16c equally agrees with the evolution of SEI and its thickness. Hence, properties other than SEI thickness has to be predicted by the continuum models to determine the LGTM. Traditionally, the SEI layer on the graphite surface has been characterized by surface analysis techniques such as X-ray photoelectron spectroscopy (XPS) and Fourier transform infrared spectroscopy (FT-IR) due to their surface sensitivity and ability to identify chemical species. In addition to this, techniques such as Raman spectroscopy, X-ray diffraction (XRD), nuclear magnetic resonance (NMR) and mass spectroscopy techniques such as secondary ion mass spectroscopy (SIMS) and temperature-programmed desorption mass spectroscopy (TPD-MS) have been used to characterize the SEI surface species.⁴⁹ However, the formation of chemical species in SEI is strongly dependent on the electrode and electrolyte conditions, temperature reduction current rate, contaminants present.⁵⁰ So it has proved very difficult to establish a universal standard qualitatively as well as quantitatively. However, it is possible to make some general considerations regarding the origin of the species in the SEI. For instance, it is generally accepted that the source of LiF and Li_xPF_y is LiPF_6 . Similarly, the carbonates in the electrolyte precipitate as Li_2CO_3 , lithium alkyl carbonate (ROCO_2Li) or other organic compounds after the reduction on the graphite surface. Inorganic species such as LiF, Li_2CO_3 , Li_2O etc remain on the surface of graphite insoluble whereas, organic species redissolves back into the electrolyte leading to the rearrangement in the SEI structure. Most of the electrolyte degradation occurs between 0.8 V to 0.2 V vs Li/Li^+ . The cyclic and linear alkyl carbonates might undergo one-electron or two-electron reductions as shown in Figure 1.18 and Figure 1.19 respectively.⁴⁹ After the initial reaction, the products formed will further undergo secondary reactions. The reaction products vary based on the initial reaction and also the moisture or other contaminants available like HF etc. Similarly, the electrolyte salts also undergo degradation reactions as shown in Figure 1.20. Dense inorganic salt formation occurs at the edge sites due to

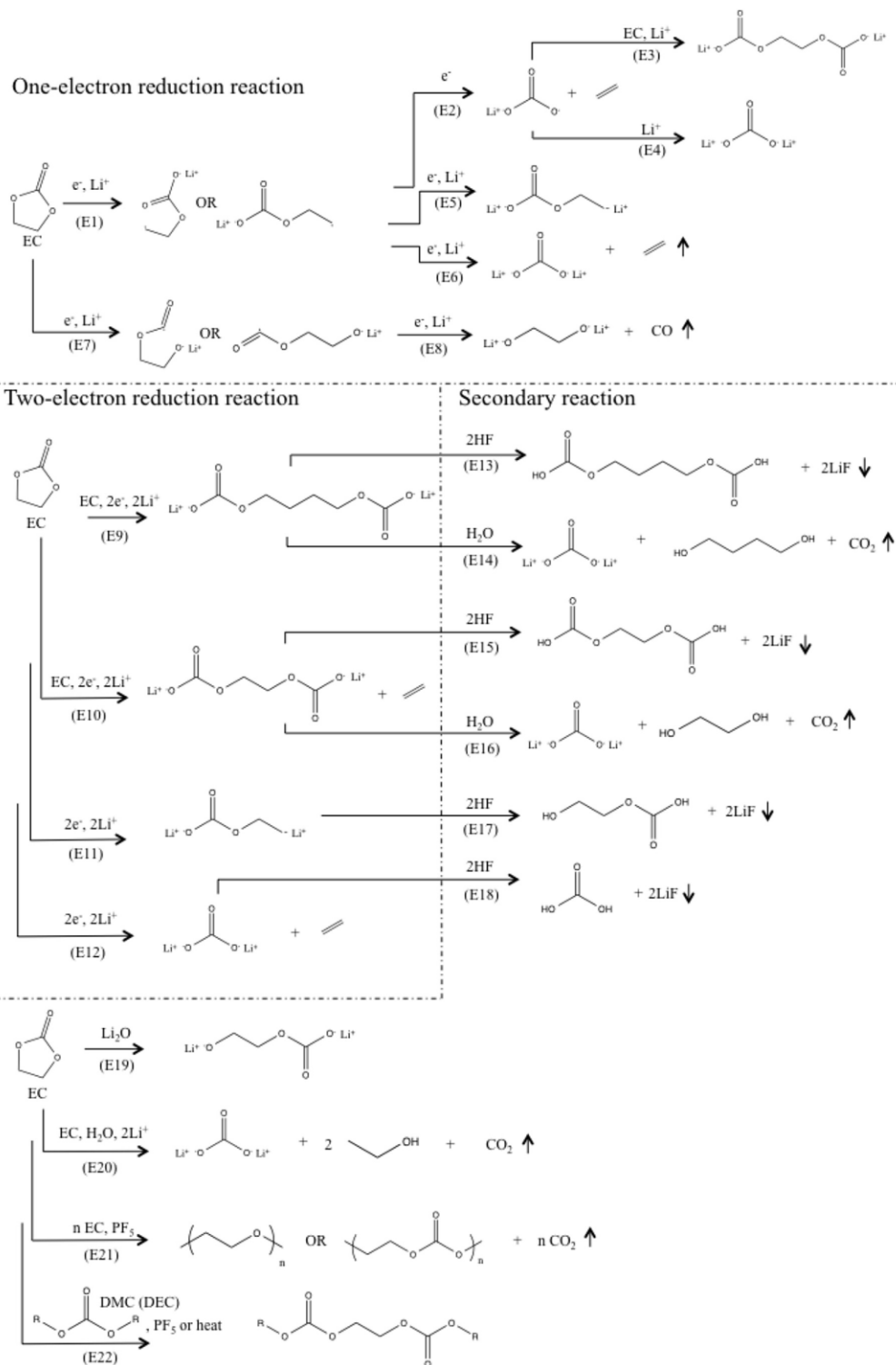


Figure 1.18 Ethylene carbonate (EC) reduction process. (adopted from 49)

the lower electronic resistance to reduce the solvent coordinated lithium ions. The charging rate also influences the composition and the morphology of the SEI. The initial charging at higher rates

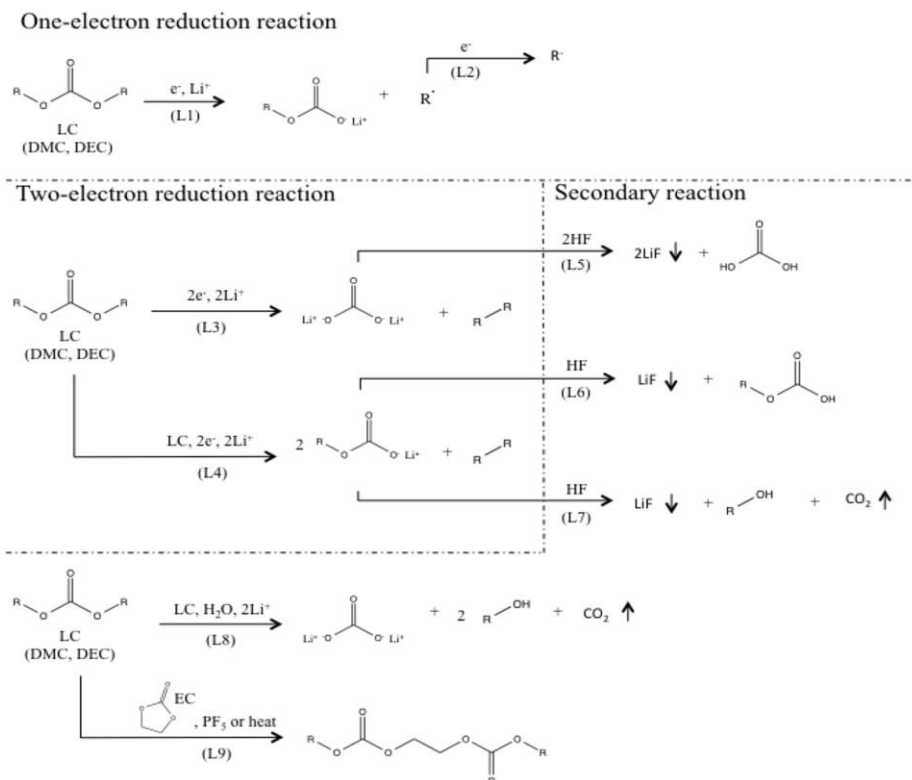


Figure 1.19 Linear carbonate (LC) reduction process. (adopted from 49)

has detrimental effects on the formation of SEI. In order to form a robust SEI, initial charge-discharge cycling is carried out at rates between 0.05C and 0.2C. However, this adds up production costs, capital expense and also slows down the production rates. Building a stable SEI at higher charging rates greater than 0.5C requires a great deal of effort in developing additives, optimizing operational conditions and modifying the surface chemistry of the active materials.

To optimize and design a robust SEI layer both in-situ or ex-situ approaches can be employed. In-situ approaches include the use of electrolyte additives and functional binders. These are the most popular in-situ approaches that have been explored in the recent past to control the growth and the composition of the SEI. Given such importance, the use of additives is still considered as a “dark art” in the electrolyte research. Most of the times, the screening of the electrolyte additives are done on a trial and error basis with no rationale on the structure-activity relationship.^{51–53} A variety of functional binders that can enhance lithium-ion conduction, assist in the SEI formation and maintain the integrity of the electrodes have been designed and were found to be effective.^{54–57} More on binders are discussed in the later section of this chapter. The ex-situ approach involves modifying the surface chemistry or pre-lithiation of the electrodes before the

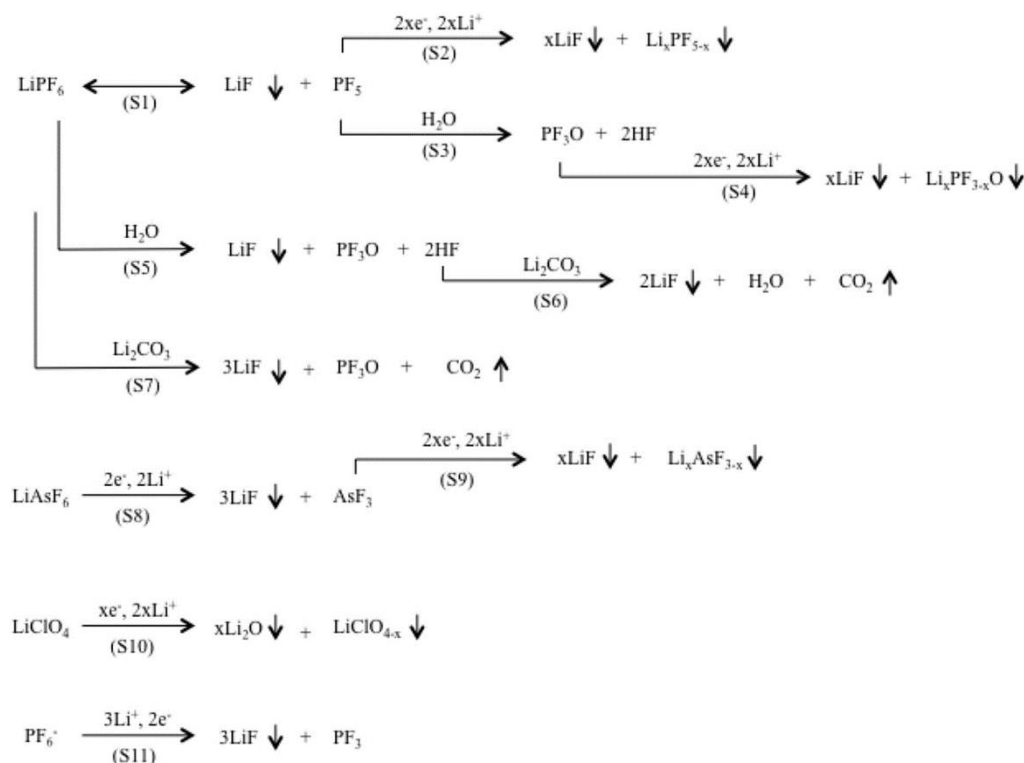


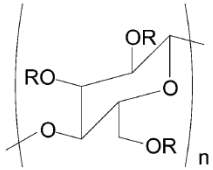
Figure 1.20 Electrolyte salt reduction process. (adopted from 49)

fabrication of the battery.^{58,59} These approaches generally referred to as artificial SEI design has been quite successful in improving the safety and the performance of the LiBs. One of the key focus of this thesis is also to improve the electrode-electrolyte interface and therefore improve the overall performance of the LiBs.

1.6 Polymeric Binders in LiBs

Polymeric binders are polymer material whose purpose is to bind the various constituents of the electrode such as active material and conductive additives to each other and the current collector. Though they constitute just about 5-20% of the total electrode mass, they play a pivotal role in maintaining the electrode integrity and their long term cyclability. Mainstream binders are poly(vinylidene fluoride) (PVDF), carboxymethylcellulose (CMC), poly(acrylic acid) and poly(ethylene glycol) (PEG) whose structures and electrode compatibility are given in Table 1.4.⁶⁰ However, these mainstream binders are being replaced functional binders which in addition to binding can also create ion-conducting pathways and assist in the SEI formation. The presence of binders becomes very significant with active materials that suffer from huge volume expansion

Table 1.4 Commonly used binders with their molecular structure and the corresponding electrode materials. (adopted from 60)

Name	Molecular structure	Electrode materials
Polyvinylidene fluoride (PVDF)	$\left(\begin{array}{c} \text{H} \quad \text{F} \\ \quad \\ -\text{C}-\text{C}- \\ \quad \\ \text{H} \quad \text{F} \end{array} \right)_n$	Graphite Si SnO ₂ SnCoC Sn Fe ₂ O ₃ NiO CuO Li ₄ Ti ₅ O ₁₂ Sulphur
Carboxymethyl cellulose (CMC)	 $\left(\begin{array}{c} \text{OR} \\ \\ \text{C} \\ \\ \text{O} \end{array} \right)_n$ <p>R = H or CH₂COONa</p>	Graphite Si SnO ₂ SnCoC Sn Fe ₂ O ₃ NiO CuO Li ₄ Ti ₅ O ₁₂ LiCoO ₂ LiFePO ₄ Li ₂ MnO ₃ -LiMO ₂ (M = Ni, Mn, or Co) LiNi _{0.4} Mn _{1.6} O ₄ LiNi _{1/3} Mn _{1/3} Co _{1/3} O ₂ Sb Sulphur Amorphous phosphorus
Polyacrylic acid (PAA)	$\left(\begin{array}{c} \text{HOOC} \\ \\ -\text{CH}_2-\text{CH}- \\ \\ \text{H} \end{array} \right)_n$	Graphite Si-graphite SnCoC Sulphur Amorphous phosphorus
Polyethylene glycol (PEG)	$\text{HO} \left(\begin{array}{c} \text{H} \quad \text{H} \\ \quad \\ -\text{C}-\text{C}-\text{O}- \\ \quad \\ \text{H} \quad \text{H} \end{array} \right)_n \text{H}$	LiCoO ₂ Sulphur

like silicon (300% of the initial volume) and pulverization during the charge-discharge cycling of the LiB. The role of binders was neglected initially, however, the pace is picking up and many novel binder designs are being synthesized. Conductive polymers,⁵⁴ self-healing polymers,⁶¹ multifunctional binders,⁶² crosslinked polymers^{63,64} and carbohydrate-based polymers⁶⁵ are being investigated as a replacement for the conventional binders. The other objectives that are yet to be researched and optimized include preserving the binder function at lower binder content, ability to bind different active materials together, improving the affinity for active materials and minimizing the lithium-ion trapping to increase coulombic efficiency. By rational design, it is possible to develop multifunctional binder that can enhance the interfacial properties, aid in better charge transfer and increase the shelf-life of the battery by trapping the acidic impurities.

1.7 Poly(ionic liquid)s in Energy Application

Ionic liquids were discovered in the year 1914 when Paul Walden synthesized a new organic salt ($[\text{EtNH}_3][\text{NO}_3]$) with an unusually low melting point of about $12\text{ }^\circ\text{C}$.⁶⁶ He classified these organic salts with a melting point less than $100\text{ }^\circ\text{C}$ as ionic liquids. However, this term became popular only in the 1990s.⁶⁷ Since then due to their interesting properties, they have been used in broad applications such as catalysis, electrochemistry, energy conversion and storage, nanotechnology etc.^{68–70}

The last two decades saw the rise in the trend of incorporating the interesting properties of electrochemical stability and ion conductivity of the ionic liquids with the mechanical and processability of the polymer architectures. Free radical polymerization of the vinyl imidazolium monomers was carried out as early as 1973 by Salamone et al.⁷¹ However, this class of polymers gained popularity towards the end of the 20th century when Ohno et al used the term poly(ionic liquid) (PIL) for the first time. PILs can be defined as a class of polymers with ionic liquid groups covalently integrated into the polymeric backbone or as a pendant group as shown in Figure 1.21.

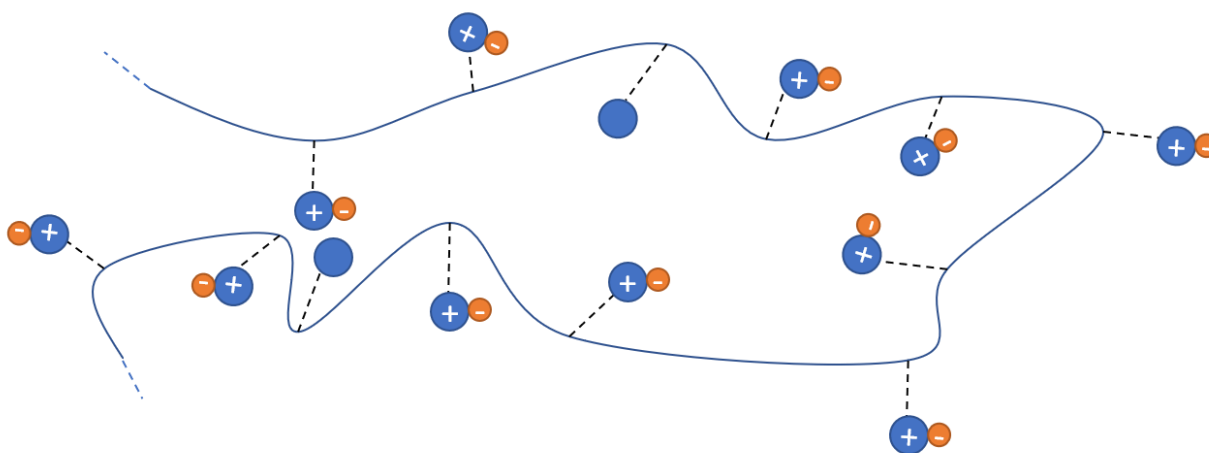
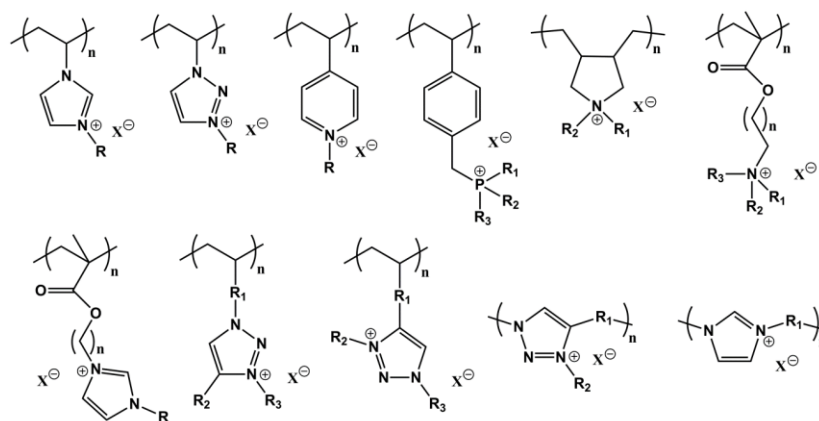
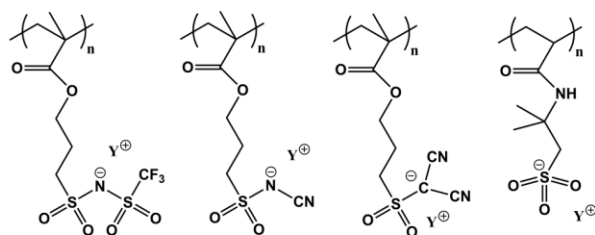


Figure 1.21 Schematic representation of a cationic PIL.

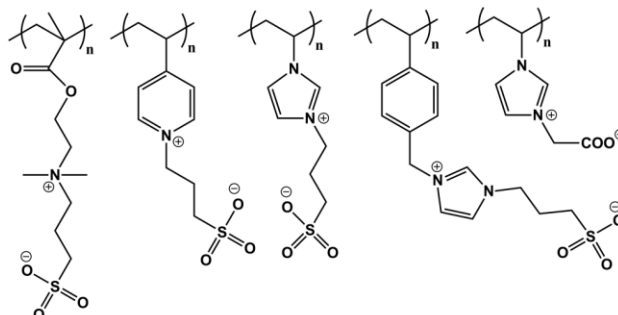
Ohno et al explored the PILs as solid polymer electrolytes as these materials have promised very good ion conduction and have published many reports.^{72–75} PILs match the rising research interest for the energy storage and conversion which is driving for establishing the structure-activity relationship. The structural diversity in this class of polymers as shown in the Figure 1.22, is immense due to the availability of a variety of basic structural units, including various permutation and combinations of various cations (imidazolium, pyridinium, alkylammonium etc.) and anions



Cationic PILs



Anionic PILs



Zwitterionic PILs

Figure 1.22 Types of PILs and some examples. (R-alkyl or other substituent, X-anion, Y-cation)

(halides, BF_4^- , PF_6^- , TFSI^- , FSI^- etc). The physical properties of PILs such as glass transition, solvent intake, gas sorption, solubility etc. can be altered by simply modifying the structure. In most of the cases, the polymerization enhances certain properties compared to the monomers. Shen et al. found that polymerization of three classic ionic monomers ([1-(4-vinylbenzyl)-3-butylimidazolium tetrafluoroborate] (VBIT), [1-(4-vinylbenzyl)-3-butylimidazolium hexafluorophosphate] (VBIH), and [2-(1-butylimidazolium-3-yl)ethyl methacrylate

overcome this, an ionic liquid monomer precursor with a smaller anion is polymerized followed by the ion exchange reaction to obtain the required PIL.

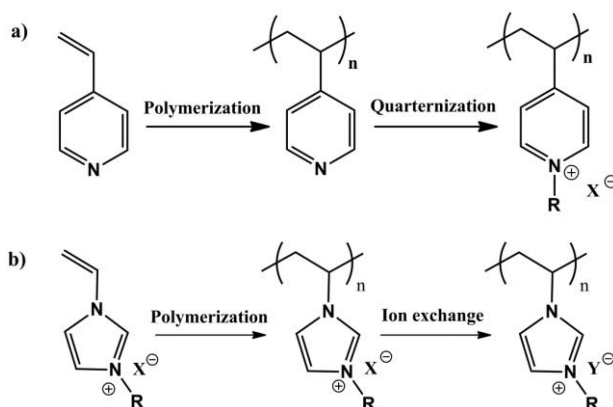


Figure 1.24 Two common approaches to obtain PILs a) ion metathesis or quaternization reaction with available polymer, b) direct polymerization of an available ionic liquid followed by ion exchange reaction.

The ever-increasing demand to create versatile polymer architectures via facile synthesis has given impetus to the researchers to explore functional polymers. The structural uniqueness associated with PILs allowing to incorporate any functional group with active nucleophilic sites in its structure has opened up unlimited possibilities. Also, the ability to custom make a PILs based on the application with desired physical and thermal properties makes it the choice of material in a variety of applications. Hence they are considered as multirole materials for a magnitude of applications.^{80–82} Porosity in the polymers is of great importance and most sought for applications such as gas sorption and separation, catalysis, chromatography, ion-conducting membranes in fuel cells, polyelectrolytes and binders for batteries etc.^{78,83,84} The porosity of the mesoporous structures of 3-alkyl-1-vinylimidazolium bromide based PILs with different chain lengths were studied and was observed that the alkyl chain length affect the pore formation.⁸⁵ Template-based porous PILs can also be prepared by using porous inorganic materials or nanostructured materials. This is achieved by the in-situ polymerization of the ionic monomers which infiltrate the porous matrix and followed by the removal of the template results in porous PILs. Sequential photopolymerization was used by Firestone et al. to prepare a liquid-crystalline IL-based interpenetrating polymer network (IPN), using a self-assembled aqueous mixture of (1-(10-(acryloyloxy)decyl)-3-methyl-imidazolium- chloride) with an acryloyl moiety at the terminus of a C10 alkyl chain of an IL cation.⁸⁶ PIL nanoparticles combine the advantages of the particles such

as high surface-to-volume ratios to the superior processability and functionality of the polymers. These particles can be prepared by emulsion and mini-emulsion processes, self-assembly, intermolecular cross-linking methods, suspension and dispersion polymerization techniques. A basic PIL catalyst was prepared via mini-emulsion polymerization using 1-ethyl-3-vinylimidazolium bromide and a crosslinker and their catalytic properties were evaluated in the synthesis of 4*H*-benzo[b]pyrans.⁸⁷ PIL incorporated poly(vinylidene fluoride-co-hexafluoropropylene) (PVDF) membranes were used as proton conducting membranes in fuel cells. These polymer electrolyte membranes showed high ionic conductivity at elevated temperatures.⁸⁸ Yan et al employed emulsion polymerization of PILs to prepare proton conducting membranes for fuel cells. These membranes exhibited good thermal stabilities, good mechanical properties and high ionic conductivity of 1×10^{-1} S/cm at 160 °C under non-humidifying conditions. This was attributed to the ion-conducting channels created by the PILs.⁸⁹ PILs have also found applications in dye-sensitized solar cells to increase conversion efficiencies and long term stability.⁹⁰ Imidazole-based ionically conductive polymers were used as effective gelators in DSSCs.⁹¹ High electrochemical stability and ionic peculiarities make PILs a very good choice as electrolyte hosts even when operating at high potentials.⁹² Shaplov et al. explored the performance of block copolymer polyelectrolytes comprising poly(lithium 1-[3-(methacryloyloxy)-propylsulfonyl]-1-(tri-fluoromethylsulfonyl)imide) and poly(ethylene glycol) methyl ether methacrylate blocks in lithium-metal batteries. These copolymers were used as solid polyelectrolytes and as binders in the formulation of lithium metal batteries with a specific capacity of up to 130 mAh/g at a rate of 0.067C.⁹³ PIL based binders were designed for various active materials for enhancing the electrode-electrolyte interfaces. Jian Yuan et al., reported a thiazolium based PIL Poly(3,4-dimethyl-5-vinylthiazolium bis(trifluoromethylsulfonyl)imide) [P(MVTh⁺TFSI⁻)] for LiFePO₄⁻ cathodes. P(MVTh⁺TFSI⁻) based cathodes exhibited about 140 mAh/g and 100 mAh/g discharge capacity at 1C and 5C rates respectively.⁹⁴ They attributed this improved performance to the enhanced ionic mobility due to PIL/electrolyte nano-heterojunction formed at the electrode-electrolyte interface. In another report from Passerini et al., an imidazolium-based PIL was utilized for graphite anodes. They reported Poly[vinylethylimidazolium bis(trifluoromethylsulfonyl)imide] (PolyVIMTFSI-c) to exhibit stable discharge capacity for about 150 cycles at 1C rate.⁹⁵ However, current electronic devices need greater durability with a stable discharge capacity. In this direction, the current work focuses on developing a

multifunctional binder that can enhance the lithium-ion transport by assisting in the formation of more conductive SEI leading to higher cycle life and improved overall LiB performance compared to its commercial counterpart.

1.8 Objective and Scope of the Thesis

Most of the commercial batteries used today use graphite-based anodes. Though the electrochemistry of the graphite electrodes is well understood, graphite-based LiBs still suffer from capacity fade over long cycling and flammability issues. Predominantly, solid electrolyte interface plays a very crucial role in the performance, durability and safety of the LiBs. To boost the performance of the LiB, it is very important to structurally and compositionally tune the SEI. For instance, this improves the driving range of the EVs in a single charge, provide longer battery life for portable electronics etc. Also, it is equally important to explore other active material such as hard carbon, silicon and TiO_2 to increase the energy density and rate capability of the LiBs.

Poly(ionic liquid)s is a very versatile class of material with synergistic properties of ionic liquids and polymers. They possess ionic conductivity, non-flammability and electrochemical stability along with mechanical strength and processability of the polymers. They can act as interfacing agents at the electrode-electrolyte interface and improve the interfacial properties. Improving parameters such as interfacial resistance, ion permeability etc. will have a direct consequence on the performance of the LiB. The objective of this thesis is to develop PIL based binders and active materials with enhanced interfacial properties as shown in Figure 1.25.

Chapter 2 elucidates the importance of the compositional and dimensional design of the solid electrolyte interface (SEI) achieved by allylimidazolium based binder. The importance of the theoretical understanding of the electronic states of the binder is also highlighted. Even at a minimal composition in the electrode, the binder can have a very crucial role in enhancing the interfacial properties.

Chapter 3 highlights the effect of the side-chain and anion structure of the imidazolium-based PIL on the composition of SEI and its impact on the performance of LiB in terms of longevity and capacity obtained. The structure-activity relationship can assist in the fine-tuning of the SEI to obtain the optimal performance of the LiBs.

Chapter 4 demonstrates the enhancement in the cycle life of silicon anodes by modifying the surface chemistry of the silicon nanoparticles via covalent functionalization. The PIL network covalently linked to the silicon nanoparticles provides a buffer for the expansion and contraction during the charge-discharge cycling. This is of great commercial importance because Silicon with its high gravimetric capacity can drastically reduce the batteries size.

Chapter 5 summarizes the properties and scope of the PIL based materials with discussion on the importance of tuning of SEI morphology and composition to improve the performance and safety of the LiBs.

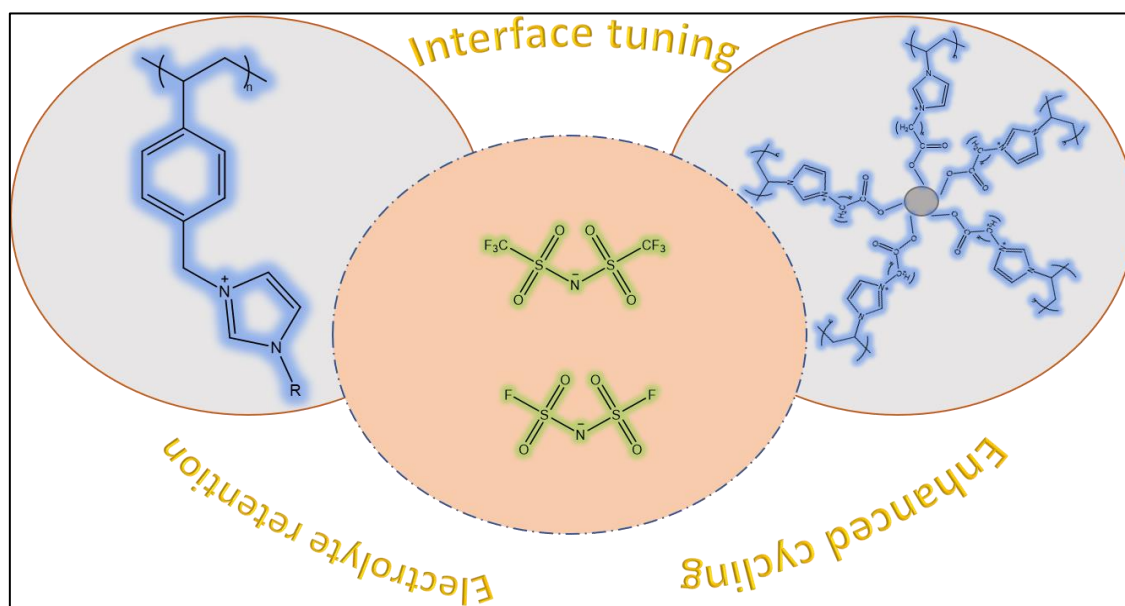


Figure 1.25 Schematic abstract of the thesis.

References

- (1) Cheng, F.; Liang, J.; Tao, Z.; Chen, J. Functional Materials for Rechargeable Batteries. *Adv. Mater.* **2011**, *23* (15), 1695–1715. <https://doi.org/10.1002/adma.201003587>.
- (2) Zhou, G.; Li, F.; Cheng, H. M. Progress in Flexible Lithium Batteries and Future Prospects. *Energy Environ. Sci.* **2014**, *7* (4), 1307–1338. <https://doi.org/10.1039/c3ee43182g>.
- (3) Tarascon, J. M.; Armand, M. Issues and Challenges Facing Rechargeable Lithium Ion Batteries. *Nature* **2001**, *414*, 359. <https://doi.org/10.1097/00006254-199510000-00002>.
- (4) Tarascon, J. M.; Armand, M. Building Better Batteries. **2008**, *451* (February), 652–657. <https://doi.org/10.1038/451652a>.
- (5) Whittingham, M. S.; Fanwood, N.J. Chalcogenide Battery. *Exxon Res. Eng. Co.* **1977**, 1–5.
- (6) Whittingham, M. S. Electrical Energy Storage and Intercalation Chemistry. **1976**, *192*.
- (7) Mizushima, K.; Jones, P. C.; Wiseman, P. J.; Goodenough, J. B. Li_xCoO_2 ($0 < x \leq 1$): A New Cathode Material for Batteries of High Energy Density. *Solid State Ionics* **1981**, *3–4* (C), 171–174. [https://doi.org/10.1016/0167-2738\(81\)90077-1](https://doi.org/10.1016/0167-2738(81)90077-1).
- (8) Thackeray, M. M.; David, W. I. F.; Bruce, P. G.; Goodenough, J. B. Lithium Insertion into Manganese Spinels. *Mater. Res. Bull.* **1983**, *18* (4), 461–472. [https://doi.org/10.1016/0025-5408\(83\)90138-1](https://doi.org/10.1016/0025-5408(83)90138-1).
- (9) Strecker, P. E. R. United States Patent (19). **1988**, No. 19.
- (10) Yazami, R.; Touzain, P. A Reversible Graphite-Lithium Negative Electrode for Electrochemical Generators. *J. Power Sources* **1983**, *9* (3), 365–371. [https://doi.org/10.1016/0378-7753\(83\)87040-2](https://doi.org/10.1016/0378-7753(83)87040-2).
- (11) Tarascon, J. M.; Gozdz, A. S.; Schmutz, C.; Shokoohi, F.; Warren, P. C. Performance of Bellcore's Plastic Rechargeable Li-Ion Batteries. *Solid State Ionics* **1996**, *86–88* (PART 1), 49–54. [https://doi.org/10.1016/0167-2738\(96\)00330-X](https://doi.org/10.1016/0167-2738(96)00330-X).
- (12) Lee, Y. G.; Fujiki, S.; Jung, C.; Suzuki, N.; Yashiro, N.; Omoda, R.; Ko, D. S.; Shiratsuchi, T.; Sugimoto, T.; Ryu, S.; Ku, J. H.; Watanabe, T.; Park, Y.; Aihara, Y.; Im, D.; Han, I. T.

- High-Energy Long-Cycling All-Solid-State Lithium Metal Batteries Enabled by Silver–Carbon Composite Anodes. *Nat. Energy* **2020**. <https://doi.org/10.1038/s41560-020-0575-z>.
- (13) Lu, J.; Chen, Z.; Pan, F.; Cui, Y.; Amine, K. High-Performance Anode Materials for Rechargeable Lithium-Ion Batteries. *Electrochem. Energy Rev.* **2018**, *1* (1), 35–53. <https://doi.org/10.1007/s41918-018-0001-4>.
- (14) Qi, W.; Shapter, J. G.; Wu, Q.; Yin, T.; Gao, G.; Cui, D. Nanostructured Anode Materials for Lithium-Ion Batteries: Principle, Recent Progress and Future Perspectives. *J. Mater. Chem. A* **2017**, *5* (37), 19521–19540. <https://doi.org/10.1039/c7ta05283a>.
- (15) Obrovac, M. N.; Chevrier, V. L. Alloy Negative Electrodes for Li-Ion Batteries. *Chem. Rev.* **2014**, *114* (23), 11444–11502. <https://doi.org/10.1021/cr500207g>.
- (16) Nishi, Y. Lithium Ion Secondary Batteries; Past 10 Years and the Future. *J. Power Sources* **2001**, *100* (1–2), 101–106. [https://doi.org/10.1016/S0378-7753\(01\)00887-4](https://doi.org/10.1016/S0378-7753(01)00887-4).
- (17) Manthiram, A.; Tsang, C. Electrode Materials for Rechargeable Lithium Batteries. *An. des la Asoc. Quim. Argentina* **1996**, *84* (3), 265–270.
- (18) Loeffler, N.; Bresser, D.; Passerini, S.; Copley, M. Secondary Lithium-Ion Battery Anodes: From First Commercial Batteries to Recent Research Activities. *Johnson Matthey Technol. Rev.* **2015**, *59* (1), 34–44. <https://doi.org/10.1595/205651314X685824>.
- (19) Aurbach, D.; Markovsky, B.; Weissman, I.; Levi, E.; Ein-Eli, Y. On the Correlation between Surface Chemistry and Performance of Graphite Negative Electrodes for Li Ion Batteries. *Electrochim. Acta* **1999**, *45* (1), 67–86. [https://doi.org/10.1016/S0013-4686\(99\)00194-2](https://doi.org/10.1016/S0013-4686(99)00194-2).
- (20) Zhao, K.; Pharr, M.; Vlassak, J. J.; Suo, Z. Fracture of Electrodes in Lithium-Ion Batteries Caused by Fast Charging. *J. Appl. Phys.* **2010**, *108* (7), 1–7. <https://doi.org/10.1063/1.3492617>.
- (21) Flandrois, S.; Simon, B. Carbon Materials for Lithium-Ion Rechargeable Batteries. *Carbon N. Y.* **1999**, *37* (2), 165–180. [https://doi.org/10.1016/S0008-6223\(98\)00290-5](https://doi.org/10.1016/S0008-6223(98)00290-5).
- (22) Zhang, X.; Qu, H.; Ji, W.; Zheng, D.; Ding, T.; Abegglen, C.; Qiu, D.; Qu, D. Fast and Controllable Prelithiation of Hard Carbon Anodes for Lithium-Ion Batteries. *ACS Appl.*

- Mater. Interfaces* **2020**, *12* (10), 11589–11599. <https://doi.org/10.1021/acsami.9b21417>.
- (23) Hassoun, J.; Bonaccorso, F.; Agostini, M.; Angelucci, M.; Betti, M. G.; Cingolani, R.; Gemmi, M.; Mariani, C.; Panero, S.; Pellegrini, V.; Scrosati, B. An Advanced Lithium-Ion Battery Based on a Graphene Anode and a Lithium Iron Phosphate Cathode. *Nano Lett.* **2014**, *14* (8), 4901–4906. <https://doi.org/10.1021/nl502429m>.
- (24) Landi, B. J.; Ganter, M. J.; Cress, C. D.; DiLeo, R. A.; Raffaele, R. P. Carbon Nanotubes for Lithium Ion Batteries. *Energy Environ. Sci.* **2009**, *2* (6), 638–654. <https://doi.org/10.1039/b904116h>.
- (25) Wang, H.; Zhang, C.; Liu, Z.; Wang, L.; Han, P.; Xu, H.; Zhang, K.; Dong, S.; Yao, J.; Cui, G. Nitrogen-Doped Graphene Nanosheets with Excellent Lithium Storage Properties. *J. Mater. Chem.* **2011**, *21* (14), 5430–5434. <https://doi.org/10.1039/c1jm00049g>.
- (26) Wu, Z. S.; Ren, W.; Xu, L.; Li, F.; Cheng, H. M. Doped Graphene Sheets as Anode Materials with Superhigh Rate and Large Capacity for Lithium Ion Batteries. *ACS Nano* **2011**, *5* (7), 5463–5471. <https://doi.org/10.1021/nn2006249>.
- (27) Ferg, E. Spinel Anodes for Lithium-Ion Batteries. *Journal of The Electrochemical Society*. 1994, p L147. <https://doi.org/10.1149/1.2059324>.
- (28) Kitta, M.; Akita, T.; Maeda, Y.; Kohyama, M. Study of Surface Reaction of Spinel $\text{Li}_4\text{Ti}_5\text{O}_{12}$ during the First Lithium Insertion and Extraction Processes Using Atomic Force Microscopy and Analytical Transmission Electron Microscopy. *Langmuir* **2012**, *28* (33), 12384–12392. <https://doi.org/10.1021/la301946h>.
- (29) Borghols, W. J. H.; Wagemaker, M.; Lafont, U.; Kelder, E. M.; Mulder, F. M. Size Effects in the $\text{Li}_{4+x}\text{Ti}_5\text{O}_{12}$ Spinel. *J. Am. Chem. Soc.* **2009**, *131* (49), 17786–17792. <https://doi.org/10.1021/ja902423e>.
- (30) Chen, Z.; Belharouak, I.; Sun, Y. K.; Amine, K. Titanium-Based Anode Materials for Safe Lithium-Ion Batteries. *Adv. Funct. Mater.* **2013**, *23* (8), 959–969. <https://doi.org/10.1002/adfm.201200698>.
- (31) Dambournet, D.; Belharouak, I.; Amine, K. Tailored Preparation Methods of TiO_2 Anatase, Rutile, Brookite: Mechanism of Formation and Electrochemical Properties. *Chem. Mater.*

- 2010**, 22 (3), 1173–1179. <https://doi.org/10.1021/cm902613h>.
- (32) Dambournet, D.; Chapman, K. W.; Koudriachova, M. V.; Chupas, P. J.; Belharouak, I.; Amine, K. Combining the Pair Distribution Function and Computational Methods to Understand Lithium Insertion in Brookite (TiO₂). *Inorg. Chem.* **2011**, 50 (13), 5855–5857. <https://doi.org/10.1021/ic2004326>.
- (33) Armstrong, A. R.; Armstrong, G.; Canales, J.; García, R.; Bruce, P. G. Lithium-Ion Intercalation into TiO₂-B Nanowires. *Adv. Mater.* **2005**, 17 (7), 862–865. <https://doi.org/10.1002/adma.200400795>.
- (34) Chan, C. K.; Peng, H.; Liu, G.; McIlwrath, K.; Zhang, X. F.; Huggins, R. A.; Cui, Y. High-Performance Lithium Battery Anodes Using Silicon Nanowires. *Nat. Nanotechnol.* **2008**, 3 (1), 31–35. <https://doi.org/10.1038/nnano.2007.411>.
- (35) Wang, C.; Wu, H.; Chen, Z.; Mcdowell, M. T.; Cui, Y.; Bao, Z. Self-Healing Chemistry Enables the Stable Operation of Silicon Microparticle Anodes for High-Energy Lithium-Ion Batteries. *Nat. Chem.* **2013**, 5 (12), 1042–1048. <https://doi.org/10.1038/nchem.1802>.
- (36) Poizot, P.; Laruelle, S.; Grugeon, S.; Dupont, L.; Tarascon, J. Nano-Sized transition-Metal oxides as Negative-Electrode Materials for Lithium-Ion Batteries. **2000**, 407 (September).
- (37) Tarascon, J. M.; Grugeon, S.; Morcrette, M.; Laruelle, S.; Rozier, P.; Poizot, P. New Concepts for the Search of Better Electrode Materials for Rechargeable Lithium Batteries. *Comptes Rendus Chim.* **2005**, 8 (1), 9–15. <https://doi.org/10.1016/j.crci.2004.12.005>.
- (38) Warshawsky, I. Discussion of “The Electrochemical Behavior of Alkali and Alkaline Earth Metals in Nonaqueous Battery Systems—The Solid Electrolyte Interphase Model” [E. Peled (Pp. 2047-2051, Vol. 126, No. 12)]. *J. Electrochem. Soc.* **1980**, 127 (6), 1324. <https://doi.org/10.1149/1.2129891>.
- (39) Geronov, Y. Electrochemical Studies of the Film Formation on Lithium in Propylene Carbonate Solutions under Open-Circuit Conditions. *Journal of The Electrochemical Society*. 1982, p 1422. <https://doi.org/10.1149/1.2124177>.
- (40) Peled, E. Advanced Model for Solid Electrolyte Interphase Electrodes in Liquid and

- Polymer Electrolytes. *J. Electrochem. Soc.* **1997**, *144* (8), L208. <https://doi.org/10.1149/1.1837858>.
- (41) Aurbach, D.; Markovsky, B.; Levi, M. D.; Levi, E.; Schechter, A.; Moshkovich, M.; Cohen, Y. New Insights into the Interactions between Electrode Materials and Electrolyte Solutions for Advanced Nonaqueous Batteries. *J. Power Sources* **1999**, *81–82*, 95–111. [https://doi.org/10.1016/S0378-7753\(99\)00187-1](https://doi.org/10.1016/S0378-7753(99)00187-1).
- (42) Goodenough, J. B.; Kim, Y. Challenges for Rechargeable Li Batteries. *Chem. Mater.* **2010**, *22* (3), 587–603. <https://doi.org/10.1021/cm901452z>.
- (43) Wang, A.; Kadam, S.; Li, H.; Shi, S.; Qi, Y. Review on Modeling of the Anode Solid Electrolyte Interphase (SEI) for Lithium-Ion Batteries. *npj Comput. Mater.* **2018**, *4* (1). <https://doi.org/10.1038/s41524-018-0064-0>.
- (44) Horstmann, B.; Single, F.; Latz, A. Review on Multi-Scale Models of Solid-Electrolyte Interphase Formation. *Curr. Opin. Electrochem.* **2019**, *13*, 61–69. <https://doi.org/10.1016/j.coelec.2018.10.013>.
- (45) Xu, K. Electrolytes and Interphases in Li-Ion Batteries and Beyond. *Chem. Rev.* **2014**, *114* (23), 11503–11618. <https://doi.org/10.1021/cr500003w>.
- (46) Xu, K. Nonaqueous Liquid Electrolytes for Lithium-Based Rechargeable Batteries. *Chem. Rev.* **2004**, *104* (10), 4303–4417. <https://doi.org/10.1021/cr030203g>.
- (47) Broussely, M.; Herreyre, S.; Biensan, P.; Kasztejna, P.; Nechev, K.; Staniewicz, R. J. Aging Mechanism in Li Ion Cells and Calendar Life Predictions. *J. Power Sources* **2001**, *97–98*, 13–21. [https://doi.org/10.1016/S0378-7753\(01\)00722-4](https://doi.org/10.1016/S0378-7753(01)00722-4).
- (48) Christensen, J.; Newman, J. A Mathematical Model for the Lithium-Ion Negative Electrode Solid Electrolyte Interphase. *Proc. - Electrochem. Soc.* **2003**, *20*, 85–94. <https://doi.org/10.1149/1.1804812>.
- (49) An, S. J.; Li, J.; Daniel, C.; Mohanty, D.; Nagpure, S.; Wood, D. L. The State of Understanding of the Lithium-Ion-Battery Graphite Solid Electrolyte Interphase (SEI) and Its Relationship to Formation Cycling. *Carbon N. Y.* **2016**, *105*, 52–76. <https://doi.org/10.1016/j.carbon.2016.04.008>.

- (50) Bhattacharya, S.; Riahi, A. R.; Alpas, A. T. Thermal Cycling Induced Capacity Enhancement of Graphite Anodes in Lithium-Ion Cells. *Carbon N. Y.* **2014**, *67* (519), 592–606. <https://doi.org/10.1016/j.carbon.2013.10.032>.
- (51) Pinson, M. B.; Bazant, M. Z. Theory of SEI Formation in Rechargeable Batteries: Capacity Fade, Accelerated Aging and Lifetime Prediction. *J. Electrochem. Soc.* **2013**, *160* (2), A243–A250. <https://doi.org/10.1149/2.044302jes>.
- (52) Buqa, H.; Würsig, A.; Vetter, J.; Spahr, M. E.; Krumeich, F.; Novák, P. SEI Film Formation on Highly Crystalline Graphitic Materials in Lithium-Ion Batteries. *J. Power Sources* **2006**, *153* (2), 385–390. <https://doi.org/10.1016/j.jpowsour.2005.05.036>.
- (53) Qian, Y.; Hu, S.; Zou, X.; Deng, Z.; Xu, Y.; Cao, Z.; Kang, Y.; Deng, Y.; Shi, Q.; Xu, K.; Deng, Y. How Electrolyte Additives Work in Li-Ion Batteries. *Energy Storage Mater.* **2019**, *20* (November 2018), 208–215. <https://doi.org/10.1016/j.ensm.2018.11.015>.
- (54) Patnaik, S. G.; Vedarajan, R.; Matsumi, N. BIAN Based Functional Diimine Polymer Binder for High Performance Li Ion Batteries. *J. Mater. Chem. A* **2017**, *5* (34), 17909–17919. <https://doi.org/10.1039/c7ta03843g>.
- (55) Jayakumar, T. P.; Badam, R.; Matsumi, N. Allylimidazolium-Based Poly(Ionic Liquid) Anodic Binder for Lithium-Ion Batteries with Enhanced Cyclability. *ACS Appl. Energy Mater.* **2020**. <https://doi.org/10.1021/acsaem.9b02376>.
- (56) Shi, Y.; Zhou, X.; Yu, G. Material and Structural Design of Novel Binder Systems for High-Energy, High-Power Lithium-Ion Batteries. *Acc. Chem. Res.* **2017**, *50* (11), 2642–2652. <https://doi.org/10.1021/acs.accounts.7b00402>.
- (57) Bresser, D.; Buchholz, D.; Moretti, A.; Varzi, A.; Passerini, S. Alternative Binders for Sustainable Electrochemical Energy Storage-the Transition to Aqueous Electrode Processing and Bio-Derived Polymers. *Energy Environ. Sci.* **2018**, *11* (11), 3096–3127. <https://doi.org/10.1039/c8ee00640g>.
- (58) Joshi, P.; Iwai, K.; Patnaik, S. G.; Vedarajan, R.; Matsumi, N. Reduction of Charge-Transfer Resistance via Artificial SEI Formation Using Electropolymerization of Borylated Thiophene Monomer on Graphite Anodes. *J. Electrochem. Soc.* **2018**, *165* (3), A493–A500.

- <https://doi.org/10.1149/2.0141803jes>.
- (59) Wu, N. L.; Weng, Y. T.; Li, F. S.; Yang, N. H.; Kuo, C. L.; Li, D. S. Polymeric Artificial Solid/Electrolyte Interphases for Li-Ion Batteries. *Prog. Nat. Sci. Mater. Int.* **2015**, *25* (6), 563–571. <https://doi.org/10.1016/j.pnsc.2015.11.009>.
- (60) Chou, S. L.; Pan, Y.; Wang, J. Z.; Liu, H. K.; Dou, S. X. Small Things Make a Big Difference: Binder Effects on the Performance of Li and Na Batteries. *Phys. Chem. Chem. Phys.* **2014**, *16* (38), 20347–20359. <https://doi.org/10.1039/c4cp02475c>.
- (61) Wang, C.; Wu, H.; Chen, Z.; Mcdowell, M. T.; Cui, Y.; Bao, Z. Self-Healing Chemistry Enables the Stable Operation of Silicon Microparticle Anodes for High-Energy Lithium-Ion Batteries. *Nat. Chem.* **2013**, *5* (12), 1042–1048. <https://doi.org/10.1038/nchem.1802>.
- (62) Jeena, M. T.; Lee, J. I.; Kim, S. H.; Kim, C.; Kim, J. Y.; Park, S.; Ryu, J. H. Multifunctional Molecular Design as an Efficient Polymeric Binder for Silicon Anodes in Lithium-Ion Batteries. *ACS Appl. Mater. Interfaces* **2014**, *6* (20), 18001–18007. <https://doi.org/10.1021/am504854x>.
- (63) Lin, C. Y.; Huang, C. H.; Hu, C. C.; Liu, Y. L. Self-Crosslinkable Nitroxide-Functionalized Poly(2,6-Dimethyl-1,4-Phenylene Oxide) through Atom Transfer Radical Coupling Reaction. *Polym. (United Kingdom)* **2018**, *135*, 154–161. <https://doi.org/10.1016/j.polymer.2017.12.025>.
- (64) Lu, W.; Shao, Z. G.; Zhang, G.; Zhao, Y.; Yi, B. Crosslinked Poly(Vinylbenzyl Chloride) with a Macromolecular Crosslinker for Anion Exchange Membrane Fuel Cells. *J. Power Sources* **2014**, *248*, 905–914. <https://doi.org/10.1016/j.jpowsour.2013.08.141>.
- (65) Murase, M.; Yabuuchi, N.; Han, Z. J.; Son, J. Y.; Cui, Y. T.; Oji, H.; Komaba, S. Crop-Derived Polysaccharides as Binders for High-Capacity Silicon/Graphite-Based Electrodes in Lithium-Ion Batteries. *ChemSusChem* **2012**, *5* (12), 2307–2311. <https://doi.org/10.1002/cssc.201200650>.
- (66) Walden, P.; Molekulargr, U. Math-Net . Ru. **2020**, *8* (6), 405–422.
- (67) Hallett, J. P.; Welton, T. Room-Temperature Ionic Liquids. Solvents for Synthesis and Catalysis. *Chem. Rev.* **1999**, *99*, 2071–2083. <https://doi.org/10.1002/chin.201136231>.

- (68) Zheng, H.; Li, B.; Fu, Y.; Abe, T.; Ogumi, Z. Compatibility of Quaternary Ammonium-Based Ionic Liquid Electrolytes with Electrodes in Lithium Ion Batteries. *Electrochim. Acta* **2006**, *52* (4), 1556–1562. <https://doi.org/10.1016/j.electacta.2006.01.085>.
- (69) Matsumi, N.; Yoshioka, N.; Aoi, K. Synthesis of Boric Ester Type Ion-Gels by Dehydrocoupling of Cellulose with Hydroboranes in Ionic Liquid. *Solid State Ionics* **2012**, *226*, 37–40. <https://doi.org/10.1016/j.ssi.2012.07.018>.
- (70) Tsunashima, K.; Kawabata, A.; Matsumiya, M.; Kodama, S.; Enomoto, R.; Sugiya, M.; Kunugi, Y. Low Viscous and Highly Conductive Phosphonium Ionic Liquids Based on Bis(Fluorosulfonyl)Amide Anion as Potential Electrolytes. *Electrochem. commun.* **2011**, *13* (2), 178–181. <https://doi.org/10.1016/j.elecom.2010.12.007>.
- (71) Salamone, J. C.; Israel, S. C.; Taylor, P.; Snider, B. Synthesis and Homopolymerization Studies of Vinylimidazolium Salts. *Polymer (Guildf)*. **1973**, *14* (12), 639–644. [https://doi.org/10.1016/0032-3861\(73\)90039-6](https://doi.org/10.1016/0032-3861(73)90039-6).
- (72) Matsumi, N.; Sugai, K.; Miyake, M.; Ohno, H. Polymerized Ionic Liquids via Hydroboration Polymerization as Single Ion Conductive Polymer Electrolytes. *Macromolecules* **2006**, *39* (20), 6924–6927. <https://doi.org/10.1021/ma060472j>.
- (73) Ohno, H.; Yoshizawa, M.; Ogihara, W. Development of New Class of Ion Conductive Polymers Based on Ionic Liquids. *Electrochim. Acta* **2004**, *50* (2-3 SPEC. ISS.), 255–261. <https://doi.org/10.1016/j.electacta.2004.01.091>.
- (74) Matsumi, N.; Ohno, H. Organoboron Polymer Electrolytes for Selective Lithium Cation Transport. *Macromol. Contain. Met. Met. Elem. Boron-Containing Part.* **2007**, *8*, 175–196. <https://doi.org/10.1002/9780470139653.ch6>.
- (75) Matsumi, N.; Ohno, H. Organoboron Ion Conductive Materials for Target Cation Transport. *Main Gr. Chem.* **2006**, *5* (4), 297–307. <https://doi.org/10.1080/10241220701448674>.
- (76) Tang, J.; Sun, W.; Tang, H.; Radosz, M.; Shen, Y. Enhanced CO₂ Absorption of Poly(Ionic Liquid)S. *Macromolecules* **2005**, *38* (6), 2037–2039. <https://doi.org/10.1021/ma047574z>.
- (77) Ricks-Laskoski, H. L.; Snow, A. W. Synthesis and Electric Field Actuation of an Ionic Liquid Polymer. *J. Am. Chem. Soc.* **2006**, *128* (38), 12402–12403.

- <https://doi.org/10.1021/ja064264i>.
- (78) Qian, W.; Texter, J.; Yan, F. *Frontiers in Poly(Ionic Liquid)s: Syntheses and Applications. Chem. Soc. Rev.* **2017**, *46* (4), 1124–1159. <https://doi.org/10.1039/c6cs00620e>.
- (79) Yuan, J.; Antonietti, M. Poly(Ionic Liquid)s: Polymers Expanding Classical Property Profiles. *Polymer (Guildf)*. **2011**, *52* (7), 1469–1482. <https://doi.org/10.1016/j.polymer.2011.01.043>.
- (80) Green, O.; Grubjesic, S.; Lee, S.; Firestone, M. A. The Design of Polymeric Ionic Liquids for the Preparation of Functional Materials. *Polym. Rev.* **2009**, *49* (4), 339–360. <https://doi.org/10.1080/15583720903291116>.
- (81) Yuan, J.; Mecerreyes, D.; Antonietti, M. Poly(Ionic Liquid)s: An Update. *Prog. Polym. Sci.* **2013**, *38* (7), 1009–1036. <https://doi.org/10.1016/j.progpolymsci.2013.04.002>.
- (82) Lu, J.; Yan, F.; Texter, J. Advanced Applications of Ionic Liquids in Polymer Science. *Prog. Polym. Sci.* **2009**, *34* (5), 431–448. <https://doi.org/10.1016/j.progpolymsci.2008.12.001>.
- (83) Kausar, A. Research Progress in Frontiers of Poly(Ionic Liquid)s: A Review. *Polym. - Plast. Technol. Eng.* **2017**, *56* (17), 1823–1838. <https://doi.org/10.1080/03602559.2017.1289410>.
- (84) Ye, Y.; Elabd, Y. A. Anion Exchanged Polymerized Ionic Liquids: High Free Volume Single Ion Conductors. *Polymer (Guildf)*. **2011**, *52* (5), 1309–1317. <https://doi.org/10.1016/j.polymer.2011.01.031>.
- (85) Feng, X.; Gao, C.; Guo, Z.; Zhou, Y.; Wang, J. Pore Structure Controllable Synthesis of Mesoporous Poly(Ionic Liquid)s by Copolymerization of Alkylvinylimidazolium Salts and Divinylbenzene. *RSC Adv.* **2014**, *4* (45), 23389–23395. <https://doi.org/10.1039/c4ra03163f>.
- (86) Becht, G. A.; Sofos, M.; Seifert, S.; Firestone, M. A. Formation of a Liquid-Crystalline Interpenetrating Poly(Ionic Liquid) Network Hydrogel. *Macromolecules* **2011**, *44* (6), 1421–1428. <https://doi.org/10.1021/ma102146r>.
- (87) Pourjavadi, A.; Hosseini, S. H.; Emami, Z. S. Cross-Linked Basic Nanogel; Robust Heterogeneous Organocatalyst. *Chem. Eng. J.* **2013**, *232*, 453–457. <https://doi.org/10.1016/j.cej.2013.07.090>.

- (88) Martinelli, A.; Matic, A.; Jacobsson, P.; Börjesson, L.; Fericola, A.; Panero, S.; Scrosati, B.; Ohno, H. Physical Properties of Proton Conducting Membranes Based on a Protic Ionic Liquid. *J. Phys. Chem. B* **2007**, *111* (43), 12462–12467. <https://doi.org/10.1021/jp0735029>.
- (89) Yan, F.; Yu, S.; Zhang, X.; Qiu, L.; Chu, F.; You, J.; Lu, J. Enhanced Proton Conduction in Polymer Electrolyte Membranes as Synthesized by Polymerization of Protic Ionic Liquid-Based Microemulsions. *Chem. Mater.* **2009**, *21* (8), 1480–1484. <https://doi.org/10.1021/cm900098r>.
- (90) Grätzel, M.; Janssen, R. A. J.; Mitzi, D. B.; Sargent, E. H. Materials Interface Engineering for Solution-Processed Photovoltaics. *Nature* **2012**, *488* (7411), 304–312. <https://doi.org/10.1038/nature11476>.
- (91) Jelfs, K. E.; Flikkema, E.; Bromley, S. T. Evidence for Atomic Mixing via Multiple Intermediates during the Dynamic Interconversion of Silicate Oligomers in Solution. *Chem. Commun.* **2012**, *48* (1), 46–48. <https://doi.org/10.1039/c1cc14674b>.
- (92) Marcilla, R.; Alcaide, F.; Sardon, H.; Pomposo, J. A.; Pozo-Gonzalo, C.; Mecerreyes, D. Tailor-Made Polymer Electrolytes Based upon Ionic Liquids and Their Application in All-Plastic Electrochromic Devices. *Electrochem. Commun.* **2006**, *8* (3), 482–488. <https://doi.org/10.1016/j.elecom.2006.01.013>.
- (93) Shaplov, A. S.; Vlasov, P. S.; Armand, M.; Lozinskaya, E. I.; Ponkratov, D. O.; Malyshkina, I. A.; Vidal, F.; Okatova, O. V.; Pavlov, G. M.; Wandrey, C.; Godovikov, I. A.; Vygodskii, Y. S. Design and Synthesis of New Anionic “Polymeric Ionic Liquids” with High Charge Delocalization. *Polym. Chem.* **2011**, *2* (11), 2609–2618. <https://doi.org/10.1039/c1py00282a>.
- (94) Grygiel, K.; Lee, J. S.; Sakaushi, K.; Antonietti, M.; Yuan, J. Thiazolium Poly(Ionic Liquid)s: Synthesis and Application as Binder for Lithium-Ion Batteries. *ACS Macro Lett.* **2015**, *4* (12), 1312–1316. <https://doi.org/10.1021/acsmacrolett.5b00655>.
- (95) Von Zamory, J.; Bedu, M.; Fantini, S.; Passerini, S.; Paillard, E. Polymeric Ionic Liquid Nanoparticles as Binder for Composite Li-Ion Electrodes. *J. Power Sources* **2013**, *240*, 745–752. <https://doi.org/10.1016/j.jpowsour.2013.04.127>.

Chapter 2

Allylimidazolium Based Poly(ionic liquid) Anodic Binder for Lithium-ion Batteries with Enhanced Cyclability.

2.1 Abstract

An allylimidazolium based poly(ionic liquid), poly(vinylbenzylallylimidazolium bis(trifluoromethane)sulfonylimide) (PVBCAImTFSI) was used as a binder for graphite anodes in lithium-ion batteries. The anodes with the synthesized binder exhibited lesser electrolyte degradation and higher lithium-ion diffusion. Electrochemical Impedance Spectroscopy (EIS) results showed decreased interfacial and diffusion resistance for PVBCAImTFSI based electrodes after cycling compared to PVDF based anodes. Dynamic Electrochemical Impedance Spectroscopy (DEIS) results indicated that the interfacial resistance of the interface formed for the PVBCAImTFSI based anodes to be three times lesser than the PVDF based anodes. Suppression of electrolyte degradation and decrease in the intercalation-deintercalation potential and improved lithium-ion diffusion coefficient for PVBCAImTFSI based half-cells were observed from cyclic voltammetry measurements. DFT based theoretical studies also speculated the suppression in the electrolyte degradation in the case of PVBCAImTFSI binder due to the positioning of its HOMO-LUMO levels. A reversible discharge capacity of 210 mAh/g was obtained for PVBCAImTFSI based half-cells at 1C rate as compared to the 140 mAh/g obtained for PVDF based anodic half-cells. After 500 cycles, 95% retention in the discharge capacity was observed. Also, PVBCAImTFSI based anodes exhibited better charge-discharge stability than the PVDF based anodes. Suppression of electrolyte degradation, reduction in the interfacial resistance, enhanced wettability and optimal SEI layer formed in the case of PVBCAImTFSI based anodes cumulatively led to enhanced stability and cyclability during the charge-discharge studies as compared to the commercially employed PVDF based anodes. Thus, the tuning of the interfacial properties leads to the improvement in the performance of the lithium-ion batteries with PVBCAImTFSI as a binder.

2.2 Introduction

The commercialization of the LIBs revolutionized the portable devices like mobile phones, laptops, cameras and other digital electronics¹⁻³ because of high volumetric and gravimetric energy density, low self-discharge, absence of memory effect and flexibility in design.⁴⁻⁸ The necessity of powering the technologically advancing electronics has led to continuous improvement in the LIBs in terms of its efficiency, performance and safety. Since the discovery of reversible intercalation of lithium ions in graphite anodes by Yazami et al.⁹, a variety of electrode materials and electrolytes were designed to enhance the performance and safety. Most of the anodes can be categorized as intercalation based (carbonaceous materials like graphite, graphene foam, carbon nanotubes, porous carbon etc., and titanium oxides like TiO_2 and LiTi_4O_5 ¹⁰⁻¹⁴), alloy-based (silicon, tin, germanium¹⁵⁻¹⁷) and conversion materials (metal oxides of iron, molybdenum, copper etc.¹⁸). Similarly, a plethora of cathode material is available with structural and compositional diversity. Most common cathodes are intercalation type like layered (LiCoO_2 and LiMnO_2), olivine (LiFePO_4 and LiMnPO_4), spinel (LiMn_2O_4 and LiCo_2O_4) and tavorite (LiFeSO_4F)¹⁹. However, conversion type cathodes like metal halides (FeF_3 , BiF_3 , NiF_2 ²⁰⁻²²) and chalcogen based (S , Li_2S , Se ²³⁻²⁵) also have significant progress. Most of the challenges that arise in the LIBs have been investigated by modifying the electrodes and electrolytes. However, the role of binders was underrated and hence the development of the binders was not much focused upon. Though present in small amounts, binders play a very crucial role in the performance of the LIBs. The key role of the binder is to maintain the integrity of the electrode by holding the active material and the conductive additives together as well as to the current collector during the charge-discharge process. Binder can perform other functions by a rational structural modification as shown in Figure 2.1. These properties can be achieved by rational design of the binder. Calculating the highest occupied molecular orbital (HOMO) and lowest unoccupied molecular orbital (LUMO) of the polymers helps in the evaluation of the feasibility of using a polymer as a binder.²⁶ Commercially, the choice of the binder has been poly(vinylidene fluoride) (PVDF) due to its good chemical, electrochemical and thermal stabilities besides good adhesion and bonding of the electrode materials together to the current collector. However, the use of PVDF as a binder is

Binders

Hold electrode material intact in the electrode laminate and maintain the integrity of the electrode.

Swell up by absorbing the electrolyte and provides pathway for the lithium transport through the active material.

Assist in the solid electrolyte interface (SEI) formation, acts as an interface.

Figure 2.1 Roles of a binder in a LiB.

accompanied by many disadvantages. On long cycling, due to the dissolution of PVDF in organic solvents, electrode integrity is compromised which results in capacity fade and drastic loss in cycle life.²⁷ PVDF on long cycling forms fluorinated salts of lithium that pose a threat to the environment. Moreover, lithium blocking is observed when PVDF is used as a binder which impedes the transport of lithium ions at the interface.²⁸ To obtain a better performance, several additives such as fluoroethylene carbonate, vinylene carbonate etc. are employed. These additives improvise the electrode interface by forming a film over the electrode leading to better performance. Though added in a very little quantity, these additives have a huge progressive effect on the performance.³² For the better functioning of the LIBs, designing the electrode-electrolyte interface plays a crucial role. Formation of a conductive and robust solid electrolyte interface (SEI) is a necessity for the functioning of a graphite anode. SEI layer allows the desolvation of the lithium ions into graphite, prevents further reduction of the electrolytes. Further, it provides the mechanical strength and flexibility to allow the expansion and contraction of the graphite layers during the intercalation and deintercalation process. Aforementioned drawbacks of PVDF have led to the exploration of alternative binders in the recent past.

Poly(ionic liquid)s commonly known as PILs, are emerging class of material which has ionic liquids integrated into a polymeric structure. As the name suggests, PILs display synergistic properties of ionic liquids and their polymeric backbones. Due to the availability of a variety of polymeric backbones as well as ionic liquids, the structural diversity that can be achieved is enormously high. PILs can be obtained via a simple synthetic process and their properties can be tuned by the choice of cation and anion to achieve the desired result. They possess very good chemical, thermal and electrochemical stability. Hence, they find application as electrolytes in fuel cells as well as batteries, binders for electrochemical water splitting electrodes, thermoresponsive materials, carbon dioxide capture agents, surfactants, coatings etc.²⁹⁻³² Due to their interesting

properties, PILs have been used as alternative binders for LiBs in the recent years. The structure of the PILs, especially the side chain attached to the heterocycle influences its properties. The PIL in this study has been designed to incorporate higher lithium-ion diffusion and mechanical strength to achieve better performance for a longer duration. Ionic liquids with allyl side chain increase its amorphous nature leading to higher ionic conductivity and lower viscosity.³⁸ Some researchers have utilized PILs as a binder for graphite anodes and lithium iron phosphate cathodes and have reported charge-discharge cycling for 150-200 cycles. However, current electronic devices require higher durability with a stable discharge capacity. In this direction, the current work focuses on developing a multifunctional binder that can enhance the lithium-ion transport by assisting in the formation of more conductive SEI leading to higher durability and improved overall LiB performance compared to its commercial counterpart.

2.3 Materials and Methods

2.3.1 Materials

Poly (vinylbenzyl chloride) (PVBC), 60/40 mixture of 3- and 4- isomers ($M_n \sim 55,000$, $M_w \sim 100,000$) and Poly (vinylidene fluoride) were purchased from Sigma-Aldrich. 1-Allylimidazole (AIm) was procured from TCI Co., Ltd. HPLC grade dimethylformamide (DMF) and silver chloride (AgCl) were purchased from Wako Pure Chemical Industries, Ltd. Lithium bis(trifluoromethanesulfonyl)imide was purchased from Kanto Chemical Co., Inc. N-Methylpyrrolidone (NMP) and 1-Allyl-3-methylimidazolium bis(trifluoromethanesulfonyl)imide (AMImTFSI) were purchased from Tokyo Chemical Industry Co., Ltd. Graphite super fine powder (<50 μm) obtained from Merck was used as the active material. Battery-grade acetylene black used as conductive additive was procured from Denka Japan Private Co., Ltd. Copper foil of thickness 20 μm was obtained from The Nilaco corporation. All chemicals were used without any further purification.

2.3.2 Instrumentation

FT-IR spectra for the polymers were recorded on Perkin Elmer 100 FT-IR spectrometer. The spectra were recorded at a resolution of 2 cm^{-1} for 10 scans in ATR mode. The SEM-EDS measurements were carried out on Hitachi TM3030plus miniscope connected to the EDS module from Oxford instruments. TGA was measured on ThermoPlus EVO II Rigaku (TGA) analyzer

with a heating rate of 5 °C/min under constant nitrogen flow. Elemental analysis was performed for the polymers before and after the tagging and ion exchange reaction using Elementar Vario EL3. The polymer samples were placed in tin foil and combusted at 1200 °C. FESEM images for the electrodes were obtained using Hitachi S-4500 at accelerating voltage of 1.0 kV. X-ray photoelectron spectroscopy (XPS) measurements were carried on Fisons instruments S-probe TM 2803. The coin-cells were de-crimped at OCV and the extracted electrodes were washed with dried EC:DEC to remove any adsorbed salt residues before carrying out the XPS measurements. DFT calculations were performed to optimize the structure and calculate the electronic levels using Gaussian 09 with B3LYP hybrid functional and 6-311g (d,p) basis set.

2.3.3 Synthesis

The synthesis of the PIL was carried out by the ion metathesis reaction of the poly(vinylbenzyl chloride) and 1-allylimidazole followed by the ion exchange reaction to replace the chloride ion with the electrochemically superior TFSI anion. This approach is chosen as the monomeric unit of the PIL under consideration would have two polymerizable groups and one group cannot be selectively polymerized. However, a model compound of the monomer has been synthesized to understand the structure.

2.3.3.1 Vinylbenzylallylimidazolium bis(trifluoromethanesulfonyl)imide (VBCAImTFSI):

The synthesis of vinylbenzylallylimidazolium bis(trifluoromethanesulfonyl)imide was carried out by quaternization reaction of vinylbenzyl chloride. 0.31 g (2 mmol) of vinylbenzyl chloride was solubilized in 20 mL of toluene. This solution was stirred at 80 °C under inert conditions and 0.24 g (2.2 mmol) of 1-allylimidazole was added dropwise. The mixture was stirred at 80 °C for 48 hours. The ionic liquid was obtained by carrying out the work up reaction in methanol. The ionic liquid was dried at 60 °C overnight to obtain the pure ionic liquid. The compound was characterized with ¹H-NMR and ¹³C-NMR as shown in Figure 2.2 a & b respectively. VBCAImCl ¹H NMR (DMSO-d₆, 400MHz): 4.85(2H,d), 5.29 (2H,t), 5.37(1H,d), 5.43(2H,s), 5.88(1H,d), 6.06(1H,m), 6.74(1H,quartet), 7.41(2H,d), 7.53(2H,d), 7.68(1H,s), 7.86(1H,s), 9.36(1H,s).

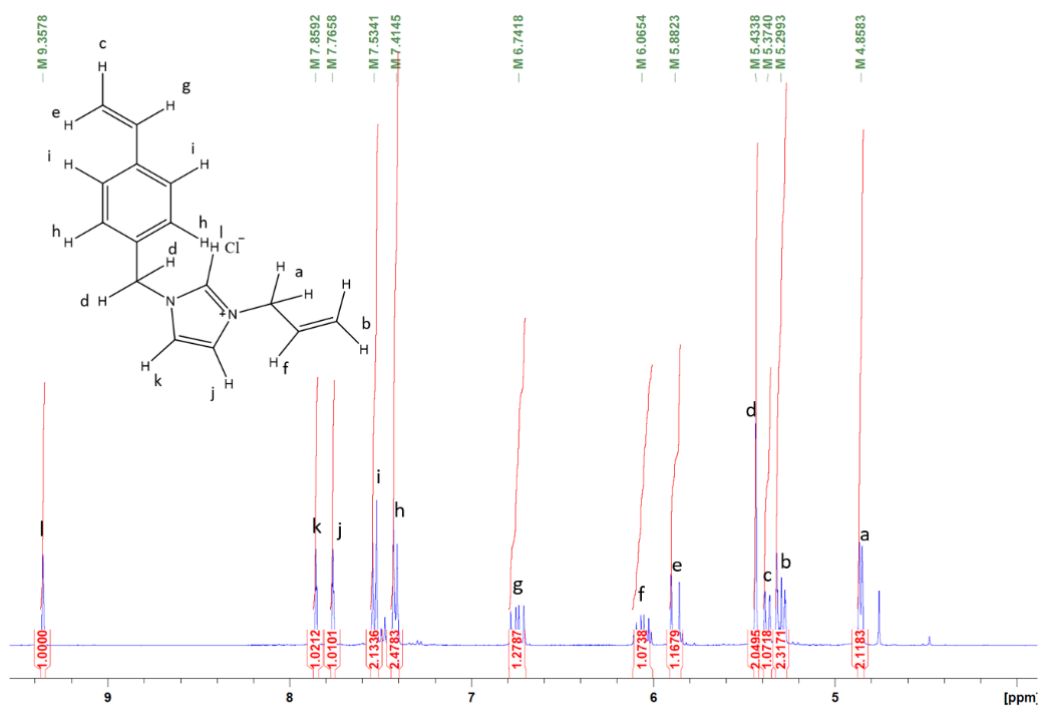


Figure 2.2 (a) ^1H -NMR of vinylbenzylallylimidazolium bis(trifluoromethanesulfonyl)imide (VBCAImTFSI).

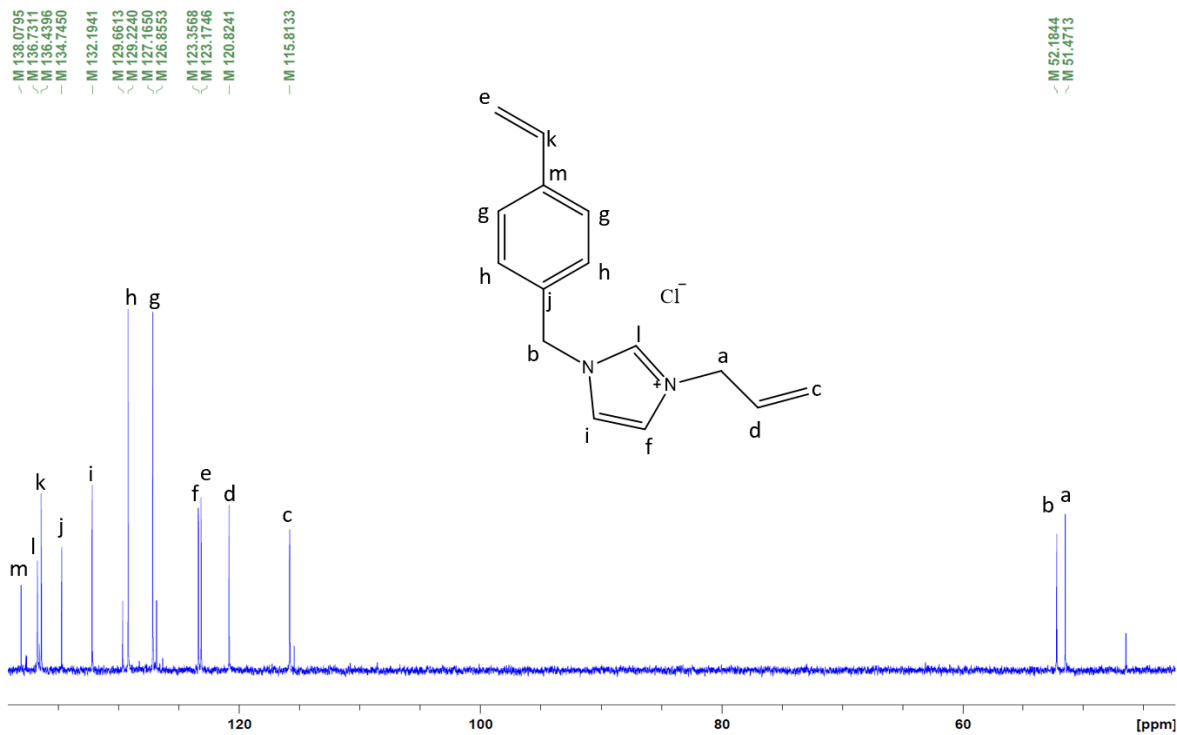
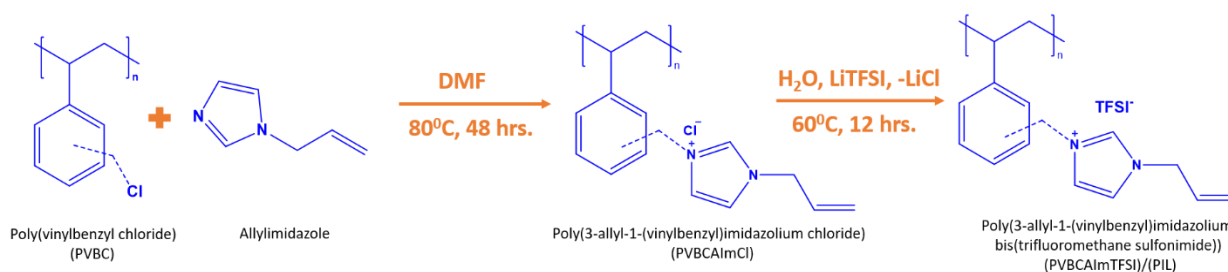


Figure 2.2 (b) ^{13}C -NMR of vinylbenzylallylimidazolium bis(trifluoromethanesulfonyl)imide (VBCAImTFSI).

2.3.3.2 Poly[vinylbenzylallylimidazolium bis(trifluoromethanesulfonyl)imide] (PVBCAImTFSI): The synthetic scheme is represented in Scheme 2.1. 0.5 g (3.275 mmol) of poly(vinylbenzyl chloride) (PVBC) was solubilized in 20 mL of dimethylformamide (DMF). This solution was stirred at 80 °C followed by dropwise addition of 0.885 g (8.186 mmol) of allylimidazole (AIm) solubilized in 5 mL of DMF. The reaction mixture was refluxed for 80 °C for 48 hours.³³ The precipitated polymer was washed with excess DMF to remove unreacted reactants and dried under vacuum at 75 °C to obtain poly(vinylbenzylallylimidazolium chloride) (PVBCAImCl). Ion exchange reaction was carried out to obtain poly[vinylbenzylallylimidazolium bis(trifluoromethanesulfonyl)imide] (PVBCAImTFSI) by solubilizing 0.131 g (0.5 mmol) of PVBCAImCl in deionized water followed by dropwise addition of an aqueous solution of LiTFSI. The mixture was stirred at room temperature overnight. The precipitated polymer was washed with deionized water.³⁴ Silver nitrate test was carried out to check the completion of ion exchange of chloride with the bis(trifluoromethane)sulfonylimide ion. The polymer obtained was dried at 75 °C under vacuum.



Scheme 2.1 Reaction scheme for the synthesis of PVBCAImTFSI.

2.3.4 Characterization

Figure 2.3 gives the FT-IR spectra for poly(vinylbenzyl chloride) (PVBC) and poly[vinylbenzylallylimidazolium bis(trifluoromethanesulfonyl)imide] (PVBCAImTFSI). Peaks were observed for PVBC at 3026, 2925 and 1263 cm⁻¹ corresponding to aromatic -CH, aliphatic -CH and -CH₂-Cl respectively. Peaks were observed at 3149 and 3090 cm⁻¹ for the spectra corresponding to PVBCAImTFSI corresponding to allylic -CH, along with 1671, 992 and 944 cm⁻¹ for allylic -C=C-. The peaks corresponding to the TFSI anion in PVBCAImTFSI was observed at 1347 and 1132 cm⁻¹ corresponding to -SO₂ antisymmetric and symmetric stretching respectively. Peaks at 1179 and 1051 cm⁻¹ correspond to -CF₃ antisymmetric stretching and -SNS- antisymmetric stretching respectively. Thus FT-IR confirms the successful ion exchange for

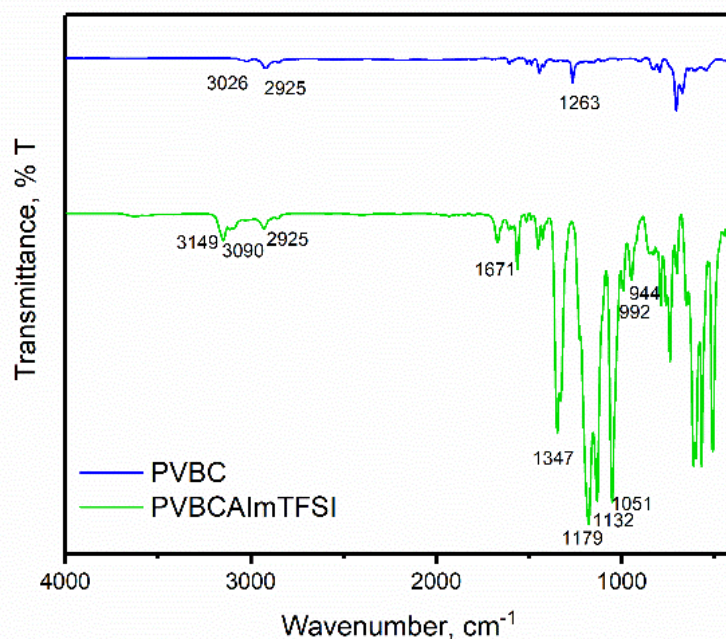


Figure 2.3 FT-IR spectra of PVBC and PVBCAImTFSI.

PVBCAImTFSI. Figure 2.4 shows the elemental mapping of PVBCAImTFSI studied by SEM-EDS which shows the uniform distribution of nitrogen, sulfur, fluoride and oxygen suggesting the uniform distribution of allylimidazolium moiety and TFSI anion. The thermogravimetric analysis

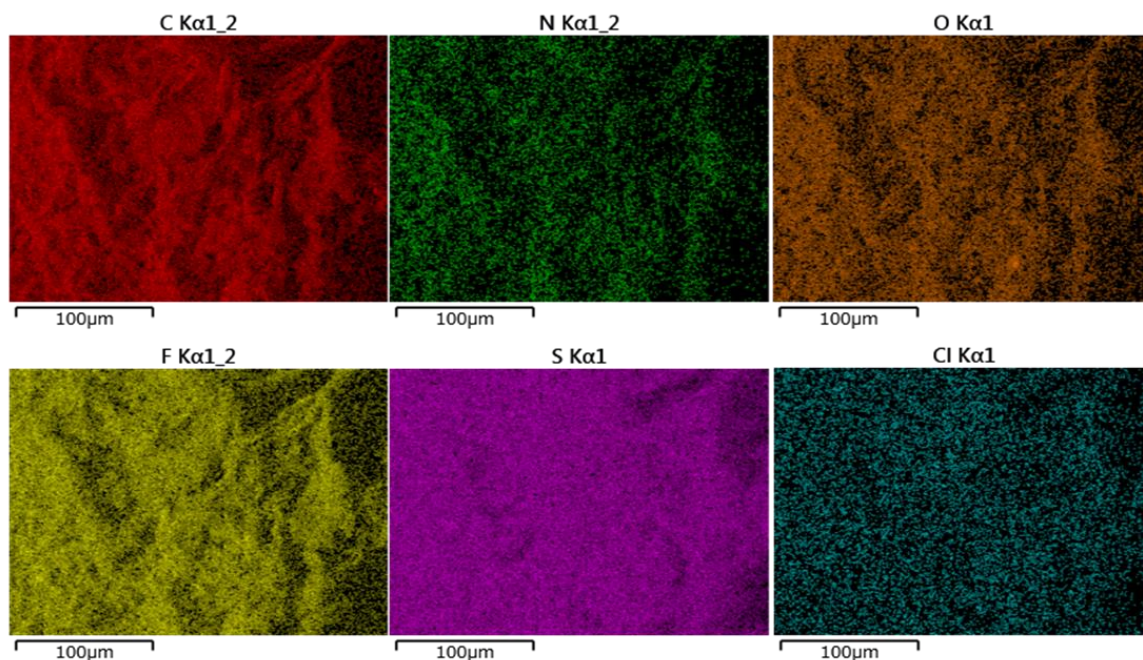


Figure 2.4 SEM-EDS imaging of PVBCAImTFSI.

for PVBC and PVBCAImTFSI is given in Figure 2.5. PVBCAImTFSI showed two decomposition peaks with a slight weight loss (<2%) in the range of 200 – 250 °C followed by the onset of the major decomposition at 326 °C. Tagging of ionic liquid moiety increased the thermal stability of

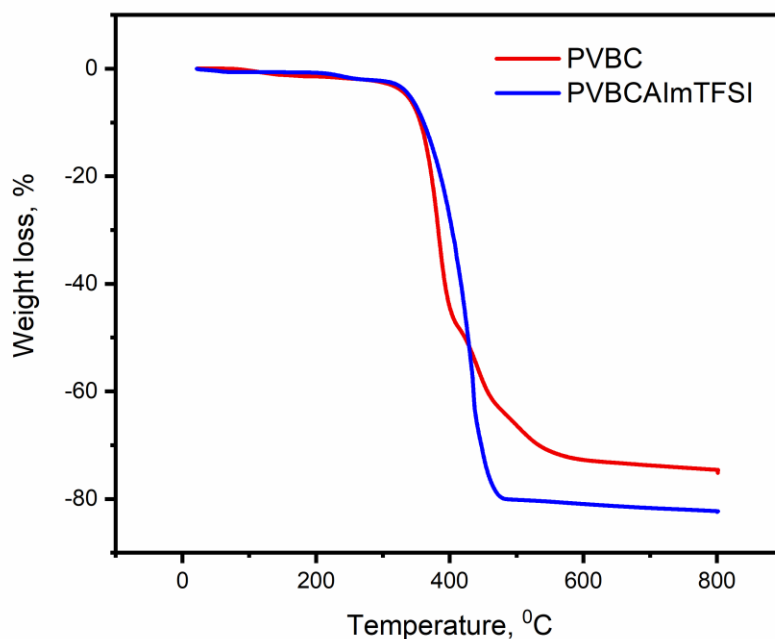


Figure 2.5 TGA traces for the PVBC (Red) and PVBCAImTFSI (Blue) recorded under N₂.

PVBC by about 25 °C. CHNS elemental analysis was carried out and the theoretical and observed percentage of elements are shown in Table 2.1. Comparing experimental and theoretical data for PVBCAImCl and PVBCAImTFSI, it is evident that almost all the chloride anions have been replaced by the TFSI anions. This was also confirmed visually by a negative AgNO₃ test for the washings of the polymer.

Table 2.1 Elemental analysis for PVBC, PVBCAImCl and PVBCAImTFSI along with theoretical values.

Polymer	Carbon	Hydrogen	Nitrogen	Sulphur
PVBC (Experimental)	69.85	6.08	0.27	-
PVBC (Theoretical)	69.91	7.17	-	-
PVBCAImCl (Experimental)	63.06	7.21	10.25	-
PVBCAImCl (Theoretical)	69.09	6.57	10.74	-
PVBCAImTFSI (Experimental)	41.66	3.51	8.79	12.36
PVBCAImTFSI (Theoretical)	40.40	3.39	8.31	12.69

2.3.5 Electrode and Cell Fabrication

Electrode slurry was prepared by mixing 92 wt% of graphite, 3 wt% acetylene black and 5 wt% binder in NMP. Electrodes were fabricated by casting the as-prepared slurry onto copper foil using a doctor blade. Electrodes were dried overnight under vacuum at 80 °C to remove NMP. The dried electrodes were hot-pressed at 80 °C for 6 hours. The dried electrodes were punched into disks with area 1.72 cm² to be used for testing in coin cells. 2025-coin cells were assembled to carry out the electrochemical testing using the as-fabricated graphite electrodes as anodes, lithium foil as counter and reference electrodes with a polypropylene separator (25 μm, Celgard 2500) and 1.0 M LiPF₆ in 1:1 EC:DEC as the electrolyte. The anodic half cells were assembled inside an argon-filled glove box (UNICO UN-650F) whose moisture and O₂ content was <0.1ppm. The assembled cells were rested for 6 hours for stabilization before carrying out the electrochemical characterization.

2.3.6 Electrochemical Instrumentation

The Electrochemical Impedance Spectroscopy (EIS) and Dynamic Electrochemical Impedance Spectroscopy (DEIS) measurements were carried out on VSP potentiostat electrochemical workstation equipped with frequency response analyzer (FRA). The EIS measurements were carried out after stabilizing as assembled cells and after charge-discharge cycling in the frequency range of 1 MHz to 100 mHz with a sinus amplitude of 10mV. The Cyclic Voltammetry (CV) studies and Linear Scan Voltammetry (LSV) were carried on a VSP potentiostat electrochemical workstation of Bio-Logic Science Instruments. The CV measurements were carried out in the potential range of 10 – 2100 mV vs Li/Li⁺ at a scan rate of 0.1 mV/s. The scan rate studies using CV was carried out at 0.1, 0.3, 0.5, 0.7 and 1.0 mV/s scan rates. The LSV measurements were carried out in the potential range of 0 – 7000 mV vs Li/Li⁺ with a stainless-steel working electrode at a scan rate of 10 mV/s. The charge-discharge measurements were carried out on the Electrofield ABE 1024 battery cycler using a CC-mode in the potential range of 10 – 2100 mV vs Li/Li⁺. Charge-discharge measurements at different rates (0.1C, 0.2C, 0.5C and 1C) were carried out to evaluate the stability of the electrodes. The DEIS measurements were carried out on the cells that were cycled for 100 cycles at 1C rate.

2.4 Results and Discussions

2.4.1 Theoretical Simulations

Rational design of the polymers is possible by understanding their properties before the actual synthesis. Understanding the optimized polymer structure and its electronic structure allows tuning of its structure to obtain desired results. The HOMO-LUMO levels of the polymer give an understanding of the electrochemical stability of the binder. Ideally, the design of the binder must be carried out such that they lie away from the working potentials of the battery so that they do not undergo reduction or oxidation. The structure of the octameric unit of the PVBCAImTFSI binder optimized using Gaussian 09 software was found to be open and dispersed as shown in Figure 2.6. The HOMO-LUMO values obtained for the octameric units of PVBCAImTFSI and PVDF binder along with EC molecule is given in Table 2.2. Higher HOMO indicates the ease of oxidation in

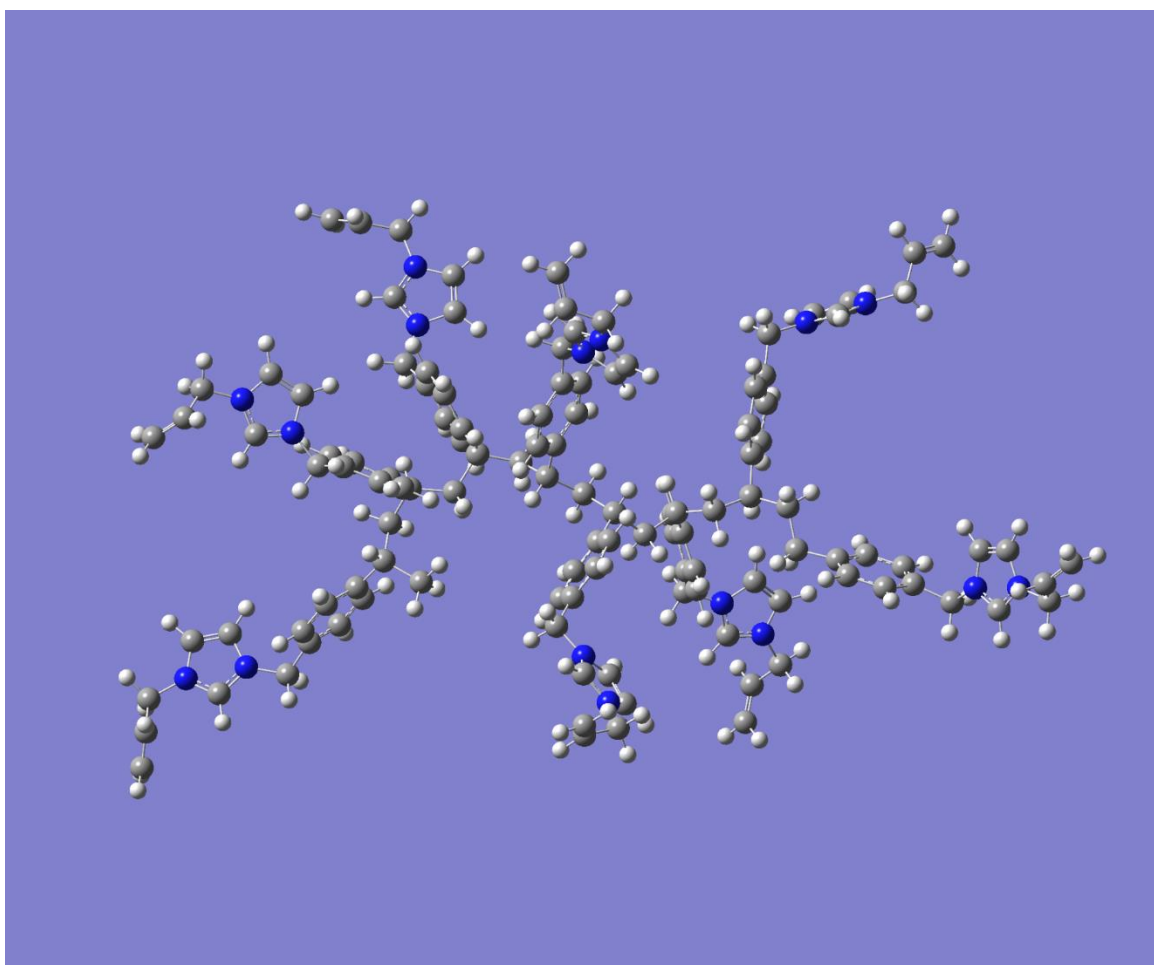


Figure 2.6 Optimized structure of the Octameric unit of PVBCAIm cationic backbone

Table 2.2 Optimized structure of the Octameric unit of PVBCAIm cationic backbone

Chemical Moiety (Octameric units except for EC)	E_{LUMO} (eV)	E_{HOMO} (eV)	Bandgap (eV)
PVBCAImTFSI (PIL)	-11.75	-16.28	4.53
PVDF	0.27	-8.76	-9.03
EC	0.63	-8.23	8.86

cathodic environment whereas lower LUMO assists in an easier reduction in the anodic environment.^{35,36} The E_{LUMO} for the PVBCAImTFSI binder was evaluated to be -11.74 eV which is very significantly lower than 0.27 eV for PVDF and 0.63 eV for EC. As E_{LUMO} of EC is lower than the PVDF, it gets degraded continuously leading to the buildup of abnormally thick SEI. Unlike PVDF, the PVBCAImTFSI binder due to its very low E_{LUMO} , it can get reduced leading to the formation of carbenes even before the reduction of EC based electrolyte starts as shown in the Figure 2.7.³² The formation of the carbene will provide the Li-ion hopping sites in the active material. The bandgap calculated theoretically for the PVBCAImTFSI binder was 4.53 eV, smaller than 8.48 eV for PVDF. The smaller bandgap along with the favourable energy levels for PVBCAImTFSI binder might help in getting it reduced in the anodic environment during charging along with the suppression in electrolyte degradation and enhanced lithium-ion mobility.

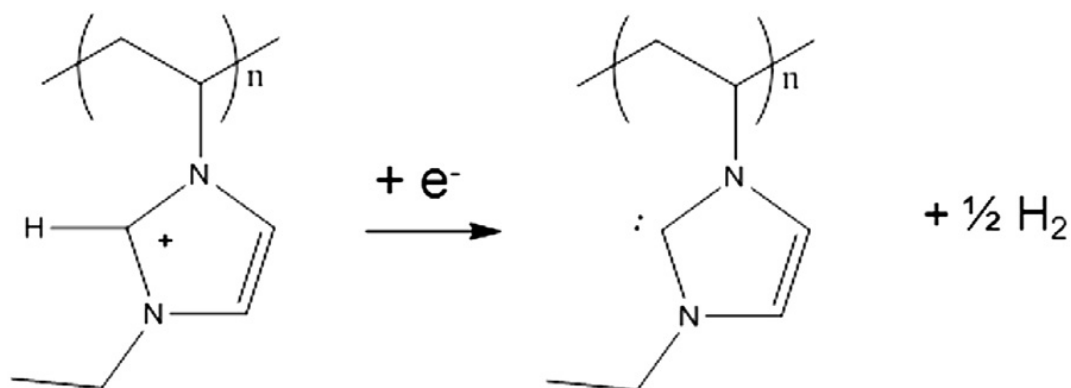


Figure 2.7 Illustration of the reduction of imidazolium heterocycle to the associated imidazol-2-ylidene.

2.4.2 Electrochemical Characterization

Linear Sweep Voltammetry was used to evaluate the electrochemical stability of the binder both in reduction and oxidation cycles as shown in Figure 2.8. A gel was prepared using LiTFSI and PVBCAImTFSI using ionic liquid AMImTFSI in 14:86 wt%. Measurements were carried out

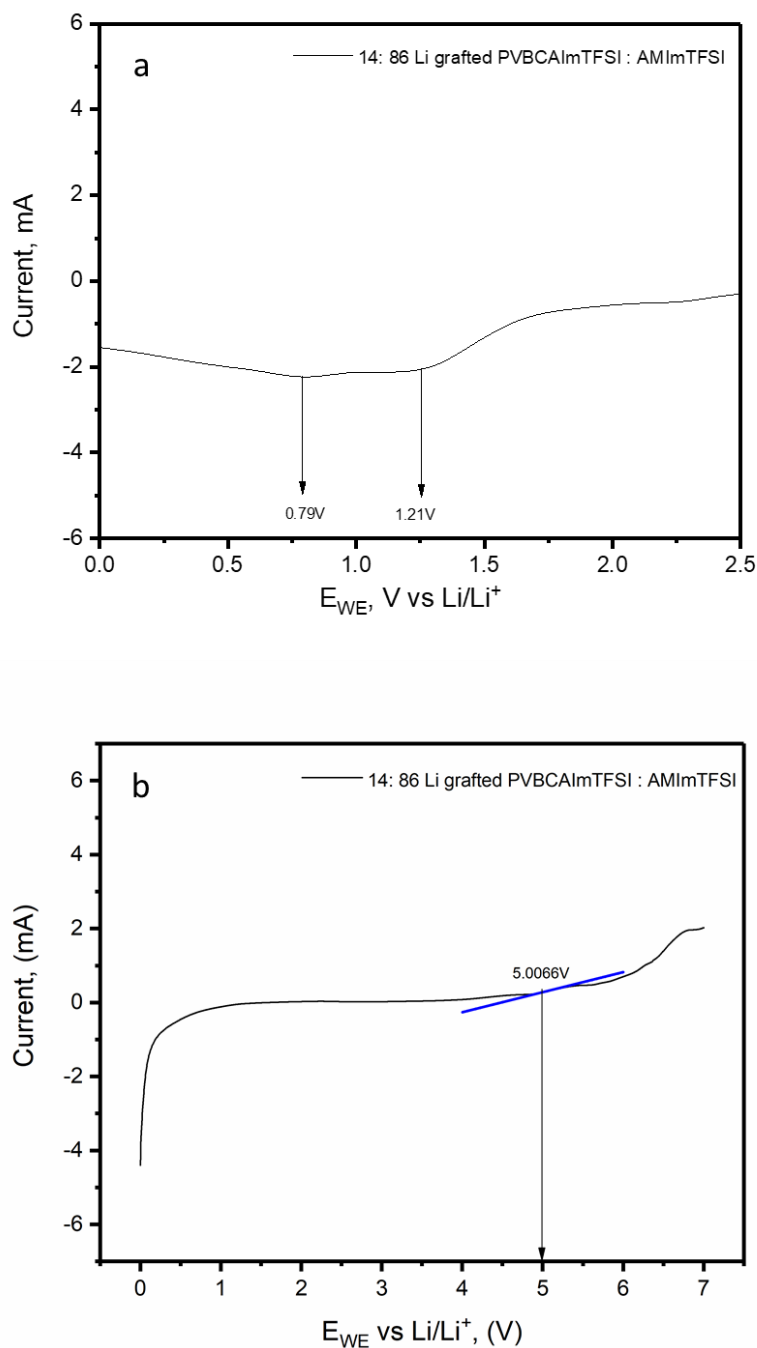


Figure 2.8 Electrochemical stability of PVBCAImTFSI (as gel in AMImTFSI) a) reduction cycle, b) oxidation cycle measured with stainless steel working electrode.

in two-electrode setup with stainless steel disc as the working electrode and lithium foil as reference and counter electrodes. Two prominent peaks were observed in the reduction cycle at 1.21V and 0.79V. The first peak at 1.21V vs Li/Li^+ corresponds to the reduction of the α -hydrogen between the two nitrogen atoms of the imidazolium ring resulting in the formation of the imidazole-2-ylidene as shown in Figure 2.7. The peak appearing at the lower potential corresponds to the further reduction of the imidazolium cation. These observations are consistent with the theoretical predictions of PVBCAImTFSI getting reduced before electrolyte degradation. No peaks were obtained in the oxidation cycle of the LSV.

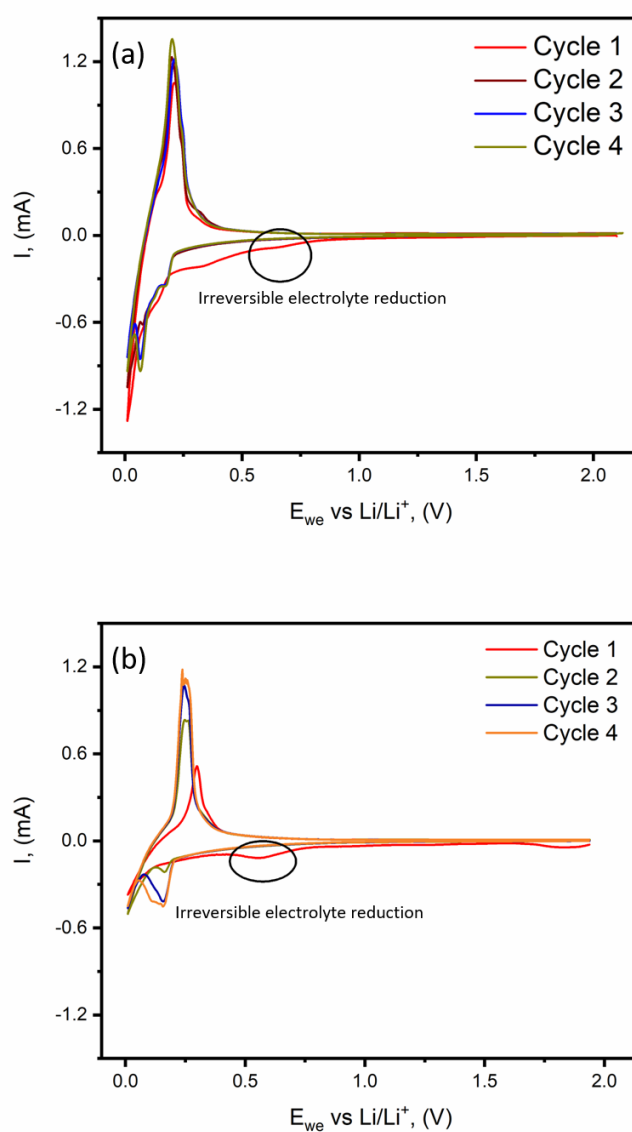


Figure 2.9 Cyclic voltammograms of a) PVBCAImTFSI, b) PVDF as binders for graphite anode in 1.0M LiPF_6 / EC : DEC at a scan rate of 0.1 mV/S.

Understanding the nature of the SEI formed gives an insight into the functioning and performance of the graphite anodes in LiBs.^{37,38} There are innumerable factors that affect the formation, structure and composition of SEI. Though a complete understanding in this regard is still unclear, there are some reports on its design and characterization.³⁹ In the current work, electrochemical techniques like CV, EIS and DEIS were employed to get an understanding of the SEI and its nature. CV measurements were carried out to understand the nature of SEI formed during the first intercalation cycle. Figure 2.9 a & b show the voltammograms for the half-cells with PVBCAImTFSI and PVDF based anodes respectively. The voltammograms show typical intercalation – deintercalation profile of a graphite anode. Figure 2.10 indicates the comparison of the first cycle for half-cells with anodes made by using PVBCAImTFSI and PVDF binders. The anodic peak corresponding to the SEI formation occurs in the potential range of 400 – 800 mV vs Li/Li⁺. The intensity and the area under the peak in voltammogram correspond to the amount of electrolyte getting reduced. This peak appears more prominent in the case of the PVDF based half-cells than that of PVBCAImTFSI. This signifies that the electrolyte reduction is higher in the former case leading to the formation of a thicker SEI compared to the latter which was also seen in the FESEM results. The intercalation – deintercalation overpotential was found to be about

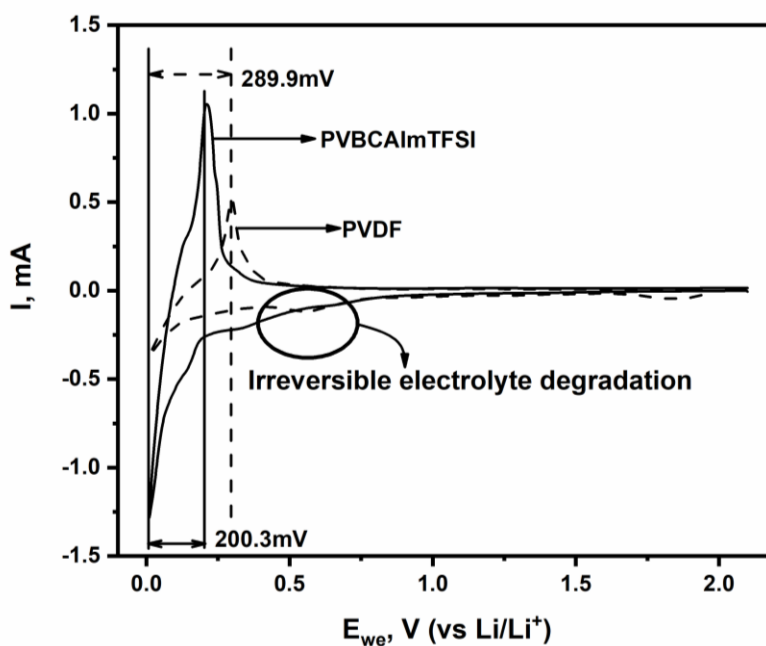


Figure 2.10 First cycle comparison of cyclic voltammograms for PVBCAImTFSI, PVDF as binders for graphite anode in 1.0 M LiPF₆ / EC : DEC at a scan rate of 0.1 mV/S.

289.9 mV and 200.3 mV for PVDF and PVBCAImTFSI based half-cells. The overpotential was reduced by 89.6 mV on replacing PVDF with PVBCAImTFSI. This indicates that the Li^+ mobility to be better in PVBCAImTFSI based half-cells. To further investigate the diffusion of the Li^+ ion in the active material quantitatively, CV based scan rate studies were performed. CV measurements were carried on half-cells with graphite anodes based on PVBCAImTFSI and PVDF binders at different scan rates. Figure 2.11 a & b show the cyclic voltammograms at different scan rates for PVBCAImTFSI and PVDF based half-cells respectively. Figure 2.11 c & d show the plots of peak current (I_p) vs square root of scan rate ($v^{1/2}$) for PVBCAImTFSI and PVDF based half-cells respectively. The peak currents followed a linear trend with respect to the square

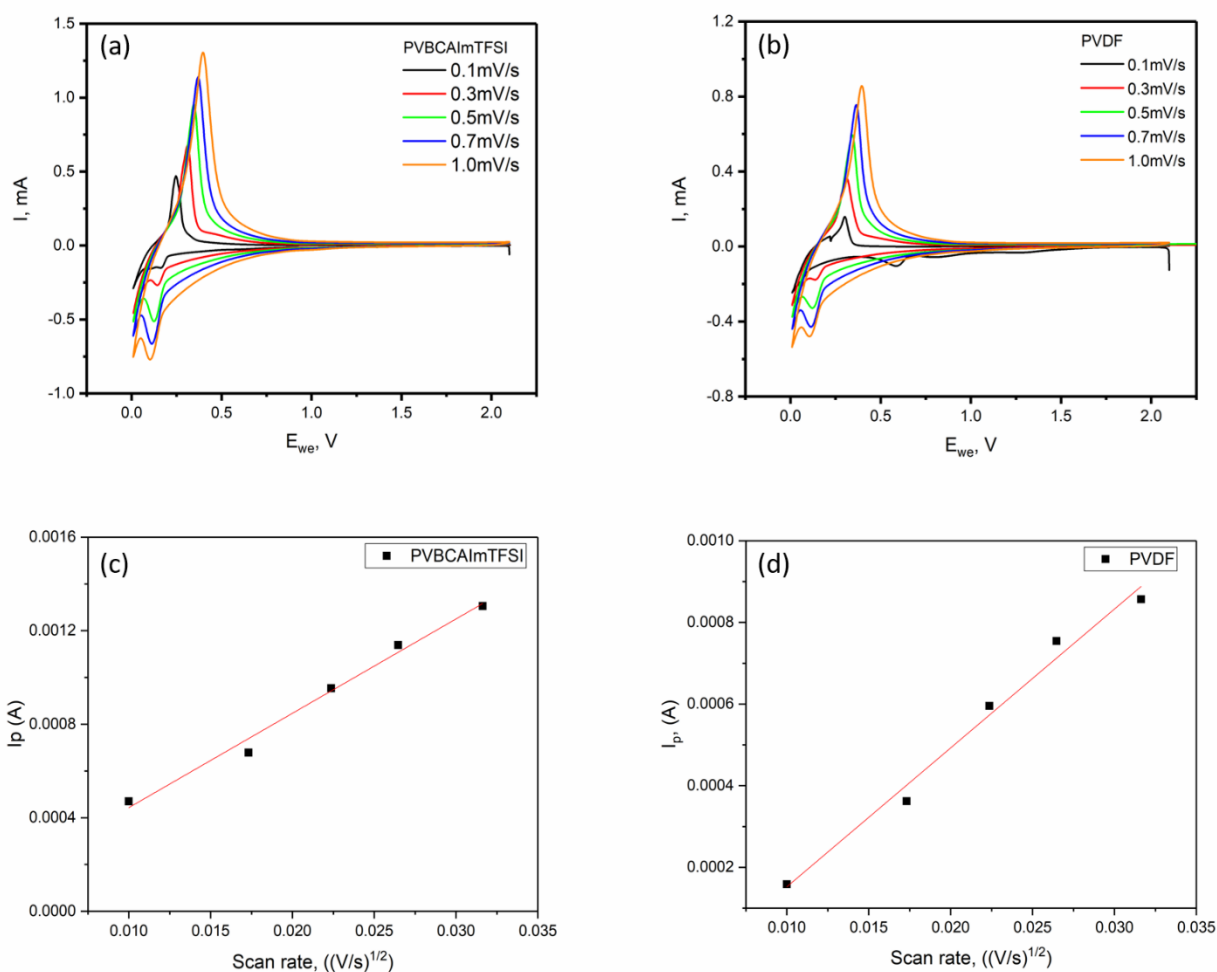


Figure 2.11 Cyclic voltammograms at different scan rates with a) PVBCAImTFSI, b) PVDF as binders for graphite anode in 1.0M LiPF_6 / EC : DEC. Plots of peak current vs square root of scan rates for c) PVBCAImTFSI, d) PVDF obtained from the CV.

root of the scan rate, increasing with the increasing scan rate. The lithium-ion diffusion coefficient (D_{Li^+}) was calculated using the Randles-Sevcik equation utilizing the slope values obtained from Figure 4c & 4d. The Randles-Sevcik equation⁴⁰ is given as:

$$I_p = 2.69 * 10^5 n^{3/2} A D_{Li}^{1/2} C_{Li}^* v^{1/2}$$

where I_p represents peak current in amps, n represents the number of electrons involved in the process, A represents the area of the electrode in cm^2 , D represents the lithium-ion diffusion coefficient in cm^2/s , C represents the concentration in mol/cm^3 and v represents scan rate in V/s . The lithium-ion diffusion coefficients evaluated for half-cells PVBCAImTFSI and PVDF based electrodes were $7.264 * 10^{-9} cm^2/s$ and $5.160 * 10^{-9} cm^2/s$ respectively. The lithium-ion diffusion coefficient was 41% higher in the graphite anodes with PVBCAImTFSI. This can be due to binder creating conducting pathways for lithium-ion mobility by swelling in the active material and SEI having a better ionic conductivity. This implies that a thicker SEI impedes the ion diffusion, whereas an optimal SEI leads to better performance.

Other important parameters to understand the SEI formed are interfacial and diffusion resistances which determines the performance of the battery. EIS technique was utilized to quantitatively determine these parameters. EIS measurements were carried out after fabrication at OCP and after cycling at C/25 for two cycles at 2.0V vs Li/Li⁺. Figure 2.12 shows the Nyquist plots for the anodic half-cells with (a) PVDF and (b) PVBCAImTFSI before and after cycling. The overall interfacial resistances of both the anodic half cells were reduced after the initial cycling. Figure 2.13 compares the Nyquist plots corresponding to PVBCAImTFSI (blue) and PVDF (red) after cycling with the high-frequency range corresponding to the interfacial processes shown in the inset. The interfacial resistance post cycling for the PVBCAImTFSI binder-based anode was lesser than half the value for the PVDF binder-based anode. The interfacial resistance for PVBCAImTFSI based half-cell was found to be about 36.39 Ω whereas 94.89 Ω for PVDF based half-cell. Also, it can be noted that the resistance corresponding to the diffusion of the of lithium-ion into the active material was drastically reduced for PVBCAImTFSI based anodes after cycling. This significant decrease in the interfacial resistance and diffusion resistance can be attributed to the optimal SEI and the wettability of the PVBCAImTFSI.

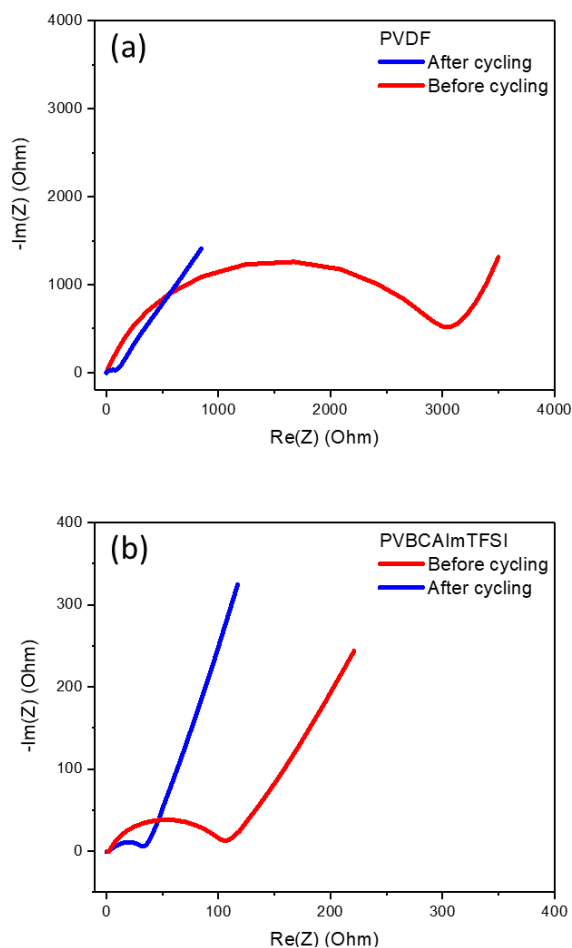


Figure 2.12 Electrochemical impedance spectroscopy measurements for graphite anode in 1.0M LiPF₆ / EC : DEC with a) PVBCAImTFSI, b) PVDF as binders.

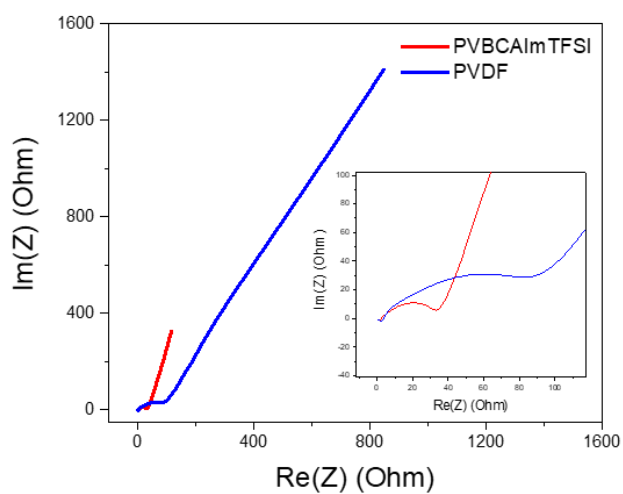


Figure 2.13 Nyquist plots of anodic half-cells with PVBCAImTFSI (Red) and PVDF (Blue) after cycling (Inset: High frequency range corresponding to the interfacial processes).

Dynamic Electrochemical Impedance Spectroscopy (DEIS) involves measuring impedance at different potentials by mimicking the charge-discharge process. In a traditional EIS measurement, the battery is adjusted to a certain state of charge (SOC) and stabilized at the equilibrium state. Then an impedance measurement is carried out without applying any DC potential. Therefore, the evolution of the interface during the charge-discharge process cannot be understood. Whereas, DEIS carries out EIS measurement by applying finite DC potentials with respect to the OCP as shown in Figure 2.14. This technique is beneficial as it provides with insights into the evolution of the interface and intercalation-deintercalation processes under real-time (information is closer to reality).^{35,41} The insights into the limitations in the intercalation and deintercalation processes and their effect on the evolution of the interface can be obtained. By fitting the obtained impedance data to the equivalent electric circuit models (EECMs), the impedance values for various processes can be separated, estimated and understood. In addition to understanding the resistance of the interface, we can also optimize the potential boundaries for the operation of the battery. To understand the impedance of the interface on charge-discharge cycling, DEIS measurement was carried out on the half-cells that were cycled at 1C for 100 cycles. Figure 2.15 a & b show the DEIS profiles during the charging cycle for both the half-cells with PVDF and PVBCAImTFSI as the binder at various potentials. Figure 2.16 a & b show the DEIS profiles during the discharging cycle for both the half-cells with PVBCAImTFSI and PVDF as the binder at various potentials. The impedance data obtained (Table 2.3 – 2.6) were fitted to the EECMs and impedance values for various processes were obtained. Figure 2.17 shows the SEI resistance (R_{SEI}) for both PVBCAImTFSI and PVDF as binders. The R_{SEI} values for the PVBCAImTFSI based graphite anodes were found to be lower at all potentials compared to the PVDF based graphite anodes. The lower resistance of the interface has a direct implication on the intercalation of lithium ions into the active material. The significant reduction in the R_{SEI} can be attributed to the PVBCAImTFSI/electrolyte interaction at the electrode interface leading to better ionic mobility.

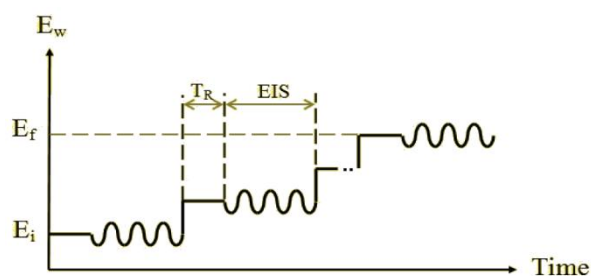
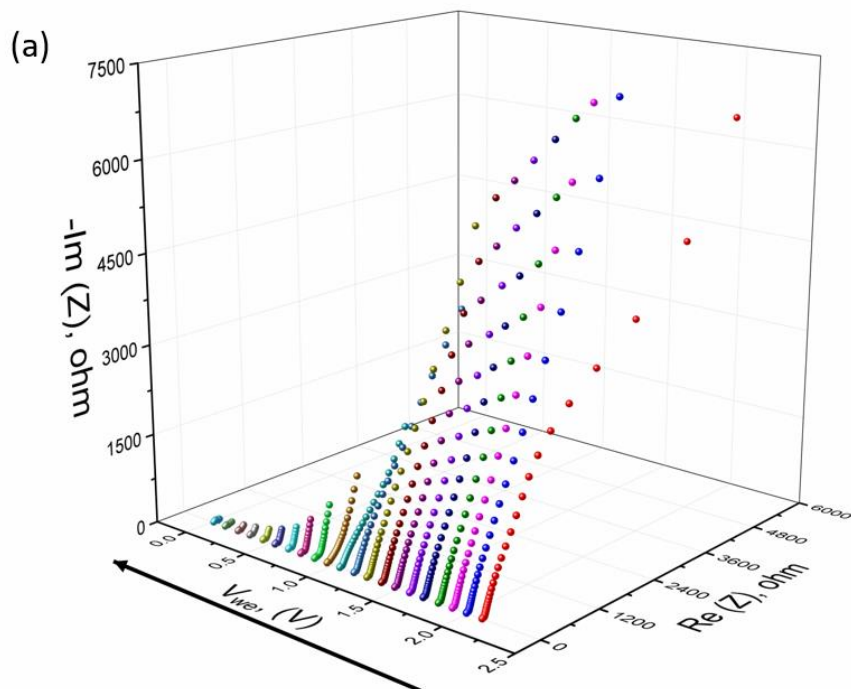
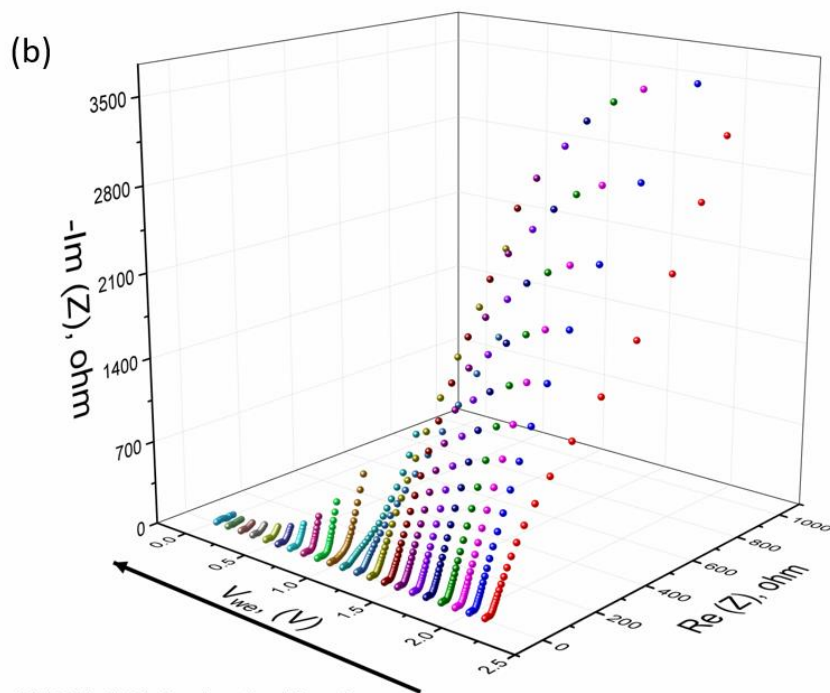


Figure 2.14 Schematic showing various parameters in DEIS measurement .



PVDF charging after 100 cycles



PVBCAImTFSI charging after 100 cycles

Figure 2.15 DEIS profiles for the charging cycle for a) PVBCAImTFSI, b) PVDF as binders for graphite anode after 100 cycles at 1C.

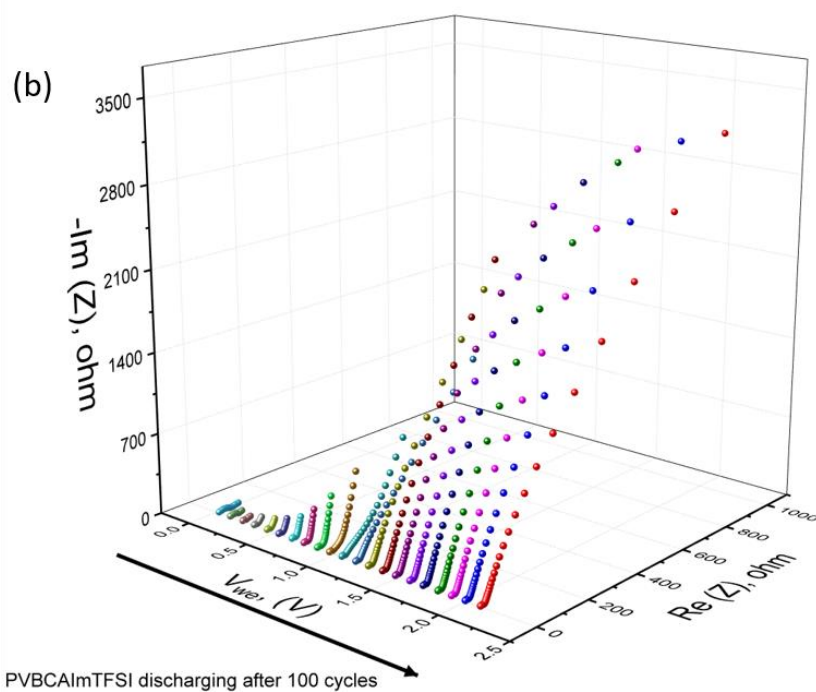
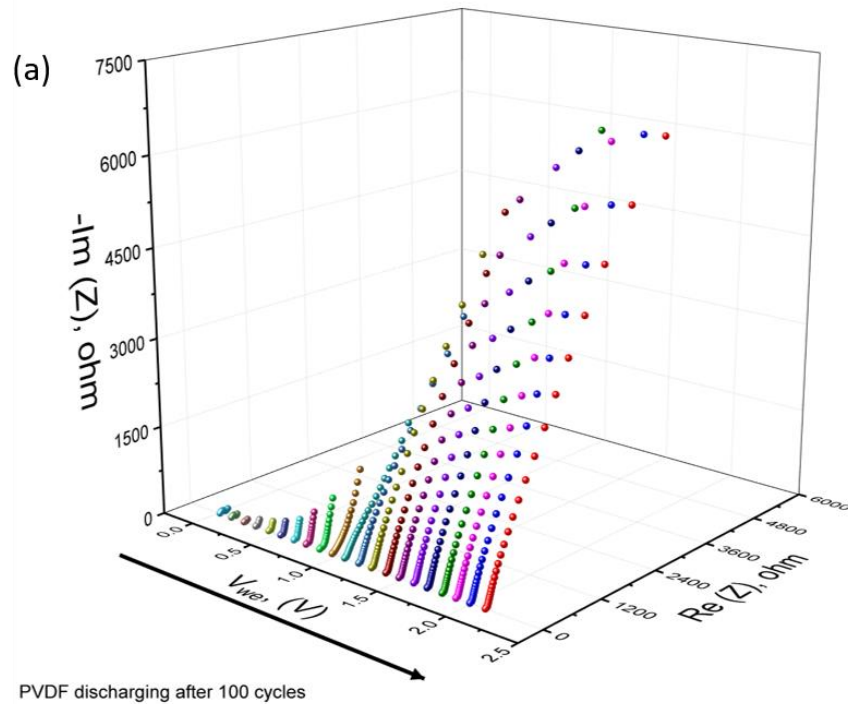


Figure 2.16 DEIS profiles for the discharging cycle for a) PVBCAImTFSI, b) PVDF as binders for graphite anode after 100 cycles at 1C.

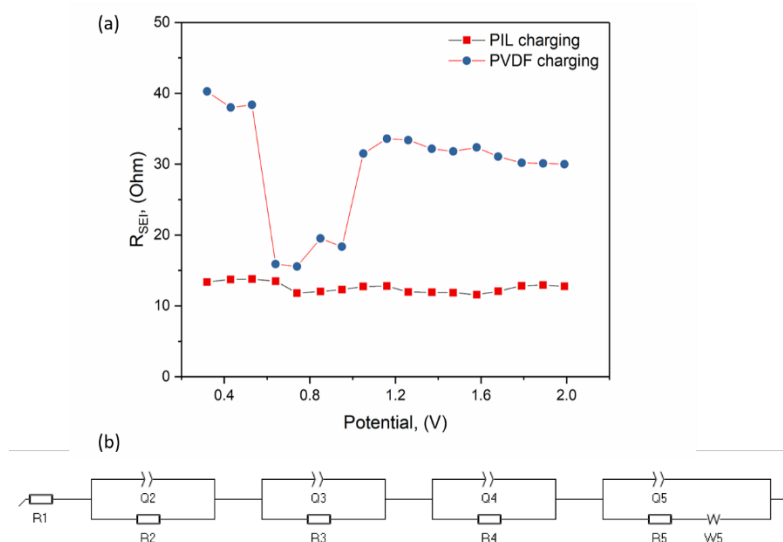


Figure 2.17 (a) R_{SEI} profiles during the charging cycle for PVBCAImTFSI and PVDF as binders for graphite anode, (b) Graphical representation of EECM.

Table 2.3 Circuit fitting data for PVBCAImTFSI based graphite anodes during the charging cycle.

V	R1	R2	R3	R4	R5	W	χ^2	Circuit
1.99	2.076	5.583	12.77	8.688	3.43E+04	0.05596	3.31E-05	R(QR)(QR)(QR)(Q(RW))
1.89	2.101	5.494	12.94	8.297	5.15E+04	3.04E+04	3.39E-05	R(QR)(QR)(QR)(Q(RW))
1.79	2.081	5.556	12.84	9.147	5.64E+04	26.01	3.14E-05	R(QR)(QR)(QR)(Q(RW))
1.68	2.039	5.639	12.07	19.05	9.06E+01	0.00018	4.37E-05	R(QR)(QR)(QR)(Q(RW))
1.58	1.996	5.656	11.57	196.9	2.71E+03	0.000265	4.27E-05	R(QR)(QR)(QR)(Q(RW))
1.47	2.021	5.595	11.88	1795	7.08E+03	0.0003	4.30E-05	R(QR)(QR)(QR)(Q(RW))
1.37	1.999	5.676	11.91	367.8	1.81E+03	3.40E-04	4.00E-05	R(QR)(QR)(QR)(C(RW))
1.26	1.989	5.703	11.96	139.1	1.06E+03	0.000495	4.60E-05	R(QR)(QR)(QR)(C(RW))
1.16	2.071	5.458	12.8	225.2	3.31E+02	0.001217	9.70E-05	R(QR)(QR)(QR)(C(RW))
1.05	2.032	5.663	12.74	357.3	8.37E+02	0.006821	4.81E-05	R(QR)(QR)(Q(RC))(Q(RW))
0.95	1.994	5.809	12.3	90.85	8.51E+03	0.00361	4.29E-05	R(QR)(QR)(QR)(C(RW))
0.85	1.987	5.625	12.03	32.84	1.55E+04	0.6472	4.19E-05	R(QR)(QR)(QR)(Q(RW))
0.74	1.795	4.386	11.82	6361	6.63E+03	3455	3.83E-05	R(QR)(QR)(QR)(Q(RW))
0.64	2.06	5.198	13.49	4384	1.23E+06	1.94E+05	3.65E-05	R(QR)(QR)(QR)(Q(RW))
0.53	2.075	5.428	13.79	78.28	2.59E+03	105.8	3.43E-05	R(QR)(QR)(QR)(Q(RW))
0.43	2.046	5.612	13.74	20.66	1.61E+00	6.30E-10	3.71E-05	R(QR)(QR)(QR)(Q(RW))
0.32	2.008	5.796	13.37	19.07	1.26E+05	2.64E-07	4.07E-05	R(QR)(QR)(QR)(Q(RW))

Table 2.4 Circuit fitting data for PVBCAImTFSI based graphite anodes during the discharging cycle.

V	R1	R2	R3	R4	R5	W	Chi2	Circuit
1.99	1.974	4.621	8.962	347.9	6830	0.000667	8.00E-05	R(QR)(QR)(QR)(C(RW))
1.89	2.477	4.926	8.822	8.522	2.21E+04	1.04E+08	5.63E-05	R(QR)(QR)(QR)(Q(RW))
1.79	1.947	4.713	8.512	274.1	5.39E+03	4.49E-04	5.10E-05	R(QR)(QR)(QR)(C(RW))
1.68	1.946	4.765	8.691	6.91	2.69E+04	1.47E+05	4.00E-05	R(QR)(QR)(QR)(Q(RW))
1.58	1.916	4.813	8.144	133.3	3.54E+03	4.13E-04	5.07E-05	R(QR)(QR)(QR)(C(RW))
1.47	2.28	6.628	8.409	5388	1.00E-03	5.59E-04	4.93E-05	R(QR)((QR)(QR))(C(RW))
1.37	1.992	4.584	8.318	507.3	5.41E+03	5.38E-04	5.99E-05	R(QR)(QR)(QR)(C(RW))
1.26	1.975	4.642	8.197	224.6	3.76E+03	7.34E-04	5.43E-05	R(QR)(QR)(QR)(C(RW))
1.16	2.023	4.481	8.811	2.943	1.10E+03	8.62E-04	3.94E-05	R(QR)(QR)(QR)(Q(RW))
1.05	2.139	4.102	8.858	189.7	6.46E+03	2.16E-03	4.93E-05	R(QR)(QR)(QR)(Q(RW))
0.95	1.907	4.874	7.676	60.41	9.00E-03	6.85E+00	3.38E-05	R(QR)(QR)(C(RQ))(Q(RW))
0.85	1.914	4.807	7.408	22.14	1.77E+04	4.33E+04	3.55E-05	R(QR)(QR)(QR)(Q(RW))
0.74	1.839	4.128	6.909	4.218	6.58E+03	1.00E-20	3.26E-05	R(QR)(QR)(QR)(Q(RW))
0.64	2.095	4.043	8.138	18.17	3.39E-02	3.05E+06	3.60E-05	R(QR)(QR)(Q(RC))(Q(RW))
0.53	2.117	4.08	8.407	44.2	1.78E+03	2.18E-05	2.77E-05	R(QR)(QR)(QR)(C(RW))
0.43	2.099	4.19	8.171	3.383	7.07E+04	1.08E-13	2.92E-05	R(QR)(QR)(QR)(Q(RW))
0.32	2.055	4.346	7.662	5.807	2.70E-02	7.34E-06	2.10E-05	R(QR)(QR)(QR)(Q(RW))

Table 2.5 Circuit fitting data for PVDF based graphite anodes during the charging cycle.

V	R1	R2	R3	R4	R5	W	Chi2	Circuit
1.99	4.446	7.313	30	416.6	2355	416.6	4.75E-05	R(QR)(QR)(QR)(C(RW))
1.89	4.443	7.363	30.12	1768	3.53E+03	0.000187	4.64E-05	R(QR)(QR)(QR)(C(RW))
1.79	4.384	7.777	30.19	349.8	7.80E+02	0.009548	1.70E-05	R(QR)(QR)(Q(RC))(Q(RW))
1.68	4.432	7.383	31.06	1996	3946	0.000191	4.50E-05	R(QR)(QR)(QR)(C(RW))
1.58	4.443	7.254	32.36	200.9	3.83E+05	2.87E+11	5.38E-05	R(QR)(QR)(QR)(C(RW))
1.47	4.402	7.44	31.82	2191	6.49E+03	0.000194	5.81E-05	R(QR)(QR)(QR)(Q(RW))
1.37	4.454	7.348	32.18	2018	3.51E-01	0.000225	6.29E-05	R(QR)(QR)(QR)(Q(RW))
1.26	4.381	7.885	33.4	5.982	4.24E+03	2.07E-05	4.23E-05	R(QR)(QR)(QR)(Q(RW))
1.16	4.377	7.99	33.6	16.15	2.10E+03	0.000511	2.92E-05	R(QR)(QR)(QR)(Q(RW))
1.05	4.366	8.075	31.49	282.5	2.93E+02	8.49E+03	3.34E-05	R(QR)(QR)(Q(RC))(Q(RW))
0.95	3.863	5.924	18.35	107.7	1.60E+02	2.45E-04	6.76E-05	R(CR)(QR)(Q(RC))(C(RW))
0.85	3.941	8.134	19.51	117.7	2.42E+04	3053	9.40E-05	R(QR)(QR)(QR)(C(RW))
0.74	1.244	9.889	15.57	120.7	7.09E+03	0.02424	4.20E-04	R(QR)(QR)(QR)(Q(RW))
0.64	2.451	4.055	15.9	51.26	4.08E+16	0.05448	3.50E-05	R(CR)(QR)(QR)(C(RW))
0.53	4.408	8.013	38.37	9.632	4.83E+03	3.64E-02	2.42E-05	R(CR)(QR)(QR)(Q(RW))
0.43	4.393	7.593	38	4.329	0.531	1.85E-11	2.55E-05	R(QR)(QR)(Q(RC))(Q(RW))
0.32	4.502	7.116	40.27	5.88E+07	0.009999	0.000625	6.08E-05	R(QR)(QR)(QR)(C(RW))

Table 2.6 Circuit fitting data for PVDF based graphite anodes during the discharging cycle.

V	R1	R2	R3	R4	R5	W	Chi2	Circuit
1.99	4.411	6.808	23.31	1097	1626	0.000342	4.48E-05	R(QR)(QR)(QR)(C(RW))
1.89	4.385	6.694	23.82	1382	2100	0.000314	7.42E-05	R(QR)(QR)(QR)(C(RW))
1.79	4.436	6.699	23.06	958.9	1521	0.000352	6.00E-05	R(QR)(QR)(QR)(C(RW))
1.68	4.46	6.634	23.35	1106	1586	0.000348	5.02E-05	R(QR)(QR)(QR)(C(RW))
1.58	4.439	6.709	23.1	1077	1413	0.000362	5.02E-05	R(QR)(QR)(QR)(C(RW))
1.47	4.479	6.561	23.45	1317	1734	0.000346	7.69E-05	R(QR)(QR)(QR)(C(RW))
1.37	4.436	6.719	22.16	807.1	1166	0.000429	5.76E-05	R(QR)(QR)(QR)(C(RW))
1.26	4.424	6.967	24.02	14.17	169.4	0.000383	2.60E-05	R(QR)(QR)(QR)(Q(RW))
1.16	4.402	6.903	21.41	46.09	95	0.000784	2.59E-05	R(QR)(QR)(QR)(Q(RW))
1.05	4.441	6.701	22.22	461.4	1187	0.000894	3.44E-05	R(QR)(QR)(QR)(C(RW))
0.95	4.061	9.154	25.76	12.91	1.87	0.005015	9.05E-05	R(QR)(QR)(C(RQ))(Q(RW))
0.85	4.386	6.964	21.19	47.26	0.02384	1.56E-02	6.66E-05	R(QR)(QR)(C(RQ))(Q(RW))
0.74	4.235	8.981	28.49	76.1	1.50E+04	28.49	6.97E-05	R(QR)(CR)(CR)(Q(RW))
0.64	2.935	9.636	37.99	9.636	5.436	0.06699	3.98E-05	R(QR)((QR)(QR))(C(RW))
0.53	4.421	6.598	19.82	12.9	1.27E+04	2.38E+04	2.76E-05	R(QR)(QR)(Q(RC))(Q(RW))
0.43	4.446	6.398	22.11	6.398	37.56	0.02015	2.23E-05	R(QR)(QR)(Q(RC))(Q(RW))
0.32	4.415	6.321	22.07	3.055	1.01E-01	0.0672	2.99E-05	R(QR)(QR)(Q(RC))(Q(RW))

Charge-discharge measurements were carried out after understanding the electrochemistry of the PIL binder in graphite anodes. Figure 2.18 a & b shows the charge-discharge profile for PVBCAImTFSI and PVDF based electrodes. In the first cycle of Figure 2.18 a, it can be observed that at around 0.7 V, some irreversible reactions taking place leading to the formation of SEI. The first cycle reversible discharge capacity of about 91 mAh/g was achieved for PVBCAImTFSI based anodes against 103.5 mAh/g for PVDF based anodes. However, on continuous cycling, due to the cementing of the electrodes, the discharge capacity obtained after 300 cycles increased to 210 mAh/g for PVBCAImTFSI based electrodes whereas, the capacity for PVDF based electrodes deteriorated to 73 mAh/g. The deterioration in the capacity was observed for PVDF based electrodes due to the non-uniform and thick SEI formation. After 500 cycles of charge-discharge cycling at 1C rate, the discharge capacity obtained was about 199 mAh/g. The Figure shows the comparison of the charge-discharge cycling performance of anodic half cells with PVBCAImTFSI binder with that of the PVDF binder. It is evident that the PVBCAImTFSI based graphite anodes significantly outperform that with PVDF binder. Initially, there is a dip in the reversible discharge capacity. However as the SEI matures with cycling, the half-cells with PVBCAImTFSI exhibited

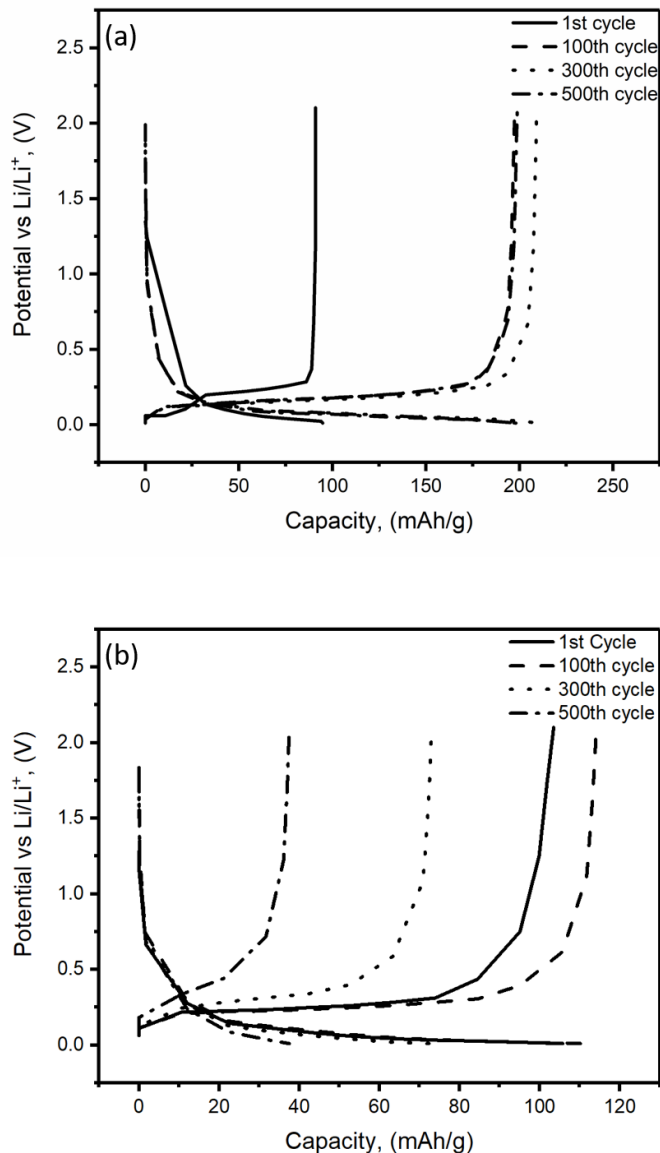


Figure 2.18 Charge-discharge profiles during the 1st, 100th, 300th and 500th cycles for graphite anodes with (a) PVBCAImTFSI as binder.

a discharge capacity of 210 mAh/g as shown in Figure 2.19. The coulombic efficiency for the first seven cycles was <99.5%. However, after the SEI stabilizes, it stabilizes at >99.9%. The maximum discharge capacity of the half-cells with PVDF binder was about 140 mAh/g after 125 cycles, which was 33% lesser than the PVBCAImTFSI based electrodes as shown in Figure 2.19. Half-cells with PVBCAImTFSI binder retained 95% of the maximum discharge capacity even after 500 cycles as compared to 40% for the half-cells with PVDF binder. This can be attributed to the robust

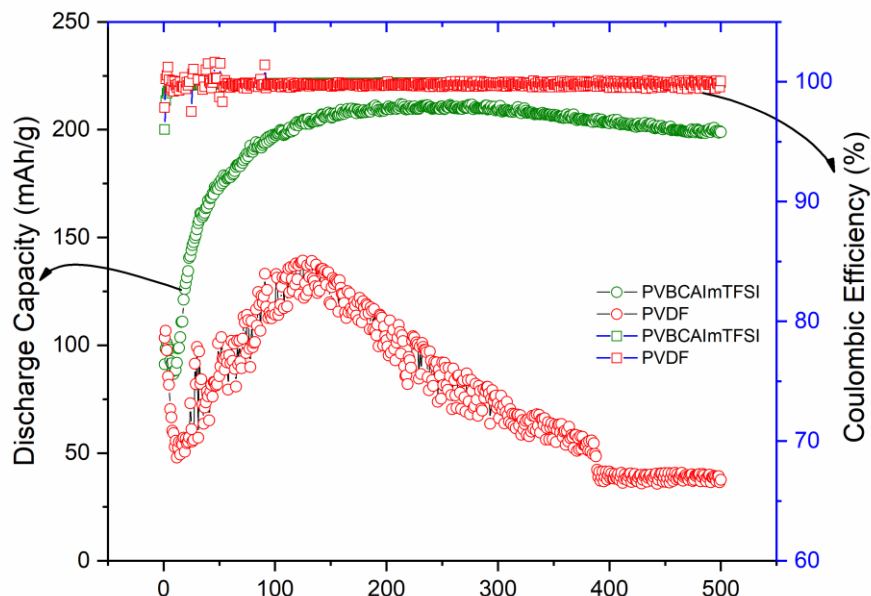


Figure 2.19 Long cycling performance of graphite anodes with PVBCAImTFSI (Green) and PVDF (Red) as binders with 1.0M LiPF₆ / EC : DEC electrolyte at 1C rate.

SEI formed during the cycling which provides for better lithium-ion mobility. To understand the significance of the sidechain and the anion on the ionic liquid moiety in the PILs, a PIL with a butyl side chain (PVBCBImTFSI) was studied and the results of which are discussed in the next chapter. The allyl group present in the PVBCAImTFSI plays a significant role in its enhanced performance as a binder. The allyl group on continuous cycling may polymerize forming a network over the electrode material leading to better adherence. The polymerization of the allyl groups over the electrode material confers an extra mechanical strength and this might be one of the reasons for the discharge capacity to get stabilized overtime.

Stability of the electrodes was evaluated by performing charge-discharge measurements at different rates. Figure 2.20 gives the charge-discharge rate studies performed at different rates for half-cells with PVBCAImTFSI and PVDF binders. Rate studies show half-cells with PVBCAImTFSI binder outperforms PVDF at all the rates. Table 2.7 gives the reversible discharge capacity obtained for the half-cells with PVBCAIMTFSI and PVDF electrodes. The better ionic mobility in the PVBCAImTFSI based electrodes assists in the quicker movement of the ions in and out of the electrode. This leads to almost 37% higher discharge capacity compared to PVDF obtained at 2C rate. The discharge capacity obtained at 0.1C rate post rate studies was 261.6 mAh/g

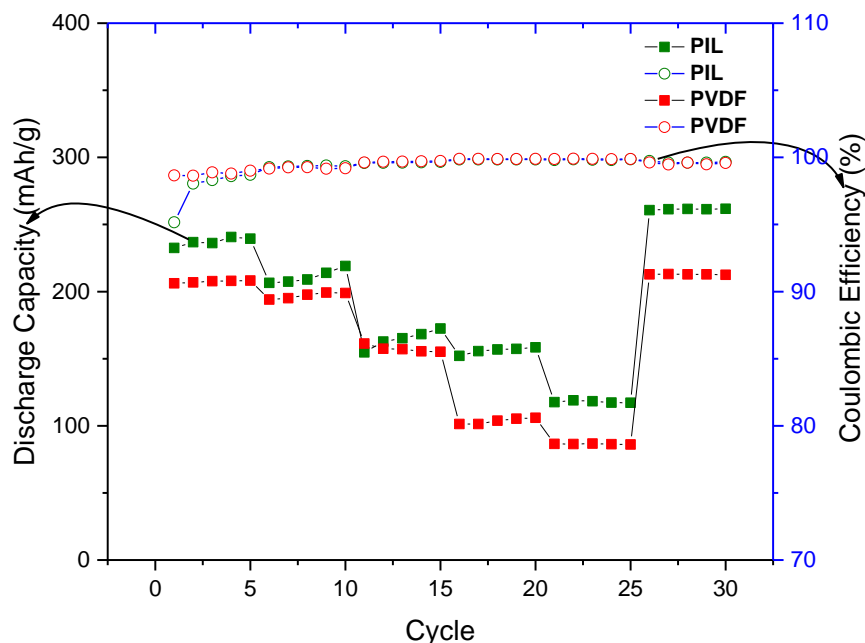


Figure 2.20 Rate performance of graphite anodes with PVBCAImTFSI (Green) and PVDF (Red) as binders with 1.0M LiPF₆ / EC : DEC electrolyte at 1C rate.

and 212.9 mAh/g for PVBCAImTFSI and PVDF respectively. This enhanced performance of the PVBCAImTFSI binder can be attributed to its improved interaction with the electrolyte leading to the formation of ion-conducting pathways in the active material.

Table 2.7 Discharge capacities at different rates for graphite anodes with PVBCAImTFSI and PVDF as binders with 1.0M LiPF₆ / EC : DEC electrolyte.

Rate	Discharge Capacity (mAh/g)	
	PVBCAImTFSI	PVDF
0.1C	236.2	207.8
0.2C	209.1	197.8
0.5C	165.3	157.1
1.0C	156.9	103.8
2.0C	118.3	86.8
0.1C (after rate studies)	261.6	212.9

2.4.3 Morphology and Composition Analysis

Physical characterization of the electrodes is very crucial to understand the morphological and compositional changes that occur due to the electrochemical measurements. This enables to correlate with the electrochemical results and also to improvise the electrode performance. To achieve these objectives, Field emission scanning electron microscopy (FESEM) imaging was carried out to understand the morphological changes and X-ray photoelectron spectroscopy measurements were carried out to understand the composition of the electrode surface. The electrodes were subjected to 500 cycles of charge-discharge cycling at 1C rate. The morphology of the electrodes prior and post cycling was investigated using FESEM. Figure 2.21 a&c show the PVBCAImTFSI and PVDF based electrodes before charge-discharge cycling. The as-prepared electrodes showed uniform distribution of the electrode constituents. Figure 2.21 b&d show the PVBCAImTFSI and PVDF based electrodes after 500 cycles charge-discharge at 1C rate. Non-

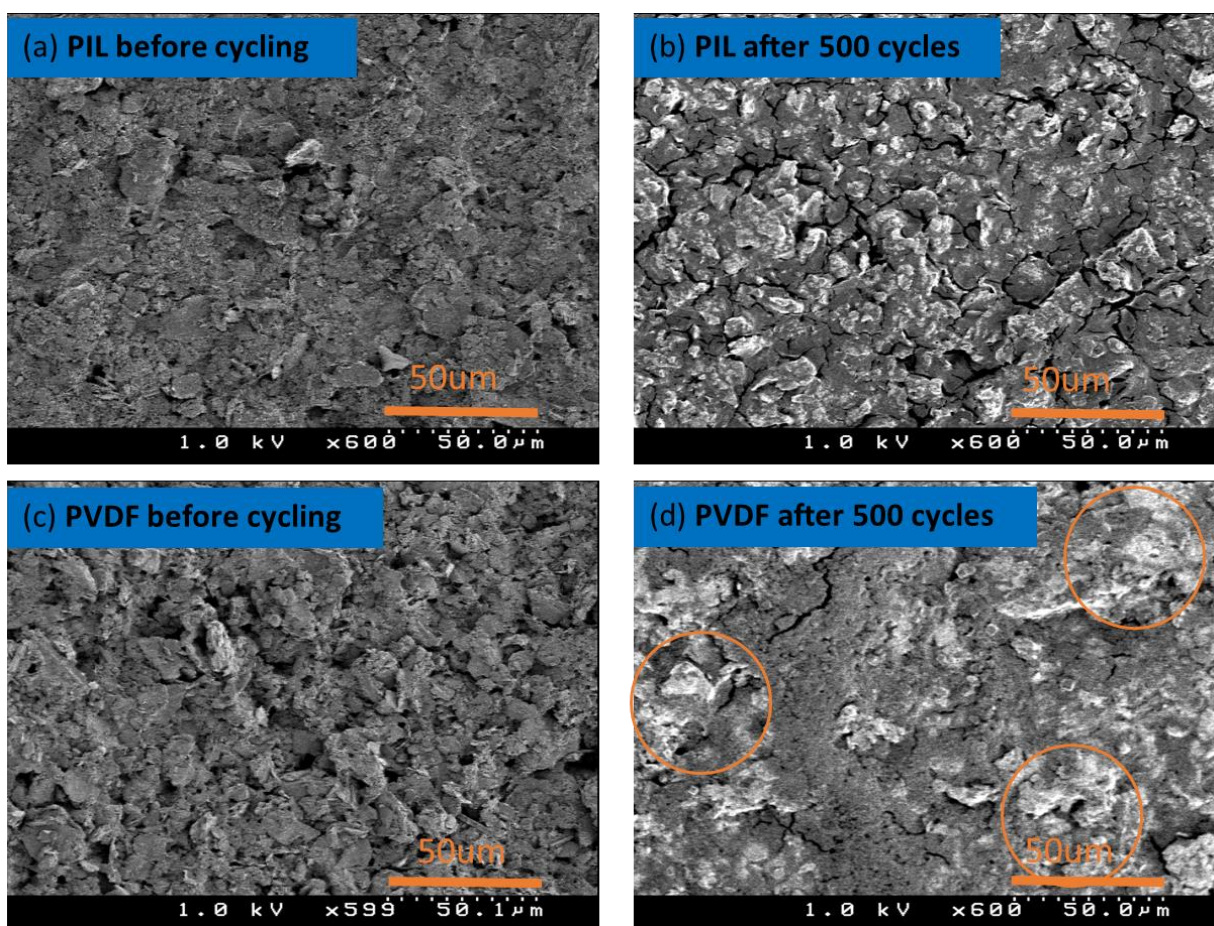


Figure 2.21 FESEM images of PIL (a) before cycling (b) after 500 cycles charge-discharge at 1C, PVDF (c) before cycling (d) after 500 cycles.

conducting entities get charged-up during the FESEM measurement resulting in a higher contrast ratio than the conductive entities. Charge-discharge cycling results in the formation of uniform SEI on the surface of the electrode. Due to the non-conducting nature of SEI, charging up of sample occurs at the spots where it is present resulting in spots with higher contrast in the micrograph. In the case of PVBCAImTFSI based electrodes, a uniform distribution of these spots was observed. However, in the case of PVDF based electrodes, a non-uniform distribution was observed. This might indicate that in the case of PVBCAImTFSI, the SEI formed was uniform compared to SEI corresponding to the PVDF based electrode.

XPS is one of the most powerful techniques available to characterize the surfaces up to 10 nm depth. It is a very useful technique to probe the SEI and to understand the composition. To understand the chemical composition of the SEI on anodes, XPS measurements were carried out after cycling the electrodes for 500 cycles. The deconvoluted XPS spectra for C 1s are given below in Figure 2.22 a & b for PVBCAImTFSI and PVDF based graphite anodes respectively. The compositional similarity was observed; however, the area of the graphitic peak was found to be 1.5 times greater in PVBCAImTFSI based anodes as compared to PVDF based electrode. This means thinner SEI layer formation in the case of PVBCAImTFSI. Also, the binding energy corresponding to N 1s for PVBCAImTFSI based anodes at about 400 eV as shown in Figure 2.23, has not shifted after charge-discharge cycling. It is well known that XPS being a surface technique can measure up to 10 nm into the surface. The appearance of the N 1s peak after charge-discharge cycling also shows that the SEI is very thin. The collective area under the peaks for the SEI components in the C 1s peak such as PEO, ether carbons etc., is lesser in the PVBCAImTFSI based anodes as shown in Table 2.8. These three observations corroborate to SEI being thinner resulting in lesser SEI resistance (evaluated by DEIS) for PVBCAImTFSI based electrodes than that of the PVDF. The XPS results support the observation made in electrochemical and SEM measurements. The F 1s and O 1s peaks corresponding to PVBCAImTFSI and PVDF based electrodes were deconvoluted as shown in Figure 2.22 and the peaks corresponding to various components along with % area under the curve are tabulated in Table 2.9 and 2.10 respectively. It is reported in the literature that the LiPF₆-mediated decomposition of Li₂CO₃ and other carbonates predominantly forms LiF, CO₂ and lithium fluorophosphates in high yield.⁴² Formation of LiF in the SEI layer is detrimental to the functioning of the LiB due to its poor ionic and electronic conductivity. We have understood that the presence of the allyl group promotes formation electrolyte (LiPF₆) based

reduction products and suppresses the formation of the LiF. PVDF based electrodes possess almost 5 times higher concentration of LiF than PVBCAImTFSI based electrodes. Presence of the PVBCAImTFSI based binder suppresses the LiPF₆ – mediated reduction of the lithium carbonates

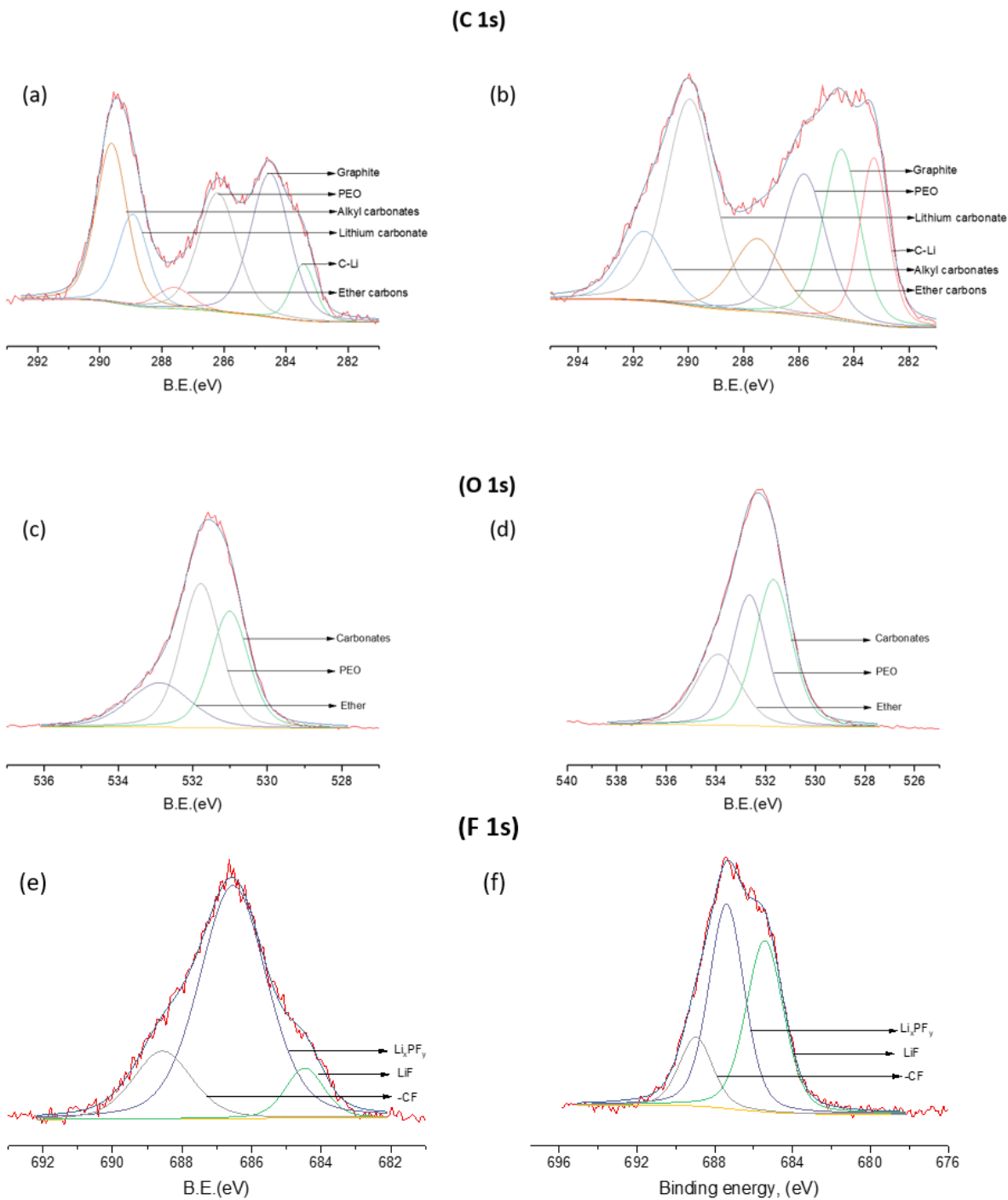


Figure 2.22 The deconvoluted XPS spectra for (a), (c) & (e) PIL and (b), (d) & (f) PVDF based graphite anodes respectively explaining various components of SEI.

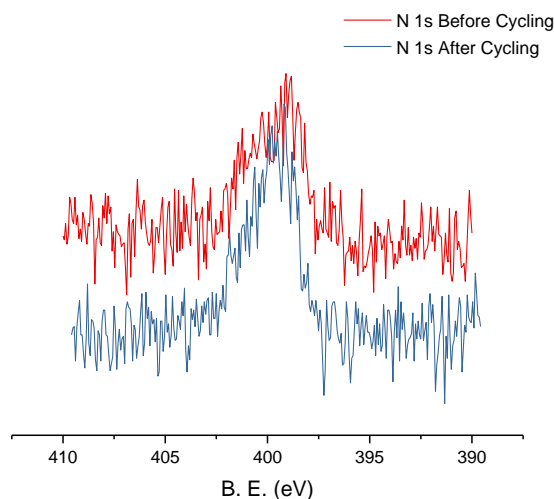


Figure 2.23 The XPS spectra of the N 1s for PIL based graphite anodes before and after charge-discharge cycling for 500 cycles at 1C rate.

leading to the lesser amount of LiF. Presence of lesser LiF in the PVBCAImTFSI based electrolytes leads to better ionic as well as electronic conductivity and maintaining the integrity of the SEI layer as observed in DEIS studies.

Table 2.8 The binding energy values and corresponding % area under the curve corresponding to C 1s for PIL and PVDF based electrodes.

Component	PIL	% area under the curve	PVDF	% area under the curve
C-Li	283.5	6.717468	283.4	13.97599
Graphite	284.6	27.94842	284.6	18.56121
PEO	286.3	22.98945	286	18.19946
Ether carbons	287.9	3.710434	287.7	10.66096
Lithium carbonate Li ₂ CO ₃	289.2	13.83353	290.1	29.16367
Alkyl carbonates (R- OCO ₂ -Li)	290.5	24.8007	291.8	9.438706

Table 2.9 The binding energy values and corresponding % area under the curve corresponding to F 1s for PIL and PVDF based electrodes.

Component	PIL	% area under the curve	PVDF	% area under the curve
LiF	684.5	8.9	685.4	40.4
Li _x PF _y	686.5	72.7	687.4	45.2
C-F	688.5	18.3	689.0	14.4

Table 2.10 The binding energy values and corresponding % area under the curve corresponding to O 1s for PIL and PVDF based electrodes.

Component	PIL	% area under the curve	PVDF	% area under the curve
Carbonate	531.0	34.4	531.6	41.5
PEO	531.8	21.4	532.6	34.6
Ether	532.9	44.2	533.8	23.8

2.4.4 Adhesion and Electrolyte Interaction

An efficient binder should i) hold the active material and electrode additives with each other and shows good adhesion to the current collector; ii) absorb electrolyte and provide a pathway for lithium-ion conduction, and iii) assist in the formation of uniform SEI during the battery cycling. Figure 2.24 shows the scotch tape test or peel test carried out to qualitatively assess the adherence of the electrode material to the current collector. Scotch tape was pasted onto the electrode affixed on a glass plate and was removed. The loss in the weight of electrode material was measured. Electrodes with PVBCAImTFSI binder showed 99.91% retention of the active material to the current collector when compared to the 99.85% for PVDF based electrodes. This qualitatively shows that the adherence properties of PVBCAImTFSI binder were much better than that of its PVDF counterparts. Wettability of the binders was studied to evaluate their interaction with the electrolyte. 1 mL of 1:1 mixture of EC: DEC was added to 40 mg of binders. In the case of PVBCAImTFSI, immediate uptake of the electrolyte and gelation of the binder were observed. Figure 2.25 shows the binder electrolyte mixture 12 days after the addition of the electrolyte. After 12 days, PVBCAImTFSI remains as a gel, whereas slow dissolution of PVDF in the electrolyte was observed. This gelation property of the PVBCAImTFSI assists in the formation of pathways for lithium transport in the active material and a better SEI formation. On the other hand, dissolution of PVDF infers that over a long period the PVDF binder along with active material may probably peel off from the current collector. This instability will lead to capacity fading over long cycling.

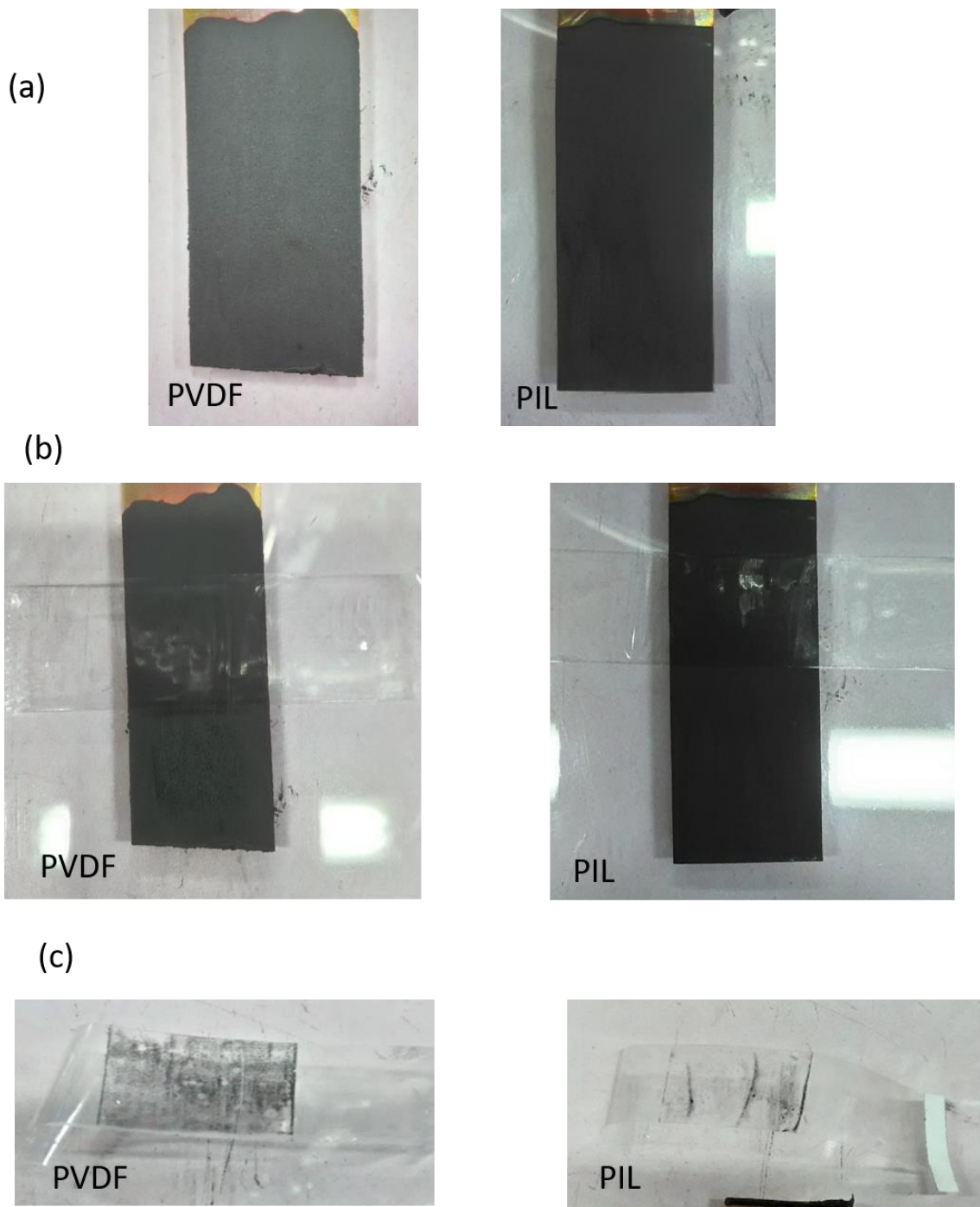


Figure 2.24 (a) Photographs of electrodes after coating and drying, (b) Photographs of electrodes with scotch tape, (c) Photographs of scotch tapes peel test.



Figure 2.25 Photographs of wettability test to evaluate the interaction of the binders with electrolytes.

2.5 Conclusions

PVBCAImTFSI as a binder in graphite anodes demonstrated an enhanced performance (Figure 2.26) as compared to the commercially employed PVDF polymer. Its improved interaction with the electrode material and the current collector helps to maintain the electrode integrity over long cycling. The wettability of the PVBCAImTFSI was found to be more profound than PVDF. Due to the lower LUMO level compared to the electrolyte, a suppressed electrolyte decomposition was observed leading to the formation of a better SEI. Cyclic voltammetry-based scan rate studies indicated that lithium-ion diffusion coefficient obtained from the for PVBCAImTFSI binder was 41 % higher than the PVDF binder. This can be due to the ion-conducting pathways that are formed in the electrode due to the swelling of PVBCAImTFSI. Cyclic voltammetry studies indicated the formation of thinner SEI compared to PVDF leading to improved interfacial properties. The reduced R_{SEI} values obtained from the DEIS measurements for PVBCAImTFSI binder-based anodes indicated the formation of a better SEI compared to PVDF binder-based anodes. These properties cumulatively led to the improved charge-discharge performance of PVBCAImTFSI binder. A discharge capacity of about 210 mAh/g was observed at 1C rate with 95 % capacity retention after 500 cycles of cycling for PVBCAImTFSI based half-cells. Also, it displayed an enhanced rate performance and higher discharge capacity than PVDF at higher charge-discharge rates indicating good stability. All these results indicate PVBCAImTFSI to be a potential alternative for PVDF as a binder in LIBs.

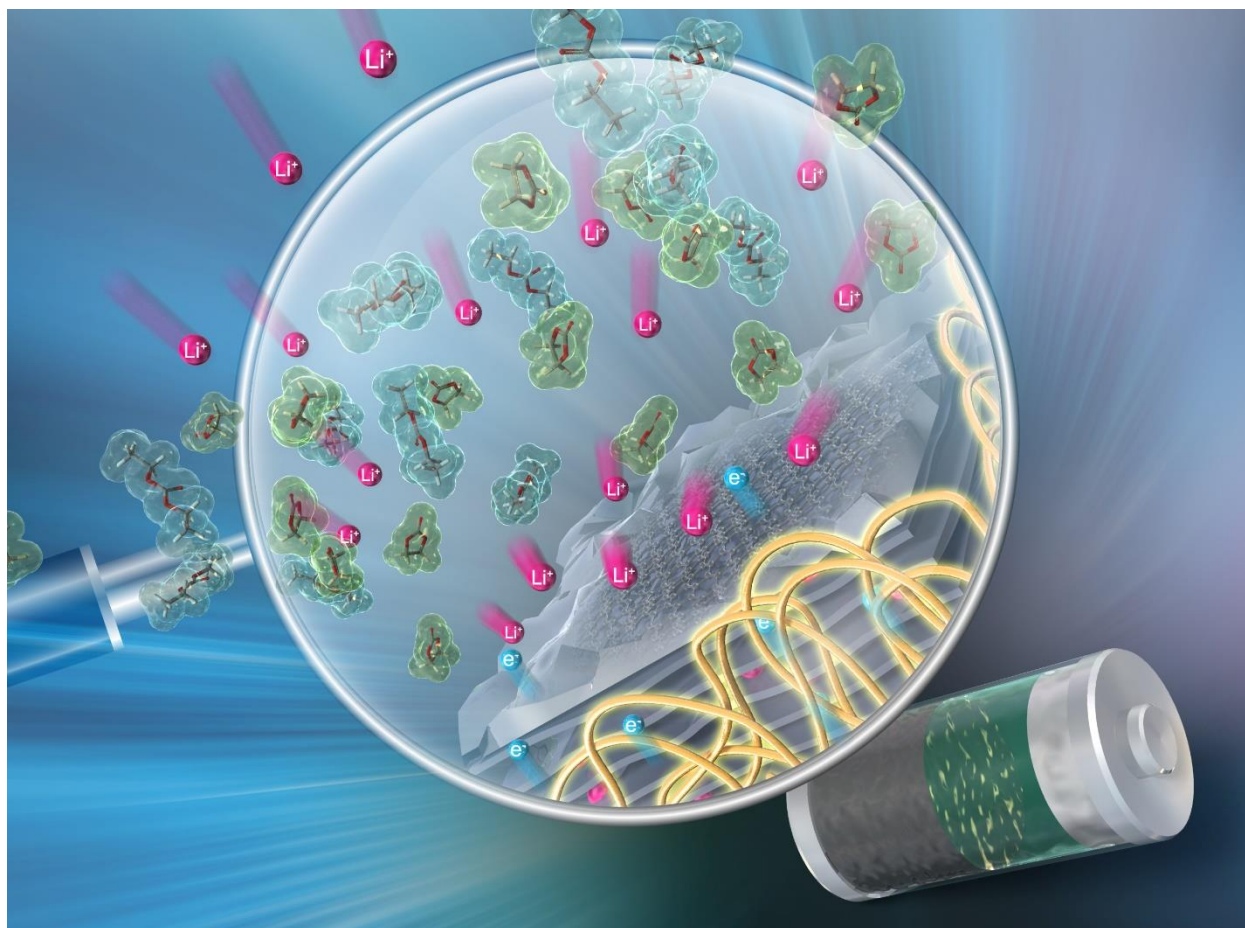


Figure 2.26 Graphical abstract of the PIL binder PVBCAImTFSI for lithium-ion battery graphite anodes.

References

- (1) Cheng, F.; Liang, J.; Tao, Z.; Chen, J. Functional Materials for Rechargeable Batteries. *Adv. Mater.* **2011**, *23* (15), 1695–1715. <https://doi.org/10.1002/adma.201003587>.
- (2) Li, H.; Wang, Z.; Chen, L.; Huang, X. Research on Advanced Materials for Li-Ion Batteries. *Adv. Mater.* **2009**, *21* (45), 4593–4607. <https://doi.org/10.1002/adma.200901710>.
- (3) Tarascon, J.M.; Armand, M. Issues and Challenges Facing Rechargeable Lithium Ion Batteries. *Nature* **2001**, *414*, 359. <https://doi.org/10.1097/00006254-199510000-00002>.
- (4) Marom, R.; Amalraj, S. F.; Leifer, N.; Jacob, D.; Aurbach, D. A Review of Advanced and Practical Lithium Battery Materials. *J. Mater. Chem.* **2011**, *21* (27), 9938–9954. <https://doi.org/10.1039/c0jm04225k>.
- (5) Vinodkumar Etacheri, Rotem Marom, Ran Elazari, G. S. and D. A. Challenges in the Development of Advanced Li-Ion Batteries: A Review. *Energy Environ. Sci.* **2011**, No. 4, 3243–3262. <https://doi.org/10.1039/c1ee01598b>.
- (6) Scrosati, B.; Garche, J. Lithium Batteries: Status, Prospects and Future. *J. Power Sources* **2010**, *195* (9), 2419–2430. <https://doi.org/10.1016/j.jpowsour.2009.11.048>.
- (7) Tarascon, J. M.; Armand, M. Building Better Batteries. **2008**, *451* (February), 652–657. <https://doi.org/10.1038/451652a>.
- (8) Goodenough, J. B.; Park, K. S. The Li-Ion Rechargeable Battery: A Perspective. *J. Am. Chem. Soc.* **2013**, *135* (4), 1167–1176. <https://doi.org/10.1021/ja3091438>.
- (9) Yazami, R.; Touzain, P. A Reversible Graphite-Lithium Negative Electrode for Electrochemical Generators. *J. Power Sources* **1983**, *9* (3), 365–371. [https://doi.org/10.1016/0378-7753\(83\)87040-2](https://doi.org/10.1016/0378-7753(83)87040-2).
- (10) Paronyan, T. M.; Thapa, A. K.; Sherehiy, A.; Jasinski, J. B.; Jangam, J. S. D. Incommensurate Graphene Foam as a High Capacity Lithium Intercalation Anode. *Sci. Rep.* **2017**, *7* (January), 1–11. <https://doi.org/10.1038/srep39944>.
- (11) Oktaviano, H. S.; Yamada, K.; Waki, K. Nano-Drilled Multiwalled Carbon Nanotubes: Characterizations and Application for LIB Anode Materials. *J. Mater. Chem.* **2012**, *22* (48),

- 25167–25173. <https://doi.org/10.1039/c2jm34684b>.
- (12) Roberts, A. D.; Li, X.; Zhang, H. Porous Carbon Spheres and Monoliths: Morphology Control, Pore Size Tuning and Their Applications as Li-Ion Battery Anode Materials. *Chem. Soc. Rev.* **2014**, *43* (13), 4341–4356. <https://doi.org/10.1039/c4cs00071d>.
- (13) Ren, H.; Yu, R.; Qi, J.; Zhang, L.; Jin, Q.; Wang, D. Hollow Multishelled Heterostructured Anatase/TiO₂ (B) with Superior Rate Capability and Cycling Performance. *Adv. Mater.* **2019**, *2*, 1805754. <https://doi.org/10.1002/adma.201805754>.
- (14) Yi, T. F.; Fang, Z. K.; Deng, L.; Wang, L.; Xie, Y.; Zhu, Y. R.; Yao, J. H.; Dai, C. Enhanced Electrochemical Performance of a Novel Li₄Ti₅O₁₂ composite as Anode Material for Lithium-Ion Battery in a Broad Voltage Window. *Ceram. Int.* **2015**, *41* (2), 2336–2341. <https://doi.org/10.1016/j.ceramint.2014.10.041>.
- (15) Feng, K.; Li, M.; Liu, W.; Kashkooli, A. G.; Xiao, X.; Cai, M.; Chen, Z. Silicon-Based Anodes for Lithium-Ion Batteries: From Fundamentals to Practical Applications. *Small* **2018**, No. January, 1702737. <https://doi.org/10.1002/sml.201702737>.
- (16) Ying, H.; Han, W. Q. Metallic Sn-Based Anode Materials: Application in High-Performance Lithium-Ion and Sodium-Ion Batteries. *Adv. Sci.* **2017**, *4* (11). <https://doi.org/10.1002/advs.201700298>.
- (17) Li, X.; Yang, Z.; Fu, Y.; Qiao, L.; Li, D.; Yue, H.; He, D. Germanium Anode with Excellent Lithium Storage Performance in a Germanium/Lithium-Cobalt Oxide Lithium-Ion Battery. *ACS Nano* **2015**, *9* (2), 1858–1867. <https://doi.org/10.1021/nn506760p>.
- (18) Goriparti, S.; Miele, E.; De Angelis, F.; Di Fabrizio, E.; Proietti Zaccaria, R.; Capiglia, C. Review on Recent Progress of Nanostructured Anode Materials for Li-Ion Batteries. *J. Power Sources* **2014**, *257*, 421–443. <https://doi.org/10.1016/j.jpowsour.2013.11.103>.
- (19) Nitta, N.; Wu, F.; Lee, J. T.; Yushin, G. Li-Ion Battery Materials: Present and Future. *Mater. Today* **2015**, *18* (5), 252–264. <https://doi.org/10.1016/j.mattod.2014.10.040>.
- (20) Li, L.; Meng, F.; Jin, S. High-Capacity Lithium-Ion Battery Conversion Cathodes Based on Iron Fluoride Nanowires and Insights into the Conversion Mechanism. *Nano Lett.* **2012**, *12* (11), 6030–6037. <https://doi.org/10.1021/nl303630p>.

- (21) Gmitter, A. J.; Gural, J.; Amatucci, G. G. Electrolyte Development for Improved Cycling Performance of Bismuth Fluoride Nanocomposite Positive Electrodes. *J. Power Sources* **2012**, *217*, 21–28. <https://doi.org/10.1016/j.jpowsour.2012.05.104>.
- (22) Lee, D. H.; Carroll, K. J.; Calvin, S.; Jin, S.; Meng, Y. S. Conversion Mechanism of Nickel Fluoride and NiO-Doped Nickel Fluoride in Li Ion Batteries. *Electrochim. Acta* **2012**, *59*, 213–221. <https://doi.org/10.1016/j.electacta.2011.10.105>.
- (23) Seh, Z. W.; Yu, J. H.; Li, W.; Hsu, P. C.; Wang, H.; Sun, Y.; Yao, H.; Zhang, Q.; Cui, Y. Two-Dimensional Layered Transition Metal Disulphides for Effective Encapsulation of High-Capacity Lithium Sulphide Cathodes. *Nat. Commun.* **2014**, *5*, 1–8. <https://doi.org/10.1038/ncomms6017>.
- (24) Nan, C.; Lin, Z.; Liao, H.; Song, M. K.; Li, Y.; Cairns, E. J. Durable Carbon-Coated Li₂S Core-Shell Spheres for High Performance Lithium/Sulfur Cells. *J. Am. Chem. Soc.* **2014**, *136* (12), 4659–4663. <https://doi.org/10.1021/ja412943h>.
- (25) Luo, C.; Zhu, Y.; Wen, Y.; Wang, J.; Wang, C. Carbonized Polyacrylonitrile-Stabilized Se_xCathodes for Long Cycle Life and High Power Density Lithium Ion Batteries. *Adv. Funct. Mater.* **2014**, *24* (26), 4082–4089. <https://doi.org/10.1002/adfm.201303909>.
- (26) Patnaik, S. G.; Vedarajan, R.; Matsumi, N. BIAN Based Functional Diimine Polymer Binder for High Performance Li Ion Batteries. *J. Mater. Chem. A* **2017**, *5* (August), 17909–17919. <https://doi.org/10.1039/C7TA03843G>.
- (27) Zhang, S. S.; Jow, T. R. Study of Poly(acrylonitrile-methyl methacrylate) as Binder for Graphite Anode and LiMn₂O₄ Cathode of Li-Ion Batteries. *J. Power Sources* **2002**, *109* (2), 422–426. [https://doi.org/10.1016/S0378-7753\(02\)00107-6](https://doi.org/10.1016/S0378-7753(02)00107-6).
- (28) Wang, Y.; Zheng, H.; Qu, Q.; Zhang, L.; Battaglia, V. S.; Zheng, H. Enhancing Electrochemical Properties of Graphite Anode by Using Poly(methylmethacrylate)-Poly(vinylidene fluoride) Composite Binder. *Carbon N. Y.* **2015**, *92*, 318–326. <https://doi.org/10.1016/j.carbon.2015.04.084>.
- (29) Qian, W.; Texter, J.; Yan, F. Frontiers in Poly(ionic liquid)s: Syntheses and Applications. *Chem. Soc. Rev.* **2017**, *46* (4), 1124–1159. <https://doi.org/10.1039/c6cs00620e>.

- (30) Yuan, J.; Mecerreyes, D.; Antonietti, M. Poly(ionic liquid)s: An Update. *Prog. Polym. Sci.* **2013**, *38* (7), 1009–1036. <https://doi.org/10.1016/j.progpolymsci.2013.04.002>.
- (31) Spanos, I.; Neugebauer, S.; Guterman, R.; Yuan, J.; Schlögl, R.; Antonietti, M. Poly(ionic liquid) Binders as Ionic Conductors and Polymer Electrolyte Interfaces for Enhanced Electrochemical Performance of Water Splitting Electrodes. *Sustain. Energy Fuels* **2018**, *2* (7), 1446–1451. <https://doi.org/10.1039/C8SE00110C>.
- (32) Von Zamory, J.; Bedu, M.; Fantini, S.; Passerini, S.; Paillard, E. Polymeric Ionic Liquid Nanoparticles as Binder for Composite Li-Ion Electrodes. *J. Power Sources* **2013**, *240*, 745–752. <https://doi.org/10.1016/j.jpowsour.2013.04.127>.
- (33) Meek, K. M.; Nykaza, J. R.; Elabd, Y. A. Alkaline Chemical Stability and Ion Transport in Polymerized Ionic Liquids with Various Backbones and Cations. *Macromolecules* **2016**, *49* (9), 3382–3394. <https://doi.org/10.1021/acs.macromol.6b00434>.
- (34) Vedarajan, R.; Matsui, K.; Tamaru, E.; Dhankhar, J.; Takekawa, T.; Matsumi, N. Ionic Liquid/Boric Ester Binary Electrolytes with Unusually High Lithium Transference Number. *Electrochem. Commun.* **2017**, *81* (June), 132–135. <https://doi.org/10.1016/j.elecom.2017.06.019>.
- (35) Patnaik, S. G.; Vedarajan, R.; Matsumi, N. BIAN Based Functional Diimine Polymer Binder for High Performance Li Ion Batteries. *J. Mater. Chem. A* **2017**, *5* (34), 17909–17919. <https://doi.org/10.1039/c7ta03843g>.
- (36) Choi, N.-S.; Ha, S.-Y.; Lee, Y.; Jang, J. Y.; Jeong, M.-H.; Shin, W. C.; Ue, M. Recent Progress on Polymeric Binders for Silicon Anodes in Lithium-Ion Batteries. *J. Electrochem. Sci. Technol.* **2015**, *6* (2), 35–49. <https://doi.org/10.5229/JECST.2015.6.2.35>.
- (37) Peled, E.; Menkin, S. Review—SEI: Past, Present and Future. *J. Electrochem. Soc.* **2017**, *164* (7), A1703–A1719. <https://doi.org/10.1149/2.1441707jes>.
- (38) Aurbach, D. Review of Selected Electrode–Solution Interactions Which Determine the Performance of Li and Li Ion Batteries. *J. Power Sources.* **2000**, 206–218.
- (39) Wang, A.; Kadam, S.; Li, H.; Shi, S.; Qi, Y. Review on Modeling of the Anode Solid Electrolyte Interphase (SEI) for Lithium-Ion Batteries. *npj Comput. Mater.* **2018**, *4* (1).

<https://doi.org/10.1038/s41524-018-0064-0>.

- (40) Li, L.; Zhang, J.; Zou, Y.; Jiang, W.; Lei, W.; Ma, Z. High-Rate and Long-Term Cycle Stability of Lithium-Ion Batteries Enabled by Boron-Doping TiO₂ Nanofiber Anodes. *J. Electroanal. Chem.* **2019**, 833, 573–579. <https://doi.org/10.1016/j.jelechem.2018.10.055>.
- (41) Smaran, K. S.; Joshi, P.; Vedarajan, R.; Matsumi, N. Optimisation of Potential Boundaries with Dynamic Electrochemical Impedance Spectroscopy for an Anodic Half-Cell Based on Organic-Inorganic Hybrid Electrolytes. *ChemElectroChem* **2015**, 2 (12), 1913–1916. <https://doi.org/10.1002/celec.201500372>.
- (42) Parimalam, B. S.; MacIntosh, A. D.; Kadam, R.; Lucht, B. L. Decomposition Reactions of Anode Solid Electrolyte Interphase (SEI) Components with LiPF₆. *J. Phys. Chem. C* **2017**, 121 (41), 22733–22738. <https://doi.org/10.1021/acs.jpcc.7b08433>.

Chapter 3

Effect of the PIL Binder Structure on the Performance of the Lithium-ion Batteries.

3.1 Abstract

Two structurally varying poly(ionic liquid)s were synthesized to understand the effect of the PIL structure on its performance as a binder in LiBs. This will help in the tuning of the polymer structure to optimize its performance in LiBs. The properties of ionic liquids such as ion conductivity, glass transition temperature, viscosity etc. can be tuned by a simple modification of the side-chain or changing the counter-ion. Side-chains such as allyl group increases the ionic conductivity and decreases the viscosity of the ionic liquids. Counter-ions especially FSI assists in the formation of a better electrode-electrolyte interface. In chapter 2, a PIL with an allyl side-chain and TFSI anion was studied. Therefore in this study, the design of PILs was carried such that one of the PILs PVBCAImFSI contain both the allyl side-chain and FSI anion and the other PIL PVBCBImTFSI has a butyl side-chain and TFSI anion. Cyclic voltammetry studies indicated a suppressed electrolyte degradation for PVBCAImFSI based anodes leading to the formation of a better interface. This was supported by the DEIS measurements whose results indicated lesser R_{SEI} values for the PVBCAImFSI based anodes. Also, the lithium-ion diffusion kinetics was found to be better in these electrodes. The charge-discharge measurements were carried out to evaluate the durability and stability of the electrodes. LiBs with PVBCAImFSI based graphite anodes showed enhanced durability up to 1500 cycles with a 60% capacity retention after 1500 cycles. By replacing the TFSI anion (PVBCAImTFSI) to FSI anion (PVBCAImFSI) lead to a 400% capacity retention after 1500 cycles. PVBCBImTFSI based half-cells showed lower capacity, lesser durability and bad capacity retention. The current study highlights the importance of the side-chain and the counter-ion present on the PIL vis-à-vis its performance as a binder in LiBs.

3.2 Introduction

Lithium-ion batteries (LiBs) have played a very crucial role in the technological advancements in the fields of communication and transportation since its inception. LiBs have an upper hand among the secondary batteries due to its salient features such as higher specific capacity, low self-discharge and absence of memory effect. The design flexibility has been the most attractive feature of LiBs making it a popular power source for most of the current day portable technologies.^{1,2} Sony Corporation successfully commercialized the LiB in the year 1991 after decades of scientific investigations by researchers such as Stanley Wittingham, John Goodenough, Akira Yoshino, Rachid Yazami, Doron Aurbach, Micheal Armand etc.³⁻⁷ Each of these well-known researchers researched on different components of the LiBs. The performance of the LiBs is predominantly dependent on the electrode-electrolyte interface over many other factors. The interface that forms at the electrode-electrolyte interface is referred to as Solid Electrolyte Interface (SEI). Till date, SEI is the most important but least understood in LiBs.⁸⁻¹¹ An effective SEI layer is very crucial for long life, enhanced cycling ability, stability, performance and safety of a LiB.^{12,13} Ideally, an SEI layer should resist the movement of the electrolyte through itself to the electrode effectively preventing the further reduction of the electrolyte and irreversible consumption of the lithium ions. The proper tuning of the SEI layer improves the lithium-ion conductivity through it, resulting in improved battery operation. Many theories are proposed on the formation and the structure of SEI. One of the most common and popular theory is referred to as the dual-structure model which describes SEI as a layered structure.^{8,14} The theory explains SEI to be composed of an inner inorganic layer at to the electrode-SEI interface composed of salts such as LiF, Li₂CO₃, LiO₂ etc. This layer is said to be compactly packed and has some electronic conductivity. The outer layer at the SEI-electrolyte interface is porous and organic in nature. This layer is mostly a polymeric phase composed of a RO₂Li, Li₂EDC etc. This layer is permeable to the lithium-ions as well as electrolyte molecules. Other popular theories include that proposed by Broussely et al, based on the continuum model. This model and others based on it describe the growth of the SEI as a continuous process.¹⁵ Salient features of the SEI are electrical resistance, cation selectivity, permeability, high mechanical strength, electrolyte insolubility, and stability over wide potentials and temperatures. However, achieving all these properties in a single system is highly challenging. Due to the solubility of some components of SEI in the electrolyte, the SEI layer can constantly undergo rearrangement. Thus there is a scope for the constant degradation of

the electrolyte and its components leading to the increase in the SEI thickness and cell resistance. Hence, it is very important to tune the SEI to enhance the performance of the LiB. Many strategies to artificially design the SEI were investigated, predominantly involving the use of binders, electrolyte and electrode additives. These strategies can be broadly classified into two categories viz., in-situ and ex-situ techniques. In-situ techniques involve the use of functional binders in electrodes and electrolyte additives which can selectively reduce at a given potential. This leads to the formation of the SEI with the desired composition.¹⁶ The ex-situ technique involves the modification of the electrode prior to the fabrication of the LiB. This includes electrocoating a layer of polymer or a matrix over the electrode surface.¹⁷ Design and developing functional polymers to improve the characteristics of the SEI has been one of the popular techniques. As per the definition, polymeric binders bind the active material and other electrode additives to the current collector. They play an important role in the maintaining of the electrode integrity thus preventing the capacity fade over long cycling. However by rational design of the binder structure, the characteristics of the SEI thickness, ion diffusivity, electrolyte retention etc., along with its composition can be improved.^{18,19}

In the recent past, an interesting class of polymers referred to as poly(ionic liquids) (PILs) that provides the synergistic benefit of polymers and ionic liquids are attracting immense interest in a variety of applications.²⁰⁻²³ Similar to ionic liquids, PILs exhibit low T_g , high thermal and electrochemical stabilities, better electrolyte retentions, high ion conductivity etc., along with the mechanical strength and processability of the polymers.²⁴ Though this class of polymers were initially explored in the 1970s, it gained popularity after Ohno et al. suggested the use of PILs as polyelectrolytes for energy applications.²⁵⁻²⁷ The properties of the PILs are strongly related to their structure and can be tuned by varying the heterocycle, side-chain or the counter-ion. Various properties such as hydrophobicity, solubility, T_g etc. can be modified by replacing one of the components with another. Replacing the halide anion with a TFSI anion will decrease the hydrophilicity of the PIL. Ohno et al. have demonstrated that the presence of the allyl group on the imidazolium-based ionic liquid can increase its ionic conductivity due to the increase in its amorphous nature.²⁸ As a plethora of polymeric backbones, substituent and counter-ions are available, the structural diversity that can be achieved is very high. This provides an opportunity to achieve the desired property by rationally modifying the PIL structure. Figure 3.1 illustrates various strategies that can be employed in the preparation of the PILs.

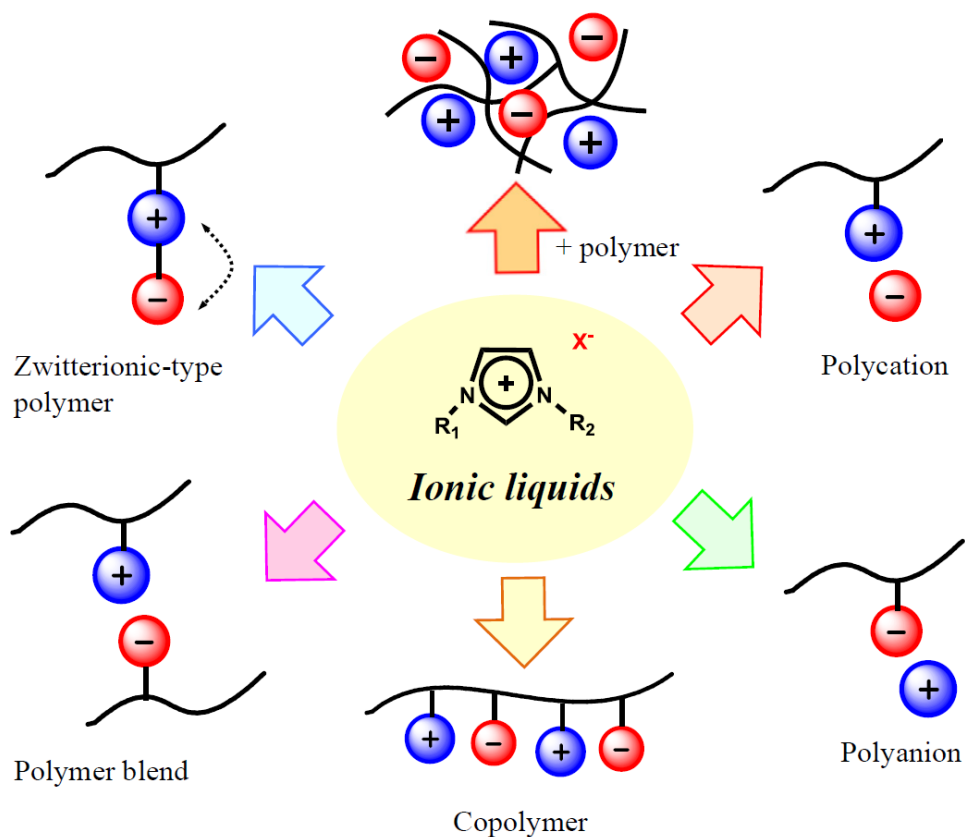


Figure 3.1 Schematic illustrating a variety of synthetic strategies to prepare PILs.
(adopted from 24)

In chapter 2, the performance of the PIL with allyl side chain and TFSI anion (PVBCAImTFSI) has been presented. In this chapter, the effect of the side-chain and the anion of the PIL on its performance as a binder for LiB has been explored. To achieve this PILs with below combinations were prepared and their performance as anodic binders for LiBs was evaluated:

- Allylimidazolium based PIL with FSI⁻ anion (PVBCAImFSI)
- Butylimidazolium based PIL with TFSI⁻ anion (PVBCBImTFSI)

3.3 Materials and Methods

3.3.1 Materials

Poly (vinylbenzyl chloride) (PVBC), 60/40 mixture of 3- and 4- isomers ($M_n \sim 55,000$, $M_w \sim 100,000$) and Poly (vinylidene fluoride) were purchased from Sigma-Aldrich. 1-Allylimidazole (AIm) was procured from TCI Co., Ltd. 1-butyylimidazole (BIm), HPLC grade dimethylformamide (DMF) and silver chloride (AgCl) were purchased from Wako Pure Chemical Industries, Ltd. Lithium bis(fluorosulfonyl)imide. N-Methylpyrrolidone (NMP) and 1-Allyl-3-methylimidazolium bis(trifluoromethanesulfonyl)imide (AMImTFSI) were purchased from Tokyo Chemical Industry Co., Ltd. Graphite super fine powder ($<50 \mu\text{m}$) obtained from Merck was used as the active material. Battery-grade acetylene black used as conductive additive was procured from Denka Japan Private Co., Ltd. Copper foil of thickness $20 \mu\text{m}$ was obtained from The Nilaco corporation. 1.0M LiPF_6 in 1:1 EC:DEC used as an electrolyte was purchased from Sigma-Aldrich. Commercial graphite anodes were procured from Piotrek Co., Ltd. All chemicals were used without any further purification.

3.3.2 Instrumentation

FT-IR spectra for the polymers were recorded on Perkin Elmer 100 FT-IR spectrometer. The spectra were recorded at a resolution of 2 cm^{-1} for 10 scans in ATR mode. FESEM images for the electrodes were obtained using Hitachi S-4500 at accelerating voltage of 1.0 kV. X-ray photoelectron spectroscopy (XPS) measurements were carried on Fisons instruments S-probe TM 2803. The coin-cells were de-crimped at OCV and the extracted electrodes were washed with dried EC:DEC to remove any adsorbed salt residues before carrying out the XPS measurements.

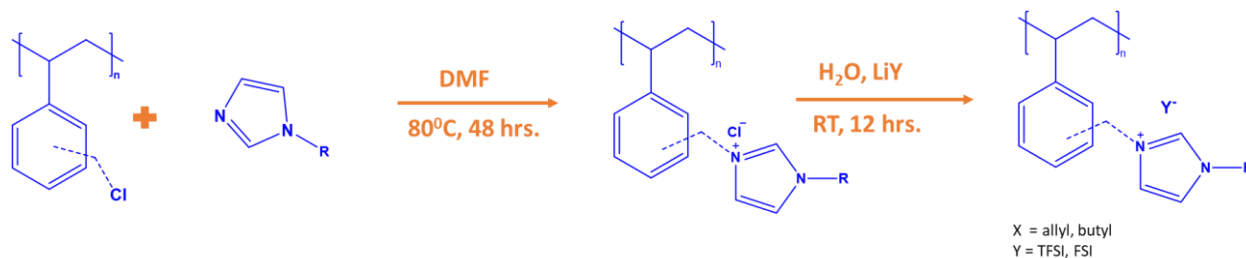
3.3.3 Synthesis

The synthesis of the PILs was carried out by the ion metathesis reaction of the poly(vinylbenzyl chloride) and imidazole precursor followed by the ion exchange reaction to replace the chloride ion with the TFSI or FSI anion. Same synthetic approach is chosen as the monomeric unit of the one of the PILs under consideration would have two polymerizable groups and one group cannot be selectively polymerized.

3.3.3.1 Poly[vinylbenzylallylimidazolium bis(fluorosulfonyl)imide] (PVBCAImFSI): The synthetic scheme is represented in Scheme 3.1. 0.5 g (3.275 mmol) of poly (vinylbenzyl chloride)

(PVBC) was solubilized in 20 mL of dimethylformamide (DMF). This solution was stirred at 80 °C followed by dropwise addition of 0.885 g (8.186 mmol) of allylimidazole (AIm) solubilized in 5 mL of DMF. The reaction mixture was refluxed for 80 °C for 48 hours.²⁹ The precipitated polymer was washed with excess DMF to remove unreacted reactants and dried under vacuum at 75 °C to obtain poly(vinylbenzylallylimidazolium chloride) (PVBCAImCl). Ion exchange reaction was carried out to obtain poly[vinylbenzylallylimidazolium bis(fluorosulfonyl)imide] (PVBCAImTFSI) by solubilizing 0.500 g (1.925 mmol) of PVBCAImCl in deionized water followed by dropwise addition of an aqueous solution of LiFSI. The mixture was stirred at room temperature overnight. The precipitated polymer was washed with deionized water.³⁰ Silver nitrate test was carried out to check the completion of ion exchange of chloride with the bis(trifluoromethane)sulfonylimide ion. The polymer obtained was dried at 75 °C under vacuum.

3.3.3.2 Poly[vinylbenzylallylimidazolium bis(fluorosulfonyl)imide] (PVBCBImTFSI): The synthetic scheme is represented in Scheme 3.1. 0.500 g (3.275 mmol) of poly (vinylbenzyl chloride) (PVBC) was solubilized in 20 mL of dimethylformamide (DMF). This solution was stirred at 80 °C followed by dropwise addition of 1.016 g (8.186 mmol) of butylimidazole (BIm) solubilized in 5 mL of DMF. The reaction mixture was refluxed for 80 °C for 48 hours.²⁹ The precipitated polymer was washed with excess DMF to remove unreacted reactants and dried under vacuum at 75 °C to obtain poly(vinylbenzylbutylimidazolium chloride) (PVBCBImCl). Ion exchange reaction was carried out to obtain poly[vinylbenzylbutylimidazolium bis(trifluoromethanesulfonyl)imide] (PVBCBImTFSI) by solubilizing 0.500 g (1.815 mmol) of PVBCAImCl in deionized water followed by dropwise addition of an aqueous solution of LiTFSI. The mixture was stirred at room temperature overnight. The precipitated polymer was washed with deionized water.³⁰ Silver nitrate test was carried out to check the completion of ion exchange of chloride with the bis(trifluoromethane)sulfonylimide ion. The polymer obtained was dried at 75 °C under vacuum.



Scheme 3.1 Synthesis scheme for preparing PVBCAImFSI and PVBCBImTFSI.

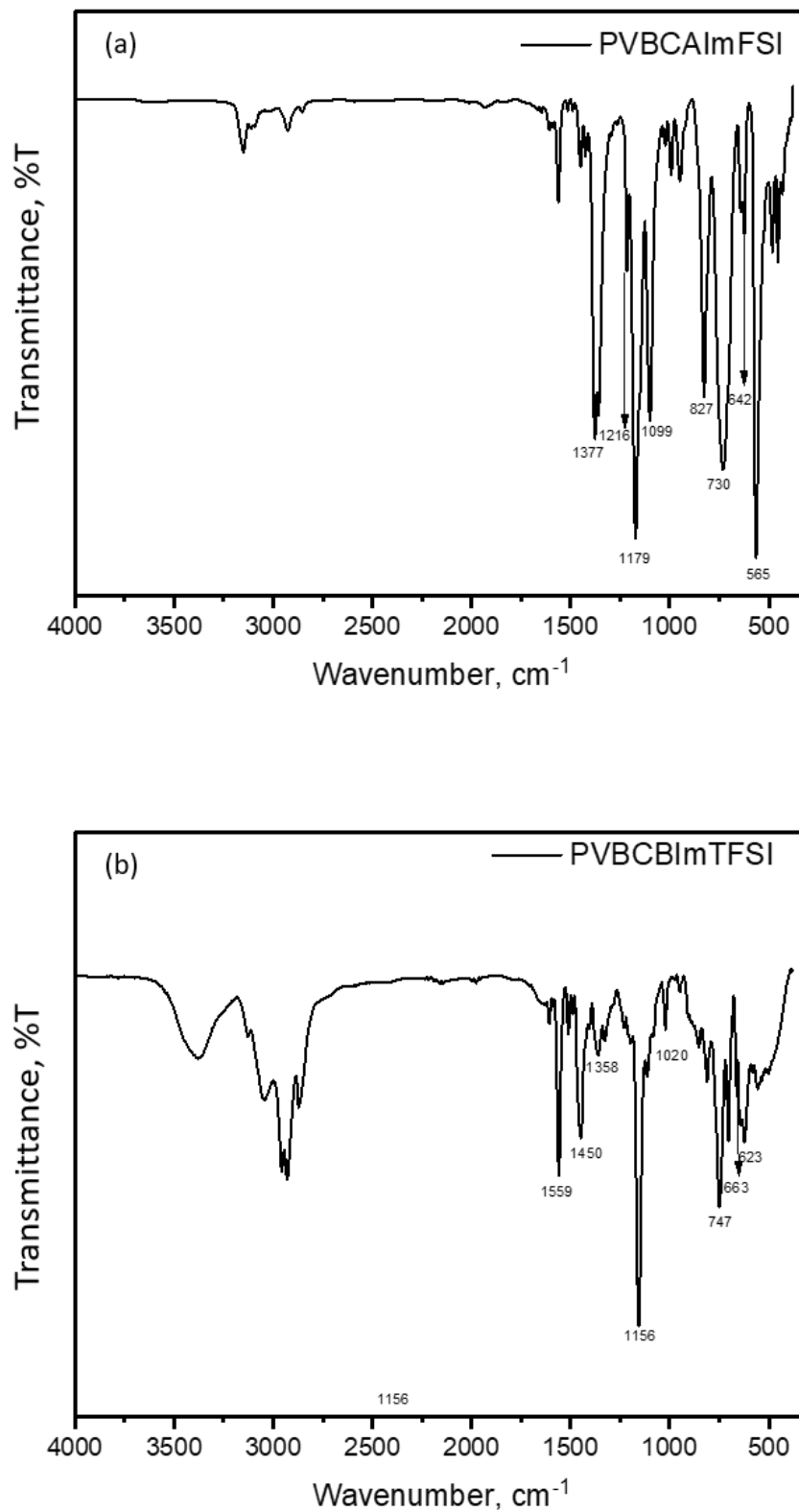


Figure 3.2 FT-IR spectra of (a) PVBCAImFSI and (b) PVBCBImTFSI.

3.3.4 Characterization

Figure 3.2 a & b gives the FT-IR spectra for poly[vinylbenzylallylimidazolium bis(fluorosulfonyl)imide] (PVBCAImFSI) and poly[vinylbenzylbutylimidazolium bis(trifluoromethanesulfonyl)imide] (PVBCBImTFSI) respectively. Peaks were observed for PVBC at 3026, 2925 and 1263 cm^{-1} corresponding to aromatic -CH, aliphatic -CH and -CH₂-Cl respectively. Peaks were observed at 3153 and 3107 cm^{-1} for the spectra corresponding to PVBCAImFSI corresponding to allylic -CH, along with 1603, 996 and 944 cm^{-1} for allylic -C=C-. The peaks corresponding to the FSI anion in PVBCAImFSI has been tabulated in Table 3.1. Similarly, the peak corresponding to the butyl chain in PVBCBImTFSI was observed at 2938 cm^{-1} and 1450 cm^{-1} corresponding to the -CH₂ bending. Peaks corresponding to the TFSI anion has been tabulated in Table 2.1. Thus FT-IR confirms the successful ion exchange for PVBCAImTFSI.

Table 3.1 FT-IR peaks corresponding to the FSI and TFSI anions in PVBCAImFSI and PVBCBImTFSI respectively.

Vibration mode	PVBCAImFSI (cm^{-1})	PVBCBImTFSI (cm^{-1})
$\delta_a\text{SO}_2$	565	623
δSNS	642	663
$\nu_s\text{SNS}$	730	747
$\nu_{as}\text{SNS}$	827	808
$\nu_s\text{SO}_2$	1099, 1216	1156
$\nu_{as}\text{SO}_2$	1377	1303
$\nu_{as}\text{CF}_3$	-	-
$\delta_a\text{CF}_3$	-	559

3.3.5 Electrode and Cell Fabrication

Electrode slurry was prepared by mixing 92 wt% of graphite, 3 wt% acetylene black and 5 wt% binder by ball-milling in NMP. Electrodes were fabricated by casting the as-prepared slurry onto copper foil using a doctor blade. Electrodes were dried overnight under vacuum at 80 °C to remove NMP. The dried electrodes were roll-pressed at 80 °C for 6 hours. The dried electrodes were punched into disks with area 1.72 cm^2 to be used for testing in coin cells. 2025-coin cells were assembled to carry out the electrochemical testing using the as-fabricated graphite electrodes as anodes, lithium foil as counter and reference electrodes with a polypropylene separator (25 μm ,

Celgard 2500) and 1.0 M LiPF₆ in 1:1 EC:DEC as the electrolyte. The anodic half cells were assembled inside an argon-filled glove box (UNICO UN-650F) whose moisture and O₂ content was <0.1ppm. The assembled cells were rested for 6 hours for stabilization before carrying out the electrochemical characterization.

3.3.6 Electrochemical Instrumentation

The Electrochemical Impedance Spectroscopy (EIS) and Dynamic Electrochemical Impedance Spectroscopy (DEIS) measurements were carried out on VSP potentiostat electrochemical workstation equipped with frequency response analyzer (FRA). The EIS measurements were carried out after stabilizing as assembled cells and after charge-discharge cycling. The measurements were carried out in the frequency range of 1 MHz to 100 mHz with a sinus amplitude of 10mV. The Cyclic Voltammetry (CV) studies was carried on a VSP potentiostat electrochemical workstation from Bio-Logic Science Instruments. The CV measurements were carried out in the potential range of 10 – 2100 mV vs Li/Li⁺ at a scan rate of 0.1 mV/s. The scan rate studies using CV was carried out at 0.1, 0.3, 0.5, 0.7 and 1.0 mV/s scan rates. The charge-discharge measurements were carried out on the Electrofield ABE 1024 battery cyclers using a CC-mode in the potential range of 10 – 2100 mV vs Li/Li⁺. Charge-discharge measurements at different rates (0.1C, 0.2C, 0.5C and 1C) were carried out to evaluate the stability of the electrodes. The DEIS measurements were carried out on the cells that were cycled for 100 cycles at 1C rate.

3.4 Results and Discussions

Structural modification of PIL will have an impact on its properties and hence its performance as the binder. The presence of the allyl group on the ionic liquid increases the amorphous nature leading to decrease in T_m , viscosity and an increase in its ionic conductivity and plasticizing nature.²⁸ These conclusions were drawn by Ohno et al. after investigating a series of allylimidazolium ionic liquids with different substituents and anions. Also, bis(fluorosulfonyl)imide (FSI) anion is considered as a “magic anion” for electrochemistry due to its properties.³¹ Ionic liquids with FSI anion exhibited low viscosity, high chemical stability and ability to form a robust SEI. These properties of the FSI anion ionic liquids assisted in the suppression of the electrolyte reduction. In addition to this, one of the advantages of FSI anion over TFSI anion is its inhibition of the electrolytic corrosion of the current collector. TFSI anion is notoriously known for accelerating the corrosion of the aluminium current collector on the cathode side.³² Some reports have proved the ability of the FSI based ILs can form exceptionally robust SEI and can also prevent the dendrite formation in lithium metal anodes and graphite-based anodes.³³ By these encouraging results, PILs with allyl side-chain and FSI anion (PVBCAImFSI) was investigated in this chapter. To support the above observations, a PIL with a butyl side-chain and TFSI anion was also prepared and investigated.

3.4.1 Electrochemical Characterization

Cyclic voltammetry was used to understand the redox properties of the graphite anodes with the above binders. Also to evaluate the lithium-ion diffusion coefficients by Randles-Sevcik equation, cyclic voltammetry based scan rate studies were performed. To further understand the properties of SEI, Electrochemical Impedance Spectroscopy measurements were carried. Figure 3.3 a & b show the voltammograms for the half-cells with PVBCAImFSI and PVBCBImTFSI based graphite anodes respectively. Both the graphite anodes show the typical lithiation-delithiation voltammograms. To understand the formation of the SEI, the first cycles of graphite anodes with both the binders have been plotted in Figure 3.4. We can observe that the extent of the electrolyte reduction is lesser in the case of the PIL with the FSI anion supporting the observations of the previous reports on FSI containing ionic liquids. Also, the lithiation and delithiation peaks were found to be broader in the case of the graphite anodes with PVBCBImTFSI binder implying slower insertion and de-insertion kinetics.

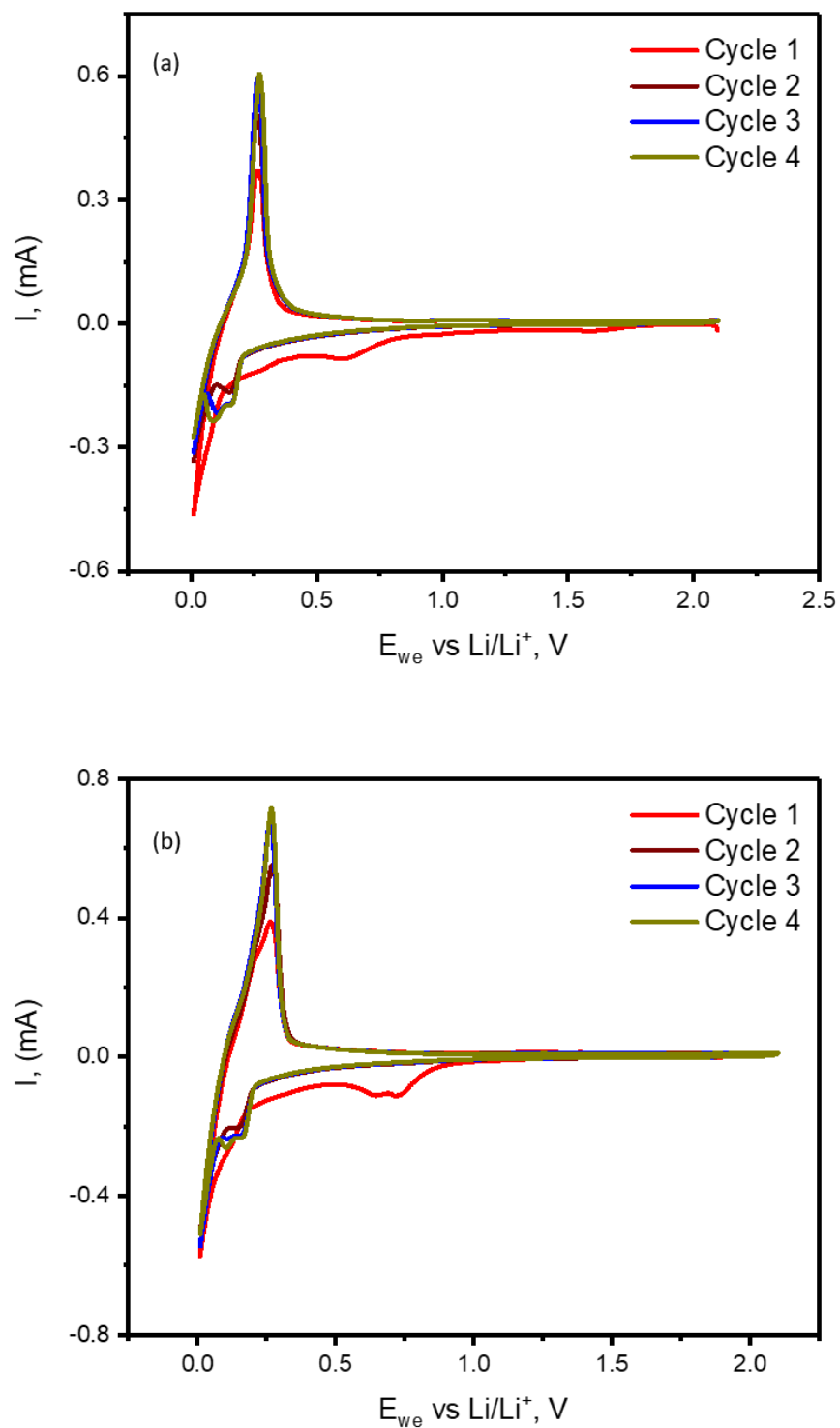


Figure 3.3 Cyclic voltammograms of a) PVBCAImFSI, b) PVBCBImTFSI as binders for graphite anode in 1.0M LiPF₆ / EC : DEC at a scan rate of 0.1 mV/S.

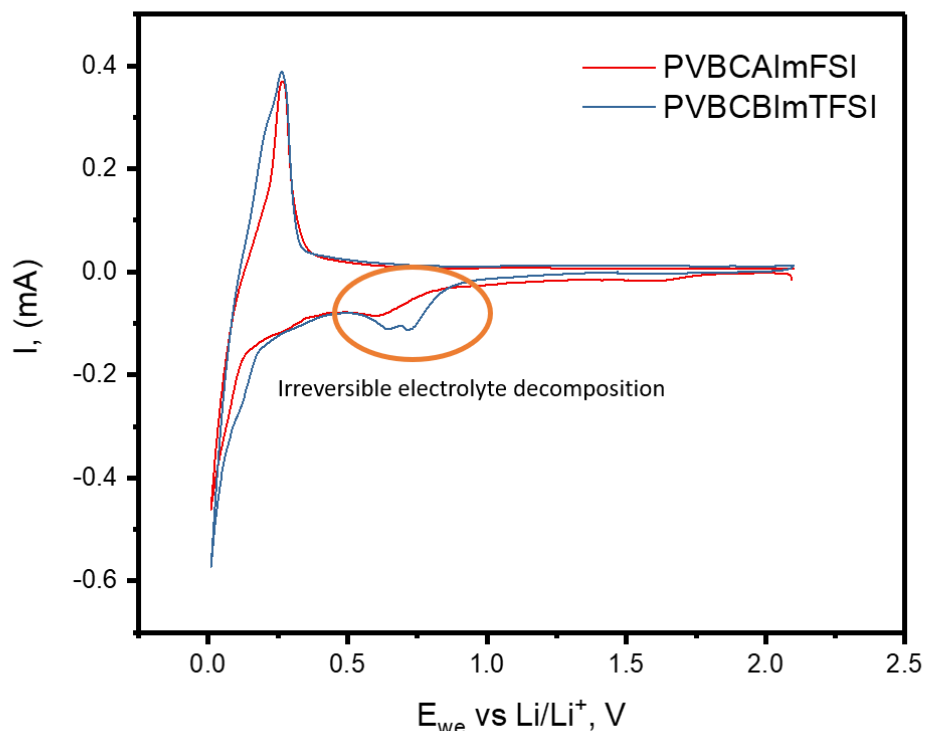


Figure 3.4 First cycle comparison of cyclic voltammograms for PVBCAImFSI (red), PVBCBImTFSI (blue) as binders for graphite anode in 1.0 M LiPF₆ / EC : DEC at a scan rate of 0.1 mV/S.

To evaluate the lithium-ion diffusion coefficient in the PVBCAImFSI and PVBCBImTFSI based anodes, cyclic voltammetry was carried out at different scan rates as shown in Figure 3.5 a & b. The peak currents I_p were plotted against the square root of the scan rates as shown in Figure 3.5 c & d. The lithium-ion diffusion coefficient was evaluated from the slope obtained from the plot and using the Randles-Sevcik equation shown below:

$$I_p = 2.69 * 10^5 n^{3/2} A D_{Li}^{1/2} C_{Li}^* v^{1/2}$$

where I_p represents peak current in amps, n represents the number of electrons involved in the process, A represents the area of the electrode in cm², D represents the Li⁺ ion diffusion coefficient in cm²/s, C represents the concentration in mol/cm³ and v represents scan rate in V/s. The lithium-ion diffusion coefficient obtained for the PVBCAImFSI and PVBCBImTFSI based anodes was 6.250*10⁻⁹ cm²/s and 4.844*10⁻⁹ cm²/s respectively. The lithium-ion diffusion coefficient (D_{Li^+}) for PVBCAImFSI based anodes is 21% higher compared to conventionally used PVDF binder based anodes. However, PVBCBImTFSI based anodes exhibit 6.2% lower diffusion coefficient

compared to PVDF based anodes. This is in line with the slower kinetics as expected from the cyclic voltammetry measurements.

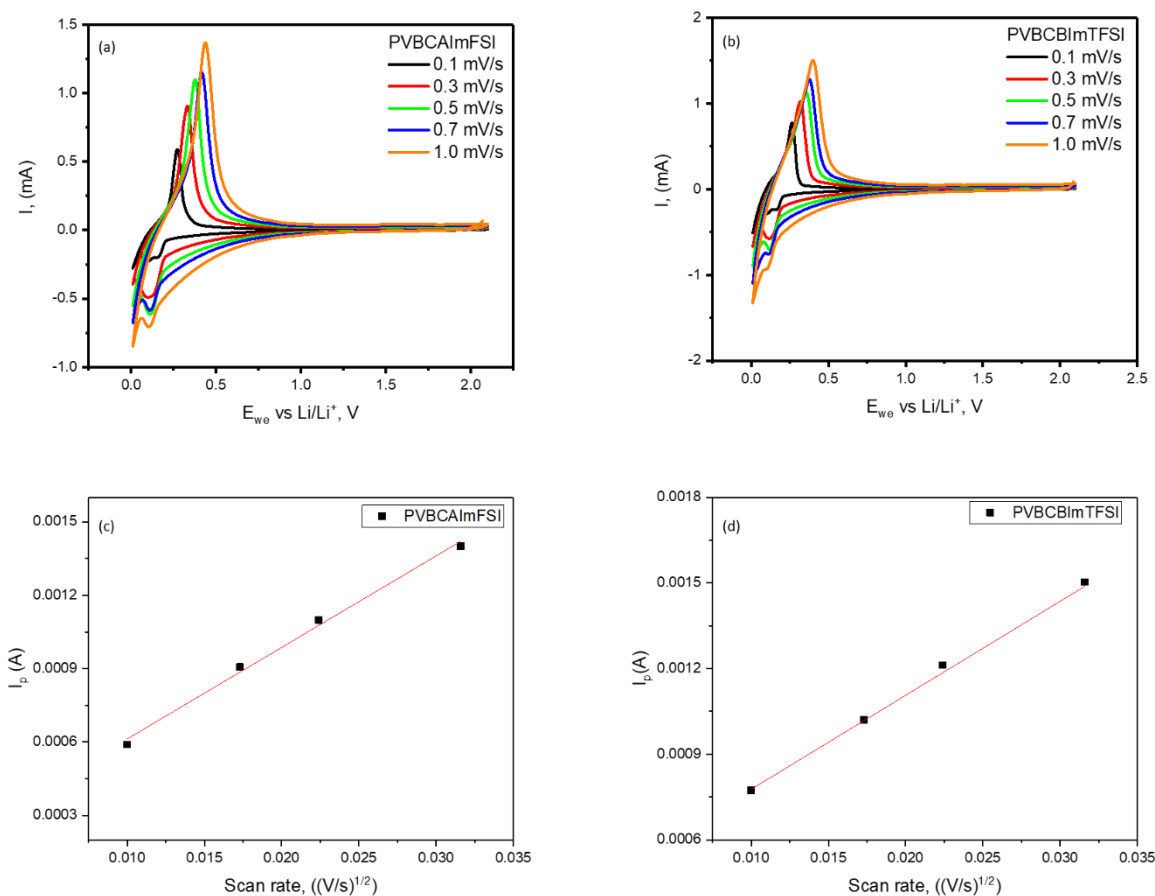


Figure 3.5 Cyclic voltammograms at different scan rates with a) PVBCAImFSI, b) PVBCBImTFSI as binders for graphite anode in 1.0M $LiPF_6$ / EC : DEC. Plots of peak current vs square root of scan rates for c) PVBCAImFSI, d) PVBCBImTFSI obtained from the CV.

Electrochemical impedance spectroscopy measurements were carried out after fabrication and after cyclic voltammetry studies. Figure 3.6 a & b show the Nyquist plots for PVBCAImFSI and PVBCBImTFSI based anodes at OCP. The interfacial resistances in both the anodes were reduced after cycling indicating a better interface. Figure 3.7 shows the Nyquist plots for PVBCAImFSI (red) and PVBCBImTFSI (blue) after cycling. Equivalent electric circuit models were used to obtain the resistances corresponding to different processes and are shown in Table 3.2. The charge-transfer resistance is lesser in the case of the PVBCAImFSI based anodes indicating a facile charge transfer leading to better intercalation and de-intercalation properties.

The robust and more conductive SEI formed due to the presence of the FSI anion in the PVBCAImFSI led to the decrease in the interfacial resistance.

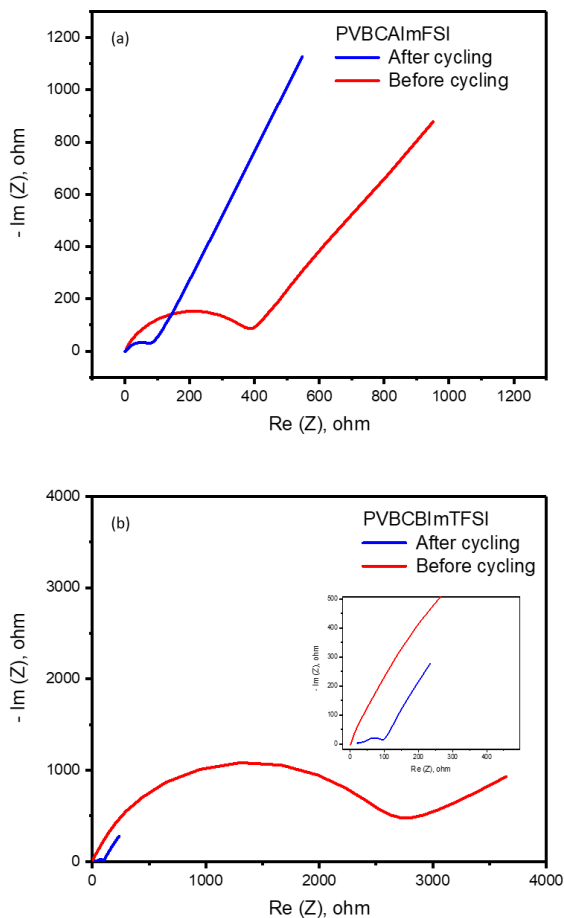


Figure 3.6 Electrochemical impedance spectroscopy measurements for graphite anode in 1.0M LiPF₆ / EC : DEC with a) PVBCAImFSI, b) PVBCBImTFSI as binders.

Table 3.2 EECM fittings for graphite anode in 1.0M LiPF₆ / EC : DEC with a) PVBCAImFSI, b) PVBCBImTFSI as binders after cycling.

Binder	R1	R2	R3	χ^2	Circuit
PVBCAImFSI	1.668	100.8	307.9	0.004318	R(QR)(Q(RW))
PVBCBImTFSI	15.98	139.4	420.3	0.004784	R(QR)(Q(RW))

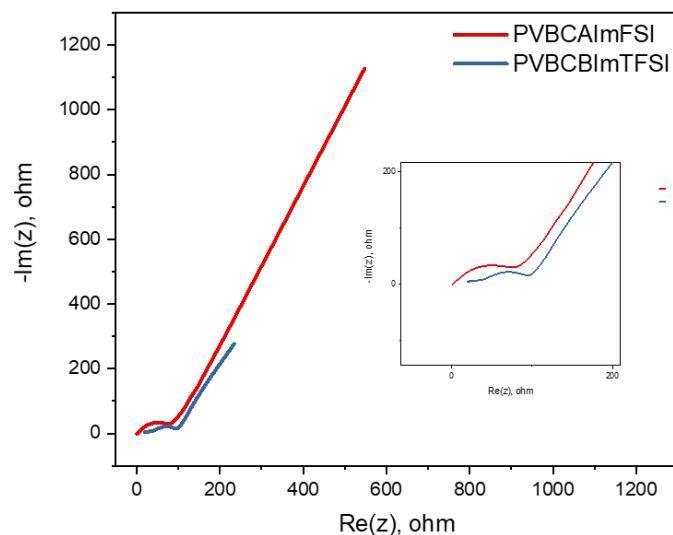
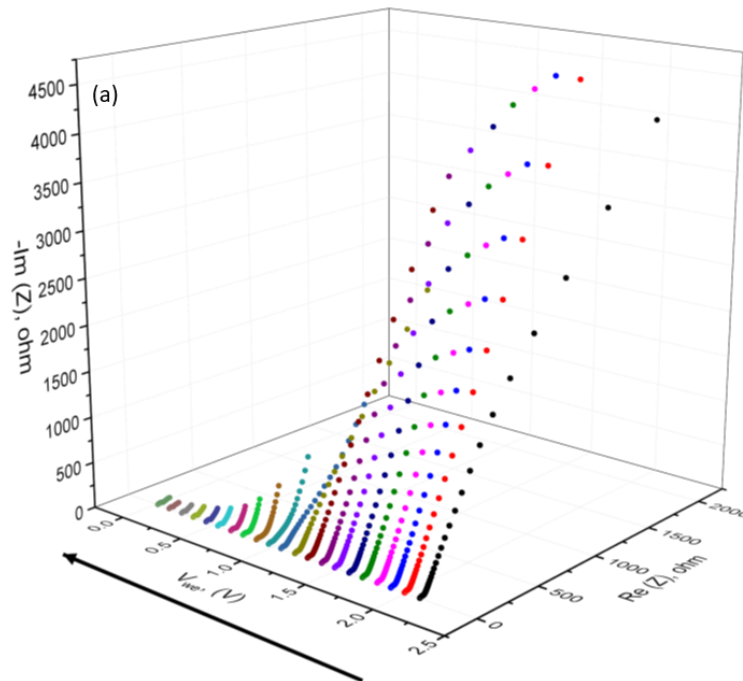


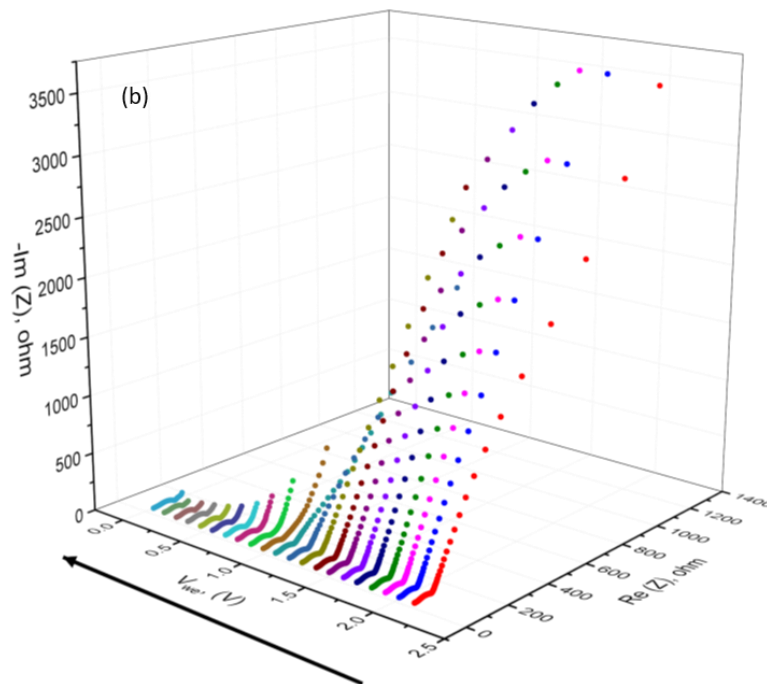
Figure 3.7 Nyquist plots of anodic half-cells with PVBCAImFSI (Red) and PVBCBImTFSI (Blue) after cycling (Inset: High frequency range corresponding to the interfacial processes).

As discussed in chapter 2, Dynamic Electrochemical Impedance Spectroscopy (DEIS) is a very versatile technique to understand the nature of the interfaces electrochemically.^{17,19,34} It is a very unique technique which allows for the understanding of the evolution of the interfaces. DEIS measurements were carried out for anodic half-cells after 100 cycles of charge-discharge cycling at 1C rate. The DEIS profiles corresponding to the charging cycle of PVBCAImFSI and PVBCBImTFSI are given in Figure 3.8 a & b respectively. Figure 3.9 a & b shows the discharge cycle corresponding to PVBCAImFSI and PVBCBImTFSI respectively. Figure 3.10 a & b shows the R_{SEI} values corresponding to the PVBCAImFSI and PVBCBImTFSI based graphite anodes for charging and discharging cycles. The impedance values obtained after fitting the data to electrical equivalent circuit models have been given in Table 3.3 – 3.6. The R_{SEI} values for PVBCAImFSI based graphite anodes were lower at all the potentials compared to the PVBCBImTFSI. This is due to the synergistic effect of the allyl group as observed in chapter 2 and FSI anion.^{19,31} Presence of FSI anion also suppresses the formation of gaseous products that might damage the SEI during cycling. Hence, the SEI formed will have more mechanical strength and hence the durability of the LiB can be expected to be high. Smaller R_{SEI} and R_{CT} resistances imply better ion transport and storage. Hence, PVBCAImFSI based anodes exhibited higher lithium-ion diffusion coefficients. To understand the durability of LiBs charge-discharge cycling was carried out for a

few hundred cycles at 1C rate. Also, to understand the stability of LiBs charge-discharge cycling was carried out at different rates.



PVBCAlmFSI charging after 100 cycles



PVBCBlmTFSI charging after 100 cycles

Figure 3.8 DEIS profiles for the charging cycle for a) PVBCAlmFSI, b) PVBCBlmTFSI as binders for graphite anode after 100 cycles at 1C.

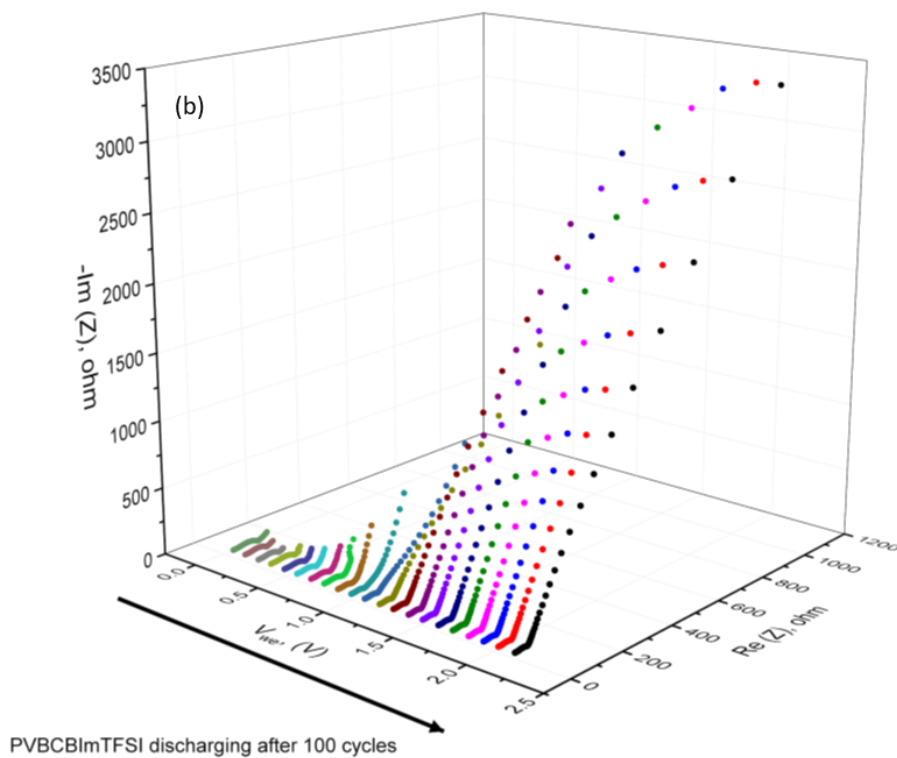
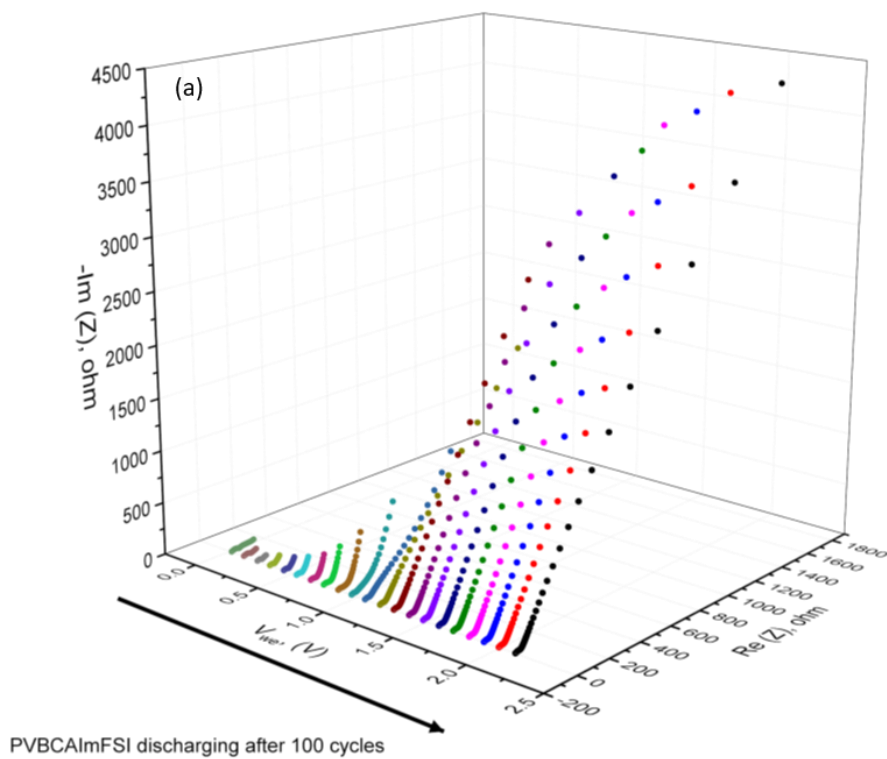


Figure 3.9 DEIS profiles for the discharging cycle for a) PVBCAImFSI, b) PVBCBImTFSI as binders for graphite anode after 100 cycles at 1C.

Table 3.3 Circuit fitting data for PVBCAImFSI based graphite anodes during the charging cycle.

V	R1	R2	R3	R4	R5	W	Chi2	Circuit
1.99	1.677	2.813	16.52	7.88E+01	8.77E+04	1.59E+04	1.45E-05	LR(QR)(QR)(QR)(Q(RW))
1.89	1.777	2.709	15.62	5.43E+01	9.53E+04	6.74E-03	1.26E-05	LR(QR)(QR)(QR)(Q(RW))
1.79	2.312	4.031	21.65	1.63E+03	2.59E+05	1.57E-04	6.38E-05	R(QR)(QR)(QR)(Q(RW))
1.68	1.687	2.949	17.9	1.26E+02	1.24E+05	2.19E+04	1.77E+05	LR(QR)(QR)(QR)(Q(RW))
1.58	1.63	2.956	18.39	9.62E+02	1.01E+05	2.44E+04	1.52E-05	LR(QR)(QR)(QR)(Q(RW))
1.47	1.725	3.262	18.9	1.72E+01	1.08E-08	1.72E+01	1.64E-05	LR(QR)(QR)(QR)(Q(RW))
1.37	1.826	3.733	19.78	7.34E+04	6.08E+08	2.46E+05	1.84E-05	LR(QR)(QR)(QR)(Q(RW))
1.26	1.643	3.109	19.12	5.34E+04	4.37E+06	4.39E+04	1.55E-05	LR(QR)(QR)(QR)(Q(RW))
1.16	1.712	3.259	18.94	2.12E+03	8.34E+03	6.28E-04	1.41E-05	LR(QR)(QR)(QR)(Q(RW))
1.05	2.339	4.505	26.81	8.70E+02	9.43E+03	1.37E-03	7.40E-05	R(QR)(QR)(QR)(C(RW))
0.95	1.938	5.485	21.67	2.31E+02	2.47E+04	4.67E+02	1.50E-05	LR(QR)(QR)(QR)(Q(RW))
0.85	1.307	1.337	13.82	2.01E+02	2.87E-01	1.50E-03	3.74E-05	LR(QR)(QR)(QR)(C(RW))
0.74	1.771	2.184	16.18	5.35E+01	2.01E+07	7.88E-14	8.08E-05	LR(QR)(QR)(QR)(Q(RW))
0.64	2.349	3.194	9.032	2.98E+01	2.43E+11	4.35E-02	7.14E-05	R(QR)(QR)(QR)(Q(RW))
0.53	2.16	4.422	31.95	3.80E+02	1.57E-02	5.80E-10	1.04E-04	LR(QR)(QR)(QR)(C(RW))
0.43	2.099	4.807	30.46	1.43E+03	3.03E+02	2.49E-07	5.35E-05	LR(QR)(QR)(QR)(Q(RW))
0.32	2.04	5.121	18.79	9.30E+01	1.32E+02	4.42E-03	3.19E-05	LR(QR)(QR)(QR)(Q(RW))

Table 3.4 Circuit fitting data for PVBCBImTFSI based graphite anodes during the charging cycle.

V	R1	R2	R3	R4	R5	W	Chi2	Circuit
1.99	1.3	4.43	39.16	7.95E+01	4.89E+04	5.70E-04	8.34E-05	LR(QR)(QR)(QR)(Q(RW))
1.89	6.872	17.51	42.82	5.13E+01	7.69E+04	3.07E+00	1.07E-06	LR(QR)(QR)(QR)(Q(RW))
1.79	2.643	3.456	40.15	7.76E+01	7.75E+04	3.83E-04	7.19E-06	LR(QR)(QR)(QR)(Q(RW))
1.68	1.761	6.11	35.87	8.15E+01	8.74E+04	1.64E+08	7.89E-06	LR(QR)(QR)(QR)(Q(RW))
1.58	5.837	44.94	65.25	8.08E+02	3.65E+04	4.20E+10	1.04E-05	R(QR)(QR)(QR)(Q(RW))
1.47	2.821	47.23	70.11	6.12E+01	7.14E+04	2.42E+02	1.41E-05	LR(QR)(QR)(QR)(Q(RW))
1.37	5.08	47.08	70.26	2.48E+04	3.17E+04	7.83E+00	1.02E-05	LR(QR)(QR)(QR)(Q(RW))
1.26	4.673	47.1	72.67	9.33E+02	1.67E+04	4.03E-04	1.03E-05	R(QR)(QR)(QR)(Q(RW))
1.16	4.759	47.81	71.43	1.45E+01	9.37E+05	2.35E-03	7.98E-06	R(QR)(QR)(QR)(C(RW))
1.05	7.443	49.86	62.76	2.46E+02	6.79E+07	1.06E-05	9.34E-06	R(QR)(QR)(QR)(Q(RW))
0.95	5.43	47.39	69.97	1.42E+02	2.74E+04	7.19E+03	7.80E-06	R(QR)(QR)(QR)(Q(RW))
0.85	6.671	47.81	61.6	1.34E+02	2.58E+03	1.71E-03	7.17E-06	R(QR)(QR)(QR)(C(RW))
0.74	0.03465	1.787	39.79	1.33E+02	5.39E+05	3.00E-13	6.09E-05	LR(QR)(QR)(QR)(Q(RW))
0.64	1.388	37.19	50.15	8.03E+01	6.37E+02	4.05E-03	3.96E-06	R(QR)(QR)(QR)(Q(RW))
0.53	4.577	52.46	66.53	7.21E+00	1.06E+03	1.02E-01	1.87E-05	R(QR)(QR)(QR)(Q(RW))
0.43	7.987	18.49	59.67	5.29E+01	2.27E+02	3.16E-16	5.39E-06	R(QR)(QR)(QR)(Q(RW))
0.32	4.712	49.52	61.56	3.50E+00	5.58E+03	7.28E-10	5.15E-05	R(QR)(QR)(QR)(Q(RW))

Table 3.5 Circuit fitting data for PVBCAImFSI based graphite anodes during the discharging cycle.

V	R1	R2	R3	R4	R5	W	Chi2	Circuit
1.99	2.054	4.178	10.94	1.83E+01	2.75E+04	1.31E-02	1.08E-04	LR(QR)(QR)(QR)(Q(RW))
1.89	2.02	4.941	20.18	4.05E+02	1.02E+03	3.74E-04	8.92E-05	LR(QR)(QR)(QR)(C(RW))
1.79	2.09	4.69	23.04	1.96E+03	1.96E+04	3.35E+02	9.53E-05	LR(QR)(QR)(QR)(C(RW))
1.68	1.949	5.697	22.09	5.70E+00	3.39E+04	1.59E-02	4.02E-05	LR(QR)(QR)(QR)(C(RW))
1.58	2.383	3.904	23.26	1.74E+03	1.82E+04	2.20E+04	9.59E-05	R(QR)(QR)(QR)(C(RW))
1.47	2.069	3.148	14.03	1.08E+01	3.43E+04	1.59E-02	3.87E-05	LR(QR)(QR)(QR)(C(RW))
1.37	2.018	4.788	19.67	4.97E+02	9.12E+02	4.31E-05	7.11E-05	LR(QR)(QR)(QR)(C(RW))
1.26	2.002	4.786	19.45	4.49E+02	5.78E+02	5.28E-04	6.00E-05	LR(QR)(QR)(QR)(C(RW))
1.16	1.938	5.349	20.43	5.90E-02	2.10E+04	8.67E+04	2.83E-05	LR(QR)(QR)(QR)(Q(RW))
1.05	2.049	4.64	21.03	6.41E+02	9.60E+03	6.03E+05	3.68E-05	LR(QR)(QR)(QR)(C(RW))
0.95	1.92	5.054	16.96	2.44E+01	2.02E+02	9.36E-04	1.20E-05	LR(QR)(QR)(QR)(Q(RW))
0.85	1.71	2.087	13.06	1.71E+00	1.09E+02	1.42E-03	7.98E-05	R(QR)(QR)(QR)(C(RW))
0.74	2.157	2.496	14.32	4.08E+01	5.24E-02	3.75E-12	8.95E-05	R(QR)(QR)(QR)(Q(RW))
0.64	1.575	2.192	18.02	3.92E+01	4.94E+01	5.03E-12	1.02E-04	LR(QR)(QR)(QR)(Q(RW))
0.53	2.361	3.022	23.92	2.01E+02	1.73E+08	2.50E-03	9.67E-05	R(QR)(QR)(QR)(C(RW))
0.43	2.366	3.181	23.32	5.58E+01	1.61E+02	2.40E-03	6.74E-05	R(QR)(QR)(QR)(C(RW))
0.32	2.357	3.282	22.05	6.81E+01	6.05E+02	1.46E+06	5.18E-05	R(QR)(QR)(QR)(C(RW))

Table 3.6 Circuit fitting data for PVBCBImTFSI based graphite anodes during the discharging cycle.

V	R1	R2	R3	R4	R5	W	Chi2	Circuit
1.99	6.042	23.73	45.47	6.86E+02	1.68E+04	2.31E+06	1.38E-05	R(QR)(QR)(QR)(Q(RW))
1.89	2.302	22.11	54.48	3.40E+04	1.41E+00	3.28E+04	1.81E-05	R(QR)(QR)(QR)(C(RW))
1.79	4.585	22.67	46.65	2.60E+00	3.66E+04	1.49E+01	1.38E-05	LR(QR)(QR)(QR)(Q(RW))
1.68	4.387	23.07	48.46	7.12E+03	2.75E+04	2.75E+04	1.20E-05	LR(QR)(QR)(QR)(Q(RW))
1.58	5.151	23.52	46.14	2.12E+04	4.22E+15	1.91E+08	2.55E-05	LR(QR)(QR)(QR)(Q(RW))
1.47	6.538	23.11	42.16	8.15E+02	1.92E+04	5.40E+00	1.10E-05	LR(QR)(QR)(QR)(Q(RW))
1.37	2.08	21.2	51.53	1.63E+04	1.82E+04	1.58E+03	1.72E-05	R(QR)(QR)(QR)(Q(RW))
1.26	6.01	24	43.81	1.04E+03	1.53E+04	2.88E-01	1.08E-05	R(QR)(QR)(QR)(Q(RW))
1.16	2.228	21.71	50.72	5.90E+01	9.01E+03	5.87E-04	1.08E-05	R(QR)(QR)(QR)(Q(RW))
1.05	4.937	23.86	45.91	1.62E+02	5.79E+04	6.49E+00	7.18E-06	R(QR)(QR)(QR)(Q(RW))
0.95	2.768	21.81	51.3	7.42E+01	1.57E+15	1.13E-01	7.68E-06	R(QR)(QR)(QR)(Q(RW))
0.85	2.254	20.74	50.7	9.49E+01	1.77E+00	1.26E-03	1.05E-05	LR(QR)(QR)(QR)(C(RW))
0.74	0.021	29.91	47.7	7.16E+01	3.50E+10	5.63E-05	8.57E-05	LR(QR)(QR)(QR)(Q(RW))
0.64	4.071	44.74	52.82	2.98E-02		1.06E-02	7.45E-04	R(QR)(QR)(C(RW))
0.53	8.511	25.16	35.68	5.39E+01	4.62E+05	7.65E-09	4.57E-06	R(QR)(QR)(QR)(Q(RW))
0.43	11.28	31.32	40.9	5.22E+01	6.91E+06	9.40E-18	1.54E-05	R(QR)(QR)(QR)(Q(RW))
0.32	11.52	20.08	43.1	6.50E+01	7.42E+16	1.08E-04	1.42E-04	R(QR)(QR)(QR)(Q(RW))

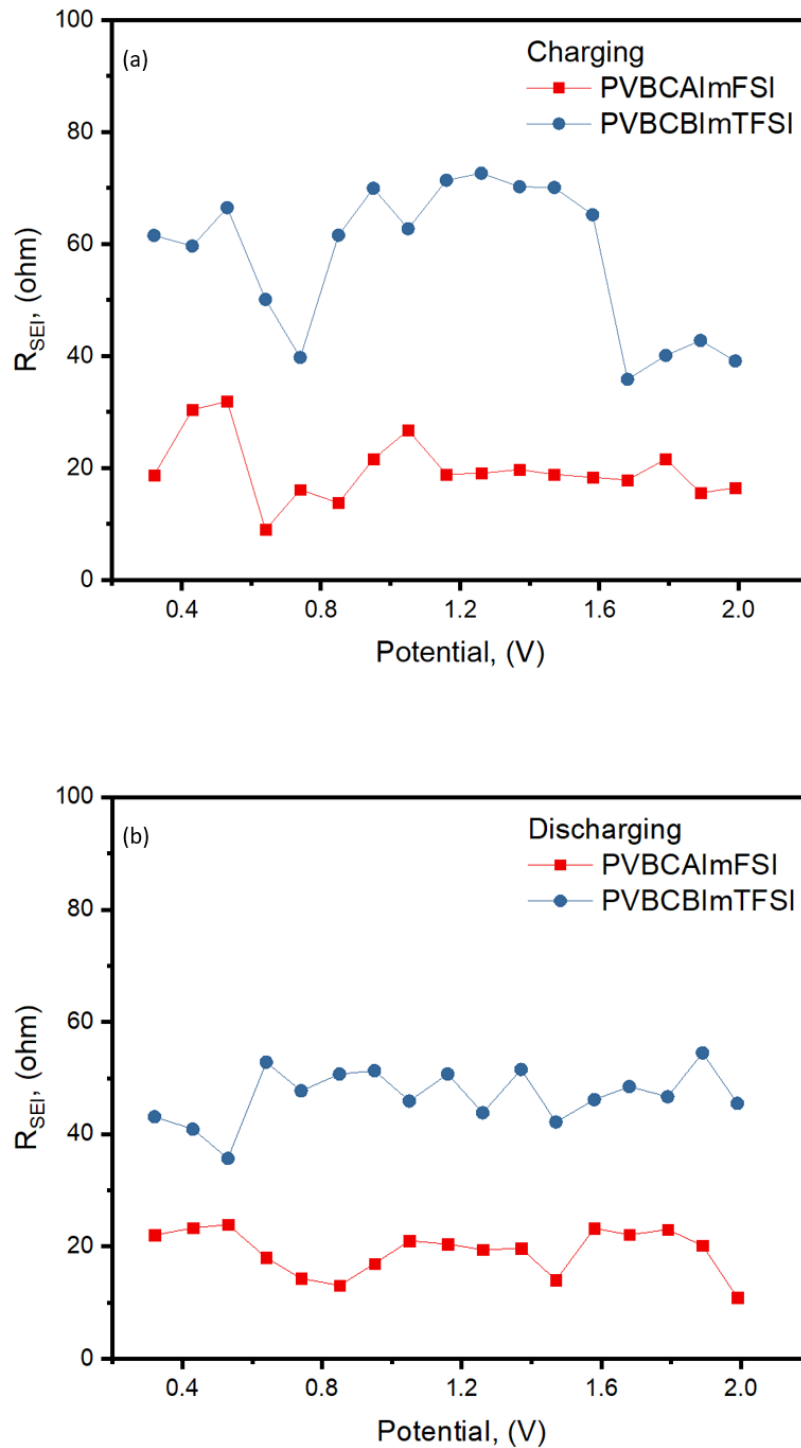


Figure 3.10 R_{SEI} profiles during the (a) Charging cycle for PVBCAImFSI and PVBCBImTFSI as binders for graphite anode, (b) Discharging cycle for PVBCAImFSI and PVBCBImTFSI as binders for graphite anode.

With the above understanding of the redox and SEI properties of the graphite anodes, charge-discharge studies were carried out. Figure 3.11 shows the long cycling charge-discharge studies for the graphite anodes with PVBCAImFSI and PVBCBImTFSI binders. To understand the effect of the anion on cyclability, half-cells with PVBCAImTFSI based anodes were also prepared under the same conditions. PVBCAImFSI based half-cells exhibited better cycling and

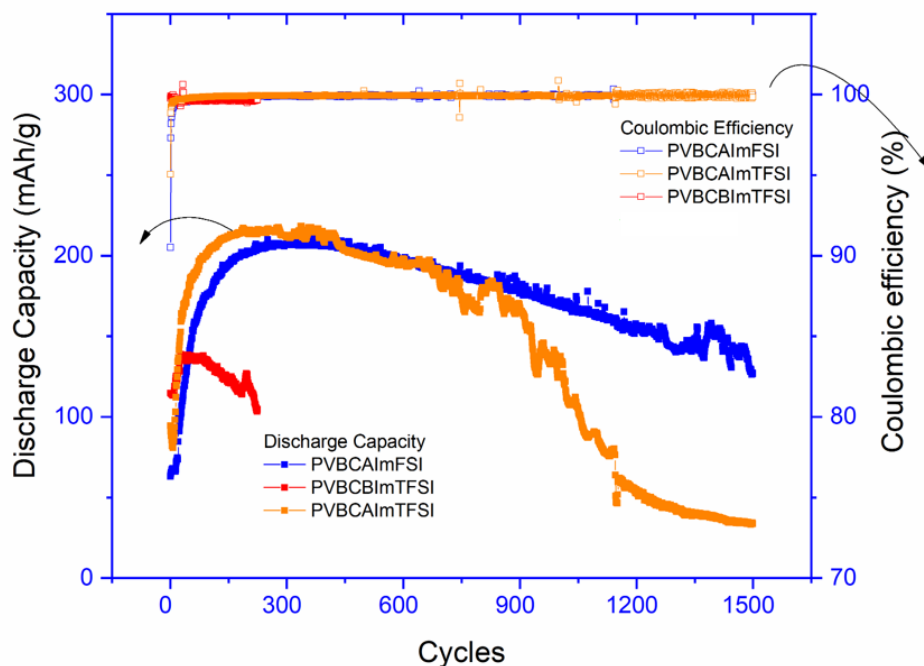


Figure 3.11 Long cycling performance of graphite anodes with PVBCAImFSI (Blue), PVBCAImTFSI (Orange) and PVBCBImTFSI (Red) as binders with 1.0M LiPF₆ / EC : DEC electrolyte at 1C rate.

capacity retention as compared to the others. Half-cells with PVBCAImFSI based anodes exhibited a maximum reversible capacity of 211.2 mAh/g as compared to 218.2 mAh/g and 206.4 mAh/g for PVBCAImTFSI and PVBCBImTFSI based anodic half cells at 1C rate respectively. Due to the superior electrochemical properties of PVBCAImFSI based anodes, they exhibited better cyclability and higher capacity. Capacity retentions of 95.6%, 80.3% and 59.9% were observed for PVBCAImFSI based anodic half cells after 500, 1000 and 1500 cycles respectively at 1C rate. From Figure 3.11, we can observe that though the discharge capacity of PVBCAImTFSI based half-cells stabilizes faster, the capacity retention becomes bad after 500 cycles. Overall, after 1500 cycles, PVBCAImFSI based anodic half cells exhibited 400% greater capacity than

PVBCAImTFSI based anodic half cells. PVBCBImTFSI based anodic half cells exhibited a maximum reversible capacity of 136.9 mAh/g which is very low compared to PVBCAImTFSI and PVBCAImFSI based anodic half cells. The observed lower capacity can be attributed to not so robust SEI and slow ion diffusion kinetics. After 200 cycles at 1C rate, a capacity of 122.86 mAh/g was observed. It is very apparent by the long cycling studies that the side-chain and the counter-ion on the PIL play a very crucial role in the performance of the LiBs. To understand the stability of the electrodes, the anodic half-cells were cycled at different rates. The reversible discharge capacities obtained at different rates is shown in Figure 3.12 a & b for PVBCAImFSI and PVBCBImTFSI based anodic half-cells. The capacities obtained at each rate has been tabulated in Table 3.7.

Table 3.7 Discharge capacities at different rates for graphite anodes with PVBCAImFSI and PVBCBImTFSI as binders with 1.0M LiPF₆ / EC : DEC electrolyte.

Rate	Discharge Capacity (mAh/g)	
	PVBCAImFSI	PVBCBImTFSI
0.067C	288.1	230.8
0.1C	268.6	229.3
0.2C	230.2	185.4
0.5C	146.8	83.5
1.0C	122.9	37.5
0.1C (after rate studies)	283.7	-

PVBCAImFSI based anodic half cells exhibited about 268.6 mAh/g of reversible discharge capacity at 0.1C rate which increased to 283.7 mAh/g at the same rate after the rate studies indicating very high stability. The robust SEI formed during the cycling results in the enhancement of the capacity. Whereas the PVBCBImTFSI based anodes show a drastic decrease in the capacity as the rate is increased due to the slow ion diffusion kinetics. The capacity reported at 1C rate after 20 cycles of initial stabilization is about 122.9 mAh/g for PVBCAImFSI based anodes which is almost 4 times higher than the PVBCBImTFSI based anodes. To draw a comparison to the performance of commercially available electrodes with the same electrolyte system, anodic half cells were fabricated with graphite anodes from Piotrek Co., Ltd. The results are plotted in Figure 3.13. At 0.1C rate, a reversible discharge capacity around 224 mAh/g was observed and there was a drastic decrease in the capacity as the rate increased. At 1C rate, a discharge capacity of about 20 mAh/g was observed indicating the need for other electrolyte additives to improve the SEI

characteristics and hence improve the performance. The better interfacial properties and the higher lithium-ion diffusion coefficient of the PVBCAImFSI based anodes even in the absence of any such additives led to better durability as well as better stability. The charge-discharge studies strongly indicated the importance of the PIL structure on its performance as a binder in the LiBs. Therefore, it becomes very crucial in the structural tuning of the binder structure to achieve higher capacities as well as better durabilities.

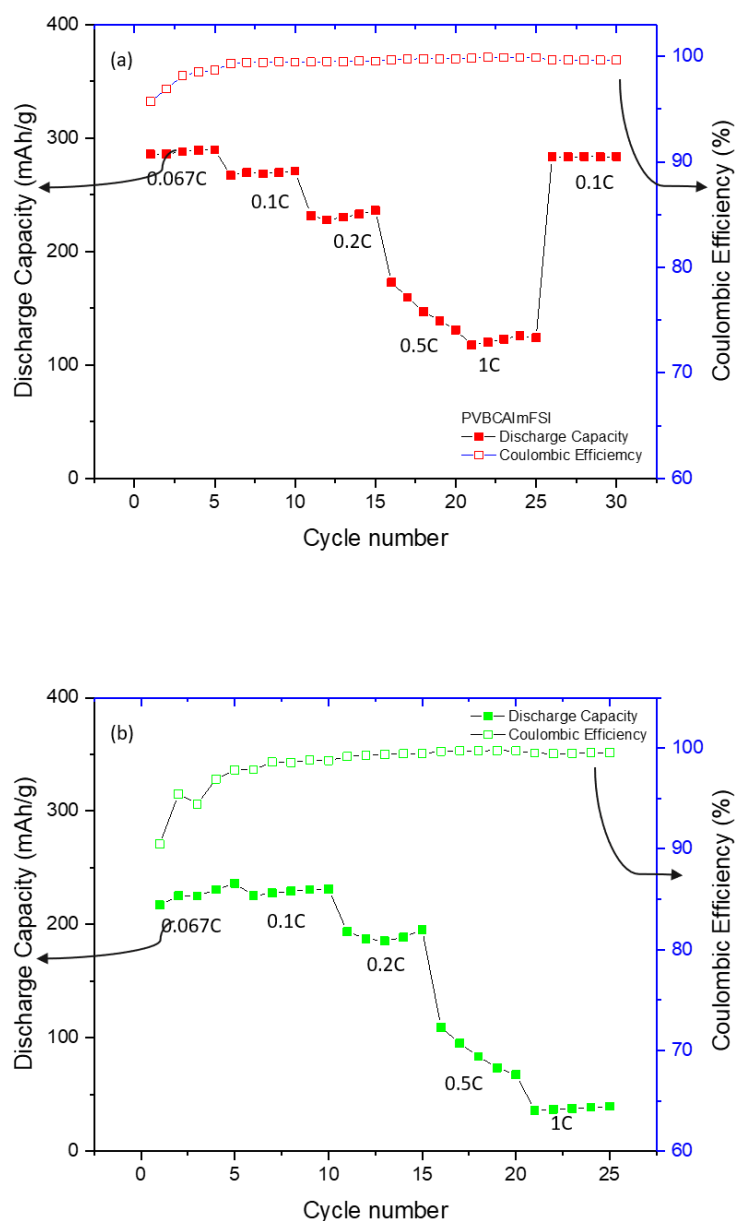


Figure 3.12 Rate performance of graphite anodes with (a) PVBCAImFSI and (b) PVBCBImTFSI as binders with 1.0M LiPF₆ / EC : DEC electrolyte.

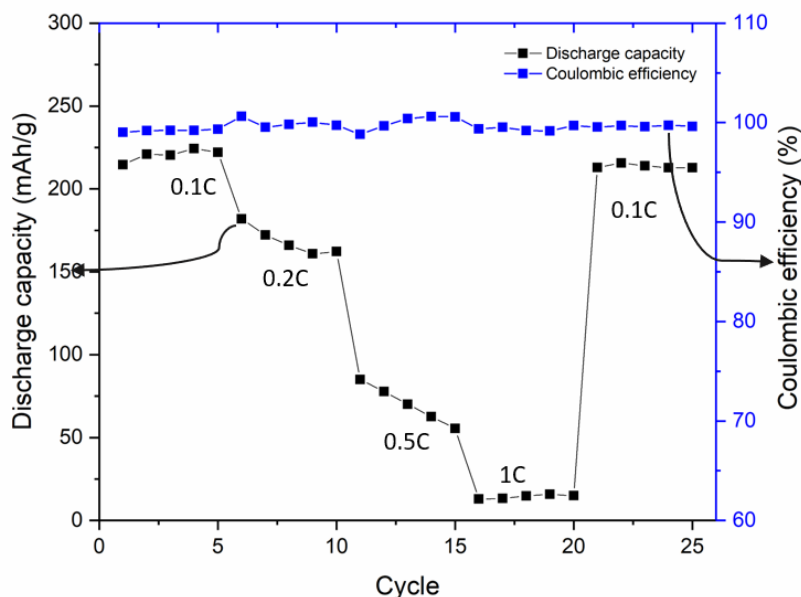


Figure 3.13 Rate performance of commercial graphite anodes with 1.0M LiPF₆ / EC : DEC electrolyte.

3.4.2 Morphology and Composition Analysis

Physical characterization of the electrodes will provide the physical evidence for the results observed electrochemically. Techniques such as FESEM and XPS are very useful in understanding the morphology and the surface composition of the electrodes. The PVBCAImFSI based anodes were cycled for 1500 cycles and PVBCBImTFSI anodes were cycled for 250 cycles at 1C rate before decrimping and characterizing them. Same protocol as chapter 2 was followed in processing the electrodes for characterization. FESEM images for PVBCAImFSI and PVBCBImTFSI based anodes after charge-discharge studies at 1C is given in Figure 3.14. We can observe that the morphology of the PVBCAImFSI is granular as seen in Figure 3.14 a & b and no extensive damage has been observed at higher magnification. The robust SEI formed can sustain the intercalation-deintercalation of the lithium-ions over long cycling without getting damaged. Moreover, lesser SEI damage implies lesser electrolyte degradation which supports the lesser interfacial resistance observed electrochemically by the DEIS studies. The PVBCBImTFSI based electrodes don't show any granular network as seen in Figure 3.14 c & d indicating extensive electrolyte degradation. Also at higher magnification, extensive damage to the electrode is observed indicating a fragile SEI formation which gets easily damaged during the charge-discharge cycling. This leads to

continuous degradation of the electrolyte increasing the cell resistance as observed electrochemically by DEIS studies. This observation explains the bad charge-discharge performance of PVBCBImTFSI based electrodes.

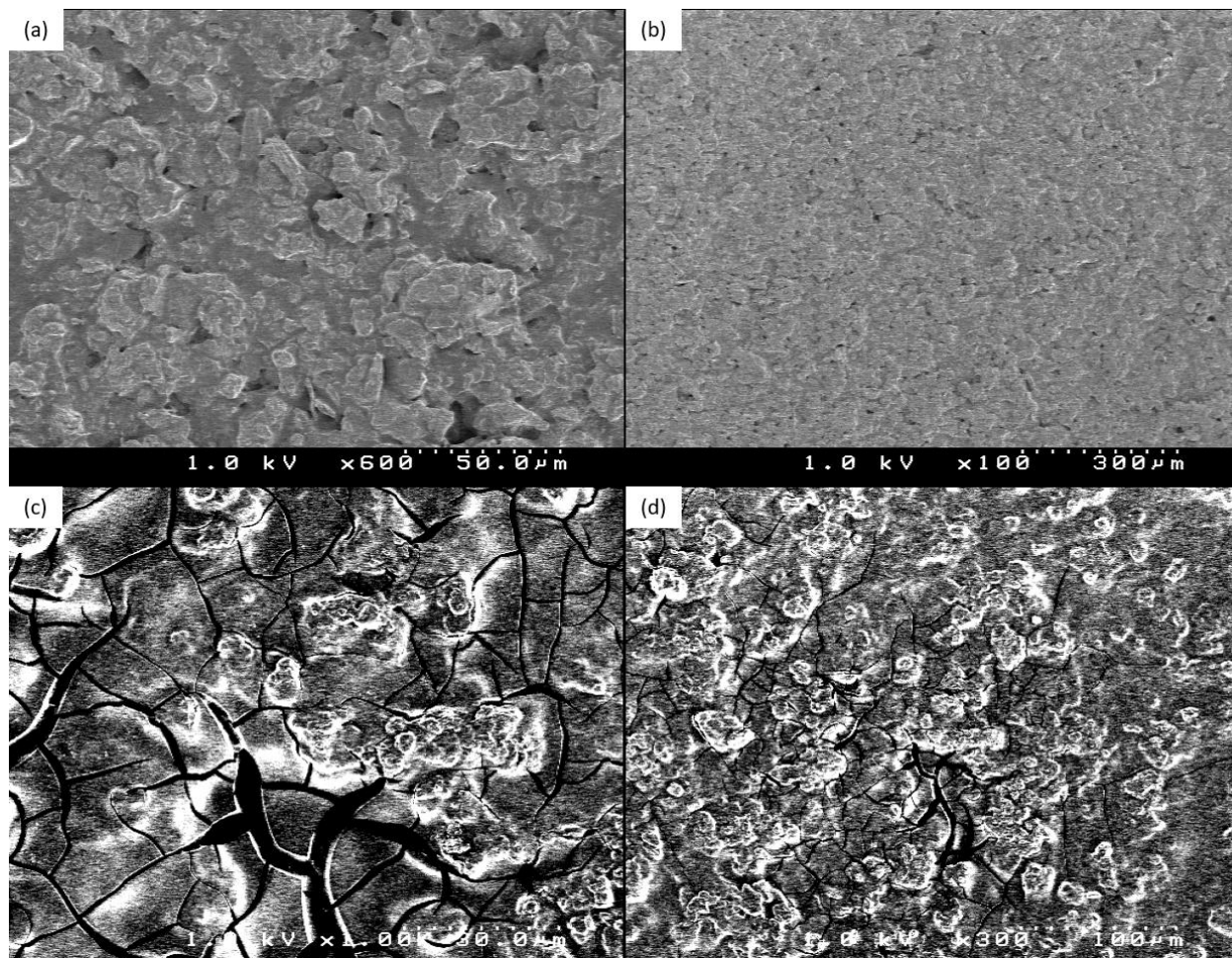


Figure 3.14 FESEM images of (a) & (b) PVBCAImFSI after 1500 cycles charge-discharge at 1C, (c) & (d) PVBCBImTFSI after 250 cycles at 1C.

XPS is a very popular technique to characterize the surfaces due to its sensitivity and specificity. Although the probe depth is about 10-20 nm, it still provides very valuable compositional information of the surfaces. To study the surface composition of the SEI, XPS measurements were carried out on the PVBCAImFSI and PVBCBImTFSI electrodes after charge-discharge cycling. The deconvoluted XPS spectra corresponding to the C 1s peak for PVBCAImFSI and PVBCBImTFSI electrodes are given in Figure 3.15 a & b respectively. The binding energy values and % area under the peak for all the individual kinds of carbon are tabulated in Table 3.8. The signal has been deconvoluted into six Gaussian-Lorentzian mixed components as shown in the table along with the peak assignment. Even after cycling the electrodes for 1500

cycles, the % area under the peak for graphite is about 14.2% in the PVBCAImFSI anodes as compared to 16.8% for PVBCBImTFSI anodes. This can be since the SEI formed with PVBCBImTFSI not being stable and hence more of the active material is exposed near the cracks. The O 1s signal has been deconvoluted into three Guassian-Lorentian mixed components as shown in Figure 3.16. The peak assignments along with the % area under the curve are given in Table 3.9. Interestingly, a peak corresponding to $\text{LiP}_x\text{F}_y\text{O}_z$ arising from LiPF_6 has been observed in the PVBCAImFSI based anodes.

Table 3.8 The binding energy values and corresponding % area under the curve corresponding to C 1s for PVBCAImFSI and PVBCBImTFSI based electrodes.

Component	PVBCAImFSI	% area under the curve	PVBCBImTFSI	% area under the curve
C-Li	283.7	19.5	284.1	13.2
Graphite	284.6	14.2	284.6	16.8
PEO	285.5	17.3	286.3	35.1
Ether carbons	286.8	16.8	288.6	5.4
Lithium carbonate Li_2CO_3	289.2	8.4	289.7	14.6
Alkyl carbonates (R- $\text{OCO}_2\text{-Li}$)	290.2	23.8		

Table 3.9 The binding energy values and corresponding % area under the curve corresponding to O 1s for PVBCAImFSI and PVBCBImTFSI based electrodes.

Component	PVBCAImFSI	% area under the curve	PVBCBImTFSI	% area under the curve
Carbonate	531.2	18.8	531.2	26.8
PEO	531.9	35.3	531.9	40.9
Ether	532.6	31.5	533.0	32.3
$\text{LiP}_x\text{F}_y\text{O}_z$	533.6	14.4		

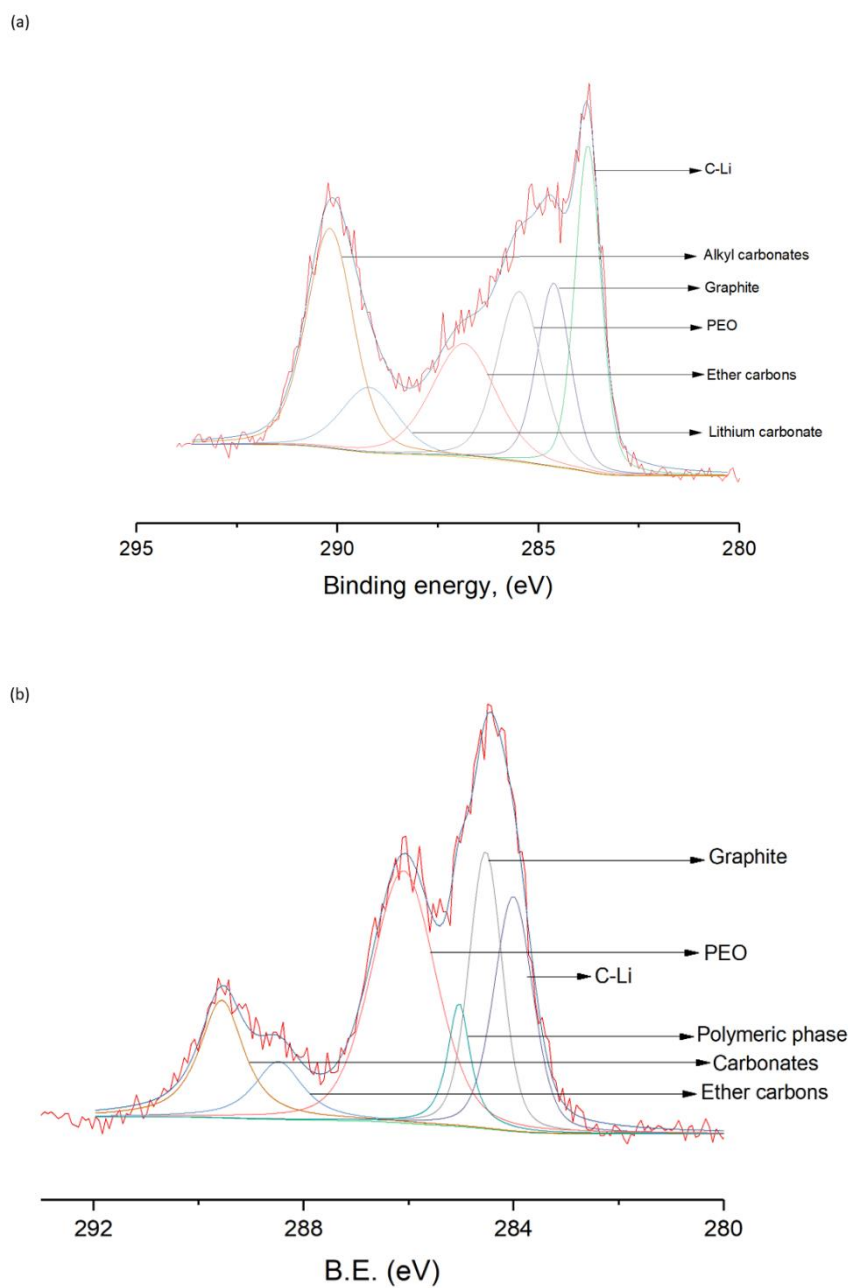


Figure 3.15 The deconvoluted XPS spectra for (a) PVBCAImFSI and (b) PVBCBImTFSI based graphite anodes after 1500 and 250 cycles respectively explaining various components C 1s signal.

3.5 Conclusions

Two PIL binders with varying side-chain and counter-ion (PVBCAImFSI & PVBCBImTFSI) have been synthesized and their performance as a binder for graphite anodes in LiBs has been evaluated. The goal of this work was to understand the effect of the PIL structure on its performance as a binder. Cyclic voltammetry studies indicated suppressed electrolyte degradation in PVBCAImFSI based anodes indicating the formation of a robust SEI. Due to the better interfacial properties, the lithium-ion diffusion coefficient was found to be higher than the PVBCBImTFSI based anodes. PVBCBImTFSI anodes exhibited lower lithium-ion diffusion coefficient due to slow ion-diffusion kinetics. Due to the suppressed electrolyte degradation, DEIS studies indicated the PVBCAImFSI binder based anodes to have better interfacial properties. The R_{SEI} values obtained was lesser than those for PVBCBImTFSI at all potentials. These observations were confirmed by the morphological characterizations. FESEM images for PVBCAImFSI showed retention of the initial granular structure of the graphite anodes whereas, PVBCBImTFSI based anodes showed extensive damage to the electrode and loss of the granular structure. The loss of granular structure indicated the formation of thicker SEI leading to capacity fade and cell failure. Charge-discharge studies were carried out for PVBCAImFSI and PVBCBImTFSI based half-cells and was compared to PVBCAImTFSI based half-cells to understand the effect of anion and side-chain of PIL on its performance as a binder. PVBCAImFSI based anodes exhibited a stable reversible discharge capacity for 1500 cycles with a capacity retention of almost 60%. Also, changing TFSI anion with FSI anion lead to an increase in capacity retention by 400% after 1500 cycles. The stability of the PVBCAImFSI based anodes was shown to be better than the PVBCBImTFSI based anodes. The above results indicated the synergy of the allyl group as a side-chain and FSI anion as counter-ion in the PIL binder structure leads to enhanced capacity and better durability.

References

- (1) Tarascon, J. M.; Armand, M. Building Better Batteries. **2008**, *451* (February), 652–657. <https://doi.org/10.1038/451652a>.
- (2) Etacheri, V.; Marom, R.; Elazari, R.; Salitra, G.; Aurbach, D. Challenges in the Development of Advanced Li-Ion Batteries: A Review. *Energy Environ. Sci.* **2011**, No. 4, 3243–3262. <https://doi.org/10.1039/c1ee01598b>.
- (3) Whittingham, M. S.; Fanwood, N.J. Chalcogenide Battery. *Exxon Res. Eng. Co.* **1977**, 1–5.
- (4) Aurbach, D.; Markovsky, B.; Levi, M. D.; Levi, E.; Schechter, A.; Moshkovich, M.; Cohen, Y. New Insights into the Interactions between Electrode Materials and Electrolyte Solutions for Advanced Nonaqueous Batteries. *J. Power Sources* **1999**, 81–82, 95–111. [https://doi.org/10.1016/S0378-7753\(99\)00187-1](https://doi.org/10.1016/S0378-7753(99)00187-1).
- (5) Thackeray, M. M.; David, W. I. F.; Bruce, P. G.; Goodenough, J. B. Lithium Insertion into Manganese Spinels. *Mater. Res. Bull.* **1983**, 18 (4), 461–472. [https://doi.org/10.1016/0025-5408\(83\)90138-1](https://doi.org/10.1016/0025-5408(83)90138-1).
- (6) Yazami, R.; Touzain, P. A Reversible Graphite-Lithium Negative Electrode for Electrochemical Generators. *J. Power Sources* **1983**, 9 (3), 365–371. [https://doi.org/10.1016/0378-7753\(83\)87040-2](https://doi.org/10.1016/0378-7753(83)87040-2).
- (7) Yoshino, A.; Sanechika, K.; Nakajima, T. US Patent 4668595A. **1986**, No. 19.
- (8) Wang, A.; Kadam, S.; Li, H.; Shi, S.; Qi, Y. Review on Modeling of the Anode Solid Electrolyte Interphase (SEI) for Lithium-Ion Batteries. *npj Comput. Mater.* **2018**, 4 (1). <https://doi.org/10.1038/s41524-018-0064-0>.
- (9) Goodenough, J. B.; Kim, Y. Challenges for Rechargeable Li Batteries. *Chem. Mater.* **2010**, 22 (3), 587–603. <https://doi.org/10.1021/cm901452z>.
- (10) Huang, L. H.; Min, Z. H.; Zhang, Q. Y. Solid Electrolyte Inter-Phase on Graphite Anodes in Li-Ion Batteries. *Rev. Adv. Mater. Sci.* **2014**, 36 (1), 13–20.
- (11) Verma, P.; Maire, P.; Novák, P. A Review of the Features and Analyses of the Solid Electrolyte Interphase in Li-Ion Batteries. *Electrochim. Acta* **2010**, 55 (22), 6332–6341.

- <https://doi.org/10.1016/j.electacta.2010.05.072>.
- (12) Peled, E.; Menkin, S. Review—SEI: Past, Present and Future. *J. Electrochem. Soc.* **2017**, *164* (7), A1703–A1719. <https://doi.org/10.1149/2.1441707jes>.
- (13) Peled, E. Advanced Model for Solid Electrolyte Interphase Electrodes in Liquid and Polymer Electrolytes. *J. Electrochem. Soc.* **1997**, *144* (8), L208. <https://doi.org/10.1149/1.1837858>.
- (14) Horstmann, B.; Single, F.; Latz, A. Review on Multi-Scale Models of Solid-Electrolyte Interphase Formation. *Curr. Opin. Electrochem.* **2019**, *13*, 61–69. <https://doi.org/10.1016/j.coelec.2018.10.013>.
- (15) Christensen, J.; Newman, J. A Mathematical Model for the Lithium-Ion Negative Electrode Solid Electrolyte Interphase. *Proc. - Electrochem. Soc.* **2003**, *20*, 85–94. <https://doi.org/10.1149/1.1804812>.
- (16) Patnaik, S. G.; Vedarajan, R.; Matsumi, N. Rational Design of a BIAN-Based Multi-Functional Additive for Higher Durability and Performance of $\text{LiMn}_{1/3}\text{Ni}_{1/3}\text{Co}_{1/3}\text{O}_2$ Cathodes. *Mol. Syst. Des. Eng.* **2019**, *4* (4), 939–950. <https://doi.org/10.1039/c9me00046a>.
- (17) Joshi, P.; Iwai, K.; Patnaik, S. G.; Vedarajan, R.; Matsumi, N. Reduction of Charge-Transfer Resistance via Artificial SEI Formation Using Electropolymerization of Borylated Thiophene Monomer on Graphite Anodes. *J. Electrochem. Soc.* **2018**, *165* (3), A493–A500. <https://doi.org/10.1149/2.0141803jes>.
- (18) Kwon, T. W.; Choi, J. W.; Coskun, A. The Emerging Era of Supramolecular Polymeric Binders in Silicon Anodes. *Chem. Soc. Rev.* **2018**, *47* (6), 2145–2164. <https://doi.org/10.1039/c7cs00858a>.
- (19) Jayakumar, T. P.; Badam, R.; Matsumi, N. Allylimidazolium-Based Poly(Ionic Liquid) Anodic Binder for Lithium-Ion Batteries with Enhanced Cyclability. *ACS Appl. Energy Mater.* **2020**. <https://doi.org/10.1021/acsaem.9b02376>.
- (20) Kausar, A. Research Progress in Frontiers of Poly(Ionic Liquid)s: A Review. *Polym. - Plast. Technol. Eng.* **2017**, *56* (17), 1823–1838. <https://doi.org/10.1080/03602559.2017.1289410>.

- (21) Qian, W.; Texter, J.; Yan, F. *Frontiers in Poly(Ionic Liquid)s: Syntheses and Applications. Chem. Soc. Rev.* **2017**, *46* (4), 1124–1159. <https://doi.org/10.1039/c6cs00620e>.
- (22) Spanos, I.; Neugebauer, S.; Guterman, R.; Yuan, J.; Schlögl, R.; Antonietti, M. Poly(Ionic Liquid) Binders as Ionic Conductors and Polymer Electrolyte Interfaces for Enhanced Electrochemical Performance of Water Splitting Electrodes. *Sustain. Energy Fuels* **2018**, *2* (7), 1446–1451. <https://doi.org/10.1039/C8SE00110C>.
- (23) Yuan, J.; Antonietti, M. Poly(Ionic Liquid)s: Polymers Expanding Classical Property Profiles. *Polymer (Guildf)*. **2011**, *52* (7), 1469–1482. <https://doi.org/10.1016/j.polymer.2011.01.043>.
- (24) Nishimura, N.; Ohno, H. 15Th Anniversary of Polymerised Ionic Liquids. *Polymer (Guildf)*. **2014**, *55* (16), 3289–3297. <https://doi.org/10.1016/j.polymer.2014.02.042>.
- (25) Ohno, H. Design of Ion Conductive Polymers Based on Ionic Liquids. *Macromol. Symp.* **2007**, *249–250*, 551–556. <https://doi.org/10.1002/masy.200750435>.
- (26) Matsumi, N.; Nakashiba, M.; Mizumo, T.; Ohno, H. Novel Polymer/Salt Hybrid Composed of Comblike Organoboron Polymer Electrolyte and Boron-Stabilized Imido Anion. *Macromolecules* **2005**, *38* (6), 2040–2042. <https://doi.org/10.1021/ma047469p>.
- (27) Matsumi, N.; Sugai, K.; Miyake, M.; Ohno, H. Polymerized Ionic Liquids via Hydroboration Polymerization as Single Ion Conductive Polymer Electrolytes. *Macromolecules* **2006**, *39* (20), 6924–6927. <https://doi.org/10.1021/ma060472j>.
- (28) Mizumo, T.; Marwanta, E.; Matsumi, N.; Ohno, H. Allylimidazolium Halides as Novel Room Temperature Ionic Liquids. *Chem. Lett.* **2004**, *33* (10), 1360–1361. <https://doi.org/10.1246/cl.2004.1360>.
- (29) Meek, K. M.; Nykaza, J. R.; Elabd, Y. A. Alkaline Chemical Stability and Ion Transport in Polymerized Ionic Liquids with Various Backbones and Cations. *Macromolecules* **2016**, *49* (9), 3382–3394. <https://doi.org/10.1021/acs.macromol.6b00434>.
- (30) Vedarajan, R.; Matsui, K.; Tamaru, E.; Dhankhar, J.; Takekawa, T.; Matsumi, N. Ionic Liquid/Boric Ester Binary Electrolytes with Unusually High Lithium Transference Number. *Electrochem. Commun.* **2017**, *81* (June), 132–135.

- <https://doi.org/10.1016/j.elecom.2017.06.019>.
- (31) Shkrob, I. A.; Marin, T. W.; Zhu, Y.; Abraham, D. P. Why Bis(Fluorosulfonyl)Imide Is a “Magic Anion” for Electrochemistry. *J. Phys. Chem. C* **2014**, *118* (34), 19661–19671. <https://doi.org/10.1021/jp506567p>.
- (32) Krämer, E.; Schedlbauer, T.; Hoffmann, B.; Terborg, L.; Nowak, S.; Gores, H. J.; Passerini, S.; Winter, M. Mechanism of Anodic Dissolution of the Aluminum Current Collector in 1 M LiTFSI EC:DEC 3:7 in Rechargeable Lithium Batteries. *J. Electrochem. Soc.* **2013**, *160* (2), A356–A360. <https://doi.org/10.1149/2.081302jes>.
- (33) Schweikert, N.; Hofmann, A.; Schulz, M.; Scheuermann, M.; Boles, S. T.; Hanemann, T.; Hahn, H.; Indris, S. Suppressed Lithium Dendrite Growth in Lithium Batteries Using Ionic Liquid Electrolytes: Investigation by Electrochemical Impedance Spectroscopy, Scanning Electron Microscopy, and in Situ ⁷Li Nuclear Magnetic Resonance Spectroscopy. *J. Power Sources* **2013**, *228*, 237–243. <https://doi.org/10.1016/j.jpowsour.2012.11.124>.
- (34) Patnaik, S. G.; Vedarajan, R.; Matsumi, N. BIAN Based Functional Diimine Polymer Binder for High Performance Li Ion Batteries. *J. Mater. Chem. A* **2017**, *5* (34), 17909–17919. <https://doi.org/10.1039/c7ta03843g>.
- (35) Smaran, K. S.; Joshi, P.; Vedarajan, R.; Matsumi, N. Optimisation of Potential Boundaries with Dynamic Electrochemical Impedance Spectroscopy for an Anodic Half-Cell Based on Organic-Inorganic Hybrid Electrolytes. *ChemElectroChem* **2015**, *2* (12), 1913–1916. <https://doi.org/10.1002/celc.201500372>.
- (36) Parimalam, B. S.; MacIntosh, A. D.; Kadam, R.; Lucht, B. L. Decomposition Reactions of Anode Solid Electrolyte Interphase (SEI) Components with LiPF₆. *J. Phys. Chem. C* **2017**, *121* (41), 22733–22738. <https://doi.org/10.1021/acs.jpcc.7b08433>.

Chapter 4

Surface Tethered Poly(ionic liquid) Silicon Nanoparticles for Lithium-ion Battery Composite Anodes.

4.1 Abstract

In this chapter, poly(ionic liquid) (PIL) tethered silicon nanoparticles were investigated as active material in combination with graphite for lithium-ion battery composite anodes. Silicon falls into the category of high energy density materials with a gravimetric energy density of over 4000 mAh/g, has immense potential to plug the current energy demand. However, due to the inherent volumetric changes researchers have failed in many attempts to commercialize silicon anode based lithium-ion batteries. Formation of a passivation layer (SEI) at the electrode-electrolyte interface is very crucial in preventing the damage to the electrode in the harsh cycling conditions. An ideal SEI layer must be ionically conductive and electronically non-conducting. The PILs are known to possess good ionic conductivity and can act as interface enhancing agents to design a better interface. In this work, PIL functionalized silicon nanoparticles were prepared by esterification of poly[1-(5-carboxypentyl)-3-vinyl-1H-imidazol-3-ium bromide] with hydroxyl functionalized silicon nanoparticles. Cyclic voltammetry studies of PIL functionalized silicon nanoparticles based composite anodes indicated an increase in the lithiation-delithiation currents with the cycling. They also exhibited a very high lithium-ion diffusion coefficient of about 1.01×10^{-8} cm/s which indicated a robust and conductive SEI formation. These electrodes exhibited about 735 mAh/g_{Si} of reversible discharge capacity after 34 cycles. This chapter presents preliminary results and performance of the anodes can be improved by more fine-tuning of the PIL structure and functionalization.

4.2 Introduction

In the past three decades, an immense advancement in technology has been achieved. For instance, computers that were the size of the room has been made into portable lightweight laptops and notebooks.¹ This is all possible because of the inventions of the portable secondary power sources such as lithium-ion batteries (LiBs). The commercialization of the lithium-ion batteries in 1991 by Sony corporation after decades of research by prominent scientists, paved way for revolutionizing the portable electronics such as laptops, mobile phones, cameras etc.²⁻⁵ LiBs have characteristic advantages such as the absence of memory effect, slow self-discharge, higher specific capacity etc., makes it the first choice over other secondary batteries. The design flexibility with LiBs allows for smarter and efficient design of the electronics. Transportation is another sector where LiBs have attracted immense attraction in the development of electric vehicles (EVs). Many automobile companies such as Nissan and Tesla have already commercialized EVs while many others in the process of commercializing their models soon. One crucial parameter that is very important for an EV is the driving range. It is defined as the distance the EV can travel on a single charge. The higher driving range requires more LiBs to be installed. Another approach that is being explored is to develop batteries with higher gravimetric energy density. This allows for increasing the driving range without increasing the number of LiBs in the EV.

Alloying type anodic materials such as silicon, tin etc. due to their high gravimetric energy density as shown in Figure 4.1, have gained immense research interest.⁶⁻⁸ Even though lithium metal has high gravimetric energy density, dendrite formation and lithium plating has been major problems yet to be addressed comprehensively.⁹ Silicon and other alloying material such as tin, germanium etc suffer from the volume expansion that occurs during the alloying and dealloying of lithium ions. This leads to the pulverization of the active material and continuous electrolyte decomposition on the active material. This leads to an increase in cell resistance, consumption of the electrolyte and capacity fade.^{10,11} Many approaches have been explored to avoid the pulverization of the active material and prevent the capacity fade. One of the long-standing approaches is the control of pulverization and mitigation of disconnection through particle size.¹² Many versions of nano-silicon such as Si nanoparticles,¹³ Si nanowires,¹⁴ Si thin flakes,¹⁵ Si nanopillars,¹⁶ Si nanostructured spheres¹⁷ or combinations of nanoparticles and nanowires have been explored as an independent component of the electrode. Other strategies include the use of

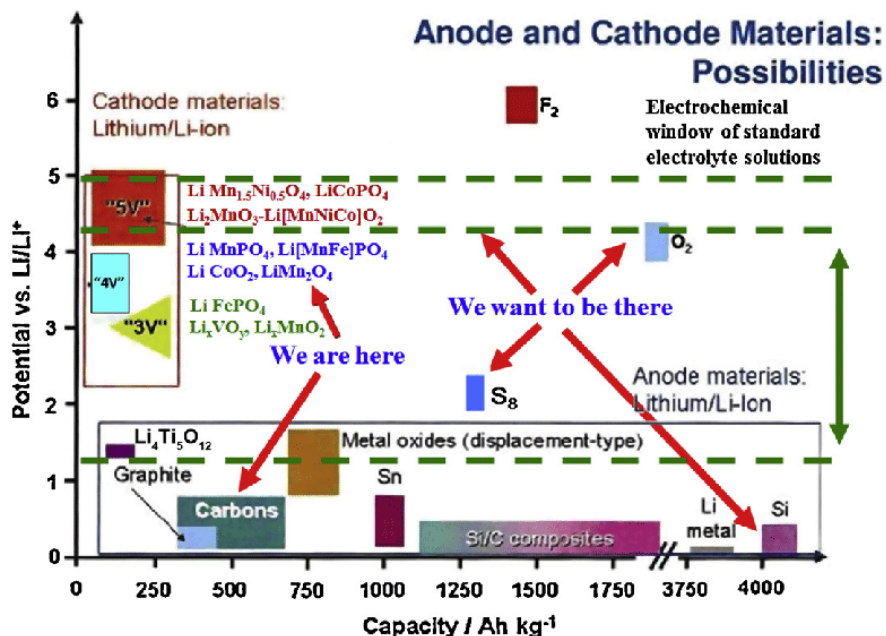


Figure 4.1 Ragone plot explaining the potential windows and theoretical gravimetric capacities of various LiB electrode materials.

Si-C core-shell structures, impregnating Si nanoparticles into carbon structures, use of functional binders for Si nanoparticles with polymers etc.¹⁸⁻²¹ While these techniques are effective to a certain degree, the volume expansion is still a challenge to be addressed. Tenhaeff et al. tethered polymers to the surface of the silicon to act as an artificial SEI.²² They demonstrated the surface passivation despite the huge volume expansion of silicon. A thin layer of polymers over the surface the silicon increased the coulombic efficiency by almost 14%. In the present study, imidzolium-based ionic liquid was tethered on the surface of Si nanoparticle and polymerized by free-radical polymerization to give a PIL covered Si nanoparticles. It is expected that the presence of the PIL on the surface of the Si nanoparticle will suppress the electrolyte reduction and leads to formation of a better interface. Also the ability of the PILs to gelate on absorbing the electrolyte can assist in better lithium-ion diffusion.

4.3 Materials and Methods

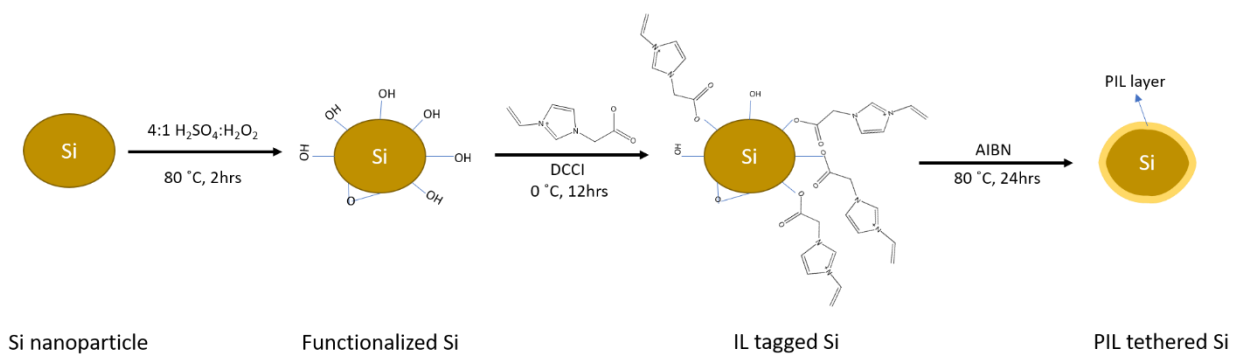
4.3.1 Materials

1-Vinylimidazole, 6-bromohexanoic acid, azobisisobutyronitrile (AIBN), vinylene carbonate and N-methylpyrrolidone (NMP) were purchased from Tokyo Chemical Industry Co., Ltd. Fluoroethylene carbonate was procured from Sigma Aldrich. N, N'-Dicyclohexylcarbodiimide was procured from Wako Pure Chemical Industries, Ltd. 30 nm silicon nanoparticles were purchased from ACS materials, LLC and graphite super fine powder (<50 μm) obtained from Merck was used as the active materials. Battery-grade acetylene black used as conductive additive was procured from Denka Japan Private Co., Ltd. Copper foil of thickness 20 μm was obtained from The Nilaco corporation. 1.0M LiPF_6 in 1:1 EC:DEC used as the electrolyte was purchased from Sigma-Aldrich. Commercial graphite anodes were procured from Piotrek Co., Ltd. All chemicals were used without any further purification.

4.3.2 Instrumentation

FT-IR spectra for the polymers were recorded on Perkin Elmer 100 FT-IR spectrometer. The spectra were recorded at a resolution of 2 cm^{-1} for 10 scans in ATR mode. NMR measurements were carried out on Bruker Avance III 400. MALDI-TOF measurements were carried out in DHB matrix on Bruker Microflex. FESEM micrographs for the electrodes were obtained using Hitachi S-4500 at accelerating voltage of 1.0 kV. TEM micrographs for the nanomaterial were recorded on Hitachi H-7100 using copper grids. X-ray photoelectron spectroscopy (XPS) measurements were carried on Fisons instruments S-probe TM 2803. The deconvolution of the XPS signals was carried out using the XPSPEAK41 software with 30% Gaussian -Lorentzian fit.

4.3.3 Synthesis



Schematic 4.1 Synthesis scheme for the preparation of PIL tethered Si nanoparticles.

The synthesis scheme to obtain PIL tethered Si nanoparticles is given in schematic 4.1. The synthesis is divided into three stages, viz., hydroxyl functionalization of Si nanoparticles, tagging of ionic liquid to hydroxyl functionalized Si and finally polymerizing the ionic liquid over the Si nanoparticle.

4.3.3.1 1-(5-carboxypentyl)-3-vinyl-1H-imidazol-3-ium bromide (HxVImBr): 1 mmol (90.2 mg) of 1-vinylimidazole, 1 mmol of 6-bromohexanoic acid (116.1 mg) was taken in 50 mL of ethanol. The reaction mixture was heated to 80 °C for 24 hours. The solvent was removed by rota-evaporation. The residue was washed with acetonitrile and dried at 70 °C to give Creamish white solid. The product was characterized by ¹H NMR and mass spectroscopy as shown in Figure 4.2 and Figure 4.3 respectively. ¹H NMR(400 MHz, DMSO-d₆) δ ppm: 12.04 (1H, s), 9.53 (1H, s), 8.21(1H, s), 7.95 (1H, s), 7.30 (1H, dd), 5.96 (1H, dd), 5.42 (1H, dd), 4.20 (2H, t), 2.22 (2H, m), 1.87 (2H, m), 1.53 (2H, m), 1.28 (2H, m). Mass spectroscopy (m/z): 209.2, 193.1, 154.1.

4.3.3.2 Hydroxyl functionalized silicon (Func Si): 1g of 30 nm Si nanoparticles were taken in a 4:1 mixture of sulphuric acid and hydrogen peroxide mixture. The reaction mixture was refluxed at 80 °C for 2 hours. The reaction was quenched by pouring the reaction mixture into ice followed by centrifugation at 14000 rpm. The material was washed with water and dried. The dried product is again redispersed into 100 mL of 5M HCl and stirred overnight at 80 °C. Hydroxyl functionalized Si nanoparticles were recovered by centrifugation at 14000 rpm and followed by drying.

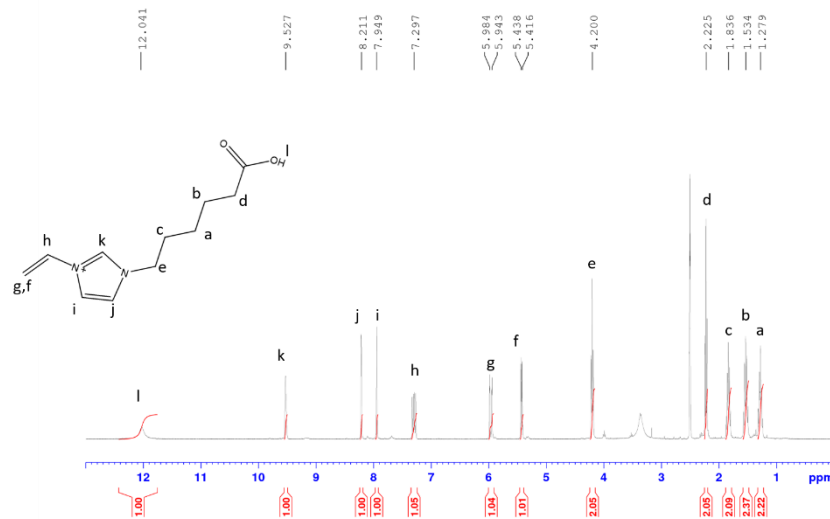


Figure 4.2 ^1H NMR spectrum of 1-(5-carboxypentyl)-3-vinyl-1H-imidazol-3-ium bromide recorded in DMSO-d_6 .

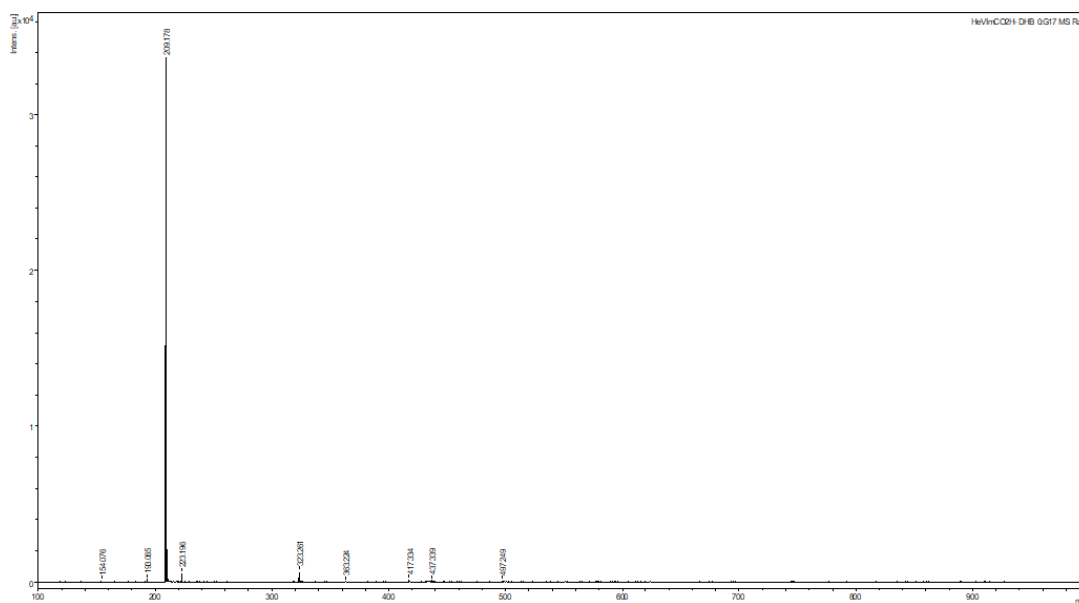


Figure 4.3 MS MALDI-TOF spectrum of 1-(5-carboxypentyl)-3-vinyl-1H-imidazol-3-ium bromide recorded in positive mode in DHB matrix.

4.3.3.3 Ionic liquid tagged silicon (IL tagged Si): 580 mg of hydroxyl functionalized silicon was dispersed in 50 mL of methanol. 2 mmol (580.3 mg) of HxVImBr was solubilized in the above mixture. The reaction mixture was cooled down to 0 °C followed by the addition of 2 mmol

(412.6 mg) of N, N'-Dicyclohexylcarbodiimide was added. The reaction mixture was stirred at room temperature overnight. The IL tagged Si was recovered by carrying out centrifugation at 14000 rpm for 30 min followed by drying.

4.3.3.3 PIL tethered silicon (FSi): Polymerization of the IL tagged Si was carried out by free radical polymerization using AIBN as initiator. Initiator to monomer ratio was taken as 1:100. 400 mg of IL tagged Si was dispersed in 50 mL of methanol. 28 mg of AIBN was added to the above dispersion and was refluxed under an inert atmosphere for 24 hours. PIL tethered silicon was obtained by filtering the reaction mixture, washing with an excess of methanol and drying.

4.3.4 Characterization

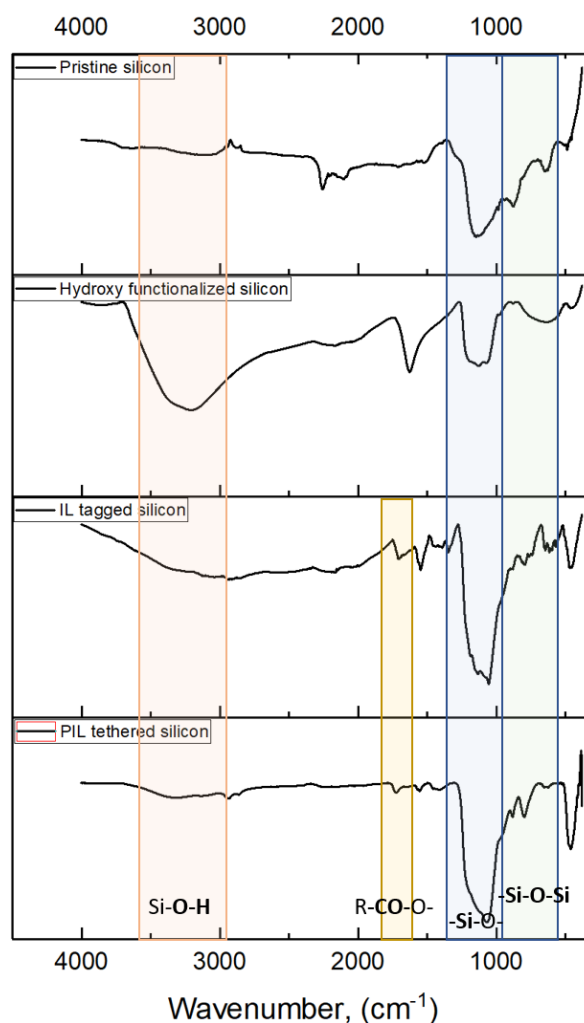


Figure 4.4 FT-IR spectrum of pristine Si, hydroxyl functionalized Si, IL tagged Si and PIL tethered Si.

To understand the composition and morphology of the material prepared, characterization of the material has been carried out using FT-IR, XPS and TEM techniques. Figure 4.4 gives the FT-IR spectra for pristine Si nanoparticles, hydroxyl functionalized Si, IL tagged Si and PIL tethered Si. The hydroxyl functionalized Si shows a distinctive broad Si-O-H peak around 3300 cm^{-1} and Si-O- around 1100 cm^{-1} indicating successful surface modification of the pristine Si nanoparticles. The IL tagging leads to the decrease in the intensity of Si-O-H peak and appearance of carbonyl peak around 1720 cm^{-1} indicating the successful esterification reaction. A -C=C- shoulder peak can also be observed around 1649 cm^{-1} which disappears in the PIL tethered Si indicated successful polymerization reaction.

XPS measurements were carried out to understand the composition of the nanomaterial. The signals corresponding to Si 2p, O 1s, C 1s and N 1s have been deconvoluted as shown in Figure 4.5 for pristine Si, hydroxyl functionalized Si, IL tagged Si and PIL tethered Si. The pristine Si was found to have a surface oxide layer due to the atmospheric oxidation. On deconvolution, the Si 2p signal was found to be composed of four signals corresponding to the elemental Si at 98.4 eV, -Si-OH at 100.2 eV, -O-Si-O- bridges at 102.1 eV and SiO₂ at 105.7 eV. Similarly, the O 1s signal was deconvoluted to three peaks corresponding to the -Si-O-Si- bridges at 531.1 eV, terminal Si-O- groups at 533.1 eV and -Si-O-O-Si- peroxy groups at 535.0 eV. The peroxy moieties were also reported earlier to be found in the defects of the Si nanoparticles.²³ On hydroxyl functionalization, the total oxygen content increased to 58.7%. The Si 2p and O 1s signal are deconvoluted as shown in Figure 4.5. On the tagging of ionic liquid the total oxygen content decreased to 39% and the total carbon content increased to 44.1% indicating the successful tagging of the ionic liquid to the surface of the hydroxyl functionalized Si nanoparticle. The signal corresponding to C 1s was deconvoluted into five signals corresponding to -C=C- at 285.4.1 eV, -C-O- at 287.7, -CO₂- at 291.1 eV. -C=C- constitutes to 36.1% of the total carbon content. On polymerization, the -C=C- share in the PIL tethered Si sample was observed to be decreased to almost 5%. This indicates the successful polymerization of the ionic liquid moieties over the Si nanoparticles. This was also supported by the TEM micrographs which show a layer around the Si nanoparticle. The peak corresponding to N 1s was also observed in the PIL tethered Si sample.

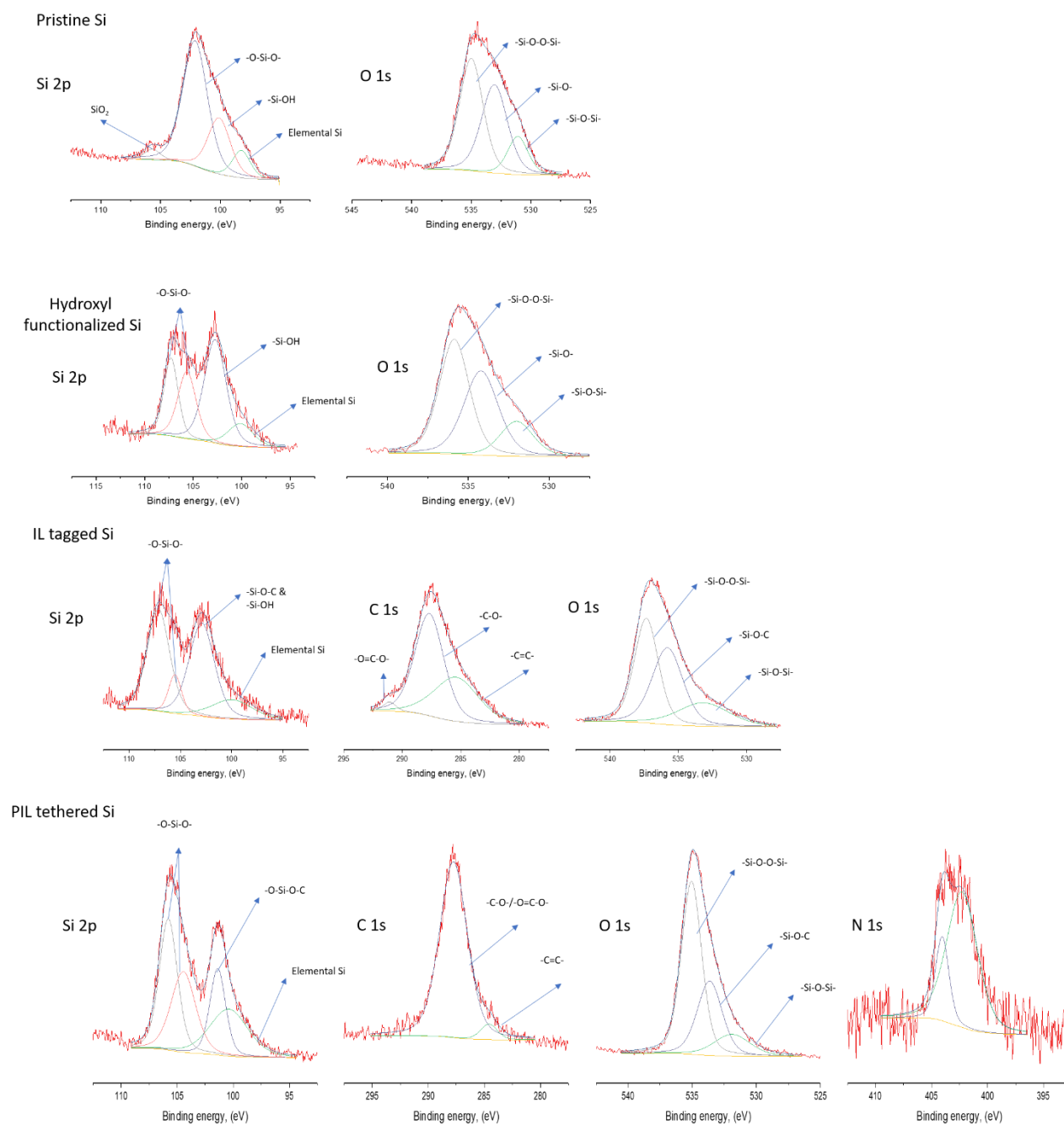


Figure 4.5 Deconvoluted XPS spectra for pristine Si, hydroxyl functionalized Si, IL tagged Si and PIL tethered Si.

The TEM micrographs are presented in Figure 4.6 for all the four samples. TEM micrographs were recorded at every stage of the reaction to understand the morphological changes that occur at the surface of the Si nanoparticle. Little change was observed after the hydroxyl functionalization. An apparent layer was observed on top of the silicon nanoparticle after the IL tagging as indicated by a circle in Figure 4.6c. This layer can be attributed to the ionic liquid forming a layer around the Si nanoparticle. Figure 4.6d shows the micrograph corresponding to the PIL tethered Si nanoparticles. On polymerization, distinctive strand-like structures were

formed a uniform layer on the Si nanoparticles encapsulating it. This leads to the conclusion that the polymerization was indeed successful.

4.3.5 Electrode and Cell Fabrication

Two variants of electrodes – one with a binder and the other without binder were investigated. Electrode slurry for the electrode without a binder (FSi_G) was prepared by ball-milling 40 wt% of PIL tethered Si, 40 wt% of graphite and 20 wt% acetylene black in NMP. The electrode slurry for the electrode with the binder (FSi_G_CMC) was prepared by ball-milling 40 wt% PIL tethered Si, 35 wt% of graphite, 20 wt% of AB and 5 wt% of CMC binder in water. Electrodes were fabricated by casting the as-prepared slurry onto copper foil using a doctor blade. Electrodes were dried overnight under vacuum at 80 °C to remove the solvent. The dried electrodes were roll-pressed at 80 °C for 6 hours. The dried electrodes were punched into disks with area 1.72 cm² to be used for testing in coin cells. 2025-coin cells were assembled to carry out the electrochemical testing using the as-fabricated graphite electrodes as anodes, lithium foil as counter and reference electrodes with a polypropylene separator (25 μm, Celgard 2500). 1.0 M LiPF₆ in 1:1 EC:DEC with 2mg/mL of VC and FEC was used as the electrolyte. The anodic half cells were assembled inside an argon-filled glove box (MBRAUN Labstar) whose moisture and O₂ content was <0.1ppm. The assembled cells were rested for 6 hours for stabilization before carrying out the electrochemical characterization.

4.3.6 Electrochemical Instrumentation

The Electrochemical Impedance Spectroscopy (EIS) measurements were carried out on Bio-Logic VMP 300 potentiostat electrochemical workstation equipped with frequency response analyzer (FRA). The EIS measurements were carried out after stabilizing as assembled cells and after cyclic voltammetry. The measurements were carried out in the frequency range of 1 MHz to 100 mHz with a sinus amplitude of 10mV. The Cyclic Voltammetry (CV) measurements were carried on a VSP 300 potentiostat electrochemical workstation from Bio-Logic Science Instruments. The CV measurements were carried out in the potential range of 10 – 1200 mV vs Li/Li⁺ at a scan rate of 0.1 mV/s. The scan rate studies using CV was carried out at 0.1, 0.3, 0.5, 0.7 and 1.0 mV/s scan rates. The charge-discharge measurements were carried out on the Bio-Logic BCS 815 battery cycler using a CC-mode in the potential range of 10 – 1200 mV vs Li/Li⁺.

4.4 Results and Discussions

Even though the energy density of silicon is very high, the direct use of silicon as active material is still challenging. A comprehensive solution is yet to be made to avoid the pulverization and capacity fade due to the volumetric changes of silicon during the charge-discharge cycling. However, it is equally important to design strategies that can incorporate silicon into the electrode matrix to increase the capacity of the conventional electrodes. To achieve this, many approaches are such as the use of additives, building a robust artificial SEI, preparing novel architectures with high-stress tolerance, use of functional binders etc. Poly(ionic liquid)s is a class of polymers with very interesting properties similar to ionic liquid monomers. They have wider electrochemical stability, can retain electrolytes and form interesting morphologies.²⁴⁻²⁷ These materials can act as interface enhancing agents increasing the ion diffusion, dissipating stress and decreasing interfacial resistance.²⁸ This motivated the design of the PIL tethered Si nanoparticles with modified surface chemistry. The presence of the PIL at the interface would not only improve the SEI properties but also act as an encapsulation preventing the pulverization of the Si nanoparticles. In this chapter, the performance of the PIL tethered Si nanoparticles was evaluated by preparing composite anodes with graphite. Though this will lead to a decrease in the gravimetric energy density that can be derived from the LiBs, it can improve the durability.

4.4.1 Electrochemical Characterization

Cyclic voltammetry measurements were carried out to understand the lithiation-delithiation and redox properties of the electrodes. As discussed in the electrode fabrication, two sets of electrodes with PIL tethered Si nanoparticles are evaluated in this chapter namely, FSi_G and FSi_G_CMC. Figure 4.7 a & b shows the cyclic voltammograms for both the electrodes. Both the anodic half cells exhibit typical lithiation-delithiation curves for Si nanoparticles and graphite. The electrolyte degradation was found to be more in the case of FSi_G anodes compared to FSi_G_CMC anodes. Also, in the case of the FSi_G_CMC, the deintercalation currents for both graphite and silicon were observed to be increasing with the cycling. This indicates the formation of a better interface during the initial cycling leading to the improvement in the diffusion coefficients. The lithium-ion diffusion coefficients (D_{Li^+}) were evaluated by the Randles-Sevcik equation analyzing the cyclic voltammetry data obtained at different scan rates. Figure 4.8 a & b shows the obtained voltammograms at different scan rates and Figure 4.8 c & d shows the peak

current I_p vs square root of scan rate plots. The evaluated lithium-ion diffusion coefficients for FSi_G was found to be 5.87×10^{-9} cm/s as compared to 1.01×10^{-8} cm/s for FSi_G_CMC. FSi_G_CMC exhibits about 70.5% higher lithium-ion diffusion coefficient. The improvement in the diffusion coefficients can be attributed to the formation of the better interface as well as better contact between all the electrode constituents. To understand the effect of cycling on the interfacial properties, EIS measurements were carried out at OCP. The Nyquist plots before and after the cyclic voltammetry are shown in Figure 4.9. The interfacial resistance reduces for both the electrodes after the cyclic voltammetry studies as shown in Figure 4.10. The impedance data were fitted to equivalent electric circuit models to obtain the values for the interfacial resistance. Table 4.1 gives the values corresponding to the solution, interfacial and diffusion resistances along with

Figure 4.9 Electrochemical impedance spectroscopy measurements for a) FSi_G, b) FSi_G_CMC anodes in 1.0M LiPF₆ / EC : DEC with 2 mg/mL VC and FEC.

the equivalent circuit model. The interfacial resistance in the case of FSi_G_CMC is lesser compared to that of the FSi_G electrodes. The decrease in the interfacial resistances can be attributed to the formation of the SEI.

Table 4.1 EECM fittings for anodic half-cells with FSi_G and FSi_G_CMC electrodes after cycling in 1.0M LiPF₆ / EC : DEC with 2 mg/mL VC and FEC.

Binder	R1	R2	R3	χ^2	Circuit
FSi_G	2.984	100.8	307.9	0.003275	R(QR)(Q(RW))
FSi_G_CMC	2.465	31.27	400.5	0.001246	R(QR)(Q(RW))

With this understanding of the redox behaviour and interfacial properties, charge-discharge behaviours were studied to evaluate the performance of these electrodes. Initially, the electrodes were subject to precycling at 0.04C rate to form the interface. This was followed by charging at 0.1C rate and discharging at 0.2C rate. Figure 4.11 shows the charge-discharge profile of the FSi_G anodes. These electrodes exhibited about 1308 mAh/g_{Si} of charging capacity in the first cycle. The reversible discharge capacity obtained was about 742 mAh/g_{Si}. An irreversible capacity of about 566 mAh/g_{Si} was observed. However, a continuous capacity fade was observed and the discharge

capacity after three cycles was mAh/g_{Si} after which the cell fails. To understand the problem, the cells were decrimped using the protocol described in Chapter 3 and FESEM micrographs were recorded. Both morphology and cross-section imaging was carried out. Figure 4.12 a & c shows the cross-sectional view of FSi_G_CMC and FSi_G electrodes before cycling. The adhesion of the electrode laminate to the current collector was better in the case of FSi_G_CMC. The loss of contact between the electrode laminate and the current collector is the reason for the deterioration in the performance. Figure 4.12 b shows the morphology of FSi_G electrode after charge-discharge. Though it retains the granular structure and has uniform SEI formation, the loss of contact between the current collector and the electrode laminate becomes even worse after the charge-discharge cycling as shown in Figure 4.12 d leading to cell failure.

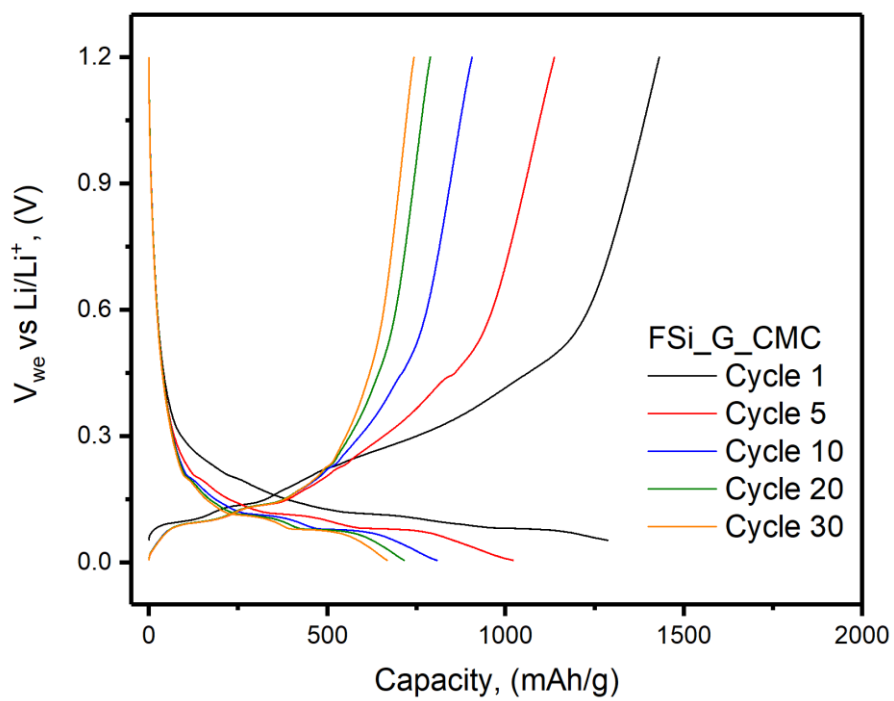


Figure 4.13 Charge-discharge profile of anodic half-cells with FSi_G_CMC in 1.0M LiPF₆ / EC : DEC with 2 mg/mL VC and FEC .

The charge-discharge profile has been shown in Figure 4.13. The LiBs with CMC binder i.e., FSi_G_CMC exhibited good charge-discharge performance. Two distinctive plateaus corresponding to lithium intercalation into graphite and alloying with Si were observed. Due to the effective pre-cycling, there was no irreversible capacity observed. The long cycling performance at 0.1C charging rate and 0.2 discharging rates is shown in Figure 4.14. The capacity is calculated based on the theoretical capacity of Si nanoparticles. The first cycle discharge capacity was found to be 1430 mAh/g_{Si}. An initial capacity fade was observed but once the interface is robust, the capacity stabilizes around 750 mAh/g_{Si}. Though the initial capacity fade was very high reducing the overall capacity by 45%, it is more than thrice the capacity of traditional graphite anodes at this cycling rate. The reversible discharge capacity was found to be higher than the charging capacity. This might be due to the effective lithiation of the composite anode during the pre-lithiation of the composite anodes. The reservoirs of lithium present in the electrode not just prevents the irreversible capacity but also exhibits higher discharge capacity. Presence of excess of lithium in the anodes exhibited less irreversible capacity and improved coulombic efficiency.³³ There is more scope for improving the charge-discharge performance of the PIL

tethered Si nanoparticles. It is believed that PIL structural optimization would result in the improvement in the discharge capacity and the stability of the electrodes. The alkyl chain length will have a crucial impact on the interface stabilization and improving the stress tolerance of the Si nanoparticles.

4.5 Composition Analysis

XPS measurements were carried out to understand the surface composition of FSi_G_CMC electrodes after 40 cycles of charge-discharge cycling. Signals corresponding to Li 1s, Si 2p, C 1s, O 1s and F 1s was observed. The high-resolution data obtained for these elements were deconvoluted into various Gaussian-Lorentzian mixed components corresponding to different chemical entities. The C 1s peak was deconvoluted into six different components as shown in Figure 4.15. The binding energy values and % area under the peak is tabulated in Table 4.2. In addition to the carbon species shown in the table, a polymeric phase was also found to be present at 286.3 eV. The graphitic component was found to be about 22% indicating that SEI is not thick.

Table 4.2 The binding energy values and corresponding % area under the curve corresponding to C 1s for FSi_G_CMC based electrodes.

Component	Binding Energy (eV)	% area under the curve
C-Li	284.1	19.5
Graphite	284.6	21.9
PEO	286.3	20.7
Ether carbons	288.4	11.8
Lithium carbonate Li_2CO_3	289.7	16.3
Alkyl carbonates (R- $\text{OCO}_2\text{-Li}$)		

Figure 4.16 shows the deconvoluted spectra corresponding to the F 1s and Li 1s signals. Due to the presence of the PIL, the formation of the LiF salt is effectively decreased and was found to be constituting about 13% of fluorine content at the interface as shown in Table 4.3. This was also confirmed by the L 1s signal which shows about 5.3% of LiF in the deconvoluted spectrum as shown in Figure 4.16 and Table 4.4. The O 1s signal was deconvoluted into three components and was assigned to different chemical species as shown in Figure 4.17. The binding energy values and the % area under peak for the components are shown in Table 4.5. A weak signal corresponding to Si 2p was also observed corresponding to -Si-O- of PIL tethered Si as shown in Figure 4.18. XPS results show that the presence of the PIL in the electrode matrix leads to the suppression of LiF formation leading to better electronic as well as ionic conducting properties.

Table 4.3 The binding energy values and corresponding % area under the curve corresponding to F 1s for FSi_G_CMC based electrodes.

Component	Binding Energy (eV)	% area under the curve
LiF	684.5	13.0
Li_xPF_y	686.6	87.0

Table 4.4 The binding energy values and corresponding % area under the curve corresponding to Li 1s for FSi_G_CMC based electrodes.

Component	Binding Energy (eV)	% area under the curve
ROCO_2Li	54.8	94.7
LiF	56.3	5.3

Table 4.5 The binding energy values and corresponding % area under the curve corresponding to O 1s for FSi_G_CMC based electrodes.

Component	Binding Energy	% area under the curve
Carbonate	530.5	18.1
PEO	531.5	61.8
Ether	532.8	20.1

4.6 Conclusions

PIL tethered Si nanoparticles were synthesized and evaluated as active material in composite anodes for LiBs. Silicon is considered as next-gen anodic material for LiBs due to its high energy density. However, due to the volumetric changes during the charge-discharge studies results in its pulverization and capacity fade. Presence of PILs at the electrode-electrolyte interface can result in enhanced interfacial properties and can assist in the design of artificial SEI. In this study, a poly(vinylimidazolium) based PIL is covalently attached to the surface of the Si nanoparticle. The lithium-ion diffusion coefficient was evaluated and was found to be 70.5% higher in the presence of an auxiliary CMC binder. The auxiliary binder was found to be crucial in maintaining the contact between the electrode laminate and the copper current collector. Electrochemical impedance measurements indicated the improvement of the interface after the cyclic voltammetry studies. The charge-discharge studies were performed for both the electrodes. However, due to the loss of contact, FSi_G electrodes showed capacity fade and cell failure. The FSi_G_CMC anodes showed an initial capacity fade. However, once the interface was matured, a stable reversible capacity of about 750 mAh/g_{Si} was achieved. XPS measurements of the cycled FSi_G_CMC anodes show suppressed LiF formation due to the presence of the PIL in the electrode matrix. The initial experiments with PIL tethered Si has shown promising results and there is a huge scope for the development by the structural tuning of the PIL.

References

- (1) Tarascon, J. M.; Armand, M. Issues and Challenges Facing Rechargeable Lithium Ion Batteries. *Nature* **2001**, *414*, 359. <https://doi.org/10.1097/00006254-199510000-00002>.
- (2) Yoshino, A.; Sanechika, K.; Nakajima, T. US Patent 4668595A. **1986**, No. 19.
- (3) Thackeray, M. M.; David, W. I. F.; Bruce, P. G.; Goodenough, J. B. Lithium Insertion into Manganese Spinels. *Mater. Res. Bull.* **1983**, *18* (4), 461–472. [https://doi.org/10.1016/0025-5408\(83\)90138-1](https://doi.org/10.1016/0025-5408(83)90138-1).
- (4) Aurbach, D.; Markovsky, B.; Levi, M. D.; Levi, E.; Schechter, A.; Moshkovich, M.; Cohen, Y. New Insights into the Interactions between Electrode Materials and Electrolyte Solutions for Advanced Nonaqueous Batteries. *J. Power Sources* **1999**, *81–82*, 95–111. [https://doi.org/10.1016/S0378-7753\(99\)00187-1](https://doi.org/10.1016/S0378-7753(99)00187-1).
- (5) Whittingham, M. S.; Fanwood; N.J. Chalcogenide Battery. *Exxon Res. Eng. Co.* **1977**, 1–5.
- (6) Lu, J.; Chen, Z.; Pan, F.; Cui, Y.; Amine, K. High - Performance Anode Materials for Rechargeable Lithium - Ion Batteries. **2018**, No. 0123456789.
- (7) Hassoun, J.; Scrosati, B. Review—Advances in Anode and Electrolyte Materials for the Progress of Lithium-Ion and beyond Lithium-Ion Batteries. *J. Electrochem. Soc.* **2015**, *162* (14), A2582–A2588. <https://doi.org/10.1149/2.0191514jes>.
- (8) Qi, W.; Shapter, J. G.; Wu, Q.; Yin, T.; Gao, G.; Cui, D. Nanostructured Anode Materials for Lithium-Ion Batteries: Principle, Recent Progress and Future Perspectives. *J. Mater. Chem. A* **2017**, *5* (37), 19521–19540. <https://doi.org/10.1039/c7ta05283a>.
- (9) Cheng, X. B.; Zhang, R.; Zhao, C. Z.; Zhang, Q. Toward Safe Lithium Metal Anode in Rechargeable Batteries: A Review. *Chem. Rev.* **2017**, *117* (15), 10403–10473. <https://doi.org/10.1021/acs.chemrev.7b00115>.
- (10) Chen, H.; Ling, M.; Hencz, L.; Ling, H. Y.; Li, G.; Lin, Z.; Liu, G.; Zhang, S. Exploring Chemical, Mechanical, and Electrical Functionalities of Binders for Advanced Energy-Storage Devices. *Chem. Rev.* **2018**, *118* (18), 8936–8982. <https://doi.org/10.1021/acs.chemrev.8b00241>.

- (11) Wang, A.; Kadam, S.; Li, H.; Shi, S.; Qi, Y. Review on Modeling of the Anode Solid Electrolyte Interphase (SEI) for Lithium-Ion Batteries. *npj Comput. Mater.* **2018**, *4* (1). <https://doi.org/10.1038/s41524-018-0064-0>.
- (12) Besenhard, J. O.; Yang, J.; Winter, M. Will Advanced Lithium-Alloy Anodes Have a Chance in Lithium-Ion Batteries? *J. Power Sources* **1997**, *68* (1), 87–90. [https://doi.org/10.1016/S0378-7753\(96\)02547-5](https://doi.org/10.1016/S0378-7753(96)02547-5).
- (13) Xu, J.; Zhang, Q.; Cheng, Y.-T. High Capacity Silicon Electrodes with Nafion as Binders for Lithium-Ion Batteries. *J. Electrochem. Soc.* **2016**, *163* (3), A401–A405. <https://doi.org/10.1149/2.0261603jes>.
- (14) Chan, C. K.; Ruffo, R.; Hong, S. S.; Huggins, R. A.; Cui, Y. Structural and Electrochemical Study of the Reaction of Lithium with Silicon Nanowires. *J. Power Sources* **2009**, *189* (1), 34–39. <https://doi.org/10.1016/j.jpowsour.2008.12.047>.
- (15) Saito, M.; Nakai, K.; Yamada, T.; Takenaka, T.; Hirota, M.; Kamei, A.; Tasaka, A.; Inaba, M. Si Thin Platelets as High-Capacity Negative Electrode for Li-Ion Batteries. *J. Power Sources* **2011**, *196* (16), 6637–6643. <https://doi.org/10.1016/j.jpowsour.2011.02.042>.
- (16) Chen, X.; Li, X.; Ding, F.; Xu, W.; Xiao, J.; Cao, Y.; Meduri, P.; Liu, J.; Graff, G. L.; Zhang, J. G. Conductive Rigid Skeleton Supported Silicon as High-Performance Li-Ion Battery Anodes. *Nano Lett.* **2012**, *12* (8), 4124–4130. <https://doi.org/10.1021/nl301657y>.
- (17) Zhou, W.; Jiang, T.; Zhou, H.; Wang, Y.; Fang, J.; Whittingham, M. S. The Nanostructure of the Si-Al Eutectic and Its Use in Lithium Batteries. *MRS Commun.* **2013**, *3* (3), 119–121. <https://doi.org/10.1557/mrc.2013.20>.
- (18) Dimov, N.; Kugino, S.; Yoshio, M. Carbon-Coated Silicon as Anode Material for Lithium Ion Batteries: Advantages and Limitations. *Electrochim. Acta* **2003**, *48* (11), 1579–1587. [https://doi.org/10.1016/S0013-4686\(03\)00030-6](https://doi.org/10.1016/S0013-4686(03)00030-6).
- (19) Shen, L.; Wang, Z.; Chen, L. Carbon-Coated Hierarchically Porous Silicon as Anode Material for Lithium Ion Batteries. *RSC Adv.* **2014**, *4* (29), 15314–15318. <https://doi.org/10.1039/c4ra01255k>.
- (20) Jeong, M. G.; Islam, M.; Du, H. L.; Lee, Y. S.; Sun, H. H.; Choi, W.; Lee, J. K.; Chung, K.

- Y.; Jung, H. G. Nitrogen-Doped Carbon Coated Porous Silicon as High Performance Anode Material for Lithium-Ion Batteries. *Electrochim. Acta* **2016**, *209*, 299–307. <https://doi.org/10.1016/j.electacta.2016.05.080>.
- (21) Technol, J. E. S.; Choi, N.; Ha, S.; Lee, Y.; Jang, J. Y.; Jeong, M.; Shin, W. C.; Ue, M. Recent Progress on Polymeric Binders for Silicon Anodes in Lithium-Ion Batteries. *J. Electrochem. Sci. Technol.* **2015**, *6* (2), 35–49. <https://doi.org/10.5229/JECST.2015.6.2.35>.
- (22) Shen, B. H.; Veith, G. M.; Tenhaeff, W. E. Silicon Surface Tethered Polymer as Artificial Solid Electrolyte Interface. *Sci. Rep.* **2018**, *8* (1), 1–11. <https://doi.org/10.1038/s41598-018-30000-z>.
- (23) Zhong, Y.; Qiu, X.; Gao, J.; Guo, Z. Chemical Structure of Si–O in Silica Fume from Ferrosilicon Production and Its Reactivity in Alkali Dissolution. *ISIJ Int.* **2019**, *59* (6), 1098–1104. <https://doi.org/10.2355/isijinternational.ISIJINT-2018-516>.
- (24) Qian, W.; Texter, J.; Yan, F. Frontiers in Poly(Ionic Liquid)s: Syntheses and Applications. *Chem. Soc. Rev.* **2017**, *46* (4), 1124–1159. <https://doi.org/10.1039/c6cs00620e>.
- (25) Mecerreyes, D. Polymeric Ionic Liquids: Broadening the Properties and Applications of Polyelectrolytes. *Prog. Polym. Sci.* **2011**, *36* (12), 1629–1648. <https://doi.org/10.1016/j.progpolymsci.2011.05.007>.
- (26) Yuan, J.; Mecerreyes, D.; Antonietti, M. Poly(Ionic Liquid)s: An Update. *Prog. Polym. Sci.* **2013**, *38* (7), 1009–1036. <https://doi.org/10.1016/j.progpolymsci.2013.04.002>.
- (27) Spanos, I.; Neugebauer, S.; Guterman, R.; Yuan, J.; Schlögl, R.; Antonietti, M. Poly(Ionic Liquid) Binders as Ionic Conductors and Polymer Electrolyte Interfaces for Enhanced Electrochemical Performance of Water Splitting Electrodes. *Sustain. Energy Fuels* **2018**, *2* (7), 1446–1451. <https://doi.org/10.1039/C8SE00110C>.
- (28) Grygiel, K.; Lee, J. S.; Sakaushi, K.; Antonietti, M.; Yuan, J. Thiazolium Poly(Ionic Liquid)s: Synthesis and Application as Binder for Lithium-Ion Batteries. *ACS Macro Lett.* **2015**, *4* (12), 1312–1316. <https://doi.org/10.1021/acsmacrolett.5b00655>.
- (29) Joshi, P.; Iwai, K.; Patnaik, S. G.; Vedarajan, R.; Matsumi, N. Reduction of Charge-Transfer Resistance via Artificial SEI Formation Using Electropolymerization of Borylated

- Thiophene Monomer on Graphite Anodes. *J. Electrochem. Soc.* **2018**, *165* (3), A493–A500. <https://doi.org/10.1149/2.0141803jes>.
- (30) Jayakumar, T. P.; Badam, R.; Matsumi, N. Allylimidazolium-Based Poly(Ionic Liquid) Anodic Binder for Lithium-Ion Batteries with Enhanced Cyclability. *ACS Appl. Energy Mater.* **2020**. <https://doi.org/10.1021/acsaem.9b02376>.
- (31) Patnaik, S. G.; Vedarajan, R.; Matsumi, N. BIAN Based Functional Diimine Polymer Binder for High Performance Li Ion Batteries. *J. Mater. Chem. A* **2017**, *5* (34), 17909–17919. <https://doi.org/10.1039/c7ta03843g>.
- (32) Shkrob, I. A.; Marin, T. W.; Zhu, Y.; Abraham, D. P. Why Bis(Fluorosulfonyl)Imide is a “Magic Anion” for Electrochemistry. *J. Phys. Chem. C* **2014**, *118* (34), 19661–19671. <https://doi.org/10.1021/jp506567p>.
- (33) Wang, L.; Fu, Y.; Battaglia, V. S.; Liu, G. SBR-PVDF based Binder for the Application of SLMP in Graphite Anodes. *RSC Advances* **2013**, *3*, 15022-15027. <https://doi.org/10.1039/c3ra42773k>.

Chapter 5

Summary and Outlook

Electrochemical power sources are becoming very relevant in today's society where demand for power and sustainable growth are equally being advocated. The use of fossil fuels in large quantities has led to an increase in greenhouse gases resulting in global warming and pollution. With better efficiency and use of resources, electrochemical power sources are believed to power the future society. The switch from traditional fossil fuel society to a modern sustainable society with electrochemical power sources has already begun. Many technologies such as solar cells, batteries, fuel cells etc. have been commercialized leading to the development of portable electronics, electric vehicles etc. However, to keep up with the ever-increasing demand for energy, it is very important to develop and commercialize materials which have higher capacities and exhibits faster rate kinetics.

Chapter 1

In chapter 1, a brief introduction to the world's current energy scenario has been discussed. Energy sources and their classifications along with few examples are discussed in brief underlining the pros and cons. A brief discussion about batteries and its evolution is made along with the classification and types. The functioning of lithium-ion batteries and their components are explained. An overview of a variety of anode materials along with their electrochemistry has been given highlighting the advantages and disadvantages associated with each of them. Various approaches taken by the researchers to overcome the drawbacks of anode materials have also been discussed in brief. The author discusses the solid electrolyte interfaces (SEI) and highlights their importance in the performance of the batteries. Various theories related to SEI formation is also discussed. Polymers are integrated in our day to day life and they play a very crucial role in our day to day life. The importance of the polymeric binders in LiBs is discussed and a variety of conventionally used binders are given. The rise of poly(ionic liquid)s (PILs) as an innovative class of binders and their scope in energy-related applications is discussed briefly. The structural

diversity of PILs and the effect of PIL structure its properties are also discussed. Finally, banking on the properties of PILs and their ability to tune the interface, the author forms the objectives and scope of the research.

Chapter 2

Chapter 2 deals with the design and synthesis of allylimidazolium based PIL (PVBCAImTFSI) as an anodic binder for application in the graphite anodes. HOMO-LUMO levels were predicted by density functional theory (DFT) to understand redox behaviour. The lower LUMO levels of the PIL lead to suppression in the electrolyte degradation leading to the formation of a better SEI. Due to this, the PIL binder gave good results and showed improvement over traditionally used PVDF binder. This leads to the improvement in the lithium-ion diffusion coefficient by almost 41% in PVBCAImTFSI based anodes as compared to the PVDF based anodes. PIL binder exhibited a very good electrolyte uptake which led to the formation of ion-conducting pathways in the active material. Also, the PIL binder showed better adhesion to the current collector. The PIL based anodes also showed enhanced interfacial properties with lower interfacial and SEI resistances compared to the PVDF based binders. These properties cumulatively led to the improved charge-discharge performance of PIL binder. A discharge capacity of about 210 mAh/g was observed at 1C rate with 95 % capacity retention after 500 cycles of charge-discharge cycling. Also, it displayed an enhanced rate performance and higher discharge capacity than PVDF at higher charge-discharge rates indicating good stability. Additionally, this study leads to highlights the importance of the rational design of binders.

Chapter 3

This chapter highlights the importance of the substituent and the counter-ion in the PIL structure on its performance as anodic binders in LiBs. Two PIL binders with varying side-chain and counter-ion (PVBCAImFSI & PVBCBImTFSI) have been synthesized and their performance as a binder for graphite anodes in LiBs has been evaluated. Cyclic voltammetry studies indicated suppressed electrolyte degradation in PVBCAImFSI based anodes indicating the formation of a robust SEI. Better interfacial properties reflected in the lithium-ion diffusion coefficient to higher than the

PVBCBImTFSI based anodes. Slower ion-diffusion kinetics in the case of PVBCBImTFSI anodes decreases the lithium-ion diffusion coefficient. Due to the suppressed electrolyte degradation, DEIS studies indicated the PVBCAImFSI binder based anodes to have better interfacial properties. The R_{SEI} values obtained was lesser than those for PVBCBImTFSI at all potentials. These observations were confirmed by the morphological characterizations. PVBCAImFSI based anodes exhibited a stable reversible discharge capacity for 1500 cycles with a capacity retention of almost 60%. The stability of the PVBCAImFSI based anodes was shown to be better than the PVBCBImTFSI based anodes. The above results indicated the synergy of the allyl group as a side-chain and FSI anion as counter-ion in the PIL binder structure leads to enhanced capacity and better durability.

Chapter 4

Chapter 4 deals with the surface modification of silicon nanoparticles with PIL and investigates its performance in composite anodes for LiBs. Silicon falls into the category of high energy density materials with a gravimetric energy density of over 4000 mAh/g, has immense potential to plug the current energy demand. However, it is plagued by extensive volume changes during the lithiation and delithiation resulting in pulverization, increase in cell resistance and capacity fade. Surface functionalization of silicon nanoparticles with PILs leads to the improvement in the interfacial properties. In this work, PIL functionalized silicon nanoparticles were prepared by esterification of poly[1-(5-carboxypentyl)-3-vinyl-1H-imidazol-3-ium bromide] with hydroxyl functionalized silicon nanoparticles. Cyclic voltammetry studies of PIL functionalized silicon nanoparticles based composite anodes indicated an increase in the lithiation-delithiation currents with the cycling. They also exhibited a very high lithium-ion diffusion coefficient which indicated a robust and conducive SEI formation. Electrochemical impedance measurements indicated the improvement of the interface after the cyclic voltammetry studies. These electrodes exhibited about 735 mAh/g_{Si} of reversible discharge capacity after 34 cycles. The results obtained in this chapter are very encouraging with a lot of scope for the improvement in the performance of the anodes by fine-tuning of the PIL structure and functionalization.

In the last two decades, the class of PILs have grown leaps and bounds with applications as thermoresponsive materials, ion sensing, CO₂ fixation, solid polymer electrolytes etc. The work presented in this thesis is one endeavour to highlight the capability of poly(ionic liquid)s in tuning

the interfacial properties at the electrode-electrolyte interface broadening its horizon as well as its scope. The results obtained presented in this thesis is just the tip of the iceberg and the author believes there is immense potential to be explored. With appropriate structural design, the author envisions that the PILs can be designed to enhance the interfacial properties of the high energy density materials such as Silicon and metallic lithium. This will be of great commercial interest and can revolutionize the battery technology and all other associated sectors. The author hopes that this work can serve as the initial impetus for more research into this class of materials.

List of Publications and Conferences

Publications:

1. Tejkiran Pindi Jayakumar, Rajashekar Badam, Noriyoshi Matsumi. “Allylimidazolium-Based Poly(Ionic Liquid) Anodic Binder for Lithium-Ion Batteries with Enhanced Cyclability.” ACS Appl. Energy Mater. 2020, 3, 4, 3337-3346. <https://doi.org/10.1021/acsaem.9b02376>.

Under preparation:

1. Tejkiran Pindi Jayakumar, Rajashekar Badam, Noriyoshi Matsumi. “Effect of PIL Structure on its Performance as Anodic Binder in Li-ion Battery.”
2. Sai Gourang Patnaik, Tejkiran Jayakumar Pindi, Yukihiro Sawamura, Noriyoshi Matsumi. “Defined poly(borosiloxane) as an artificial solid electrolyte interface layer for thin-film silicon anodes.”

Oral Presentations:

1. Tejkiran Pindi Jayakumar, Rajashekar Badam, Noriyoshi Matsumi. “Allylimidazolium based Poly(ionic liquid)s Binders for Li-ion Batteries with Enhanced Interfacial Properties.” **60th Battery Symposium, Kyoto, Japan. (Nov 2019)**
2. Tejkiran Pindi Jayakumar, Rajashekar Badam, Noriyoshi Matsumi. “Poly(ionic liquid) Based Anodic Binder with Enhanced Cyclability for Lithium-ion Batteries.” **236th ECS Meeting, Atlanta, Georgia, USA. (Oct 2019)**
3. Tejkiran Pindi Jayakumar, Rajashekar Badam, Noriyoshi Matsumi. “Poly(Ionic Liquid) Binders for Li-Ion Battery Anodes with Improved Interfacial Properties and Enhanced Cyclability.” **SPSJ 68th Symposium on**

Macromolecules, Bunkyo Campus, Fukui University, Fukui, Japan. (Sept 2019)

4. Tejkiran Pindi Jayakumar, Rajashekar Badam, Noriyoshi Matsumi. “Poly(ionic liquid) Anodic Binder with Enhanced Cyclability for Lithium-ion Batteries.” **ANEM2018-Advanced Nano and Energy conference, The University of Western Australia, Perth, Australia. (Dec 2018)**
5. Tejkiran Pindi Jayakumar, Rajashekar Badam, Noriyoshi Matsumi. “Polymerized Ionic Liquid Type Anodic Binder for Li-ion Battery Application with Enhanced Cyclability.” **59th Battery Symposium, Osaka, Japan. (Nov 2018)**
6. Tejkiran Pindi Jayakumar, Rajashekar Badam, Noriyoshi Matsumi. “Ionic Liquid Tagged Polymer as Binder Material for Li-ion Batteries.” **ECSJ Fall Meeting, in Kakuma Campus, Kanazawa University, Kanazawa, Ishikawa, Japan. (Sep 2018)**

Poster Presentations:

1. Tejkiran Pindi Jayakumar, Rajashekar Badam, Noriyoshi Matsumi. “Polymerized Ionic Liquid as Anode Binder for Li-ion Secondary Batteries.”, **CSJ Regional Meeting, Toyama University, Toyama, Japan. (Nov 2018).**
2. Tejkiran Pindi Jayakumar, Rajashekar Badam, Noriyoshi Matsumi. “Allylimidazolium Based Poly(ionic liquid) Binder for Lithium-ion Batteries with Enhanced Cyclability.” **JAIST Japan-India Symposium on Advanced Science 2019, Nomi, Japan. (Mar 2019)**
3. Tejkiran Pindi Jayakumar, Rajashekar Badam, Noriyoshi Matsumi. “Poly(ionic liquid) Based Functional Anodic Binder for Li-ion Batteries.” **68th SPSJ Annual Meeting, Osaka, Japan. (May 2019)**

4. Tejkiran Pindi Jayakumar, Rajashekar Badam, Noriyoshi Matsumi. “Effect of the Structure of Poly(ionic liquid) Anodic Binders on the Performance of Lithium Ion Batteries.” **69th SPSJ Annual Meeting, Fukuoka, Japan. (May 2020)**